

Some pages of this thesis may have been removed for copyright restrictions.

If you have discovered material in AURA which is unlawful e.g. breaches copyright, (either yours or that of a third party) or any other law, including but not limited to those relating to patent, trademark, confidentiality, data protection, obscenity, defamation, libel, then please read our [Takedown Policy](#) and [contact the service](#) immediately

INVESTIGATION OF THE EFFECTS OF LOW ENERGY HIGH DOSE ION BOMBARDMENT IN METALS AND COMPOUND SEMICONDUCTORS

HARPREET KAUR SANGHERA

Doctor of Philosophy

THE UNIVERSITY OF ASTON IN BIRMINGHAM

November 1998

This copy of the thesis has been supplied on condition that anyone who consults it is understood to recognise that its copyright rests with its author and no quotation from the thesis and no information derived from it may be published without proper acknowledgement.

INVESTIGATION OF THE EFFECTS OF LOW ENERGY HIGH DOSE ION
BOMBARDMENT IN METALS AND COMPOUND SEMICONDUCTORS

Harpreet Kaur Sanghera
Doctor of Philosophy
1998

Summary

The effect of low energy nitrogen molecular ion beam bombardment on metals and compound semiconductors has been studied, with the aim to investigate at the effects of ion and target properties. For this purpose, nitrogen ion implantation in aluminium, iron, copper, gold, GaAs and AlGaAs is studied using XPS and Angle Resolve XPS. A series of experimental studies on N_2^+ bombardment induced compositional changes, especially the amount of nitrogen retained in the target, were accomplished. Both monoenergetic implantation and non-monoenergetic ion implantation were investigated, using the VG Scientific ESCALAB 200D system and a d. c. plasma cell, respectively.

When the samples, with the exception of gold, are exposed to air, native oxide layers are formed on the surfaces. In the case of monoenergetic implantation, the surfaces were cleaned using Ar^+ beam bombardment prior to implantation. The materials were then bombarded with N_2^+ beam and eight sets of successful experiments were performed on each sample, using a rastered N_2^+ ion beam of energy of 2, 3, 4 and 5 keV with current densities of $1 \mu A/cm^2$ and $5 \mu A/cm^2$ for each energy. The bombarded samples were examined by ARXPS. After each complete implantation, XPS depth profiles were created using Ar^+ beam at energy 2 keV and current density $2 \mu A/cm^2$. As the current density was chosen as one of the parameters, accurate determination of current density was very important. In the case of glow discharge, two sets of successful experiments were performed in each case, by exposing the samples to nitrogen plasma for the two conditions: at low pressure and high voltage and high pressure and low voltage. These samples were then examined by ARXPS.

On the theoretical side, the major problem was prediction of the number of ions of an element that can be implanted in a given matrix. Although the programme is essentially on experimental study, but an attempt is being made to understand the current theoretical models, such as SATVAL, SUSPRE and TRIM. The experimental results were compared with theoretical predictions, in order to gain a better understanding of the mechanisms responsible.

From the experimental results, considering possible experimental uncertainties, there is no evidence of significant variation in nitrogen saturation concentration with ion energy or ion current density in the range of 2-5 keV, however, the retention characteristics of implantant seem to strongly depend on the chemical reactivity between ion species and target material. The experimental data suggests the presence of at least one thermal process. The discrepancy between the theoretical and experimental results could be the inability of the codes to account for molecular ion impact and thermal processes.

Keywords: Ion implantation, Ion bombardment, Depth profiling, Surface segregation, Sputtering, Nitridation, XPS, Angle Resolved XPS (ARXPS), TRIM, SATVAL, SUSPRE.

Dedicated to....

my son, Sachveen
and
my husband, Mubarak

.....for making it all worth while

ACKNOWLEDGEMENTS

I am indebted to

Prof. John L. Sullivan for his keen interest, hard work and inspiration

George Pearce for his great support and encouragement

Dr. Sayah Saied for her guidance and cooperation

Zdzislaw Wronski for his enthusiasm and suggestions

Dr. Andy Abbot for his technical support

GEC Marconi Technology, Caswell for supplying samples

All at Surface Science Group for their friendship, help and good humour

My family for their affection, inspiration, patience and fathomless cooperation

Table of Contents

	Page
Chapter 1	
Literature Survey.....	(21-67)
1.1	Introduction.....21
1.2	Target Materials.....22
1.3	Ion beam modifications techniques.....24
1.4	Ion solid interactions.....26
	Primary effects.....28
	Secondary effects.....28
1.4.1	Stopping power.....29
	Nuclear stopping.....29
	Electronic stopping.....31
	Total stopping.....31
1.4.2	Ion Range.....31
1.4.3	Ion implantation profiles.....33
1.4.4	Sputtering.....38
	Sputter Yield.....38
	Sigmund's Theory of Sputtering.....38
	The factor α39
	Binary collision approximation.....41
	Some Other Sputtering Theories.....41
	Bombardment with molecular ions.....43
1.4.5	Preferential Sputtering.....43
	Malherbe's Theory.....44
	Kelly's model of nonstoichiometric sputtering.....45
1.4.6	Segregation.....46
	1.4.6.1 Gibbsian Segregation (adsorption).....46
	1.4.6.2 Radiation-induced Segregation.....47
	2.4.6.3 Other Segregation Models.....48
	Kelly's model for BIGS.....48
	Thermodynamic interpretation to equilibrium segregation.....48
	Miedema's model.....49

	Plessis and Wyk model.....	49
	Weidrasch's model (non-equilibrium segregation).....	50
	Some other models.....	50
1.4.7	Radiation-Enhanced Diffusion.....	51
1.4.8	Recoil implantation.....	52
1.4.9	Cascade (Isotropic, Displacement) Mixing.....	52
1.4.10	Phenomenological model for surface compositional changes.....	52
1.4.11	Chemical Sputtering.....	54
1.5	Surface Binding Energy.....	54
1.6	Computer Simulations.....	57
	Trajectory Simulations.....	57
	Analytic Simulation.....	57
1.6.1	Trajectory Simulations.....	57
	1.6.1.1 Binary Collision (or Event Store Codes).....	58
	Binary Collision Approximation.....	58
	1.6.1.2 Monte Carlo Codes.....	60
	1.6.1.3 Multiple Interaction Simulations.....	60
	1.6.1.4 Hybrid Models.....	60
	1.6.1.5 Boltzmann Transport Approach.....	61
1.6.2	High Dose Effects.....	61
	1.6.2.1 Evaluation of High Dose Profiles.....	61
1.6.3	Computer Simulations Available.....	63
	1.6.3.1 TRIM.....	63
	1.6.3.2 SUSPRE.....	64
	1.6.3.3 SATVAL.....	65
1.7	Concluding Notes.....	65
1.8	Research Programme.....	66

Chapter 2 Surface Analytical Techniques and Depth Profiling..(68-88)

2.1	Introduction.....	68
2.2	Surface Analytical Techniques.....	68
	2.2.1 X-ray Photoelectron Spectroscopy (XPS).....	69
	2.2.1.1 Spectrum Analysis.....	69

	Characterization of a Surface.....	69
	Chemical State Information.....	72
	Plasmon Loss Features.....	72
	Valence Band Structure.....	72
	Shake-up Peaks.....	75
	X-ray Ghosts.....	75
	Multiple (or Exchange or Electrostatic) Splitting.....	75
2.2.1.2	Spectrum Processing.....	77
	Smoothing.....	77
	Energy Calibration.....	77
	Background removal.....	77
	Curve synthesis and curve fitting.....	77
2.2.1.3	Quantitative Analysis.....	78
2.3	Depth Profiling.....	80
2.3.1	Sputter Depth Profiling.....	81
	2.3.1.2 Measured profiles.....	81
	Achievable depth resolution.....	82
	Erosion rate.....	82
	2.3.1.3 Artefacts in Depth Profiling.....	83
2.3.2	Profiling by Variation of Electron Emission Angle (ARXPS).....	86

Chapter 3 Experimental Apparatus and Procedures.....(89-108)

3.1	Introduction.....	89
3.2	Apparatus.....	89
	3.2.1 VGScientific ESCALAB 200D Spectrometer.....	89
	3.2.1.1 Vacuum System.....	91
	3.2.1.2 Ion gun.....	91
	3.2.1.3 X-ray source.....	92
	3.2.1.4 Energy Analyser.....	92
	3.2.1.5 Data System.....	97
	3.2.2 Plasma cell (Glow discharge chamber).....	97
3.3	Selection of experimental materials.....	98
3.4	Determination of Current Density.....	101

3.5	Experimental procedure and measurements.....	101
3.5.1	Sample preparation.....	101
3.5.2	Monoenergetic implantation.....	103
3.5.2.1	Sample mounting and transport.....	103
3.5.2.2	General procedure.....	103
3.5.2.3	Experimental conditions for ion bombardment.....	104
3.5.2.4	XPS measurements.....	104
3.5.2.4.1	Spectra collection and calibration.....	105
3.5.2.4.2	Data processing.....	107
3.5.3	Glow discharge chamber.....	107
3.5.3.1	Routine procedure.....	107
3.5.3.2	Experimental conditions.....	108

Chapter 4 Experimental Results.....(109-180)

4.1	Monoenergetic implantation.....	109
4.1.1	Aluminium.....	109
4.1.1.1	Nitrogen implantation.....	109
4.1.1.2	Argon ion bombardment.....	113
4.1.1.3	Al spectra.....	113
4.1.1.4	ARXPS results.....	120
4.1.2	Iron.....	120
4.1.2.1	Nitrogen implantation.....	124
4.1.2.2	Argon ion bombardment.....	129
4.1.2.3	Fe spectra.....	129
4.1.2.4	ARXPS results.....	129
4.1.3	Copper.....	133
4.1.3.1	Nitrogen implantation.....	134
4.1.3.2	Argon ion bombardment.....	135
4.1.3.3	Cu spectra.....	135
4.1.3.4	ARXPS results.....	143
4.1.4	Gold.....	143
4.1.4.1	Nitrogen implantation.....	143
4.1.4.2	Au spectra.....	143

4.1.5	GaAs.....	143
4.1.5.1	Nitrogen implantation.....	143
4.1.5.2	Argon ion bombardment.....	151
4.1.5.3	GaAs spectra.....	151
4.1.5.4	ARXPS results.....	159
4.1.6	AlGaAs.....	159
4.1.6.1	Nitrogen implantation.....	159
4.1.6.2	Argon ion bombardment.....	159
4.1.6.3	AlGaAs spectra.....	169
4.1.6.4	ARXPS results.....	169
4.1.7	Arsenic.....	175
4.2	Plasma implantation.....	176
4.2.1	Aluminium.....	176
4.2.2	Iron.....	179
4.2.3	Copper.....	180
 Chapter 5 Theory and Computer Simulations.....(181-217)		
5.1	Introduction.....	181
5.2	Stopping power.....	181
5.2	Range of ions in various target materials.....	183
5.3	Ion and Recoil distributions.....	185
5.4	Surface Binding Energy.....	188
	Sublimation energy.....	189
	Heat of atomization.....	189
	Kelly's Model.....	190
	Malherbe's model.....	190
	Pair bond Model.....	190
	Surface tension.....	190
5.5	Implant surface concentration.....	191
5.6	Preferential sputtering of implanted Nitrogen.....	193
5.6.1	Calculation of scattering parameter, m	195
5.6.2	Depth of sputtered particles.....	197
5.6.3	Etch rate.....	202

5.7	Theoretical modelling of implantation.....	203
5.7.1	SATVAL code.....	203
5.7.2	SUSPRE code.....	211
5.7.3	Conclusions.....	212
5.8	Surface segregation and diffusion.....	212
5.8.1	Surface segregation.....	213
5.8.1.1	Radiation induced surface segregation.....	213
5.8.1.2	Segregation due to athermal processes.....	215
5.8.2	Radiation enhanced/induced diffusion.....	215
Chapter 6 Discussion.....		(218-255)
6.1	Monoenergetic implantation.....	218
6.1.1	Aluminium.....	218
6.1.1.1	Nitrogen implantation.....	218
6.1.1.2	Argon ion bombardment.....	221
6.1.1.3	Al spectra.....	221
6.1.1.4	ARXPS results.....	223
6.1.2	Iron.....	223
6.1.2.1	Nitrogen implantation.....	223
6.1.2.2	Argon ion bombardment.....	226
6.1.2.3	Fe spectra.....	226
6.1.2.4	ARXPS results.....	229
	Surface segregation.....	230
6.1.3	Copper.....	232
6.1.3.1	Nitrogen implantation.....	232
6.1.3.2	Argon ion bombardment.....	232
6.1.3.3	Cu spectra.....	233
6.1.3.4	ARXPS results.....	233
6.1.3.5	Implantation mechanism.....	234
6.1.4	Gold.....	235
6.1.5	GaAs.....	236
6.1.5.1	Nitrogen implantation.....	236
6.1.5.2	Argon ion bombardment.....	237

6.1.5.3	GaAs spectra.....	238
6.1.5.4	ARXPS results.....	240
6.1.5.5	Implantation mechanism.....	240
6.1.6	AlGaAs.....	242
6.1.6.1	Nitrogen implantation.....	242
6.1.6.2	Argon ion bombardment.....	243
6.1.6.3	AlGaAs spectra.....	243
6.1.6.4	ARXPS results.....	244
6.1.6.5	Implantation mechanism.....	245
6.1.7	As.....	246
6.2	Plasma implantation.....	246
6.3	Summary.....	248
Chapter 7	Conclusions and Future Work.....	(256-260)
7.1	Conclusions.....	256
7.2	Future Work.....	260
	References.....	261
	Publications.....	274

List of Tables

Table	Page
Table 1.1 Kelly's classification of sputtering processes.....	45
Table 2.1 Tabulation of optimised depth profiling conditions.....	85
Table 3.1 Arrangement of XPS system in VGScientific ESCALAB 200D.....	89
Table 3.2 Specification of EXO5 Ion Gun.....	91
Table 3.3 Inlet and exit apertures used in the analyser.....	97
Table 3.4 Values of heat of formation of nitrides (eV/atom), at 25 ⁰ C.....	98
Table 3.5 Determination of current density values for electron take-off angle of 0 ⁰	102
Table 3.6 Determination of current density values for electron take-off angle of 25 ⁰	102
Table 3.7 Time scale for a typical ion bombardment experiment.....	104
Table 3.8 Values of Relative Sensitivity Factor used with Al K _α and Mg K _α X-ray sources.....	107
Table 3.9 The experimental conditions for exposure of nitrogen plasama, for various samples.....	107
Table 4.1 Tabulation of measured (N / Al) saturation ratios.....	109
Table 4.2 The values of Al 2p binding energies (eV) and KLL kinetic energies (eV) for clean, N ₂ ⁺ bombarded, and then Ar ⁺ bombarded are tabulated in first three rows. The last two rows show the value of the above mentioned parameters for pure aluminium and standard AlN.....	120
Table 4.3 Tabulation of ARXPS data at various energies and current densities.....	121
Table 4.4 Tabulation of (N/Fe)saturation values.....	124
Table 4.5 The values of Fe 2p _{3/2} binding energies (eV) and L ₃ VV kinetic energies (eV) for as received, Ar ⁺ ion cleaned, N ₂ ⁺ bombarded, and then Ar ⁺ bombarded are tabulated in first four rows. The last two rows show the value of the above mentioned parameters for pure iron and standard mixture of Fe _{2,3,4} N. The values inside the brackets are the FWHM of the peak.....	133
Table 4.6 The values of N 1s binding energies (eV) and KL ₂₃ L ₂₃ kinetic energies (eV) for N ₂ ⁺ bombarded, standard mixture of Fe _{2,3,4} N, nitrogen present in C-N bonding, along with the values of Auger parameter.....	133
Table 4.7 ARXPS data of nitrogen ion implantation in iron, at various ion energies and current densities.....	134
Table 4.8 Tabulation of (N/Cu)saturation values.....	135
Table 4.9 The values of Cu 2p _{3/2} binding energies (eV) and L ₃ VV kinetic energies (eV) for as received, Ar ⁺ ion cleaned, N ₂ ⁺ bombarded, and then Ar ⁺ bombarded are tabulated in first four rows. The last two rows show the value of the above mentioned	

parameters for pure copper and standard Cu_3N . The values inside the brackets are the FWHM of the peak.....	141
Table 4.10 ARXPS data of nitrogen ion implantation in copper, at various ion energies and current densities.....	144
Table 4.11 The values of Ga 3d binding energies (eV) and Ga $\text{L}_3\text{M}_{45}\text{M}_{45}$ kinetic energies (eV) for as received, Ar^+ ion cleaned, N_2^+ bombarded, and then Ar^+ bombarded GaAs are tabulated in first four rows. The last three rows show the value of the above mentioned parameters for pure Ga, GaAs and GaN.....	158
Table 4.12 The values of As 3d binding energies (eV) and As $\text{L}_3\text{M}_{45}\text{M}_{45}$ kinetic energies (eV) for as received, Ar^+ ion cleaned, N_2^+ bombarded, and then Ar^+ bombarded GaAs are tabulated in first four rows. The last two rows show the value of the above mentioned parameters for pure As, and GaAs.....	158
Table 4.13 The values of N 1s binding energies (eV) and $\text{KL}_{23}\text{L}_{23}$ kinetic energies (eV) for N_2^+ bombarded GaAs, along with the values of Auger parameter.....	159
Table 4.14 ARXPS data of nitrogen ion implantation in GaAs, at various ion energies and current densities.....	160
Table 4.15 The values of Ga 3d binding energies (eV) and Ga $\text{L}_3\text{M}_{45}\text{M}_{45}$ kinetic energies (eV) for Ar^+ ion cleaned, N_2^+ bombarded, and then Ar^+ bombarded AlGaAs are tabulated in first four rows. The last three rows show the value of the above mentioned parameters for pure Ga, GaAs and AlGaAs and GaN.....	175
Table 4.16 The values of As 3d binding energies (eV) and As $\text{L}_3\text{M}_{45}\text{M}_{45}$ kinetic energies (eV) for Ar^+ ion cleaned, N_2^+ bombarded, and then Ar^+ bombarded AlGaAs are tabulated in first four rows. The last two rows show the value of the above mentioned parameters for pure As, GaAs and AlGaAs.....	175
Table 4.17 The values of Al 2p binding energies (eV) and KLL kinetic energies (eV) for clean, N_2^+ bombarded, and then Ar^+ bombarded AlGaAs are tabulated in first three rows. The last two rows show the value of the above mentioned parameters for pure aluminium and standard AlN.....	176
Table 4.18 The values of N 1s binding energies (eV) and $\text{KL}_{23}\text{L}_{23}$ kinetic energies (eV), along with the values of Auger parameter, for N_2^+ bombarded AlGaAs and Al and for standard GaN are also reported	176
Table 4.19 ARXPS data of nitrogen ion implantation in AlGaAs, at various ion energies and current densities.....	177
Table 4.20 ARXPS data of nitrogen glow discharge exposure to aluminium.....	179
Table 4.21 ARXPS data of nitrogen glow discharge exposure to Iron.....	179
Table 4.22 ARXPS data of nitrogen glow discharge exposure to Copper.....	180
Table 5.1 Some Physical properties of target materials.....	181
Table 5.2 Ion range and straggle in different target materials, at various ion energies.....	185

Table 5.3 Tabulation of energy losses by ions and recoils in the form of ionization, vacancies and phonons, The calculations are made using TRIM.....	188
Table 5.4 Some physical properties of the target elements [Lide, 1991].....	189
Table 5.5 Bond strength values (eV) of A-B system at room temperature [Lide, 1991].....	189
Table 5.6 List of surface concentration of implantant in the target materials, using sputter yield values calculated as mentioned above. Here E is the ion beam energy in units of keV.....	191
Table 5.7 Tabulation of surface concentration of implantant in the target materials, using sputter yield values obtained by SUSPRE. Here E is the ion beam energy in units of keV.....	193
Table 5.8 A list of the ratio of sputter yields, (Y_T / Y_N), for target-nitride system.....	193
Table 5.9 The ratio of ion beam energy to reduced energy.....	195
Table 5.10 Average sputter depth Δx_0 for the target materials. Here atomic density is expressed in Atoms/ \AA^3 and depth in \AA	202
Table 5.11 Erosion rate values (nm/s), calculated for various target materials by using SUSPRE code, for ion beams at a given energy and a current density of $5 \mu\text{A}/\text{cm}^2$	202
Table 5.12 The nitrogen to target atomic concentration ratios (saturated), at various ion energies. These values are predicted by SATVAL.....	204
Table 5.13 The saturated nitrogen to target atomic concentration ratios, predicted by SUSPRE.....	211
Table 5.14 Surface tension, melting point and area of one bulk atom of the elements [Lide, 1992].....	214
Table 5.15 Tabulation of initial bulk composition and the surface composition values as a result of bombardment induced segregation.....	215
Table 5.16 List of initial bulk composition and the collision cascade induced surface segregation composition values.....	215
Table 5.17 The first ionisation energy of the target elements [Lide, 1992].....	217
Table 6.1 Nuclear and electronic stopping powers of nitrogen ions in iron, calculated using SUSPRE code.....	229
Table 6.2 Summary of monoenergetic ion implantation results.....	249
Table 6.3 Radius of one bulk atom of the elements, r and radius of an interstitial site, r_i , in the crystal lattice.....	250
Table 6.4 Calculation of stored nitrogen ion fluence at saturation, $F_{r,s}$, and nitrogen saturation concentration value, for various target materials. The values outside the bracket are for implantation at ion energy 2 keV and those inside the bracket are for implantation at ion energy 5 keV.....	251

List of Figures

Figure	Page
Figure 1.1 Schematic representation of (a) direct ion implantation and (b) plasma source ion implantation.....	25
Figure 1.2 Various possible ion-solid interaction processes [After Malherbe, 1994].....	27
Figure 1.3 Nuclear and electronic stopping power of an ion as a function of energy [After Sigmund, 1981].....	32
Figure 1.4 Schematic presentation of penetrated path length R , projected range R_p and the penetration depth x , for an ion of initial velocity v and energy E_0 , incident at an angle θ w.r.t. the surface normal.....	34
Figure 1.5 A schematic illustration of effect of low and high-dose ion implantation Figures (a) represents an ion A^+ striking the target B and (b) the resultant profile of A, for low-dose ion implantation and Figures (c) represents ions of type A^+ striking the target B and (d) the resultant profile of A, for high-dose ion implantation [After Liao and Mayer, 1978].....	36
Figure 1.6 (a) dependence of α on mass ratio, solid curve derived by Sigmund, dotted by Andersen and Bay (b) dependence of α on angle of incidence and (c) dependence of α on mass ratio.....	40
Figure 1.7 Schematic of binary collision approximation (elastic collision).....	42
Figure 1.8 Effects of various combinations of GA, PS, RED, DM and RIS on the time evolution of the surface concentration of Cu during sputtering at 400°C, for 5 keV Ar^+ bombardment.....	53
Figure 1.9 Representation of the binary collision approximation.....	59
Figure 1.10 Some of the important effects considered during simulation [Webb, 1992].....	62
Figure 2.1 Principle of X-ray Photoelectron Spectroscopy.....	70
Figure 2.2 XPS spectrum of oxidised aluminium.....	71
Figure 2.3 XPS spectrum of (a) pure Al and (b) nitrided Al.....	73
Figure 2.4 Plasmon loss fine structure associated with the aluminium 2p, 2s and KLL Auger spectrum. The successive bulk plasmon losses are indicated as B1 and B2.....	74
Figure 2.5 VBXPS of (a) pure Al and (b) nitrided Al.....	76
Figure 2.6 Deconvolution of various chemical states in Al 2p spectrum.....	79
Figure 2.7 Angular dependence of energy re-emission coefficient for self-sputtering of nickel at two different impact energies. (from Briggs and Seah).....	84
Figure 2.8 Variation of electron intensity with depth.....	87

Figure 3.1 Layout of VGScientific ESCALAB 200D.....	90
Figure 3.2 Schematics of ion optics in EXO5 ion gun system.....	93
Figure 3.3 Structure of twin anode X-ray source.....	94
Figure 3.4 Schematic of a 150 ^o Hemispherical sector analyser.....	95
Figure 3.5 A schematic of energy levels of a hemispherical sector analyser.....	96
Figure 3.6 Schematics of the apparatus used for generating dc plasma.....	99
Figure 4.1 XPS time profile of nitrogen implantation in aluminium at E = 2, 3, 4 and 5 keV; $\mu = 1 \mu\text{A}/\text{cm}^2$	110
Figure 4.2 XPS time profile of nitrogen implantation in aluminium at E = 2, 3, 4 and 5 keV; $\mu = 5 \mu\text{A}/\text{cm}^2$	111
Figure 4.3 XPS time profile of nitrogen to aluminium relative atomic concentration ratios for implantation in aluminium at E = 2, 3, 4 and 5 keV; and current densities of (a) $\mu =$ $1 \mu\text{A}/\text{cm}^2$ and (b) $\mu = 5 \mu\text{A}/\text{cm}^2$	112
Figure 4.4 XPS time profile of nitrogen ion implantation at (a) 2 keV, (b) 3 keV, (c) 4 keV and (d) 5 keV at current densities of $1 \mu\text{A}/\text{cm}^2$ and $5 \mu\text{A}/\text{cm}^2$	114
Figure 4.5 Nitrogen depth and time profile using Ar ⁺ of energy 2 keV and $2 \mu\text{A}/\text{cm}^2$ after nitrogen implantation on aluminium at E = 2, 3, 4 and 5 keV and current densities of (a) $\mu = 1 \mu\text{A}/\text{cm}^2$ and (b) $\mu = 5 \mu\text{A}/\text{cm}^2$. The time scale is converted to the depth scale using the etch rate value calculated from SUSPRE.....	115
Figure 4.6 Photoelectron spectra of N 1s.....	116
Figure 4.7 Auger spectrum of (a) pure aluminium and (b) nitrided aluminium (Al 2p peak is shown inset).....	117
Figure 4.8(a) Deconvolution of various chemical states in Al 2p spectra, after 1 minute of nitrogen ion bombardment (uncalibrated spectra).....	118
Figure 4.8 (b) Deconvolution of various chemical states in Al 2p spectra, after 80 minutes of nitrogen ion bombardment at 4 keV and $1 \mu\text{A}/\text{cm}^2$ (uncalibrated spectra).....	119
Figure 4.9 Variation of N/Al _{Nit} and N/Al _{tot} with the implantation time at E = 2, 3, 4 and 5keV; (a) $\mu = 1 \mu\text{A}/\text{cm}^2$. and (b) $\mu = 5 \mu\text{A}/\text{cm}^2$	122
Figure 4.10 Al 2p photoelectron spectrum of nitrided aluminium, at different take-off-angles, (a) 0 ^o , (b) 25 ^o , (c) 50 ^o , (d) 60 ^o and (e) 75 ^o , here angle is measured w.r.t. the normal to the sample surface.....	123
Figure 4.11 XPS time profiles of nitrogen ion implantation in iron at 2, 3, 4 and 5 keV at a current density of $1 \mu\text{A}/\text{cm}^2$. The relative atomic concentrations of oxygen, nitrogen and carbon are multiplied by 5 for clarity.....	125
Figure 4.12 XPS time profiles of nitrogen ion implantation in iron at 2, 3, 4 and 5 keV at a current density of $5 \mu\text{A}/\text{cm}^2$. The relative atomic concentrations of oxygen,	

nitrogen and carbon are multiplied by 5 for clarity.....	126
Figure 4.13 XPS time profile of nitrogen to iron relative atomic concentration ratio for implantation in iron at E = 2, 3, 4 and 5 keV; and current densities of (a) $\mu = 1 \mu\text{A}/\text{cm}^2$ and (b) $\mu = 5 \mu\text{A}/\text{cm}^2$	127
Figure 4.14 XPS profile of nitrogen to iron relative atomic concentrations, as a function of ion dose, at ion energies of (a) 2 keV, (b) 3 keV, (c) 4 keV and (d) 5 keV at current densities of $1 \mu\text{A}/\text{cm}^2$ and $5 \mu\text{A}/\text{cm}^2$	128
Figure 4.15 Depth and time profile of nitrogen implanted in iron, using Ar^+ of energy 2keV and $2 \mu\text{A}/\text{cm}^2$ after nitrogen implantation on iron at E = 2, 3, 4 and 5 keV and (a) $1 \mu\text{A}/\text{cm}^2$ and (b) $\mu = 5 \mu\text{A}/\text{cm}^2$. The time scale is converted to the depth scale using the etch rate value calculated from SUSPRE.....	130
Figure 4.16 Fe 2p, Valence Band X-ray Photoelectron Spectra (VBXPS) and Auger spectra of (a) before and (b) after N_2^+ ion bombardment of iron sample. In all these figures, the spectras are normalized for comparison.....	131
Figure 4.17 N 1s and Auger spectra of nitrogen ion bombarded iron sample, using XPS.....	132
Figure 4.18 XPS time profiles of nitrogen ion implantation in copper at 2, 3, 4 and 5 keV at a current density of $1 \mu\text{A}/\text{cm}^2$. For clarity, the nitrogen, carbon and oxygen atomic concentration values are multiplied by 5.....	136
Figure 4.19 XPS time profiles of nitrogen ion implantation in copper at 2, 3, 4 and 5 keV at a current density of $5 \mu\text{A}/\text{cm}^2$. For clarity, the nitrogen, carbon and oxygen atomic concentration values are multiplied by 5.....	137
Figure 4.20 XPS profile of nitrogen to copper relative atomic concentration ratios for ion implantation in copper at 2, 3, 4 and 5 keV at current densities of (a) $1 \mu\text{A}/\text{cm}^2$ and (b) $5 \mu\text{A}/\text{cm}^2$	138
Figure 4.21 XPS Ar^+ depth and time profile of nitrogen implanted in copper, using Ar^+ of energy 2 keV and $2 \mu\text{A}/\text{cm}^2$ after nitrogen implantation on iron at E = 2, 3, 4 and 5 keV and (a) $1 \mu\text{A}/\text{cm}^2$ and (b) $\mu = 5 \mu\text{A}/\text{cm}^2$. The time scale is converted to the depth scale using the etch rate value calculated from SUSPRE.....	139
Figure 4.22 The normalized Cu 2p, Auger spectra and Valence Band X-ray Photoelectron Spectra (VBXPS) of (a) before and (b) after N_2^+ ion bombardment of copper sample.....	140
Figure 4.23 N 1s spectra obtained from (a) nitrogen ion bombarded copper sample (b) Cu_3N standard sample.....	142
Figure 4.24 Au 4d, 4f and Valence band spectra of (a) before and (b) after N_2^+ ion bombardment of gold sample.....	145
Figure 4.25 N 1s spectra of nitrogen obtained from nitrogen ion bombarded gold sample...	146

Figure 4.26 XPS time profile of nitrogen ion implantation in GaAs at 2, 3, 4 and 5 keV at a current density of 1 $\mu\text{A}/\text{cm}^2$	147
Figure 4.27 XPS time profile of nitrogen ion implantation in GaAs at 2, 3, 4 and 5 keV at a current density of 5 $\mu\text{A}/\text{cm}^2$	148
Figure 4.28 Variation of ratio of relative atomic concentration of nitrogen to target, N/(Ga+As), as a function of implantation time, for implantation at 2, 3, 4 and 5 keV at current densities of (a) 1 $\mu\text{A}/\text{cm}^2$ and (b) 5 $\mu\text{A}/\text{cm}^2$	149
Figure 4.29 Variation of ratio of relative atomic concentration of arsenic and gallium, (As/Ga), as a function of implantation time at 2, 3, 4 and 5 keV at current densities of (a) 1 $\mu\text{A}/\text{cm}^2$ and (b) 5 $\mu\text{A}/\text{cm}^2$	150
Figure 4.30 Nitrogen depth and time profile using Ar^+ of energy 2keV and 2 $\mu\text{A}/\text{cm}^2$ after nitrogen implantation on GaAs at $E = 2, 3, 4$ and 5 keV at current densities of (a) $\mu = 1 \mu\text{A}/\text{cm}^2$ and (b) $\mu = 5 \mu\text{A}/\text{cm}^2$. The time scale is converted to the depth scale using the etch rate value calculated from SUSPRE.....	152
Figure 4.31 Variation of ratio of relative atomic concentration of arsenic and gallium, (As/Ga), as a function of Ar^+ bombardment time after N_2^+ implantation at 2, 3, 4 and 5 keV at a current density of (a) 1 $\mu\text{A}/\text{cm}^2$ and (b) 5 $\mu\text{A}/\text{cm}^2$	153
Figure 4.32 GaAs 3d and Auger spectra of (a) before and (b) after N_2^+ ion bombardment of GaAs sample. The spectra are normalized for comparison.....	154
Figure 4.33 Deconvolution of various chemical states in Ga 3d spectra, after (a)1 minute and (b) 40 minutes of nitrogen ion bombardment at 2 keV and 5 $\mu\text{A}/\text{cm}^2$. The table gives the parameters chosen for peak fitting, The values outside the brackets are for case (a) and those inside the brackets are for case (b). The G/L ratio was same for both cases.....	155
Figure 4.34 Variation of N/Ga(GaN) with the implantation time at 2, 3, 4 and 5 keV at current densities of (a) 1 $\mu\text{A}/\text{cm}^2$ and (b) 5 $\mu\text{A}/\text{cm}^2$	156
Figure 4.35 Ga 2p and As2p spectra of (a) before and (b) after N_2^+ ion bombardment of GaAs sample. The spectra are normalized for comparison.....	157
Figure 4.36 N 1s and Auger spectra of nitrogen obtained from nitrogen ion bombarded GaAs sample.....	161
Figure 4.37 GaAs Valence Band X-ray Photoelectron Spectra (VBXPS) of (a) before and (b) after N_2^+ ion bombardment of GaAs sample. The spectra are normalized for comparison.....	162
Figure 4.38 XPS time profile of nitrogen ion implantation in AlGaAs at 2, 3, 4 and 5 keV at a current density of 1 $\mu\text{A}/\text{cm}^2$	163
Figure 4.39 XPS time profile of nitrogen ion implantation in AlGaAs at 2, 3, 4 and 5 keV at a	

current density of $5 \mu\text{A}/\text{cm}^2$	164
Figure 4.40 Variation of ratio of relative atomic concentration of nitrogen and the sum of that for aluminium, gallium and arsenic $[\text{N}/(\text{Al}+\text{Ga}+\text{As})]$ as a function of implantation time at 2, 3, 4 and 5 keV at current densities of (a) $1 \mu\text{A}/\text{cm}^2$ and (b) $5 \mu\text{A}/\text{cm}^2$	165
Figure 4.41 Variation of ratio of relative atomic concentration ratio of implantant and target atoms, as a function of N_2^+ bombardment time, for implantation at $\mu = 5 \mu\text{A}/\text{cm}^2$..	166
Figure 4.42 Variation of ratio of relative atomic concentration of arsenic and gallium, (As/Ga) , as a function of implantation time at 2, 3, 4 and 5 keV at current densities of (a) $1 \mu\text{A}/\text{cm}^2$ and (b) $5 \mu\text{A}/\text{cm}^2$	167
Figure 4.43 Nitrogen depth and time profile using Ar^+ of energy 2 keV and $2 \mu\text{A}/\text{cm}^2$ after nitrogen implantation on AlGaAs at $E = 2, 3, 4$ and 5 keV and current densities of (a) $\mu = 1 \mu\text{A}/\text{cm}^2$ and (b) $\mu = 5 \mu\text{A}/\text{cm}^2$. The time scale is converted to the depth scale using the etch rate value calculated from SUSPRE.....	168
Figure 4.44 Variation of ratio of relative atomic concentration ratio of implantant and target, $\text{N}/(\text{Al}+\text{Ga}+\text{As})$, as a function of Ar^+ bombardment time, after nitrogen implantation on AlGaAs at $E = 2, 3, 4$ and 5 keV and current densities of (a) $\mu = 1 \mu\text{A}/\text{cm}^2$ and (b) $\mu = 5 \mu\text{A}/\text{cm}^2$	170
Figure 4.45 Variation of ratio of relative atomic concentration of arsenic and gallium, (As/Ga) , as a function of Ar^+ bombardment time, after nitrogen implantation at 2, 3, 4 and 5 keV at current densities of (a) $1 \mu\text{A}/\text{cm}^2$ and (b) $5 \mu\text{A}/\text{cm}^2$	171
Figure 4.46 Comparison of Al 2p, GaAs 3d and As $\text{L}_3\text{M}_{45}\text{M}_{45}$ spectra of (a) before and (b) after N_2^+ ion bombardment of AlGaAs sample.....	172
Figure 4.47 Comparison of AlGaAs Valence band and Ga Auger spectra of (a) before and (b) after N_2^+ ion bombardment of AlGaAs sample.....	173
Figure 4.48 N 1s and Auger spectra of nitrogen obtained from nitrogen ion bombarded AlGaAs sample.....	174
Figure 4.49 N 1s spectra for the target samples (a) aluminium, (b) iron and (c) copper, exposed to nitrogen glow discharge.....	178
Figure 5.1 Variation of (a) nuclear and electronic stopping powers; and (b) reflection coefficient, with nitrogen ion beam energy, for various target materials. The calculations are made using SUSPRE code, for nitrogen ions incident on a given target at an angle of 51.6°	182
Figure 5.2 Variation of ion range, with nitrogen ion beam energy, for various target materials. The calculations are made using SUSPRE code, for nitrogen ions incident on a given target at an angle of 51.6°	184
Figure 5.3 Nitrogen ion and target atom recoil distribution for nitrogen ion bombarded iron and AlGaAs targets.....	186

Figure 5.4 Sputter yield values as a function of ion beam energy, for target materials, (a) calculated and (b) obtained from SUSPRE code.....	192
Figure 5.5 Reduced energy parameter, as a function of ion beam energy.....	194
Figure 5.6 TF and Biersack screening radii, as a function of target atomic number and, universal nuclear stopping power as a function of ion beam energy.....	196
Figure 5.7 Comparison between ZBL and TF nuclear stopping power.....	198
Figure 5.8 The scattering parameter, m , as a function of ion beam energy and Atomic number.....	199
Figure 5.9 The correction factor f for target-nitrogen system, as a function of ion beam energy.....	200
Figure 5.10 Sputter yield ratio, corrected for difference in power scattering parameter for elements with different mass, as a function of ion beam energy. Here it represents the ratio of sputter yield of target material to nitrogen.....	201
Figure 5.11 Relative areas under the nitrogen ion concentration curves at different energies vs. depth for saturated concentration of nitrogen in aluminium (using SATVAL code).....	205
Figure 5.12 Time profile of nitrogen ion implantation on aluminium using SATVAL code at energies $E = 2, 3, 4$ and 5 keV and $\mu = 5 \mu A/cm^2$	206
Figure 5.13 XPS time profile of nitrogen ion implantation in iron at $2, 3, 4$ and 5 keV at a current density of $5 \mu A/cm^2$, calculated from SATVAL code.....	207
Figure 5.14 XPS time profile of nitrogen ion implantation in copper at $2, 3, 4$ and 5 keV at a current density of $5 \mu A/cm^2$, calculated using SATVAL code.....	208
Figure 5.15 XPS time profile of nitrogen ion implantation in Gold at $2, 3, 4$ and 5 keV at a current density of $5 \mu A/cm^2$, simulated using SATVAL code.....	209
Figure 5.16 XPS time profile of nitrogen ion implantation in GaAs at $2, 3, 4$ and 5 keV at a current density of $5 \mu A/cm^2$, simulated using SATVAL code.....	210
Figure 5.17 Distribution of collision events in aluminium, iron and AlGaAs, for ion beam energy of 2 and 5 keV.....	216
Figure 6.1 Layered structure of aluminium target.....	224
Figure 6.2 The saturated relative atomic concentration ratios of nitrogen and target atoms, (N/T), as a function of electronegativity difference between the electronegativity values of nitrogen and target atoms.....	252
Figure 6.3 Relation between probability of nitride formation and heat of formation, for nitrogen ion bombardment of aluminium, iron and copper. The probability of nitride formation is calculated using our experimental data and method outlined by Pu et al., [1981].....	254

Chapter 1

Introduction and Literature survey

1.1 Introduction:

A dominant trend in the semiconductor industry has been the decrease in the dimensions of devices. This stimulated the research in the dry etching processes using ion beams. However, these ion beams cause damage to the surface. To minimise the radiation-induced damage, low energy ion beams are preferred over high energy ion beams. The application of this technique is well established in the semiconductor industry. But these days high dose low energy ion bombardment is used for various materials including metals and insulators. Ion bombardment modification of surfaces is considered as one of the significant scientific and technological developments of last three-four decades. The use of ion beams for altering the properties of materials were pioneered in the 1960s and in the 1970s, it became widely adopted by the microelectronic industry. These days high dose low energy ion bombardment is used for various materials including metals and insulators.

Nowadays the ion implantation of metals and non-metals is used for creating surface layers and buried layers with unique and desirable properties. The implantation causes changes in surface composition and chemical bond structure, leading to the formation of new metastable compounds and alloy layers [Dearnaley, 1990]. Bombardment may also form lattice imperfections due to radiation damage and cause structural changes within the near surface region of the solid [Goel et al., 1993]. The implantation of oxygen and nitrogen has been widely used in metals to form wear resistant coatings and in semiconductors, to form buried insulating and barrier layers. At room temperature nitrogen implantation into metals can lead to the formation of metal nitrides [Kelly, 1982], which are hard, durable refractory materials with a wide number of applications including wear resistant, reflective coatings and catalysts. All of the observed property changes in the target are due to either compositional, microstructural or topographical changes.

As compared to alternative surface modification techniques, ion implantation has a number of advantages:

- thermal distortion of components is not a problem (a low temperature process)
- no interface problems (not a coating process)
- dimension changes negligible

- non-equilibrium process
- distribution of implanted atoms on microscopic and sometimes atomic scale

In this chapter, after introduction, the aim of the project and the materials selected for this project are discussed briefly. This follows the ion beam modification techniques used in this project. As ion solid interactions govern the implantation mechanism, so the various possible ion interaction processes are discussed. Some theoretical models describing these processes are also included. Bonding of surface atoms is one of the critical factors influencing ion bombarded compound surface, so surface binding energy and the models available for calculation of surface binding energy are also discussed. This follows a brief introduction to computer simulation models available and used in this project. The chapter is concluded with a brief description of the research programme.

1.2 Target Materials:

The aim of this project was to investigate the effects of low energy nitrogen ion implantation in metals and compound semiconductors. Both monoenergetic implantation and non-monoenergetic ion implantation (using dc glow discharge) were being employed. The programme is essentially on experimental study, but an attempt is being made to understand the current theoretical models. On the basis of varying chemical reactivity with nitrogen, the following materials were chosen.

Aluminium: It is well known that nitrogen ion implantation into aluminium leads to the formation of AlN and in recent years there has been particular interest in the use of this technique to form aluminium nitride films [Ohira and Iwaki, 1989], [Lieske and Hezel, 1981], [Raole et al., 1987], [Taylor and Rabalais, 1981], [Rauschenbach and Somer, 1989], [Sullivan et al., 1995], [Rauschenbach et al., 1990], [Carlo et al., 1994], [Terwagne et al., 1991] and [Simson et al., 1996] for applications as diverse as microelectronic and optoelectronic devices and wear and corrosion resistant layers.

AlN is a very interesting ceramic because of its unusual combination of high thermal (up to $320 \text{ W m}^{-1} \text{ K}^{-1}$) and low electrical conductivity. Further to this, AlN is a hard material with high thermal and chemical stability (decomposition temperature 2400°C). It has a low thermal expansion coefficient and is transparent in the visible and infra-red region. AlN is a III-V wide band gap (6.2 eV) semiconductor which crystallises in a wurtzite hexagonal close packed structure. There are other processes for the formation of AlN layers on aluminium

substrates, for example, reactive sputtering deposition and chemical vapour deposition, but the surface deposited films formed by these techniques are in many ways inferior to those produced by implantation.

Iron: High energy nitrogen implantation into iron leads to various nitride phases and is an effective method to improve the mechanical and chemical properties of iron, such as microhardness, wear resistance and corrosion resistance of the metal surface. Not enough work has been done on low energy implantation to fully evaluate the benefits. A large number of papers have been published on nitrogen ion implantation in iron [Ohira and Iwaki, 1989], [Fujihana et al., 1992], [Rauschenbach et al., 1983], [Ohtani et al., 1995], [Fukui et al., 1981], [Rauschenbach, 1993], [Belyi et al., 1995], [Shinno et al., 1997] and [Yamamoto et al., 1997], but most of the work has been done at high energies (> 40 keV) and/or at high temperature ($> 200^{\circ}\text{C}$). The use of low energy high dose conditions is potentially economically more desirable, but may result in significant effects that are negligible under highenergy low dose nitrogen implantation conditions. These include sputtering of the target, back diffusion and loss of implanted nitrogen due to shallow profiles. Published results of low energy nitrogen ion bombardment at room temperature are rare [Jagielski et al., 1994] and Pu and Rabalais, 1981].

Copper: It is well known that nitrogen is insoluble in copper using conventional techniques, but it forms metastable compounds with copper by ion implantation [Prabhawalkar et al., 1985] and [Liu et al., 1989]. Because of difficulty in implantation of nitrogen in copper, there are only a few publications on this work.

Gold: It has no chemical interaction with oxygen or nitrogen and it has not been shown that nitrogen ion bombardment of gold does not lead to formation of any bonds [Prabhawalkar et al., 1985] and [Liu et al., 1989]. Probably due to this reason, the publications on nitrogen ion bombardment of gold are very rare.

GaAs: It is known that energetic nitrogen ion bombardment of GaAs [DeLouise, 1992 and 1993], [Makimoto et al., 1997] and [Troost et al., 1991] results in the formation of nitrides. III-V nitrides are promising optoelectronic materials emitting in the blue and UV spectral ranges. For these devices, AlGa_N/Ga_N/InGa_N double heterostructures are required [Yang et al., 1996] and GaAs is the most commonly used substrate for their heteroepitaxy [Strite et al., 1991], [Okamura et al., 1991] and [He et al., 1994].

There is a rapid growing interest in research to deposit thick GaN films for visible, direct band gap laser and light emitting diode (LED) applications and thin GaN interfacial layers for metal-insulator semiconductors (MIS). For GaAs based devices, the existence of thin nitride layer can effectively reduce the high surface state density and hence improve surface quality and device performance [Xu et al., 1996]. A thin GaN film may also be used as an in-situ mask for selective area epitaxy of GaAs. Because of limited availability of GaN substrates, GaN based devices are grown on other substrates such as GaAs. However, due to large lattice mismatch (~20%), this type of growth is difficult. Nitrogen ion bombardment of GaAs is expected to form GaN and the thickness of this layer can be controlled by incident ion beam parameters.

As: As and N are both group V elements and so chemical interaction between these will be expected to be weak. In order to understand the nitrogen bombardment of GaAs, As samples were chosen to see if the nitrogen bombardment will result in any chemical interaction between As and N.

AlGaAs: There are many electronic and optoelectronic devices fabricated from $\text{Al}_x\text{Ga}_{1-x}\text{As}/\text{GaAs}$ epitaxial films [Shin et al., 1991]. To our knowledge, nitrogen ion bombardment of AlGaAs has not been studied. It will be interesting to see the effect of N_2^+ bombardment on this material.

1.3 Ion beam modifications techniques:

There are a large number of methods to produce modifications in the surface of target materials, but for this project, direct ion bombardment and plasma ion implantation were investigated. In direct ion implantation, the target is bombarded with a beam of monoenergetic ions of a certain ion energy, while in plasma ion implantation, the target is placed directly in the plasma source and is then biased to high negative potential. A plasma sheath forms around the target and ions are accelerated normal to the target surface, across the plasma sheath. The schematic of both processes shown in Figure 1.1. These process involve ion-solid interaction and the physical processes which bring the compositional changes, microstructural and phase changes, metastable phase formation and amorphization etc. In this project, the main focus was on the compositional changes and processes responsible for these compositional changes such as sputtering, recoil implantation, cascade mixing, radiation enhanced diffusion, radiation induced segregation and Gibbsian segregation. These processes will be discussed in the next section.

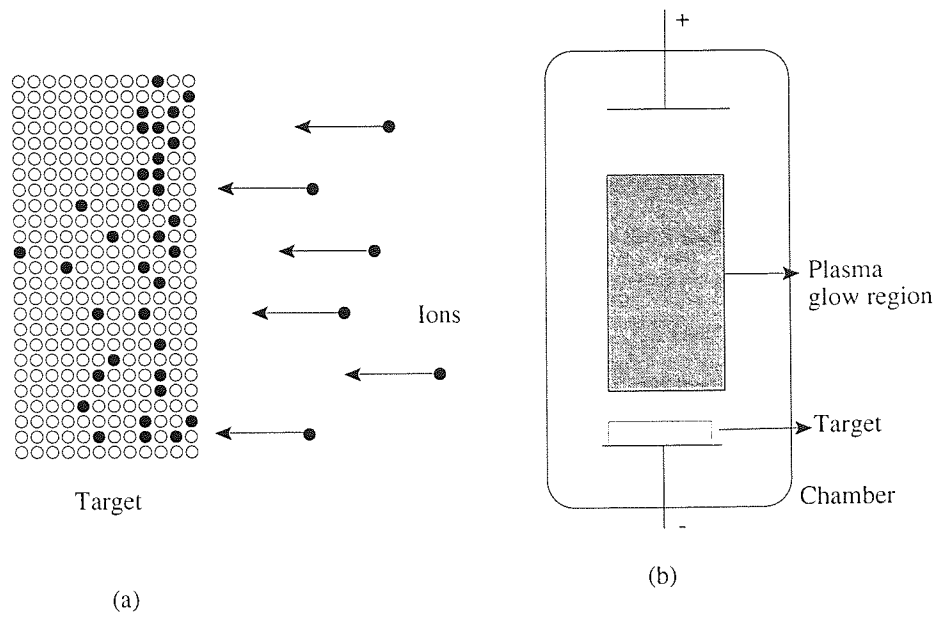


Figure 1.1 Schematic representation of (a) direct ion implantation and (b) plasma source ion implantation

1.4 Ion solid interactions:

When an ion strikes the target surface, a number of processes are possible depending on the transfer of energy and momentum. Figure 1.2 shows some of the possible interactions. Many factors determine which effects will dominate, the major ones being the energy, mass and the angle of incidence of the ion and, the mass and type of the target atoms, the crystal orientation and texture of the substrate [Malherbe, 1994]. In many of these interactions, the resulting effects and processes can not be discussed independent of each other. The three main effects of ion bombardment, of main interest are:

- Chemical reaction (and/or adhesion)
- Implantation (or doping)
- Sputtering

If the bombarding ion strikes an atom of a molecule, the latter may dissociate. The impinging ion may react with the surface atoms and become adsorbed if the ion energy is low enough ($< 0.01\text{eV}$, chemisorption). At higher ion energies, the ion may be reflected or can penetrate the target lattice. The probability of an ion being trapped inside the substrate increases with increasing ion energy, decreases with the ion mass and also depends on ion-target chemical interaction. This probability is measured by sticking probability (defined as, the ratio of the number of deposited atoms to the number of incident ions). In the energy range selected for this project, the value of this generalized sticking probability is about 0.3-0.4 [Rabalais and Marton, 1992]. In the very low energy regime, ($E < 500\text{ eV}$), condensation and chemical reactions are dominant but for $E > 1\text{ keV}$, ion implantation and sputtering dominates.

An incident particle entering the solid will lose energy in collisions with the atoms and the electrons of the target. These processes are described by elastic collisions (or nuclear energy loss) and inelastic (or electronic) excitation processes. Elastic collisions result in atomic displacements. If the energy transferred to the target atoms exceeds a certain limit, that atom may be dissipated permanently, leaving a vacancy behind. If a recoiling atom ends up at the solid vacuum interface with an outward directed momentum and an energy exceeding the surface binding energy, then the surface atom is removed and this process of surface erosion is called sputtering. Besides sputtering several other effects are observed. These include desorption of surface layers [Taglauer and Heiland, 1978], backscattering, re-emission of incident particles, the emission of electrons and a change in surface topography [Behrisch, 1981].

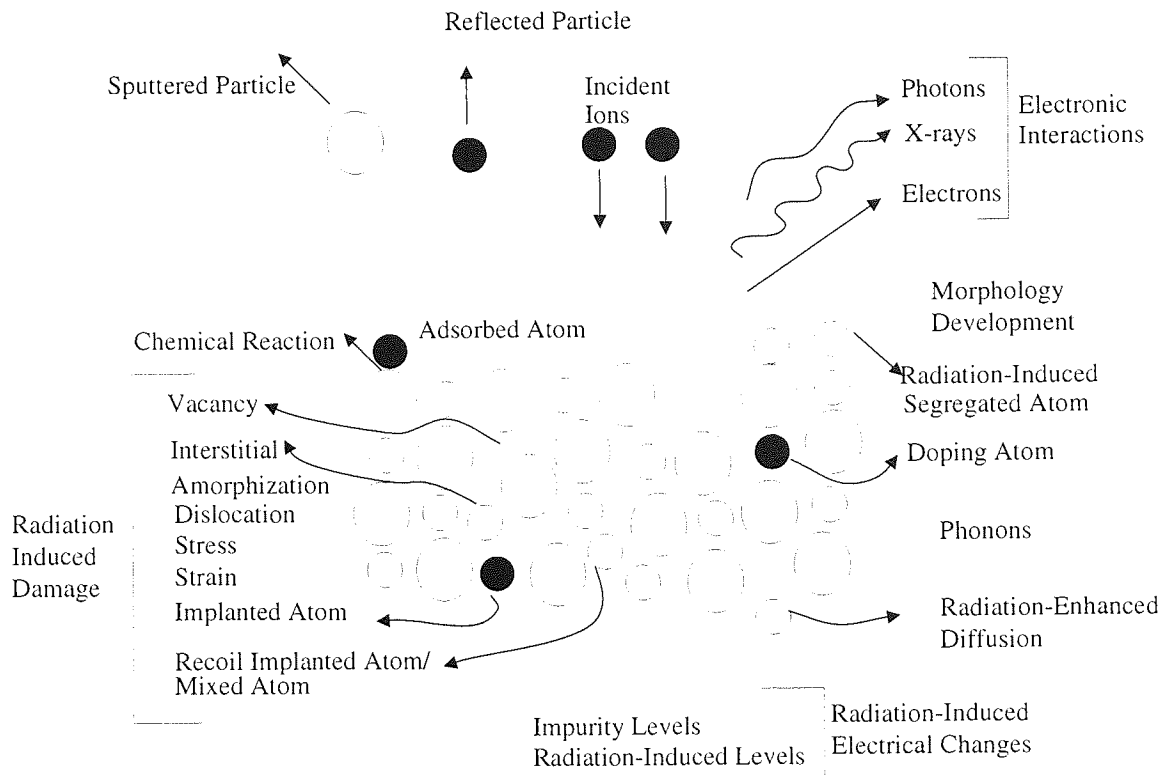


Figure 1.2 Various possible ion-solid interaction processes [After Malherbe, 1994]

The temporal development of cascade can be divided into three phases:

- a collisional phase, lasting between 0.1 and 1 ps, during which energy transferred to the primary knock-on atom is dissipated among successive recoils.
- a relaxation phase of about 0.5 ps, during which Frenkel pairs spontaneously recombine due to their close proximity.
- a cooling phase lasting only a few ps, in which the highly disordered region cools to reach equilibrium with the surroundings.

In addition, thermal processes may also become significant, leading to processes such as Gibbsian segregation, radiation-enhanced diffusion, radiation-induced segregation etc. These processes are discussed in detail in the following subsections. Until 1970, preferential sputtering was considered the cause of these changes. Since altered layers were found to extend far beyond the depth of origin of sputtered atoms, so compositional changes generated by preferential sputtering were assumed to propagate into the bulk by diffusion [Pickering, 1976]. The ion beams also cause mixing phenomena. Actually cascade mixing and recoil implantation are important but the role of surface segregation can not be ignored as a contributing factor [Andersen, 1979 and Kelly, 1980]. Radiation damage introduced by ion implantation is found to be structure dependent, the damage depths being often large in metals with face centred cubic lattices [Friedland and Fletcher, 1992]. Two distinguishable effects related with the ion bombardment are:

(a) Primary Effects: These represent the physics of an individual sputtering event on a target with a given composition.

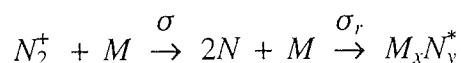
(b) Secondary Effects: These include changes in target composition caused by prolonged bombardment and can be broadly classified as;

- athermal processes which are 'prompt' processes in a collision cascade, for which the rate-determining quantity is ion fluence $d\Phi = J_0 dt$, where J_0 is the ion current density and dt is a real time interval [Sigmund, 1992]. Examples are sputtering, recoil mixing and spike phenomena. Experimentally, these are identified by their dependence on ion fluence and non-dependence on ion current density.
- thermal processes proceed in real time scale and depend on ion current density J_0 as well as on the target temperature. Examples are Gibbsian segregation, radiation-enhanced diffusion and radiation-induced segregation.

For molecular ion beams, such as N_2^+ , Pu et al., [1981] have proposed a model for low-energy

beam reaction dynamics, according to which an energetic molecular ion approaching a target surface undergoes a charge-exchange neutralization in the form of resonance or Auger processes, while it is only a few angstroms from the surface. At the kinetic energies chosen for this project, the energetic nascent molecules are believed to undergo efficient collision dissociation upon impact with the surface [Baldwin et al., 1981]. These energetic atoms can be scattered from surface or they can penetrate into the lattice, losing energy until they eventually chemically react or are simply thermalized. After thermalization, they can diffuse to the surface and be emitted if their chemical affinity for the lattice is small. For low doses of active ion bombardment, the concentration of impinging atoms in the lattice is determined by their reaction probability with the lattice atoms and by the probability of sputtering the reaction product by impinging ions.

Based on Pu et al.,'s model for nitridation of rhenium [1980], the reaction of N_2^+ with metals can be described as;



here σ represents the combined cross-section of collisional neutralization and dissociation, σ_r represents the cross-section of chemical nitration reaction and N^* is the nitrogen in the form of nitride. The nitride concentration at any given time is;

$$[N^*] = \frac{[M]_0 \sigma_r [N]}{A}$$

here, $[M]_0$ is the initial number of metal atoms available for reaction in the surface area A of bombardment. In above equation some important processes such as penetration of bombarding ions beyond the mean escape depth of photo-electrons, diffusion of nitride formed near the surface to bulk and lateral diffusion of nitride product out of the XPS sampling area, are ignored. In this project, this model was employed for calculation of probability of nitride formation in the case of metallic targets only.

1.4.1 Stopping power:

As discussed in section 1.4, The energetic ions lose their energies through a series of collisions with electrons and nuclei in the substrate and finally come to rest and this procedure is discussed below;

Nuclear stopping: The process of slowing down of the incoming particle due to transfer of

energy to target atoms during the collision is called nuclear stopping. As electrons move randomly around the nucleus, the interaction between the nuclei of ion-target system can not be described by the simple Coulomb potential. The most commonly adopted screening potential is given as,

$$U(R) = \frac{Z_1 Z_2 e^2}{R} \phi\left(\frac{R}{a}\right) \quad (1.1)$$

Here $Z_1 e$ and $Z_2 e$ are ion and target nuclear charges; a is a screening radius and $\phi(R/a)$ is a screening function. Sigmund used Thomas-Fermi potential defined as

$$\phi\left(\frac{R}{a}\right) = \frac{k_s}{a} \left(\frac{a}{R}\right)^{s-1}; \quad a \cong \frac{0.8853a_0}{(Z_1^2 + Z_2^2)^{\frac{1}{2}}} \quad (1.2)$$

where k_s and s are constants and a_0 is Bohr radius, with a value of 0.059 nm. For Rutherford scattering, the nuclear stopping power cross section is given by

$$S_n(E) = \int_0^{T_m} T d\sigma = \frac{C_m}{1-m} \left[\frac{4M_1 M_2}{(M_1 + M_2)^2} \right]^{1-m} E^{1-2m} \quad (1.3)$$

where

$$m = \frac{1}{s}; \quad C_m = \frac{1}{2} \pi \lambda_m a^2 \left(\frac{M_1}{M_2}\right)^m \left(\frac{2Z_1 Z_2 e^2}{a}\right)^{2m} \quad (1.4)$$

Here m is the power scattering parameter and depends on the mass of ions and atoms and range of energy. λ_m is a dimensionless function of parameter m and varies slowly from $m=1$ at high energies down to $m \approx 0$ at very low energies. $S_n(E)$ can be simplified to

$$S_n(\varepsilon) = 4\pi a Z_1 Z_2 e^2 \frac{M_1}{M_1 + M_2} s_n(\varepsilon) \quad (1.5)$$

here $s_n(\varepsilon)$ is a universal nuclear stopping power and depends on the detailed form adopted for interatomic potential. The reduced energy parameter ε is given as,

$$\varepsilon = \frac{4\pi\varepsilon_0}{Z_1 Z_2 e^2} \cdot \frac{a M_2}{M_1 + M_2} E \quad (1.6)$$

Many different expressions exist for $s_n(\varepsilon)$ and most of them show good agreement at intermediate and high energies, but significant differences are noticed at low energies. Biersack and Ziegler [Biersack and Ziegler, (1982)] obtained a more realistic potential by

fitting an equation to the rms average of 500 interatomic screening functions, and obtained the following expression,

$$s_n(\epsilon) = \frac{0.5 \ln(1 + 1.383\epsilon)}{\epsilon + 0.013218\epsilon^{0.21226} + 0.19594\epsilon^{\frac{1}{2}}}; \quad a_B = \frac{0.8853a_0}{(Z_1^{0.23} + Z_2^{0.23})} \quad (1.7)$$

Here a_B is the Biersack screening length.

Electronic stopping: Electronic stopping results from the Coulomb interactions between the moving ion and the target electrons and as result the electrons become excited and are transferred to higher bound states or continuum or ionisation states with eventual relaxation. So several phenomena can be observed, for example, the emission of photons, emission of ion induced photoelectrons and ion induced auger electrons. For high velocity ions, energy loss to electrons dominates the slowing down of the ion and stopping cross section is given as (Sigmund,1981)

$$S_e = \frac{4\pi q_1^2 Z_2}{mv^2} e^2 \left(\log \frac{2mv^2}{I} + \text{correction terms} \right) \quad (1.8)$$

where q is the projectile charge and I is the mean ionization potential. At lower velocities,

$$S_e \cong 8\pi \xi_e \frac{Z_1 Z_2 e^2}{(Z_1^2 + Z_2^2)^{\frac{1}{2}}} a_0 \frac{v\hbar}{e^2} \quad (1.9)$$

where ξ_e is a function of Z_1 .

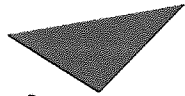
Total stopping: The total stopping power is sum of electronic and nuclear stopping power. In addition to these losses, the fast moving ions may lose energy into collective motions known as phonons. Figure 1.3 shows the nuclear and electronic stopping power of an ion as a function of energy. In this figure, ϵ , is the reduced energy [Lindhard et al.,1963], defined as:

$$\epsilon = \frac{a}{Z_1 Z_2 e^2} \cdot \frac{M_2}{M_1 + M_2} E \quad (1.10)$$

1.4.2 Ion Range:

In section 1.4.1, the procedure of slowing down of the projectile was discussed. The mean penetrated path length of a projectile before coming to rest is called ion range and is given as,

$$R(E) = \int_0^\infty \frac{dE'}{NS(E')} \quad (1.11)$$



Aston University

Content has been removed for copyright reasons

h

Figure 1.3 Nuclear and electronic stopping power of an ion as a function of energy
(Sigmund, 1981)

here N is the atomic density of the target and $S(E)$ is the total stopping power. The projection of range $R(E)$ on the incidence direction of ion beam is called as mean projected range, $R_p(E)$, defined as;

$$R_p(E) = \int \langle \cos \theta \rangle dR \quad (1.12)$$

The relationship between $R(E)$ and $R_p(E)$ is shown more clearly in Figure 1.4. Since the number of collisions per unit distance and the energy lost per collision are random variables, there will be a spatial distribution of ions having the same mass and same initial energy.

1.4.3 Ion Implantation profiles:

In the previous section, the ion range was considered, which represents the distribution of the implantant only for idealized case of infinitesimal small dose and any noncollisional processes were ignored. In case of an amorphous target, the implantation profile may sometimes be very close to Gaussian distribution. For such cases, the implanted ion density distribution, n , is given as [Gibbons et al., 1975];

$$n(R_p) = \frac{F}{\sigma_p \sqrt{2\pi}} \exp\left[-\frac{(R_p - \bar{R}_p)^2}{2\sigma_p^2}\right] \quad (1.13)$$

Here F is the implanted ion dose, \bar{R}_p is the average projected range and σ_p is the standard deviation. The full width at half maximum (FWHM) is given as $2.35\sigma_p$. However departures from an idealized Gaussian distribution occur at very low ion energies, with crystalline targets, at high doses and in general near the surface. Kelly [1984] predicted the distribution of ions "i" as;

$$C^{diff}(x) dx = \left(\frac{dx}{\sqrt{2\pi}\Delta x}\right) \exp\left(-\frac{\xi^2}{2}\right) \left\{1 - \frac{1}{6}\beta_1^{\dagger} (3\xi - \xi^3) + \frac{\beta_1}{72} (15\xi^2 - 10\xi^4 + \xi^6)\right\} \quad (1.14)$$

here, ξ is depth variable $\left(\equiv \frac{x - \langle x \rangle}{\Delta x}\right)$; $\langle x \rangle$ is the mean projected range,

Δx is standard deviation in the mean projected range $\left(\equiv \sqrt{\langle \Delta x^2 \rangle}\right)$;

β_1^{\dagger} is skewness $\left(\equiv \frac{\langle \Delta x^3 \rangle}{\langle \Delta x^2 \rangle^{\frac{3}{2}}}\right)$.

Assuming a Gaussian range distribution for the bombarding ions, the equilibrium implantant concentration of distribution $C(x)$ in the presence of the sputtering is given by [Schultz and Wittmack, 1976],

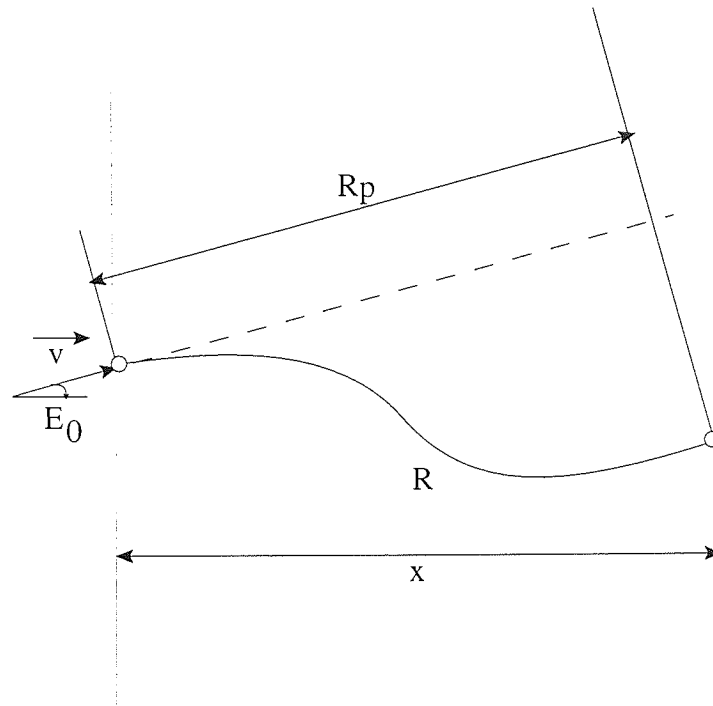


Figure 1.4 Schematic presentation of penetrated path length R , projected range R_p and the penetration depth x , for an ion of initial velocity v and energy E_0 , incident at an angle θ w.r.t. the surface normal.

$$C(x) = \frac{1}{2Y} \left\{ 1 - \operatorname{erf} \left(\frac{x - \bar{R}_p}{\sqrt{2\Delta R_p}} \right) \right\} \quad (1.15)$$

where x is the depth inside the sputtered surface, \bar{R}_p and ΔR_p are the projected ion range and range straggling, respectively. The implantation profile at any time $t=t_2$, is a superposition of what is left in the target from the implantation in the previous time interval ($t_1, t_1+\Delta t$) plus what is implanted in the time interval ($t_1+\Delta t, t_2+\Delta t$). The concentration of implanted primary ions may vary with time at the initial stage of implantation process, but finally arrives at a steady-state saturation value [Tsai and Morabito, 1974], when a depth of about $\bar{R}_p + 2\Delta R_p$ has been sputtered away. The steady state is achieved after a time t^* given as;

$$t^* \cong \frac{2\Delta \bar{R}_p}{v_s} = \frac{2\Delta \bar{R}_p n_T e}{\mu Y} \quad (1.16)$$

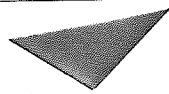
Here v_s is erosion rate, n_T is the target atomic density, e is electronic charge and μ is the current density.

Another important quantity is the amount of ions retained in the target per cm^2 , and this is related to the incident dose density. For $t \geq t^*$, the number of ions retained is equal to the number of ions sputtered away through the surface and this is also called saturation state. Assuming a constant sputter yield, for a one-sided infinite sample with permeable boundary and including the diffusion, Collins and Carter [1975] derived an expression for the stored ion fluence at saturation $F_{r,s}$, as;

$$F_{r,s} [\text{ions}/\text{cm}^2] = \frac{n_T \bar{R}_p}{Y_T} \quad (1.17)$$

Clearly, the saturation ion dose density is independent of both the primary ion current density and the coefficient of diffusion, which play a role only in the situation before steady state is reached. Carter et al. [1979] considered the effect of preferential sputtering on the implant profile for the case where the sputter yield of the implants is greater than that of target, ($Y_i > Y_T$) and found that in the time dependent situation, the surface concentration does not depend on diffusion but the time to reach saturation dose does depend on this coefficient. When the effect of local trapping is included the equilibrium and instantaneous concentration depends on the ion current density [Carter and Collins, 1976].

There is a pronounced change in the distribution of implantant due to sputtering, Figure 1.5 [Liau and Mayer, 1978]. For low dose implantation, the implanted atoms are located at a depth within the sample given by \bar{R}_p and the spread in the ion distribution (ΔR_p), Figure 1.5(a)



Aston University

Content has been removed for copyright reasons

Figure 1.5 A schematic illustration of effect of low and high-dose ion implantation
Figures (a) represents an ion A^+ striking the target B and (b) the resultant profile of A, for low-dose ion implantation and Figures (c) represents ions of type A^+ striking the target B and (d) the resultant profile of A, for high-dose ion implantation [Liau and Mayer, 1978].

and (b). In Figure 1.5(c), the sample surface is eroding during implantation and as a result of sputtering of both target and the implanted ions, the resultant profile changes from 1.5(b) to 1.5(d). By applying the conservation of atoms and assuming that the species A and B have different sputtering probabilities, such that r is the ratio of probability for a B atom near the surface to be sputtered to that of an A atom near the surface;

$$\frac{N_A}{N_B} = \frac{r}{(S - 1)} \quad (1.18)$$

here N_A is the concentration of the implanted species, N_B is the concentration of the target species and S is the total sputter yield. The steady state is reached after sputter removal of $\sim rW$, W being the width of the implanted layer. For compound targets, considering implantation of atomic species A into a mixture of AB,

$$\frac{N_A}{N_B} = \frac{r(S + 1)}{(S - 1)} \quad (1.19)$$

As lower mass elements tend to be preferentially sputtered, higher concentration of heavy elements than of light elements in substrate ensues. Due to the atomic mixing along the track of incident ion beam, the depletion of lower mass ions will spread throughout the target over the depth of the implanted distribution. The authors have shown that the predicted profiles agree quite well for elemental targets, by assuming $r = 1$. However, due to lack of data, this model is difficult to apply in actual practice, especially for compound targets.

From equation (1.15), the saturation surface concentration is,

$$C_m \equiv C(0) = \frac{1}{2Y} \left\{ 1 - \operatorname{erf} \left(\frac{-R_p}{\sqrt{2\Delta R_p}} \right) \right\} \approx 1/2Y \quad (1.20)$$

Malherbe [1994] has reported the comparison made by some experimentalists for the surface concentration of the noble gas implantants and above equation. For high dose implantation, the surface concentration of the implantants were much smaller than the predicted value but good agreement is found for low dose implantation.

In the models discussed here only sputtering was taken into account, however, the surface concentration of the implantant depends on several parameters, such as the sputter depth, ion range distribution and chemical reactivity of the ion/target combination. In the following sections, the various mechanisms that may occur during implantation are discussed.

1.4.4 Sputtering:

The thrust of this project is the concentration limit that can be achieved with ion implantation, but implantation in the energy range chosen for this programme must necessarily be accompanied by sputtering. Sputtering was observed by Grove in 1853, but it was explained after nearly half a century by Goldstein [Sigmund, 1981]. The explosion of research in this field began in 1956 with the publication of a paper on the controlled sputtering of Hg ions [Sigmund, 1981].

Sputter Yield: The degree of sputtering is measured by the sputter yield Y , defined as the mean number of atoms removed from the surface of the solid per incident particle. In this project work, it is essential to have the accurate knowledge of the total sputter yield as

- Sputtering changes the implantation profiles.
- To obtain depth profile, sputter yield values are needed to convert the time scale into the depth scales.

Despite the apparent universality of the sputtering phenomena, many mechanisms have been proposed in the last few decades. Controversies have been going on between the support of various mechanisms. At present the general consensus is that no single mechanism explains all the observations.

Sigmund's Theory of Sputtering:

Sigmund [1969] based his theory on the basis of Boltzmann's equation, by making certain assumptions and using sophisticated mathematical treatment and Legendre Polynomials, Sigmund found an analytical solution for sputtering yield given as ;

$$Y(E, \eta) = H(0, E, \eta) = \frac{3}{4\pi^2} \frac{D(0, E, \eta)}{NC_0U} = 0.042 \frac{\alpha S_n(E)}{U} \quad (1.21)$$

Here $H(0, E, \eta)$ represents the backward sputtering yield; $D(0, E, \eta)$ represents the energy deposited by an ion of energy E ; U is the binding energy between the target atoms and η is the total amount of energy ending up in electronic excitation. α is a dimensionless parameter determining the amount of energy available for sputtering and depends on the relative masses and the incident angle. Equation (1.21) is the basic equation in yield calculation and has been widely used in computer simulations such as TRIM and SUSPRE.

The factor α : For low energies, α is practically independent of energy, however, for high energies, it depends weakly on the energy. The dependence of α on mass ratio (for normal incidence) and angle of incidence of the ions is given in Figure 1.6(a) and (b) respectively [Sigmund, 1981]. Sigmund calculated these values for elastic scattering only and no surface correction was applied. Andersen and Bay [1979] found that at normal incidence for large mass ratios, the experimental values are considerably smaller than the theoretical predictions by Sigmund, Figure 1.6(c). The experimental results do contain contribution from inelastic collisions, but the difference is mainly due to surface correction at large mass ratios. Steinbrüchel [1985] approximated the experimental curve obtained by Andersen and Bay [1979] as,

$$\alpha(M_2/M_1) = 0.15 \left(1 + \frac{M_2}{M_1}\right)^{0.7} \quad (1.22)$$

But he argued that the best fit to low energy sputter data is obtained by an α intermediate between Sigmund and Andersen and Bay curve, defined as

$$\alpha(M_2/M_1) = 0.15 \left(1 + \frac{M_2}{M_1}\right)^{0.85} \quad (1.23)$$

By studying Sigmund's formula and substituting measured sputter yield values of a large number of mono-elemental targets and using heat of sublimation as surface binding energy, Strydom and Gries, [1984] gave the following expression for best fit of α ;

$$\begin{aligned} \alpha(M_2/M_1) &= 0.120; & \text{for } l \leq -1.2 & \quad \text{and} \\ \alpha(M_2/M_1) &= 0.0857 l^5 + 0.289 l^4 + 0.402 l^3 + 0.350 l^2 + 0.220 l + 0.189; \\ & & \text{for } -1.2 < l \leq -0.144 & \quad \text{and} \\ \alpha(M_2/M_1) &= 0.0449 l^6 - 0.107 l^5 + 0.209 l^4 + 0.314 l^3 + 0.207 l^2 + 0.156 l \\ & & + 0.183; & \quad \text{for } -0.144 < l \leq 1.8 \end{aligned} \quad (1.24)$$

$$\text{where } l = \log_{10}(M_2/M_1) \quad (1.25)$$

The above formulae are for normal incident ions, but if the bombarding ions are incident on the target at angle θ , then α is given as [Sigmund, 1969]

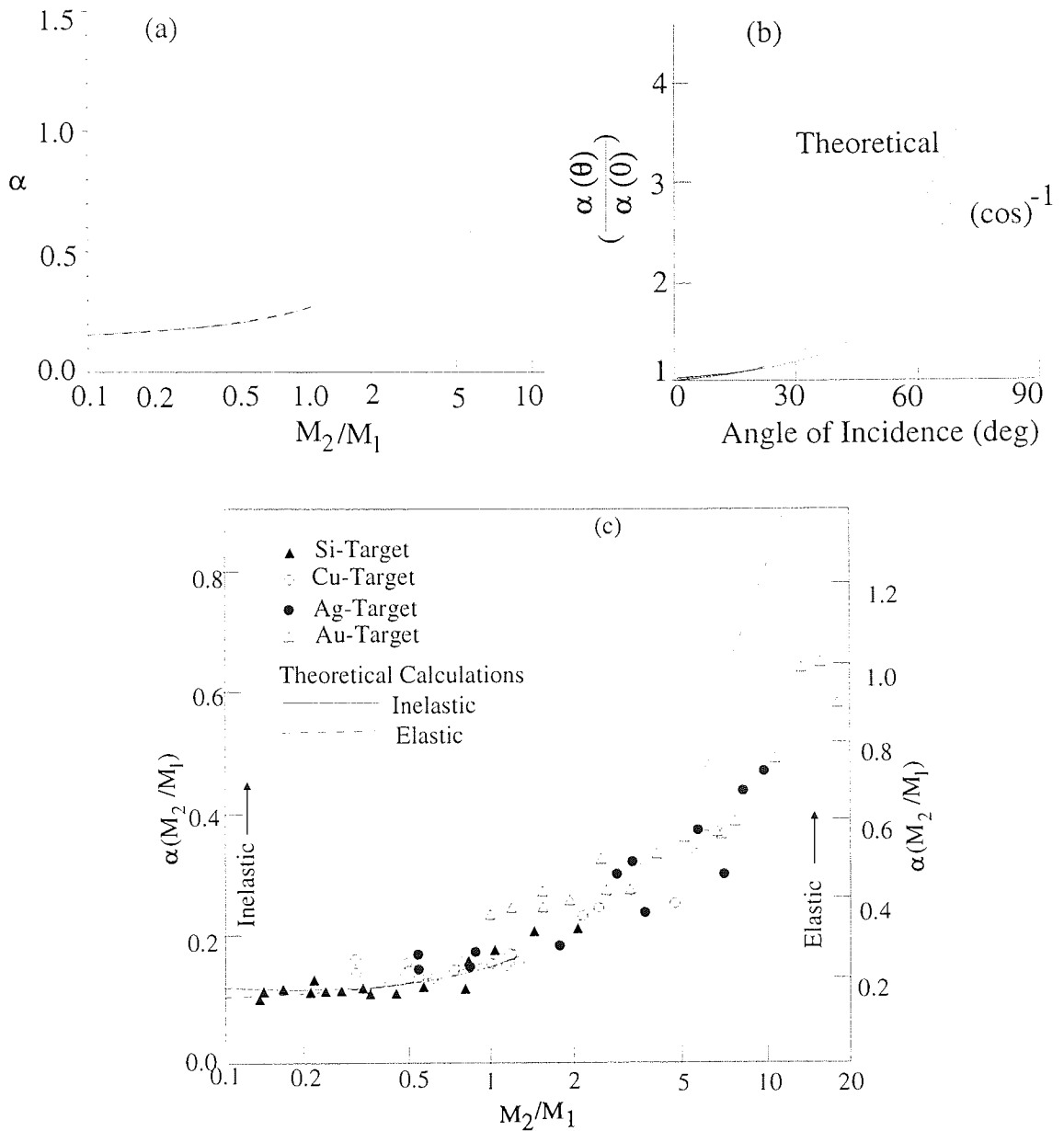


Figure 1.6 (a) dependence of α on mass ratio, solid curve derived by Sigmund, dotted by Andersen and Bay (b) dependence of α on angle of incidence and (c) dependence of α on mass ratio

$$\alpha(M_2, M_1, \theta) = \alpha(M_2/M_1) \cos^{-f} \theta; \quad \text{with } f \cong \frac{5 \pm 2}{3} \text{ and } \theta \leq 60^\circ \quad (1.26)$$

By analysing experimental data for several ion-metal combinations, Oechsner [1975] concluded that the above description of angle dependence was too simplified. Yamamura [1984] proposed the following formula for the angular dependence of α and hence, the sputter yield

$$\frac{Y(\theta)}{Y(0)} = \frac{\alpha(\theta)}{\alpha(0)} = (\cos^{-f} \theta) \exp \left[\sum \left(1 - \frac{1}{\cos \theta} \right) \right] \quad (1.27)$$

In above equation, there are two adjustable parameters, f and \sum . The angle of incidence at maximum yield is given by,

$$\cos \theta_m = \frac{\sum}{f} \quad \text{and} \quad \frac{f}{\sqrt{U}} = 0.94 - 0.0133 \frac{M_2}{M_1} \quad (1.28)$$

Binary collision approximation:

A schematic of collision between two particles is shown in Figure 1.7. If M_1 and $E = \frac{1}{2}M_1v_0^2$ represent the mass and initial energy of the incoming particle; $E_1 = \frac{1}{2}M_1v_1^2$ the final energy of the same after collision at scattering angle θ , M_2 and $T = \frac{1}{2}M_2v_2^2$ represent the mass and the received energy of target particle, then according to the conservation laws of energy and momentum, one obtains

$$T = \frac{4M_1M_2}{(M_1 + M_2)^2} \sin^2 \theta \quad (1.29)$$

$$\theta = \pi - 2P \int_{R_0}^{\infty} \frac{\frac{dR}{R}}{\left[1 - \frac{U(R)}{E_R} - \frac{P^2}{R^2} \right]} \quad (1.30)$$

where P is the impact parameter; R is the interatomic distance; R_0 is the shortest distance between the particles; $U(R)$ is the interatomic potential (defined in the next section) and E_R is the reflected energy such that

$$E_R = \frac{M_2}{M_1 + M_2} E; \quad (1.31)$$

Some Other Sputtering Theories: For the very low energy regime, the basic assumption of the Sigmund's theory are not valid. For this energy range, Zalm [1983, 1984] and Wilson et al., [1977] introduced some expressions to accommodate the threshold effects, but these are

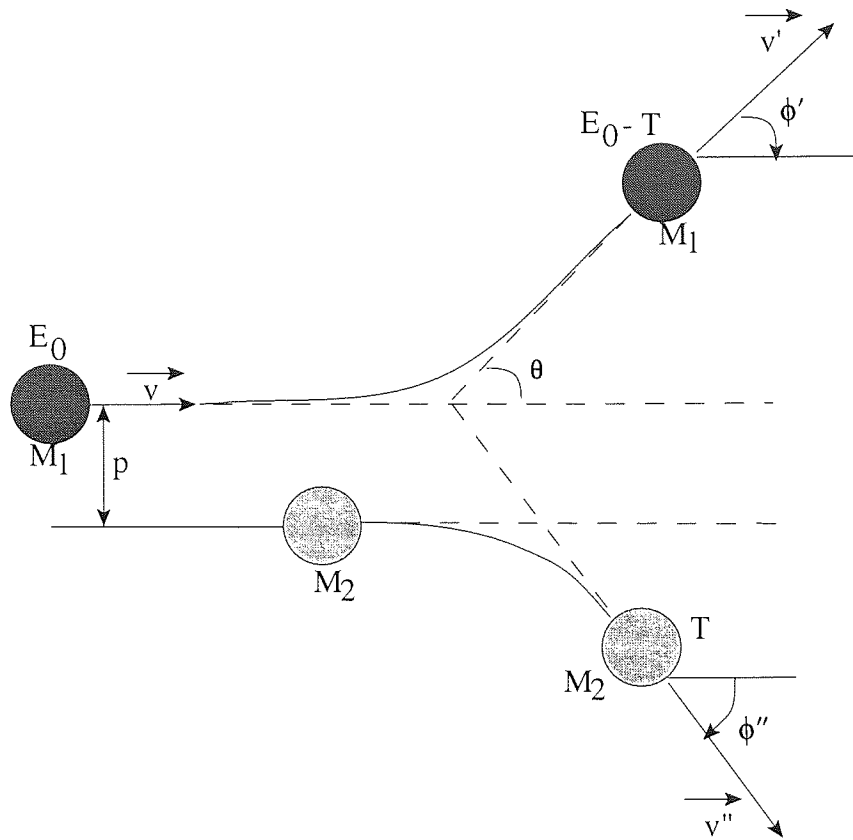


Figure 1.7 Schematic of binary collision approximation (elastic collision)

not discussed here, as for the energy range chosen for this project, Sigmund approximation gives good results.

Bombardment with molecular ions: When molecular ions strike the target surface, the binary collision theory breaks down, as there are two projectile particles, striking at the same point. The Sigmund's theory also breaks down because the assumption of a collision cascade moving with recoil atoms colliding only with atoms initially at rest, may not be fully justified. The collision cascade initiated by the individual atoms may overlap and lead to an increase in sputter yield compared to the yield of a single atom of the same velocity. To a first order approximation, the penetration of energetic molecules may be looked at as the sum of events induced by independent atoms. However, Sigmund et al., [1996] have pointed towards a number of sources of nonlinearities and correlations. Andersen and Bay [1974] found an increase by a factor of 2.15 of the yield per atom for gold target bombarded with Te_2^+ of energy 45 keV. Johar and Thompson [1979] and Thompson and Johar [1979] studied the effect of molecular and atomic beams on platinum and gold and found the increase in sputter yield was greater in the case of gold. These effects are because of the sputter yield no longer varies linearly with stopping power. Andersen and Bay [1981] found that for projectile masses larger than ~ 10 amu, the predicted proportionality to nuclear stopping power holds except for heavy projectiles and/or targets.

1.4.5 Preferential Sputtering:

The concentration limit of the implantant may be influenced by preferential sputtering, for example due to smaller mass, the implanted nitrogen will have a tendency for preferential sputtering. Preferential sputtering occurs when the composition of the flux of sputtered particles is different from their concentration on the surface of multicomponent target [Betz and Wehner, 1983]. The preferential removal of a component from the surface region of a target results in the formation of an "altered layer" with a composition different from bulk stoichiometry. The thickness of altered layer is of the order of ion projected range. Conard and Urbassek [1992] have shown that the sputtered flux approaches stoichiometric composition only after an ion fluence of $\sim 10^{16}/\text{cm}^2$. The partial sputter yield may be split into contributions from different depths. If the target can be characterized by monolayers, then

$$Y_i = \sum_{l=1}^{\infty} y_i^{(l)} c_i^{(l)} \quad (1.32)$$

here $l=1$ represents the top surface layer, $c_i^{(l)}$ is the fraction of i -atoms in the l th layer, and $y_i^{(l)}$

is a dimensionless quantity called component sputter yield of species i from layer l .

In general, the main factors contributing to the preferential sputtering effects are the composition of the target, mass differences and surface binding energy differences of the constituent atomic species in the target. Several theoretical models are put forward to explain this phenomena quantitatively, the most popular being Sigmund's theory [1995], giving ratio of sputter yields as;

$$\frac{Y_1}{Y_2} = \frac{c_1}{c_2} \cdot \left(\frac{M_2^{2m_2}}{M_1^{2m_1}} \right) \cdot \left(\frac{U_2^{1-2m_2}}{U_1^{1-2m_1}} \right) \quad (1.33)$$

For $M_1 \cong M_2$, the power scattering parameters are equal ($m_1 = m_2 = m$). So

$$\frac{Y_1}{Y_2} = \frac{c_1}{c_2} \left(\frac{M_2}{M_1} \right)^{2m} \left(\frac{U_2}{U_1} \right)^{1-2m} \quad (1.34)$$

This equation predicts that the lighter species tend to sputter preferentially. However this depends on the value of m . At high energies, $m = 1$ (Rutherford scattering); for medium energies (10-100 keV), $m = 0.5$ and at low energies m lies between 0 and 0.5. For most applications in sputtering the relevant values for m are in the range $0 \leq m \leq 0.2$. Malherbe et al [1986] found $2m = 0.33$, which fits fairly well with experimental data and theory. For $M_1 = M_2$, equation (2.35) shows that the least bound species are removed preferentially. However the situation is more complicated in the case of very different masses.

Malherbe's Theory:

Based on Sigmund's theory, Malherbe et al (1986) predicted the changes in the composition of ion bombarded surfaces of metallic oxides. According to their model,

$$\frac{\left(\frac{X_m}{X_0} \right)_s}{\left(\frac{X_m}{X_0} \right)_b} = \left(\frac{M_m}{M_0} \right)^{2m} \left(\frac{U_m}{U_0} \right)^{1-2m} \quad m=0.165 \quad (1.35)$$

Where X , M and U stand for the concentration, atomic mass and surface binding energy respectively. The subscripts m , o , s and b stand for metal, oxide, surface and bulk respectively. The superscript m is the power scattering cross section. Malherbe and Barnard [1991] used these formulae for sputtering of InP and found a good agreement between

theoretical prediction and experimental results. Yu [1995] has pointed that due to a significant mass difference between metal cation and oxygen anion, the m value can not be same for both metal and oxygen.

Kelly's model of nonstoichiometric sputtering:

Kelly's theories are generally based on experimental observations. An initial model [Kelly, 1978] which was based on linear collision cascade theory but with certain assumptions, gives;

$$\frac{Y_1}{Y_2} = \frac{(x_1 + x_2\gamma)}{(x_2 + x_1\gamma)} \cdot \frac{U_2}{U_1} \quad (1.36)$$

here γ is the maximum energy transfer factor. For a random binary alloy Kelly [1980] obtained

$$\frac{Y_1}{Y_2} = \frac{x_1 + x_2\gamma(1 + x_2^s)H_2 + (1 - x_2^s)H_1}{x_2 + x_1\gamma(1 + x_1^s)H_1 + (1 - x_1^s)H_2} \quad (1.37)$$

Here H_1 and H_2 are the heat of atomisation. The predictions from this model are in general agreement with experimental results for many alloys, but the enrichment observed from experiments is much greater than the same predicted from the above equation. Kelly [1980] concluded that recoil sputtering contains a significant mass dependence but cascade sputtering is governed more by chemical binding than by mass. Kelly [1984] reviewed the theories on sputtering of metals and alloys and concluded that the mass effect is important in preferential sputtering of isotopes or for sputtering near threshold conditions. On the basis of time scale, he classified the sputtering mechanism into several processes, Table 1.1. Kelly [1990] found that the yield of thermal sputtering is much greater than that of collisional sputtering.

Table 1.1 Kelly's classification of sputtering processes

Process	Time range (s)
Prompt collisional	$10^{-15} - 10^{-14}$
Slow collisional	$10^{-14} - 10^{-12}$
Prompt thermal	$10^{-12} - 10^{-10}$
Slow thermal	$10^{-10} - 10^0$
Exfoliation	$10^0 - 10^1$
Electronic transition	$10^{-13} - 10^0$

1.4.6 Segregation:

The role of segregation induced and/or enhanced by ion implantation is important in explaining the sputtering effects and implantation profiles. When an ion strikes a target surface, the collision and cascade collisions result in production of many vacancies and interstitials, greater in number than that are present at thermal equilibrium [Li, 1993]. The migration of these defects can cause an enhanced diffusion and as a result a segregation is induced at the surface [Li et al, 1982]. In this process, separate phases form at the surface which prevent the development of a steady state. If the exchange of atoms between the surface and inner layers is sufficiently fast, then the surface composition of a binary compound under thermal equilibrium is,

$$\frac{C_1^s}{C_2^s} = \frac{C_1}{C_2} \exp\left(-\frac{\Delta G_s}{kT}\right) \quad (1.38)$$

where ΔG_s is the segregation free energy.

Sigmund and Oliva [1992] considered a dilute solution of some component i in a matrix and on the basis of assumption that i -atoms tend to segregate to the surface, they derived the kinetic equation to describe surface segregation. Segregation is generally classified into two categories, Gibbsian segregation and radiation-induced Segregation, which are discussed in the next two subsections.

1.4.6.1 Gibbsian Segregation (adsorption):

The adjustment of the surface composition of a homogeneous alloy to a composition different from that in the bulk is known as Gibbsian or surface or equilibrium segregation, and is due to a thermodynamic force responsible for minimizing the free energy of the system [Skinner et al, 1983]. This process can lead to substantial changes in composition in the first one or two atom layers at the surface, while leaving the bulk composition practically unaffected due to large bulk to surface volume ratio. However at room temperature, the driving force caused by minimising surface free energy is so small that the process of segregation may not occur, or may occur very slowly. During ion bombardment, the surface atoms may obtain sufficient energy from ions or recoils, to overcome the binding forces and become mobile within the solid. This movement greatly speeds up the surface segregation process [Yu, 1995].

Gibbsian segregation and preferential sputtering are closely connected. As a rough rule, the weakly bounded species segregate and hence gets preferentially sputtered. For metallic alloy, the two processes oppose each other [Betz and Wehner, 1983]. Segregation is governed significantly more often by binding than by alternatives of size, surface chemistry, an interstitial flux, or long range ordering. Cascade mixing ends between 0.1 and 1 ps, but bombardment induced Gibbsian segregation (BIGS) can take many seconds to reach completion and hence cascade mixing does not prevent BIGS.

Nowadays it is well known that alloy sputtering correlates significantly with BIGS. Sigmund [1987] has remarked, *"We all have to realise, sooner or later, that bombardment induced composition changes may have very little to do with sputtering"*. However preferential sputtering may be expected to play a role with the limited number of non - alloy systems showing mass correlated effects or for the systems where preferential sputtering arises from chemical changes at the outer surface provided segregation effects are absent.

1.4.6.2 Radiation-induced Segregation:

Radiation-induced Segregation (RIS) is a non equilibrium segregation, driven by kinetic processes. Bombardment induced defects can cause radiation enhanced segregation in the target. The following two conditions are must for the existence of RIS [Wiedersich and Lam, 1983];

- a flux of defects into or out of certain spatial regions that persist in time.
- a preferential coupling of certain alloying elements to these fluxes.

This combination induces and maintains local concentration gradients that will decay in the absence of defect fluxes. As a result, defect fluxes will preferentially transport solute atoms into or out of local regions, causing segregation. The size difference between solute and solvent atoms plays a strong role in the magnitude and direction of RIS through the reduction of strain energy stored in the lattice [Rehn et al, 1978]. This provides the driving force for the undersize substitutional atoms to preferentially exchange with solvent atoms in the interstitial sites.

The magnitude of the defect fluxes are temperature and ion dose rate dependent. By theoretical predictions, RIS growth rate constant should vary as the fourth root of the dose rate, Averbek et al [1983] investigated the dose rate effect of radiation-induced formation of Ni₃Si, and observed that dependence of the RIS rate on dose rate is slightly weaker than

predicted, but agreement is quite reasonable.

1.4.6.3 Other Segregation Models:

Recently the failure of models based on mass and binding energy for sputtering of alloys have been emphasized and the conclusion that RIS, mainly ion bombardment induced segregation [Kelly and Oliva, 1986] plays a dominant role in preferential sputtering in a wide range of materials has been reached. The situation is manifested in the conflict of evidence between different techniques employed for investigations, for example many Ion Scattering Spectroscopy (ISS) experiments show contradictory results to those obtained from AES and XPS due to the different sampling depth [Yu et al., 1994 and Sullivan et al., 1994]. There are several segregation models but we will be discussing only few of them.

Kelly's model for BIGS:

Kelly's model [Kelly, 1986] is based on the conservation of matter, and the boundary condition that the loss of material at the surface leads to a steady state in the outer most layer, but BIGS was assumed to extend over only one atomic layer. Nakamura et al [1981] introduced a subsidiary condition for the second atom layer, but the profiles obtained using those equation are known to be wrong. A surface composition spike is found to due to BIGS in a number of systems investigated [Swartzfager et al, 1981]. To correct these profiles, Kelly [1986] assumed the second layer to obey certain condition and for bombardment induced segregation (BIS) and based on minimizing the free energy of the system, Kelly [1989] obtained;

$$\frac{\alpha_{A(2)}^{\infty}}{\alpha_{B(2)}^{\infty}} = \frac{\alpha_{A(3)}}{\alpha_{B(3)}} \exp\left(\frac{\Delta H_{seg}}{kT}\right) \exp\left(\frac{-\Delta S_{seg}}{k}\right) = \frac{\alpha_{A(3)}}{\alpha_{B(3)}} \exp\left(\frac{\Delta G_{seg}}{kT}\right) \quad (1.39)$$

where $\alpha_{i(2)}^{\infty}$ and $\alpha_{i(3)}$ are the steady-state (∞) surface (2) composition and bulk (3) composition; ΔH_{seg} and ΔS_{seg} are heat and entropy of segregation. The sign convention used for ΔG_{seg} is appropriate if $\Delta G_{seg} > 0$.

Thermodynamic interpretation to equilibrium segregation:

Considering the change in free energy due to exchange of a surface atom B with a bulk atom A, for a binary system AB, on the basis of assumption that total number of A and B atoms

being fixed and the condition for the system to have minimum free energy at equilibrium, Zangwill [1988] found a relation of the surface composition to the bulk composition. Assuming pressure, volume, temperature and chemical potential of the system to remain unchanged during the surface segregation, one obtains;

$$\frac{x_A^s}{x_A^b} = \frac{x_B^s}{x_B^b} \exp\left(-\frac{Q}{kT}\right) \quad (1.40)$$

This is the well known Langmuir-McClean equation [Kirschner, 1985]. Q is called the heat of segregation and is equal to the difference in surface energy between atoms A and B. Hence the surface may be expected to be enriched with component of lower surface binding energy.

Miedema's model:

This model [Miedema, 1978] is based on Langmuir-McClean equation, but the heat of solution term for dilute alloys is also included to account for the modified environment of the exchanged atoms in the bulk and at the surface. He also showed that the surface energy or surface tension is related to the electron density at the boundary of a bulk atomic cell, so some relaxation of the electron density distribution and the position of the atoms at the surface layer were also taken into account. Due to this consideration, he assumed that only 24% of the surface area of a surface layer is in contact with vacuum. Miedema considered not only the effect of surface energy but also that of mismatch between two kinds of elements in sizes. According to this model, the heat of segregation for a metal A diluted into metal B is given as,

$$Q = f\Delta H_{sol}(A, B) - \frac{g}{3}(\gamma_A - \gamma_B)V_A^{2/3} \quad (1.41)$$

here ΔH_{sol} is the partial molal heat of solution of metal A in metal B, V_A is the molar volume of A, γ is the surface enthalpy, f is the relaxation factor with a value of 0.71 and the constant $g=4.0 \times 10^8$. Miedma calculated surface energies for some transition metal alloy systems and found good agreement with experimental values.

Plessis and Wyk model:

Considering that segregation is "uphill diffusion", Plessis and Wyk [1989] based their model on Fick's diffusion equations. They described the kinetics of segregation in terms of the difference in Gibbs free energy between surface and bulk and other adjacent cells, by equation

given below

$$\frac{\partial X_1^\phi}{\partial t} = \frac{M_1^{B-\phi} X_1^{B_1}}{a^2} [\Delta G_1 + RT \ln \frac{X_1^{B_1} (1 - X_1^\phi)}{X_1^\phi (1 - X_1^{B_1})} - 2\Omega_{12} (X_1^{B_1} - X_1^\phi)] \quad (1.42)$$

here X_1^i is the fractional concentration of species 1 in i-th cell, $M_1^{B-\phi}$ is the mobility of the species 1 in moving from the bulk to the surface, $X_1^{B_1}$ is the concentration in the first subsurface layer, a is interatomic distance and Ω_{12} is the interaction coefficient.

Weidrasch's model (non-equilibrium segregation):

This model [Weidersich et al, 1979] is based on the concept of preferential coupling between defect fluxes and fluxes of certain alloying element. This model was summarised by Wagner et al. [1983]. In a binary alloy AB, the defect fluxes and atom fluxes may be expressed in terms of partial diffusion coefficients of A and B components. By taking into account the defect production rate and the efficiency with which only a fraction of the defects produced in a cascade will escape spontaneous recombination and clustering and contribute to the RIS, the steady state concentration gradient becomes,

$$\nabla C_A = \frac{C_A C_B d_{Av} d_{Bv}}{C_B d_{Bi} D_A + C_A d_{Ai} D_B} \cdot \left(\frac{d_{Av}}{d_{Bv}} - \frac{d_{Ai}}{d_{Bi}} \right) \cdot \nabla C_v \quad (1.43)$$

Here, D_k is the partial diffusion coefficient, C is the concentration and d_{kv} is the diffusivity coefficient of k atoms via vacancies. Similarly, the subscript i represents the same for interstitials. During ion bombardment, the defect concentration always decrease towards a defect sink, and so above equation predicts enrichment of element A at sink if $d_{Av}/d_{Bv} < d_{Ai}/d_{Bi}$.

Some other models:

Robins and Falicov [1983] developed another model by taking the results of first principle calculations for elemental solids as an input quantity to calculate heat of formation between 4d metals to predict surface segregation. Kumar et al [1976] have based their studies on semiempirical theory and described segregation over whole range of temperatures. The phenomena of chemically induced segregation can be tractable by this approach.

The tight binding approximation [Kerker et al., 1977] is widely used to predict surface segregation in d-band metals. A common agreement is that segregation should strongly

depend on more open crystal surfaces and weakly dense planes. An embedded cluster model [Muskat, 1982] found that surface potential plays an important role in surface segregation. Similarly Barnett et al [1983] proposed an electron theory by using local ionic pseudo potential and linear response model.

Generally speaking, none of the models claims to be universally applicable but within their range of validity the agreement with experiments is quite good. However, due to lack of required data, it is not possible to use these in all the cases.

1.4.7 Radiation-Enhanced Diffusion:

Ion bombardment also influences the diffusion in the solids. In the absence of radiation, the diffusion of vacancies and interstitials is characterized by a random walk process, described by the equation,

$$D = D_0 \exp\left(-\frac{\Delta H_m + \Delta H_f}{RT}\right); \quad D_0 = \alpha a_0^2 \nu \exp\left(\frac{\Delta S_m + \Delta S_{th}}{k}\right) \quad (1.44)$$

here $\Delta H_{f,m}$ is the defect formation and defect migration enthalpy, T is the temperature, α depends on crystal structure, a_0 is the lattice parameter, ν is the Debye frequency, $\Delta S_{th,m}$ are the configurational and mixing entropies, respectively and k is the Boltzmann's constant. As the extent of mixing is sensitive to the sign and magnitude of ΔH_m , this suggest a role not only for random motion, but also for chemical driving forces [Miotello and Kelly, 1994]

Normally, at room temperature a little or no diffusion takes place but ion bombardment can enhance diffusion [Sizmann, 1978] either by changing the concentration of point defects in the target to far exceed the concentration of same at the thermodynamic equilibrium or by creating other diffusion mechanisms via defect species, which are usually not operative. This phenomena is known as radiation-enhanced diffusion (RED). The steady state concentration of vacancies and interstitials depend on temperature, sink concentration, total dose and dose rate. In addition to atomic displacements, ion bombardment may also induce inelastic ionisation processes which provide additional force for diffusion [Appleton, 1984]. These latter effects are more important for semiconductor materials.

The element diffusion sputtering and cascade mixing are generally dominant at low temperatures at which the defects generated by ion bombardment are immobile, but the radiation induced defects can lead to an enhancement of the diffusion coefficients, thereby lowering the temperatures at which diffusion dominates. The flux of defects gives rise to

material transport [Hofmann, 1985], which can extend as far as bulk of target, may be over distances exceeding the primary ion range. In real alloy systems, the diffusion kinetics can be influenced by many factors including defect aggregation, defect-impurity binding, defect concentration gradients and chemical effects etc.

1.4.8 Recoil implantation:

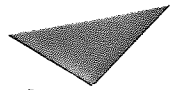
In alloys, the recoil cross section and range of the recoiling atoms depend on the charge and mass of the nucleus in such a way that generally the lighter component atoms will be transported relative to the heavier components in the beam direction, which is compensated by an opposite flux of the remainder of components to maintain atomic density at the proper value. The mean recoil implantation depth $\langle z \rangle$ depends on the distance of closest approach in an ion-impurity collision and ion fluence [Sigmund and Gras-Marti, 1981]. As a rule of thumb, z_m is smaller (greater) than the residual ion range $R(x)$ at x if the impurity is heavier (lighter) than the matrix. The fact that recoil implantation is both anisotropic and preferential implies a depletion of the preferentially implanted species in the surface region which may be mistaken for being caused by sputter depletion [Sigmund, 1979].

1.4.9 Cascade (Isotropic, Displacement) Mixing:

Cascade mixing is a random process resulting from the motion of secondary recoil collisions. Although the ion fluence generates an anisotropic distribution of knock-ons, the statistical independence of subsequent events produces nearly isotropic mixing. Collision relocation of materials generates density and pressure gradients that can not persist in a stable material [Collins and Sigmund, 1992] and in response, relaxation may take place. Sigmund [1995] defined the relocation cross section for preferential sputtering accompanied by isotropic, preferential cascade mixing. Kelly and Miotello, [1992] studied the problem of ion beam mixing and concluded that this process is in part ballistic and in part chemically guided.

1.4.10 Phenomenological model for surface compositional changes:

Wiedersich et al. [1983] showed the effects of different processes on the time evolution of the surface concentration and on the steady state profiles in a Cu(40 atomic%)-Ni alloy bombarded with 5 keV Ar⁺ at 400° C, as shown in Figure 1.8. The calculations were performed with various combinations of preferential sputtering (PS), displacement mixing (DM), RED, Gibbsian adsorption (GA) and RIS. Clearly, in the absence of irradiation, GA



Aston University

Content has been removed for copyright reasons

Figure 1.8 Effects of various combinations of GA, PS, RED, DM and RIS on the time evolution of the surface concentration of Cu during sputtering at 400°C, for 5 keV Ar⁺ bombardment [Wiedersich et al., 1983] .

leads to a strong Cu enrichment in the first atomic layer (Curve 1). Considering only PS and RED during irradiation (Curve 2) concentration of Cu at the surface shows a monotonic decrease to the steady state value, however if GA is included in the calculations, the surface concentration of copper increases rapidly at short times due to radiation enhanced adsorption and then decreases slowly to a steady state value (Curve 3) and the inclusion of DM reduces the effect of GA (Curve 4). Accounting only for PS, RED and RIS, the surface concentration of copper decreases rapidly to a steady state value (Curve 5) due to dominant effect of segregation. If GA is added, then the effect of RIS is masked (Curve 6) and finally, with the addition of DM, the surface concentration of copper first increases and then decreases towards the steady state value.

Accounting for the effects of all the processes described in the previous sections, Lam and Wiedersich [1987] proposed a phenomenological model, however, because many of the parameters needed in the model are unknown, quantitative comparisons with experiment are difficult. Sigmund and Oliva [1993] defined the kinetic equation for the composition profile accounting for athermal and thermal processes, but so far, full analytic solution of that kinetic equation has not been reported for any system.

1.4.11 Chemical Etching:

When a solid is bombarded with other than noble gas ions, it generally results in a chemical reaction between the incident ions and the atoms of the solid. The altered chemical composition of the surface layers changes the surface binding energy and sputter yield values. In chemical etching, the incident particles induce chemical reactions to produce new compounds on the target surface. These are often volatile and will be removed to a vacuum. Based on the fact that sputtering is a "physical" event, chemical removal by ion bombardment is generally called "etching". The final physical state of implanted material depends on the interplay between the gradual addition of impurity ions and radiation damage resulting from atomic collisions. If the concentration for solubility is exceeded, well defined stoichiometric compound phases may be formed. At low temperatures, metastable alloys may form which are not accessible by conventional methods [Paote, 1978].

1.5 Surface Binding Energy:

As discussed in section 1.4, from the point of view of implantation, preferential sputtering and segregation are very important processes. From the models outlined for these two, it is clear

that the knowledge of surface binding energy is very important. The surface binding energy can be influenced by contamination or adsorption on the surface, but even if these factors are disregarded, then the most important factors influencing the surface binding energy are:

- surface composition,
- surface roughness
- surface stress
- crystallite orientation.

Determination of correct value of surface binding energy, U_0 is a difficult problem, especially in the case of alloys and compound semiconductors. For elemental and metallic targets, generally, sublimation energy (ΔH_s) is used to represent U_0 and it gives reasonable agreement between theory and experiment. Some people use heat of atomization, ΔH_a , as representation for U_0 . For elemental substrates, it is evaluated by correcting the experimentally measured heats of sublimation (or vaporization) to 273K.

The choice of surface binding energy representation by ΔH_s or ΔH_a is only a generalized energy for the substrate. The surface binding energy for individual surface atoms may vary considerably, depending on the position of the atom, its neighbours and the bonds between the atoms. The surface binding energy of a substrate may change when a crystalline substrate changes to amorphous state under ion bombardment. In addition, an atom or molecule, at a kink site, will have a different binding energy. So the surface binding energy should be a population weighted average over the individual binding energy [Malherbe, 1994]. The number of link, ledge and corner sites may depend on the defects created by the ion bombardment process. So the surface binding energy may depend on the ion flux and the substrate temperature. Experimental evidence suggest that surface binding energies indeed depend on alloy composition.

For the sputtering of compounds, one faces the problem of correctly recognising the sputtered species and so, the correct quantity to represent surface binding energy is not obvious. For example, for low energy argon bombardment of GaAs, only 0.6% of the sputtered flux was found to consist of GaAs molecules, while 99.4% of the sputtered particles were Ga and As species [Comas and Cooper, 1967].

For a random binary alloy the surface binding energies were expressed by Kelly [1980] as a function of the nearest-neighbour bond strengths U_{11} and U_{12} thus the surface binding energy for 1-atoms is,

$$U_1 = -x_1^s Z_s U_{11} - x_2^s Z_s U_{12} \quad (1.45)$$

here Z_s is the surface co-ordination number and $x_{1,2}^s$ are surface atomic concentrations of two elements. To first order approximation U_{11} and U_{12} are replaced with the heat of atomisation H_1 and H_2 . In 1985, Kelly and Harrison [1985] gave a 'quasi-chemical' model for calculation of surface binding energy;

$$U_0 = \left(\frac{2Z_2'}{Z_3}\right)\Delta H_a = (1.42 \pm 0.08)\Delta H_a \quad (1.46)$$

here Z_2' is the surface ("2") co-ordination number and Z_3 is the bulk ("3") co-ordination number.

Kelly [1987] considered the problem of site dependent surface binding energy and on the basis of argument that vaporization or sublimation takes place from ledges and corners whereas sputtering takes place from a flat surface and hence involves extra bonds. He suggested that the process of a metal atom sputtering from a solid should take place in two steps, characterized by surface-vacancy formation energy, E_f^s , and heat of atomisation, ΔH_a , and hence, for an undisturbed surface,

$$U_0 = E_f^s + \Delta H_a \approx 9.7kT_m + \Delta H_a \quad (1.47)$$

here k is the Boltzmann's constant and T_m is the melting point. The resultant surface binding energy is about 30% larger than the heat of atomisation.

Harrison [1988] has pointed that in the midst of cascade situation it is possible for an atom to be ejected during sputtering event even when its kinetic energy never exceeds the value of surface binding energy. Under these circumstances it seems best to use heat of sublimation or heat of atomisation in the case of elemental targets.

Malherbe et al (1986) proposed a new approach to calculate the binding energies of metal oxides by modifying the Pauling formalism for the formation of covalent bond. For M_xO_y the average binding energy is given as (Pauling, 1967)

$$D(M_xO_y) = \frac{x}{x+y}D(M-M) + \frac{y}{x+y}D(O-O) + \frac{x}{x+y}D(M-O) + \frac{1}{2}(\epsilon_M - \epsilon_O)^2 \quad (1.48)$$

here $D(M - M)$ is metal-metal bond energy, $D(O - O)$ is the dissociation energy of the oxygen molecule, $D(M - O)$ is the metal-oxygen bond energy of diatomic metal oxides and ϵ_M , ϵ_O are the electronegativities of metal and oxygen, respectively. The average energy required to remove only an oxygen atom is given by [Malherbe et al., 1986]

$$U_o = \frac{y}{x + y}D(O - O) + \frac{x}{x + y}D(M - O) + \frac{1}{2}(\epsilon_M - \epsilon_O)^2 \quad (1.49)$$

For a metal atom in oxides,

$$U_M = H_s + \frac{1}{2}(\epsilon_M - \epsilon_O)^2 \quad (1.50)$$

Here H_s is the sublimation energy of the pure metal.

1.6 Computer Simulations

The computer simulation of the effect of energetic ion bombardment on solid surfaces has been studied for nearly three decades. Due to development of fast personal computers with large memory, even quite complicated calculations can be performed fast and without any specialist computer hardware. There are a number of different methods used for simulation of the interaction of ion beams with solid, with varying degree of accuracy from the simulation and the time for simulation. The simulation methods can be classified as:

(a) Trajectory Simulations: These involve the effects of a single ion on a solid matrix and repeat the calculation over a large number of different ion collisions to give a result which will predict what will happen when the matrix is irradiated by a large number of particles.

(b) Analytic Simulation: These are based on the solutions of transport theory and involve approximations to scattering or multiple-scattering equations. Solutions are found for a global ensemble of particles simultaneously.

1.6.1 Trajectory Simulations:

In this case, as the ion penetrates the target, the path of individual ion is followed, and then, depending on the degree of accuracy and the amount of information required, the path of the recoiling target atoms is also followed. In their most simple form, the equations of motion of all particles in the system are solved simultaneously. Although, this is conceptually the

simplest form of simulation, there are very few assumptions but, this is the most complex to write and the slowest to run. Two types of simulations are used for cascade development, binary collision and multiple interaction simulations.

1.6.1.1 Binary Collision (or Event Store Codes) :

In these calculations, one recoil is followed at a time storing information about all others, so that it can come back and continue the calculation of those when it has finished dealing with the current one. This model is based on the assumption that each particle interacts with only one other particle at a time and one of these particles is initially stationary. This assumption inhibits this code in a number of ways, for example;

- in describing the behaviour of cascades as the energy decreases.
- in describing low energy implantation, where $E < \text{few hundreds of eV}$.
- calculation of the correct path of a particle passing between two other particles. The best way is to treat such events using a multiple collision algorithm [Robinson and Torrens, 1974]. The codes which correctly treat these simultaneous collisions are called as pseudo binary codes. Some codes never allow such collisions to occur.

In this simulation, we deal with sequential collision with non-sequential timing, so the exact cascade development is incorrectly modelled. But it is interesting that the average phenomena like implantation range and induced defect distributions are predicted accurately because of ensemble averaging over many ion trajectories.

Binary Collision Approximation:

This is based on the classical solution of the scattering for a spherical symmetric potential. The approximation means that the calculation does not need to follow the complete path of the colliding particles but find only the asymptotic scattering angle in the centre-of-mass system. Figure 1.9 shows as long as no other collisions occur before the straight line paths match the asymptotes, then the approximation is valid. The asymptotic scattering angle θ is given by equation (1.30) and the potential is generally taken as the screened Coulomb form of potential, defined as;

$$V(r) = \frac{Z_1 Z_2 e^2}{a r} \Phi(r) \quad (1.51)$$

here $\Phi(r)$ is the screening function and a is the Bohr radius.

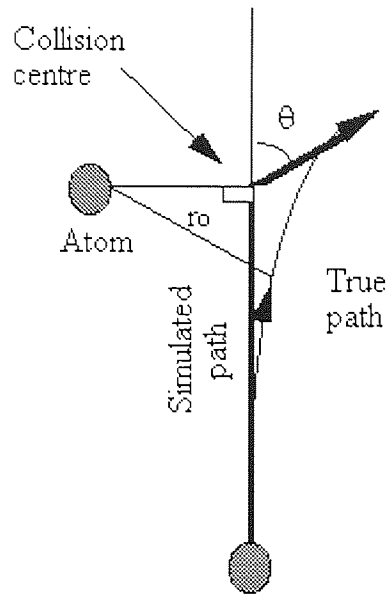


Figure 1.9 Representation of the binary collision approximation

Trajectory simulations need to solve these equations for each collision made by the particles. To speed up calculations, TRIM (to be discussed later) uses a fitted algebraic relation between θ and r for various forms of interaction potential [Wilson et al., 1977]. Some other simulators use 'look up' tables of r_o against θ as suggested by Hautala [1984].

1.6.1.2 Monte Carlo Codes:

Binary collision codes are often incorrectly called Monte Carlo Codes. In binary collision codes, a random number generator determines the initial impact site on the target for the different trajectories and the rest of the trajectory is usually deterministic. But this choice of random number does not make them true Monte Carlo codes. In some codes, a small random perturbation of target atoms due to thermal vibrations determines the initial impact site but again the rest of the trajectory is deterministic. This makes such codes slightly more Monte Carlo but not true Monte Carlo codes. In true Monte Carlo codes, a random number weighed by the collision cross-section determines the collision dynamics of the particles for amorphous targets and a future random number determines the particle species in the multicomponent targets. For single crystals where thermal vibrations are ignored, it is better to use evenly distributed sample of impact points across a surface to make a full set of representative points, rather than a random start point [Harrison, 1988].

1.6.1.3 Multiple Interaction Simulations:

In these simulations, all collisions are calculated simultaneously as the ion penetrates the solid. Hence these codes follow reality closely and so are much more accurate. The interaction potential is chosen carefully so that it matches,

- as many of the bulk and surface elastic properties of the target as possible.
- as closely as possible, many of the dimer and trimer properties of binding and bond angles.

Some simulators use the full many-body potentials [Tersoff, 1986]. These codes can simulate even non-linear collision cascades without any logical errors. However, these codes tend to be very computer intensive.

1.6.1.4 Hybrid Models:

The calculations using the multiple interactions are very time consuming and would pose

serious problems if many trajectories were run to obtain statistically meaningful results. So the crystal is often terminated in a number of ways depending on the information required. Webb et al [1986] attempted to use a binary collision code as a boundary to multiple interaction model. In this hybrid model, particles leaving the boundary were followed by using TRIM; any particles coming back from binary collision were timed and flagged back into the multiple interaction collection at the correct time. The other form of hybrid model is to use a binary collision logic for the high energy parts of the collision cascade and then drop into a multiple interactions calculations at the end, when the cascade has become non-linear.

1.6.1.5. Boltzmann Transport Approach:

This technique is based on the numerical integration of the linearized Boltzmann transport equation and yields the quickest method of simulation. The solution of this equation tends to be a 'forward-looking solution'. As the calculation proceeds to the deeper regions, the energy distribution broadens. The final depth distribution is the probability distribution of particles with zero energy. The problem with this approach is the ignoring of back scattered particles. This problem is solved by flagging the number of back scattered particles as the calculation proceeds and then to return back to them after completing the range profile.

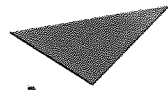
1.6.2 High Dose Effects:

When the ion dose is low, each implanted ion does not see the effect of any previous ions but if the ion dose exceeds about 10^{13} ions/cm², then the cascade starts to overlap in the region of target where cascades from previous ones have left behind stable defects. These effects are illustrated in Figure 1.10. So new simulation models are required which,

- allow the target to relax after implantation of large doses of ion. This can result in target swelling out around the implant.
- which allow the surface of target to recede as it is sputtered away.
- consider the mixing of target matrix and implant due to both recoil and cascade mixing.

1.6.2.1 Evaluation of High Dose Profiles:

Usually, the implantation is broken into a number of dose increments and then the simulation is run initially into an unbombarded target, producing a sputter yield and an initial range



Aston University

IS

Content has been removed for copyright reasons

**Figure 1.10 Some of the important effects considered during simulation.
[Webb, 1992]**

profile. Then the target is allowed to relax and the simulation is continued into this new intermediate relaxed target, which has also had an amount of material removed from the target surface to simulate the effect of sputtering. During the next dose increments, the mixing of the implant and target is calculated and the target is modified by the subsequent increments. This procedure is continued until the full dose required is reached. There are a number of simulation models capable of performing these calculations. Most of them are based on the trajectory simulation technique, but some of them are based on a diffusion equation model to describe all the mixing, relaxing and erosion effects. The initial parameter to evaluate diffusion coefficients are found by running a number of trajectory simulations.

1.6.3 Computer Simulations Available:

There are a number of computer simulations available - TRIM [Biersack and Haggmark, 1980], TRIM.SP [Biersack and Eckstein, 1984], EVOLVE [Rousch et al., 1981], TRIDYN [Moller and Eckstein, 1984], MARLOWE [Shulga, 1983], COSIPO [Harrison, 1988], Boltzmann transport [Giles and Gibbons, 1985], SUSPRE [Surrey University Sputter Profile Resolution from Energy deposition program, Version 1.4, 1987], QDYN [Wilson et al., 1977], SATVAL [Sielanko and Szyszko, 1985] and many more. For this project, only TRIM, SUSPRE and SATVAL were being used.

1.6.3.1 TRIM:

TRIM stands for TRansport of Ions in Matter. This is probably the most famous of the event store type codes. Originally, it was written by Biersack and Haggmark [1980] but Ziegler has recently improved it [Webb, 1992]. TRIM-85 was the original release and in recent years, it has been changed. For this project, TRIM version 95.07 was used. With TRIM one can calculate transport of ions (10 eV - 2 GeV/amu) into solids using a full quantum mechanical treatment. The calculation is made by the use of the statistical algorithms which allow the ion to make jumps between the calculated collisions and then averaging the results over the intervening gap. During the collision, the ion and the atom have a screened coulomb collision, including exchange and correlation interactions between the overlapping electron shells. The ion has long range interactions creating electron excitation and plasmons within the target. The charged state of the ion within the target is described using the concept of effective charge, which includes a velocity dependent charge state and a long range screening due to collective electron sea of the target. The flight of the ion (or recoil) is assumed to be a straight line and the flight distance is determined by mean free flight path, L [Biersack, 1987].

The particle's energy is reduced after each free flight path by the amount of electronic energy loss and then after each collision by nuclear energy loss. For the calculation of energy losses, [Ziegler, 1988], the screening radius, a_U , defined as equation (1.7) and screening function, Φ_U , is used;

$$\Phi_U = 0.1818 \exp(-3.2x) + 0.5099 \exp(-0.9423x) + 0.2802 \exp(-0.4028x) + 0.2817 \exp(-2.016x) \quad (1.52)$$

Here the screening function is the best fit obtained from a large number of experimental results and is known as universal screening function.

In TRIM, if a cascade atom leaves the target volume from front surface or the rear surface, it is discarded. However, the atoms leaving sideways are followed indefinitely. If an incident ion with an atomic number Z_1 and energy E collides with the target of atomic number Z_2 , and after the collision, the ion and target have energy E_1 and E_2 respectively. Let E_d , E_b represent the displacement and binding energy of the target and E_f be the final energy of the moving atom, below which it is considered to be stopped, then

- If $E_2 > E_d$, a displacement occurs.
- If $E_1 > E_d$ and $E_2 > E_d$, a vacancy occurs.
- If $E_2 < E_d$, then struck atom vibrates back to its original site releasing E_2 as phonons.
- If $E_1 < E_d$, $E_2 > E_d$ and $Z_1 = Z_2$, then incoming atom will remain at the site (replacement collision) and E_1 is released as phonons.
- If $E_1 < E_d$, $E_2 > E_d$ and Z_1 is not equal to Z_2 , then projectile becomes an interstitial atom.
- If $E_1 < E_d$, $E_2 < E_d$, then projectile becomes an interstitial atom and $(E_1 + E_2)$ is released as phonons.

This program assumes a cylindrical symmetry in the final distributions with the cylindrical axis being perpendicular to the target surface at the point of ion impact, if the initial ion beam is normal to the target surface.

1.6.3.2 SUSPRE:

SUSPRE stands for Surrey University Sputter PRofile from Energy deposition. This is based on a set of analytic and numerical calculations. It performs a very fast calculation of majority

of effects during implantation and is used as a first order calculation to see what might happen during implantation. It first of all performs a range of calculations using PRAL (Projected Range ALgorithm) which is based on a method for directly connecting the angular spread of the direction cosines of the incident particles to the nuclear energy loss. From PRAL, SUSPRE calculates the energy deposition profile, then uses this to calculate the sputter yield. It treats angle of incidence using the lateral spread parameter, calculated using PRAL. Cascade broadening effects are calculating by calculating a diffusion frequency (based on the diffusion approximation), which is used to calculate diffusion coefficients. It can also convolute the broadening effects of sputter profiling.

1.6.3.3 SATVAL:

This model uses Monte Carlo simulations. In the case of the targets gradually loaded with primaries due to implantation process, the trajectories of primary ions are evaluated by considering the possibility of scattering on the target atoms as well as the previously implanted ions. Also in the treatment of cascade, the trajectory of each atom - primary implanted or target atom, is followed until they sputter or stop in the target. The positions of the last one are stored and are taken into account when the probability of scattering has been calculated. For this purpose the target is divided into equal thin layers with surface area small enough to have the possibility of the high dose irradiation by following 3000 - 10000 histories of incoming ions [Sielanko and Szyszko, 1986]. The probability of collision between a moving atom with a previously implanted one is calculated by

$$P = \frac{N_i(x)}{N_i(x) + N_t(x)} \quad (1.53)$$

where $N_i(x)$ and $N_t(x)$ are the number of ions and target atoms, respectively in the layer at depth x . $N_i(x)$ are changing during bombardment due to implantation, sputtering, cascade mixing or recoiling. The kind of scattering centre is selected by a random number RND in following way

RND > P	target atom
RND ≤ P	implanted ion

The additional assumptions used in this simulation are:

- the implanted ions occupy the same volume as target atoms, which means that there

is no change in mean free path length in the implanted layer.

- ion bombardment under low beam current conditions, that is, evaporation by high flux ion beam and thermal spikes are ignored.

1.7 Concluding Notes:

Within the last three decades, substantial amount of work has been done on ion implantation in various materials. The interpretation of experimental observations requires a good understanding of theoretical models and correct theoretical analysis needs experimental evidence. On the theoretical side, the major problem is prediction of the number of ions of an element that can be implanted in a given matrix. The codes are also unable to account for molecular ion impact. For molecular ions, the binary collision and Sigmund's theory breaks down and so the models based on Sigmund's theory are not valid. However, to first order approximation, the penetration of energetic molecules may be looked at as the sum of events induced by independent atoms and so the models can be used. The models available, for the calculation of amount of ions implanted in the target, are generally not applicable to compound targets. Moreover, these models are too simple considering only the sputtering processes and ignoring some very important processes such as surface segregation and diffusion. There are some segregation models which we used successfully in this work but in some cases the input information required is either unavailable or not very accurate.

1.8 Research Programme:

This project aims to accomplish a series of experiments on N_2^+ implantation on metals and compound semiconductors, to study bombardment induced compositional changes, especially the amount of nitrogen retained in the target and the depth distribution of the implanted nitrogen. This will help in understanding the mechanisms and the factors responsible for the retention of nitrogen. The effect of ion properties, such as energy, current density and dose and the target properties such as mass, binding energy, density, chemical interaction with ions, was studied.

For obtaining experimental data, the surface analytical technique, XPS was chosen and effectively used. To gain insight into both physics and chemistry of the processes, the ion implantation experiments were carried on target materials of varying chemical reactivity and masses. Both monoenergetic implantation and non-monoenergetic ion implantation were being employed. To obtain the in-depth distribution of implanted nitrogen, both destructive

(sputter depth profiling) and non-destructive techniques (ARXPS) were used. After initial preparation, the samples were sputter cleaned with low energy Ar⁺ beam to remove the surface contaminants. These samples were then implanted with nitrogen beam of required energy and current density. These samples were then analysed by ARXPS. Then the depth profiles of implanted nitrogen were created using Ar⁺ beam. For non-monoenergetic implantation, after initial preparation, the samples were cleaned with argon plasma and then were exposed to nitrogen plasma. After cooling, these samples were then analysed by ARXPS.

In order to understand the measured implantation profiles, the experimental data was compared with the computer simulated data. For this purpose, the computer simulation codes, TRIM, SUSPRE and SATVAL were used. It is hoped that this work will provide more information about the ion bombardment compositional changes, especially the amount and depth profiles of implanted nitrogen and will improve the understanding of the mechanism responsible for this phenomena.

Chapter 2

Surface Analytical Techniques and Depth Profiling

2.1 Introduction:

In N_2^+ implantation, the determination of chemical composition and chemical states of implanted nitrogen is very important and so XPS was considered as the best choice for this study. The knowledge of in-depth distribution of implanted nitrogen is also important. Depth profiling was performed using sputter depth profiling and Angle Resolved XPS (ARXPS). This chapter is divided in two sections. The first section covers the surface analytical techniques, mainly XPS and the depth profiling is discussed in the second section.

2.2 Surface Analytical Techniques:

Surface analysis is an important technique for determination of elemental composition and chemical states of components in the surface. A recent compilation of physical examination and analytical techniques identified almost 150 methods which could be used for material analysis. The majority of these techniques are specialist methods requiring careful specimen preparation and experimentation. Others are applicable to a fairly limited portion of the periodic table or accept specimens in only one particular form. Four types of techniques for surface analysis are available in our research group:

- Auger Electron Spectroscopy (AES)
- X-ray Photoelectron Spectroscopy (XPS)
- Ion Scattering Spectroscopy (ISS)
- Secondary Ion Mass Spectroscopy (SIMS)

SIMS has the highest sensitivity in elemental analysis but mass interference, matrix dependence and strong influence of charging effects on sputter yields, makes reliable quantitative analysis very difficult. ISS enables the detection of the first monolayer on a surface, but is difficult for insulators and semiconductor materials, because of surface charging, ion neutralisation and shallow effect. AES and XPS have detection limit of about 0.1%, sampling depth of 3λ , (λ , the electron inelastic mean free path), quantification within $\pm 10\%$ and a large amount of support data. XPS has advantages of chemical state information and very little beam damage. Hence, XPS was considered to be best for this project.

2.2.1 X-ray Photoelectron Spectroscopy (XPS):

XPS has origins in the discovery of the photoelectric effect at the end of the last century and a schematic of the process of X-ray induced photoelectron emission is shown in Figure 2.1. When a X-rays with sufficient energy, $h\nu$, strike a solid, some electrons within the atom may be excited and receive sufficient energy to overcome the binding forces between the electron and nucleus, then these electrons can escape from the solid surface. If E_k is the kinetic energy of photoelectrons emitted, then by Einstein's photoelectric equation,

$$E_k = h\nu - \phi - E_b \quad (2.1)$$

where E_b is the binding energy of the electron in the solid and ϕ is the work function, its value being dependent on both the sample and spectrometer. The energy of the emitted photoelectrons is analysed by an electron spectrometer and the data is represented as a graph of intensity (or counts per second) versus electron energy. Since binding energy of core level electrons is associated with a specific species of the atoms, the electron energy spectrum is a fingerprint of the type of the target atoms. By measuring the intensity and energy of the electron, one can calculate the relative concentration of an element in the solid.

2.2.1.1 Spectrum Analysis:

Characterization of a Surface:

This step involves identification of the elements present on the sample surface. To achieve this, a wide scan spectrum over a region -20 to 1000 eV on a binding energy scale was recorded. The individual peaks can be identified from the NIST database. Figure 2.2 shows the photoelectron peaks and the Auger lines resulting from the de-excitation process.

From Figure 2.2, it is clear that the electron background increases in a step like manner after each spectral peak. This is because of the scattering of the characteristic Auger or photoelectrons by the matrix bringing about a loss of kinetic energy. If the photoelectron peaks have a horizontal background or a slightly negative slope, then the sample is perfectly clean but, the presence of a positive slope shows the surface is covered with a thin overlayer. The peaks from the buried phase result in a positive slope. In the most severe case the peak itself will be absent and there will be only a change in background slope at the appropriate energy.

The recorded spectra not only consists of photoelectron peaks (used for compositional and chemical state determination), but also Auger peaks, loss peaks, valence peaks and X-ray satellites (in non monochromatic sources).

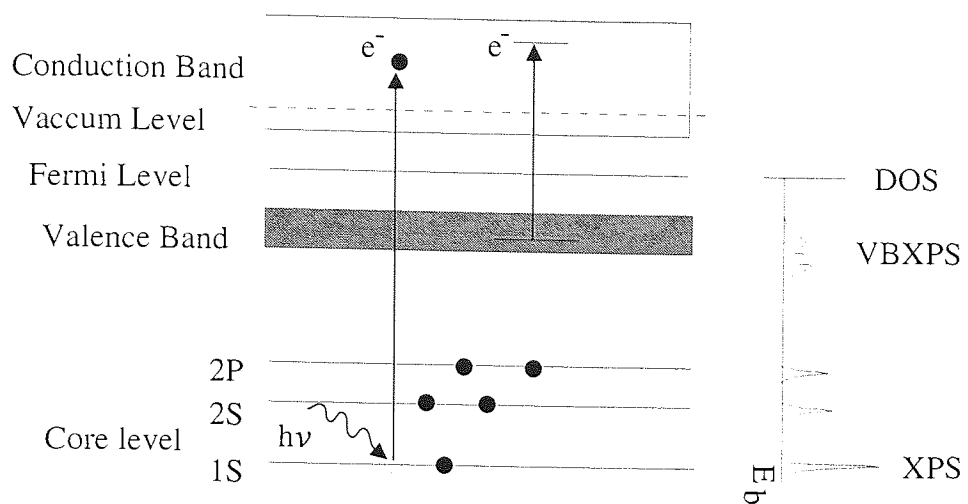


Figure 2.1 Principle of X-ray Photoelectron Spectroscopy

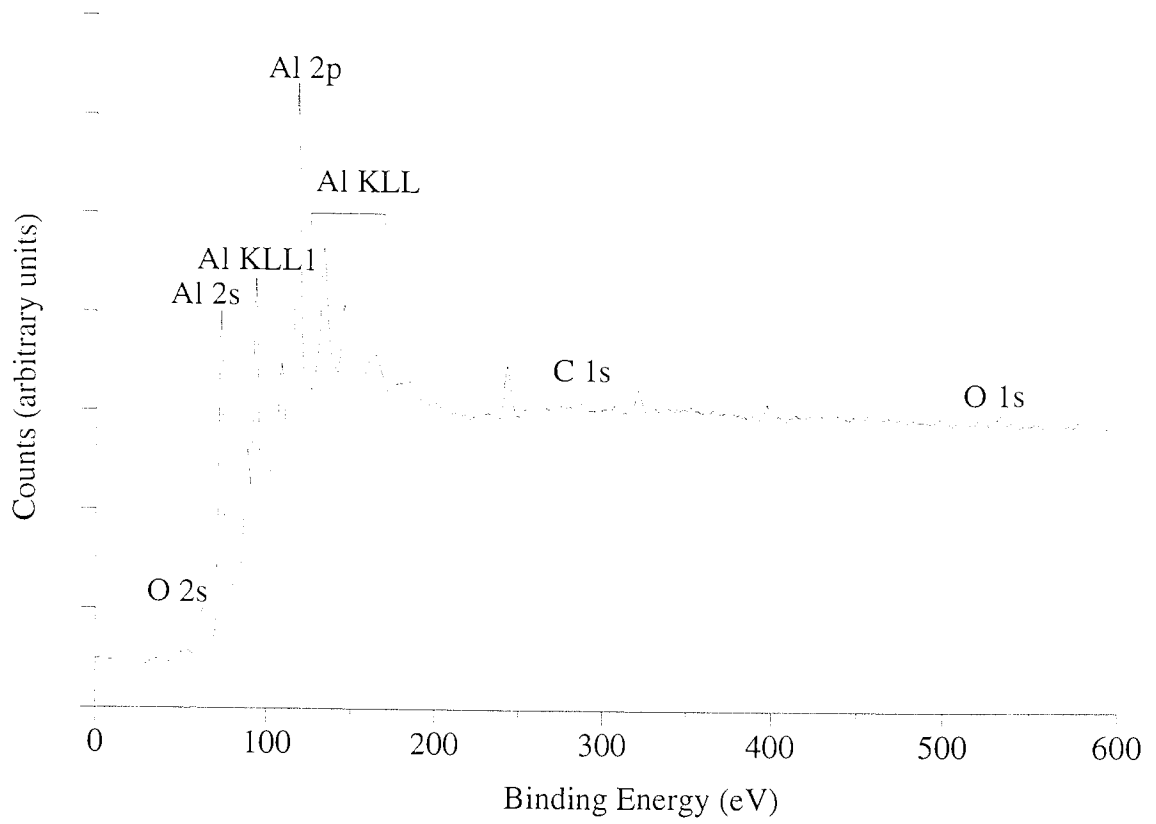


Figure 2.2 XPS spectrum of oxidised aluminium

Chemical State Information:

When the atoms of a particular element are in different chemical environment and chemical states, the binding energies of core electrons are different, which can be explained by the redistribution of electric charge accompanying the formation of chemical bond [Seighbahn et al., 1967]. This model is known as charge potential model. When the atom is bound to other atoms in a molecule or crystal, the charge density of valence electrons will vary, resulting in a change in binding energy of core electrons. A partial decrease in the valence electron density associated with a species of an atom results in an increase in binding energy and an increase in electron density results in results in a decrease in binding energy. In addition to this charge effect, the distribution and the type of the surrounding atoms will also cause a binding energy shift. Briggs and Rivie're [1990] have made this description more accurate by considering the final state effects.

Figure 2.3 shows the chemical shift in aluminium spectra. N_2^+ bombardment of aluminium results in the formation of AlN and the redistribution of electronic charge in the formation of AlN increases the nuclear charge on aluminium ($Al^{+\delta}N^{-\delta}$), but as the fermi level is fixed, so this results in shrinkage of bands and hence an increase in binding energy.

Plasmon Loss Features:

Any electron of sufficient energy passing through a solid can excite one or other of the modes of the collective excitation of the sea of the conduction electrons. These oscillations have frequencies characteristic of the material of the solid, and therefore need characteristic energies for excitation. An electron that has given up energy equal to one of these characteristic energies is said to have suffered a plasmon loss. Within the solid, the loss is said to be 'bulk plasmon loss'. If ω_b be the fundamental characteristic frequency of bulk plasmon, then plasmon energy loss is $\hbar\omega_b$. Since the harmonics of the fundamental frequency can be excited but with progressively lower efficiency (a series of losses, all equally spaced by $\hbar\omega_b$, but of decreasing intensity). However, at a surface, a rather localised type of collective oscillations of frequency ω_s can be excited. This is known as "Surface plasmon loss" and is a surface cleanliness diagnostic [Massignon et al., 1980]. The plasmon losses associated with the 2p, 2s and KLL peak of aluminium are shown in Figure 2.4. Here, the surface plasmon loss peaks for aluminium are almost absent, and this is due to surface contamination by oxygen.

Valence Band Structure:

Valence levels are those occupied by electrons of low binding energy (say 0-20 eV) which are involved in de-localized or bonding orbitals. As these levels are very closely spaced and thus

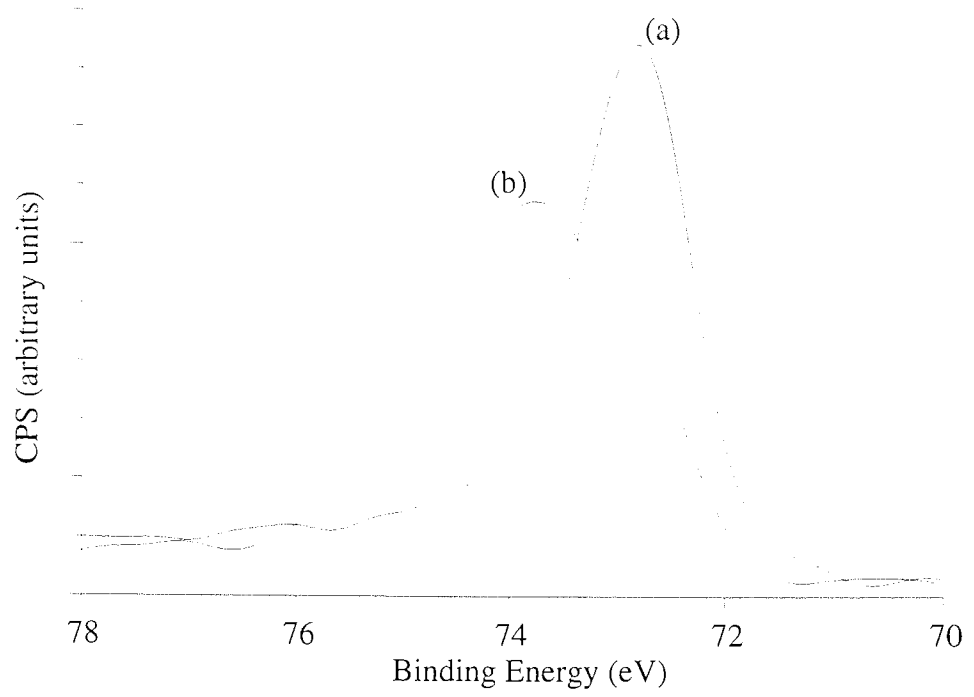


Figure 2.3 XPS spectrum of (a) pure Al and (b) nitrated Al.

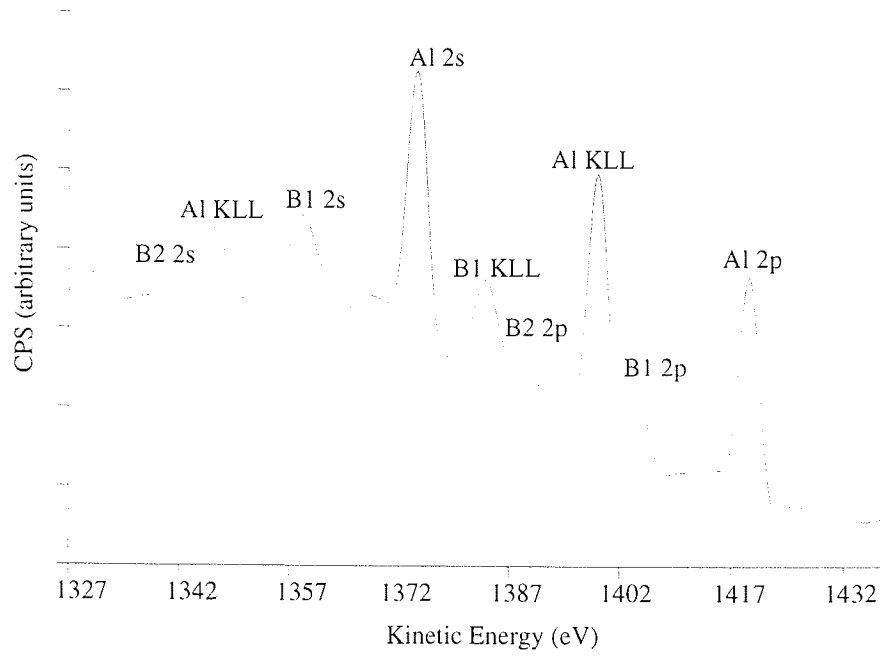


Figure 2.4 Plasmon loss fine structure associated with the aluminium 2p, 2s and KLL Auger spectrum. The successive bulk plasmon losses are indicated as B1 and B2.

give rise to a band structure. In the case of insulators, the occupied valence band is separated from the empty conduction band, whilst in the case of a metal these bands overlap. The valence band spectra is very closely related to the density of occupied states. This fact helps in study of electronic structure of materials, fundamental to many aspects of device applications, and in checking accuracy of band structure calculations. Figure 2.5 shows the comparison of aluminium valence band spectra, before and after nitrogen ion bombardment. The creation of additional gap after nitrogen ion implantation shows the change of metallic aluminium to insulating AlN.

Shake-up Peaks:

When the outgoing photoelectron interacts simultaneously with a valence electron and excites it to a higher level; the energy of the core level electron is then reduced slightly, giving a satellite structure a few eV above the core level position (on BE scale). These features are rarely seen as discrete features of the spectrum but more usually as broadening of the core level peak or contribution to the inelastic background. However, very strong "shake-up" peaks are sometimes observed in certain transition metals which have unpaired 3d and 4f levels. Hence, these peaks can be used to obtain information about the valence state of certain elements, for example, closed shell systems such as Cu^+ , $3d^{10}$ (Cu_2O) do not exhibit "shake-up", but Cu^{++} , $3d^9$ (CuO) does.

X-ray Ghosts:

Standard X-ray sources are not monochromatic. There can be excitation arising from impurity elements in X-ray source which result in several peaks at a constant distance below the main photoelectron peaks, known as X-ray satellites (if excited by a minor component of the X-ray spectrum) and X-ray ghosts (arising as a result of cross talking in a twin anode gun). These features just complicate the X-ray spectrum and are of no analytical use. In either case the problem can be reduced to an inconsequential level by overhauling and readjusting by the X-ray gun.

Multiplet (or Exchange or Electrostatic) Splitting:

Multiplet splitting of a photoelectron peak can occur when the system has unpaired electrons in the valence band, and arises from different spin distributions in the electrons of band structure. This results in a doublet of the core level peak and occurs strongly in the 4s level of rare earth metals. In the case of Fe spectra, there are 5 levels for $2p_{3/2}$ peak which lead to peak broadening and non-symmetrical peaks. The large amount of coupling between the core hole created by photoemission and the high spin states of iron result in a very complex spectra. However, this does not give any information, but is a nuisance.

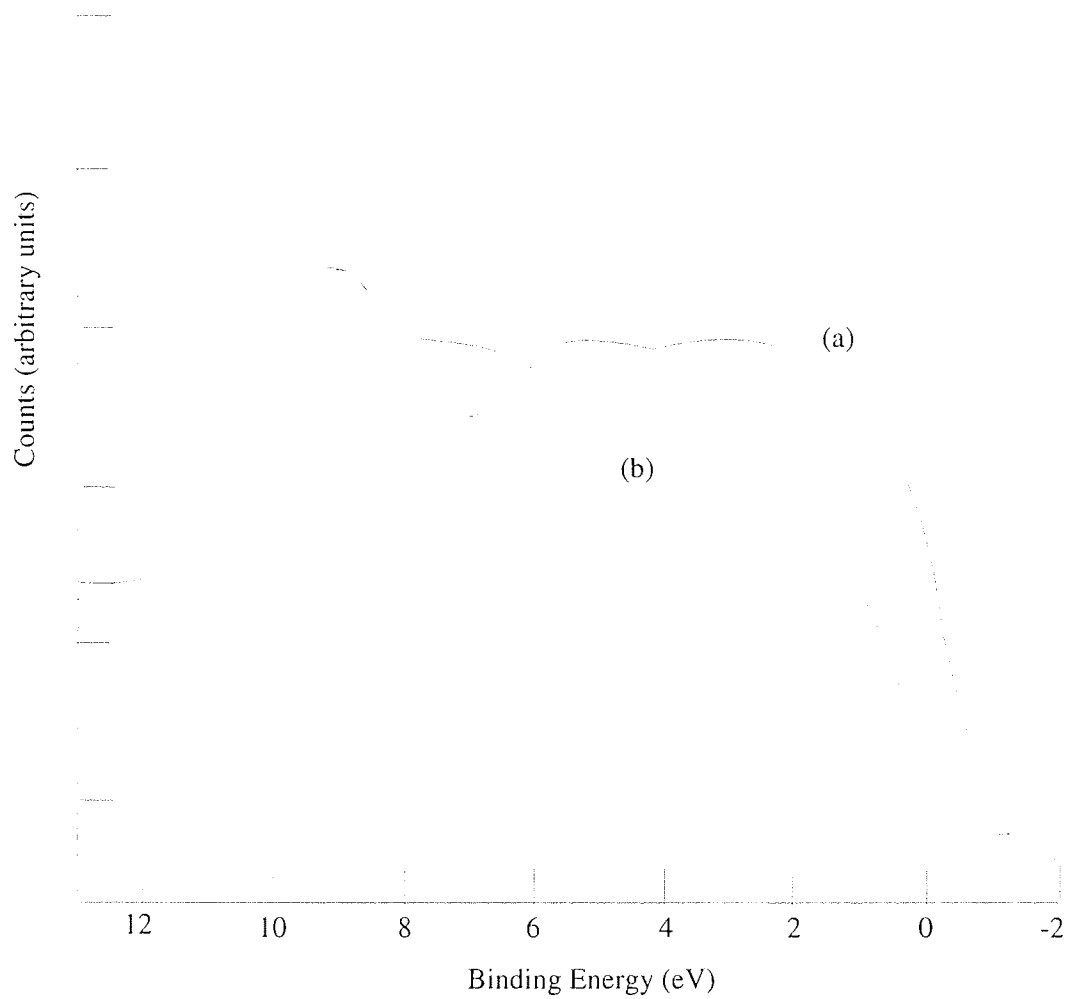


Figure 2.5 VBXPS of (a) pure Al and (b) nitrided Al.

2.2.1.2 Spectrum Processing:

To extract the maximum amount of information, the original XPS spectrum is processed in the following order;

(i) **Smoothing:** In practice, a certain statistical noise always exist in original data. By increasing the acquisition time for the experiment, one can get higher signal to noise ratio, but this is very time consuming. Smoothing is a mathematics process to increase the correlation between data points and suppress uncorrelated noise. Sherwood [1990] method of smoothing was used for this work.

(ii) **Energy Calibration:** The cornerstone of any spectral analysis is the peak position. The two possible errors in determination of peak position are spectrometer calibration and electrostatic charging of the spectrum. The spectrometer can be calibrated using standard samples (generally Cu and Au). The latter is resolved by proper mounting. But for insulators and semiconductors, there is always a possibility of a shift due to charging. In that case, one can use an internal standard such as the adventitious carbon 1s peak position, but this is not particularly accurate, as it varies with form and amount of carbon. However, one can calibrate spectra using Auger Parameter ' α ' defined as

$$\alpha = E_b + E_k - h\nu \quad (2.2)$$

where is the E_b binding energy of the photopeak and E_k is the kinetic energy of the Auger transition. The C 1s peak position, defined at 284.6 eV, is the most widely used method throughout this work.

(iii) **Background removal:** When looking at a typical XPS spectra, Figure 2.2, one finds that the XPS as well as Auger peaks are always superimposed on a background. This is due to photoelectrons produced within the target materials that have been subject to one or more inelastic scattering processes before emission from the surface. The background also arises due to individual photo-emission lines acting as a source of additional electrons to undergo scattering events [Smith, 1990]. There are many ways to remove background, the most common are, linear [Sherwood,1990] and non-linear methods such as due to Shirley [1972]. In this work, the latter method was used, which achieves subtraction of background by an iterative method.

(iv) **Curve synthesis and curve fitting:** A spectrum, in which there is more than one chemical state present may not be resolved by the electron energy analyser. It is necessary to synthesis the individual peaks to produce a final function that closely represent the experimental spectrum. Sherwood [1990] gave a fitting method based on simple addition of

guessed peaks (curve synthesis) or after a least squares refinement (curve fitting). The basis XPS peak is Lorentzian type function, modified by some instrumental and other factors to give a Gaussian contribution. Usually a mixed Gaussian-Lorentzian product function is used [Ansell et al., 1979]. An example of convolution of two or more chemical states in a single spectrum, is shown in Figure 2.6.

2.2.1.3 Quantitative Analysis:

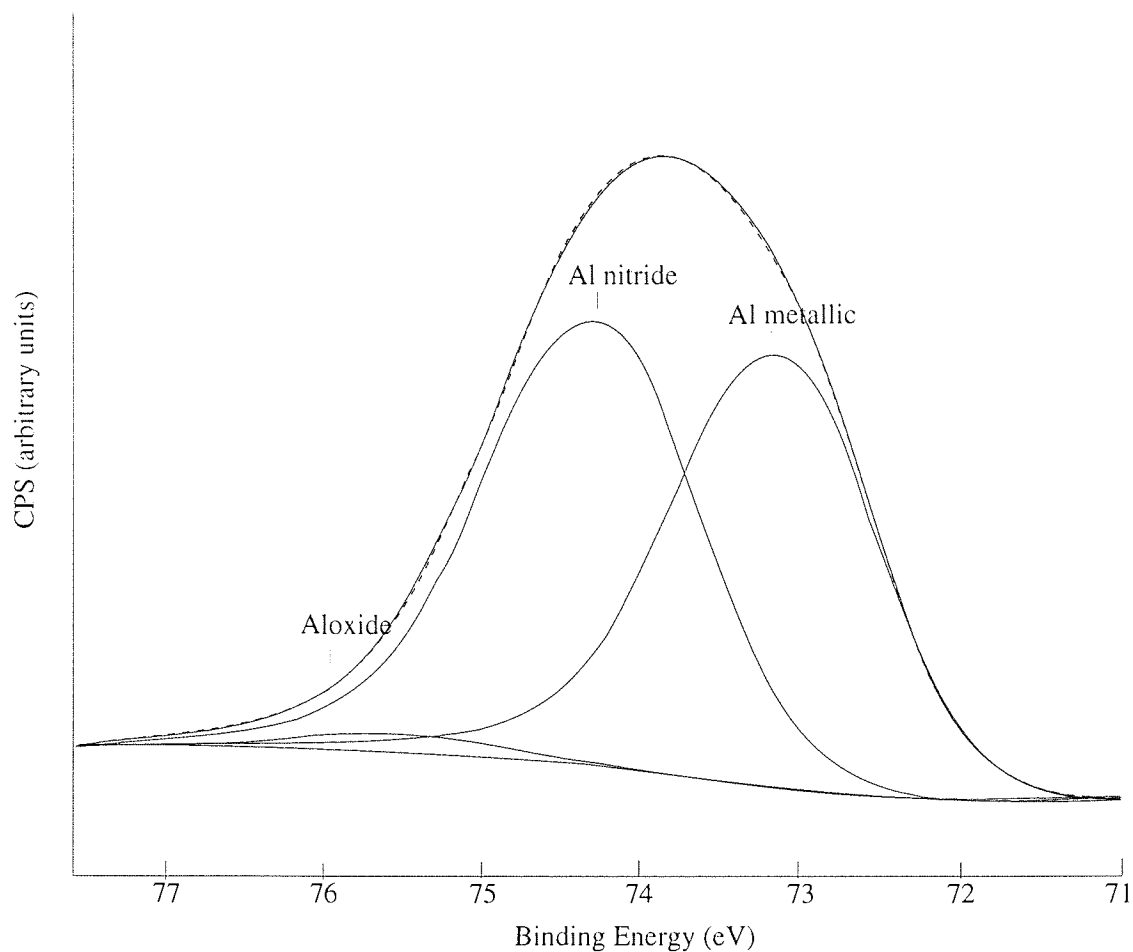
The absolute quantification of an XPS data is not straightforward. The intensity of a photoelectron peak from a solid surface is given by

$$I = J\sigma(h\nu) L(\gamma) D(E_k) T(E_k) \int_0^{\infty} n(z) \exp\left[-\frac{z}{\lambda(E_k) \cos \theta}\right] dz \quad (2.3)$$

where J is the X-ray flux, σ is the cross-section of photoelectron production, L is angular asymmetry of the intensity, D is detector efficiency, T analyser transmission function, $n(z)$ is atomic density at depth z , λ is the electron inelastic mean free path [IMFP] and θ is electron take-off angle.

The surface sensitivity of the XPS is based on the fact that the number of electrons will be reduced exponentially by a factor of $\exp[-z/\lambda \cos \theta]$ after travelling a distance z . So the maximum sampling depth of XPS ($\theta=0^\circ$) for a specific core level of an atom is approximately $3\cdot\lambda$. Many formalisms have been proposed for the relation of λ with electron energy and characteristics of materials, however, the models of Seah and Dench [1979], give values of almost all core levels are in the range of 2 to 10 atomic layers. Tanuma et al., [1991a, 1991b] have calculated the values of IMFP for elements and inorganic compounds, such as GaAs in the energy range of 50-2000 eV. Tanuma et al., [1996] have also pointed towards the problems to use IMFP for the quantitative analysis as it ignore the elastic scattering effects. Cumpson and Seah [1997] found that the elastic scattering causes attenuation lengths to be typically between 10% and 25% shorter than IMFPs. Hence in the presence of elastic scattering, these are not appropriate for use as attenuation lengths.

Accurate calculation of the intensity of photoelectrons using equation (2.3) is rather difficult, since the theoretical calculations for photoelectron cross-section, angular asymmetry coefficient, electron detection efficiency and transmission function are impossible without some assumptions. The electron detection efficiency and the transmission function vary from one instrument to another, depending on the type of the analyser and the geometry of the instrument used. In above equation, the specimen is assumed to be homogeneous within the volume sampled by XPS, which is rarely the case. Hence the absolute measurement of surface concentration using equation (2.3) is impossible for accurate quantitative analysis but even so, the above method provides a valuable means of comparing similar specimens.



Peak	Centre (eV)	FWHM (eV)	Height (%)	G/L (%)	Area (%)
Al metallic	73.1	1.37	56.4	30	47.3
Al nitride	74.2	1.47	57.9	30	50.9
Al oxide	75.4	1.52	2.1	30	1.8

Figure 2.6 Deconvolution of various chemical states in Al 2p spectrum.

A common way of quantification is by comparing the intensities of photoelectrons peaks for each element obtained in the spectra, I_i , with intensities in standard spectra of the elements, I_i^∞ , or with relative sensitivity factors for the elements, S_i , which is the relevant value of the intensity in standard spectrum for an element to that of a specific peak, usually C 1s or F 1s. For a homogeneous material with components A and B, the equation (2.3) can be expressed as;

$$\frac{I_A / I_A^\infty}{I_B / I_B^\infty} = \left[\frac{\lambda_{AB}(E_A) \lambda_B(E_B)}{\lambda_{AB}(E_B) \lambda_A(E_A)} \right] \left[\frac{R_B^\infty}{R_A^\infty} \right] \left[\frac{N_A / N_A^\infty}{N_B / N_B^\infty} \right] \quad (2.4)$$

Here λ_{AB} represents the attenuation length in AB system, R represents the factors of effect of surface roughness and N 's are the atomic densities of element A or B in AB compound and in pure reference sample. The above equation is further simplified as;

$$\frac{X_A}{X_B} = F_{AB} \left[\frac{I_A / I_A^\infty}{I_B / I_B^\infty} \right] \quad (2.5)$$

Here F_{AB} is the matrix factor. So, the concentration of element i in a compound containing n elements can be written as;

$$c_i = \frac{(I_i / I_i^\infty)}{\sum_{j=1}^n (I_j / I_j^\infty)} = \frac{(I_i / S_i)}{\sum_{j=1}^n (I_j / S_j)} \quad (2.6)$$

In the equation, usually intensity is taken as the area under the envelope of the peak after background removal. The intensities in the standard spectrum or the sensitivity factors may be referred to either systematically measured experimental data (Wagner data) or theoretical calculations (Scofield data) [Seah, 1990].

It is obvious that the above equation contains a number of approximations and may lead to certain errors in the quantification. Firstly, of all the measurements for the standard intensities or the sensitivity factors may be done using different type of equipment under different experimental conditions and secondly, it has been found that there are variations in the relative signal intensities which are sample dependent [Smith, 1990]. The other factors leading to errors in quantification are surface roughness and the intensities calculated at different energies and under different experimental conditions. To achieve the greatest accuracy in quantitative analysis in a specific XPS equipment, it is essential to calibrate every core line to be studied using standard samples and use self generated relative sensitivity factors. In this work, whenever possible, the relative sensitivity factors calculated by our group for the ESCALAB 200D were used. The accuracy for quantification was about $\pm 10\%$ at best.

2.3 Depth Profiling:

The depth profiling of the implanted nitrogen was an important part of this project. Depth

profiling is the analysis of one or more elements as a function of the distance normal to the original sample surface. When the sample composition is non-uniform in the plane of the surface and below, three dimensional characterization is usually desirable. This can be achieved either by destructive or non-destructive techniques. There are many techniques available but as XPS was chosen as surface analytical technique and hence, sputter depth profiling using XPS and Angle Resolved XPS (ARXPS) were selected as depth profiling techniques.

Sputter Depth Profiling: By bombardment with a particle beam of well-defined average current density, the sample can be eroded in a controlled manner, almost layer by layer. The analysis of the flux of sputtered material or determination of the composition of the instantaneous surface at certain chosen intervals, provides the information about the composition of the sample as a function of depth. This method is called sputter depth profiling. In actual practise, the process of sputter erosion deviates from ideal case of a layer by layer sectioning, depending on the quality of the depth profiling experiments.

Angle Resolved X-ray Photoelectron Spectroscopy (ARXPS): ARXPS is a potential method for non-destructive determination of a composition depth profile of a surface region to a depth comparable to the mean free path of the photoelectrons. This is based on the principle of profiling by variation of the photoelectron emission angle.

2.3.1 Sputter Depth Profiling:

In this project, the near surface composition of the sample was analysed with XPS, intermittently between certain chosen periods of sputter erosion. Hence, the measured sputter profile, consists of a signal intensity of the detected elements, I (peak areas, in XPS), as a function of sputtering time t . The main task is to obtain the distribution of original concentration X with depth, by an appropriate conversion of the measured data [Hoffmann, 1980]. For this purpose,

- the sputtering time scale should be calibrated in terms of eroded depth, and
- the intensity of XPS signal must be calibrated in terms of local element concentration, by taking into account the profile distortions.

2.3.1.2 Measured profiles:

In principle, it is impossible to derive any detailed information about the internal distribution of atoms from only the sputter profile [Wittmack, 1982]. The sputter-induced compositional and topographical changes can cause very complicated alterations of the measured profiles [Hofmann, 1990] and these generally result in broadening of the profiles. The profile is also

broadened due to escape depth effect by $\approx 1.6\lambda$, λ being the escape depth of photoelectrons. Two parameters of main interest are:

- **Achievable depth resolution**, which defines the quality of depth profiling experiment.
- **Erosion rate**, which determines the time required for analysis.

Depth resolution is the difference of the depth co-ordinate z between 84% and 16% of the intensity change at the interface [Morrison et al., 1979] and it depends in a complex manner on the instrumental factors, bombardment conditions, sample characteristics and radiation-induced effects. In general, depth resolution function is of non-symmetrical shape. Wittmack [1991] has discussed the effect of low, moderate and high ion fluence on bombardment induced broadening. The actual number of target atoms ejected in an individual collision shows large fluctuations, however, with available surface analytical techniques, we can not determine these yield fluctuations. The computer simulations show this distribution extends from zero to some upper statistical limit. These high sputtering events will result in the roughening of the ion bombarded surface, which in turn affects the depth resolution.

As an approximation, the erosion rate \dot{z} is determined by

$$\dot{z} = \frac{M}{\rho N_A e} Y j_p \quad (2.7)$$

here M is target molecular mass, ρ is density, N_A is Avogadro number, e is electronic charge, Y is sputter yield and j_p is the primary ion current density. As M , ρ and Y depend on the instantaneous surface composition, so this calculation gives only a rough estimate. Hofmann and Zalar [1979] found that as a result of variation in surface composition, the dependence of \dot{z} with sputtering time becomes non-linear. For a two component system, a weighed sputter yield can be used [Wang and Storms, 1976], however, it is difficult to use the above formula when sputtering takes place through layers of varying composition and hence varying sputter yields. There are some methods for in-situ measurement of the sputter rate, but as these methods were not available on the equipment used for this project and they are not discussed here.

In sputter depth profiling, a large variety of adverse physical and chemical phenomena are encountered, even in simple cases. Some interesting information about the spatial distribution of sample atoms can be obtained from the computer simulations, based on Sigmund models and Monte Carlo calculations. From such simulations, it is predicted that;

- The majority of displaced atoms travel distances of the order of 1nm before coming to rest. Only very small number of atoms go up to 3 nm and very occasionally up to 7 nm.
- Short-range transported atoms are distributed almost symmetrically about the depth of the

original location, while long-range outgoing relocated atoms centre around the direction of beam incidence.

- Lateral displacement from beam axis can be up to 5 nm.
- The mean depth of origin of sputtered particles is less than 1 nm. According to Robinson [1983], the majority of sputtered particles originate from 0.3 nm layer at the surface. Only a very small fraction (4% or less) is ejected from the depths greater than 0.5 nm.

However, these are generalizations based on simulation. Based on analysis of experimental data and theoretical arguments, Kelly and Oliva [1986], Falcone et al. [1987] and Oliva et al., [1987], concluded that most of the sputtered particles are ejected from the topmost monolayer. The basic problem in the use of sputter depth profiling is the poor efficiency (typically about 1 to 10%). The energy ΔE_s , transported into vacuum by sputter particles is only a small fraction of primary energy E . Two parameters energy re-emission coefficient due to scattered particles, Y_E , and energy re-emission coefficient due to reflected particles, R_E , are defined as;

$$Y_E = \frac{\Delta E_s}{E} \quad \text{and} \quad R_E = \frac{\Delta E_r}{E} \quad (2.8)$$

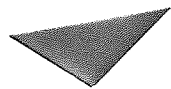
Both Y_E and R_E depend upon the mass of projectile and target atoms, the primary ion energy and the angle of beam incidence θ . The fraction of energy available for sputtering and relocation of target atoms is equal to $(1 - R_E)$. When this fraction is small, the re-emission coefficient is defined as $(Y_E / (1 - R_E))$. Figure 2.7 shows the variation of these re-emission coefficients with θ . Clearly,

- Y_E first increases with increasing θ , passes through a maximum (energy dependent position) and finally drops to zero as $\theta \rightarrow 90^\circ$.
- As $\theta \rightarrow 90^\circ$, $R_E \rightarrow 1$. i. e., almost all primary ions are reflected without any appreciable energy loss.
- The energy re-emission coefficient continues to increase beyond 50° , and reaches maximum at above 80° .

For mass ratios, M_2/M_1 , not substantially larger than one, the main part of the reflected energy is carried by the sputtered species, whilst the reflected projectiles dominate for $M_2/M_1 \gg 1$ [Andersen and Bay, 1981].

2.3.1.3 Artefacts in Depth Profiling:

There are a large number of effects which cause the measured profile to deviate from the true profile. These artefacts can be divided into instrumental factors and ion matrix factors. In general, the instrumental factors can be eliminated or kept low by a suitable choice of instrumental and operative parameters, while the ion matrix effects are intrinsically connected



Aston University

Content has been removed for copyright reasons

Figure 2.7 Angular dependence of energy re-emission coefficient for self-sputtering of nickel at two different impact energies [Wittmack, 1992].

with the method and in general set the limit for the performance of this method. Hoffmann [1990] has surveyed the optimised depth profiling conditions, which are represented in Table 2.1. Here we will limit our discussion to ion matrix effects.

Table 2.1 Tabulation of optimised depth profiling conditions.

Instrumental factors	Sample ambient	Low residual gas pressure ($<10^{-8}$ Pa) Free sample mount
	Ion beam	Pure gas supply No neutrals Rastered beam of constant intensity Low beam energy High ion mass or reactive species Large incidence angle for smooth sample Low incidence angle for rough sample Two different inclined beams and / or sample rotation
	Analysing conditions	Sputtered area large against analysed area Small spot analysis centred in sputtered area Selection of low kinetic energy signal
Sample Characteristics		Smooth, polished surface Non-crystalline, no second phase Components with similar sputter yield Good electrical and thermal conductivities Low interdiffusivities Low Gibbsian segregation

The interaction between primary ions and target, such as primary ion implantation and recoil implantation of surface adsorbed species may change the surface composition. This will result in the change in sputter yield and surface binding energy. Sputtering, recoil mixing and radiation enhanced diffusion are basic damage phenomena associated with ion bombardment and these will result in the broadening of a given concentration depth profile [Benninghoven et al., 1987]. The broadening of the profile due to cascade mixing increases monotonically with primary ion energy and becomes smaller the heavier the projectile ion. This broadening can be estimated from $U/4E_{d,min}$, here U being the surface binding energy and $E_{d,min}$ is the

minimum displacement energy [Andersen,1979]. Radiation enhanced diffusion may also contribute to preferential sputtering [Tarn and Fisher, 1978]. In addition to this, the Gibbsian segregation may disturb the sputter profiling analysis. In the course of depth profiling, the deposition of sputtered material onto the actual sample may disturb the measured profile. The surface roughness or any surface topographical development will deteriorate the depth resolution and may result in an incorrect determination of depth scale [Wehner and Hajicek, 1971]. Hösler and Palmer [1993] investigated the effect of layer crystallinity on the resolution of underlying interfaces and found that ion channelling imposes the severest limitations on the depth resolution available. From the above discussion, it is clear that one can not expect this method to be ideal, however, one can try to minimise the distortions by selecting bombardment conditions which cause distortions to a tolerable and controlled level.

2.3.2 Profiling by Variation of the Electron Emission Angle (ARXPS):

It is based on the dependence of intensity of photoelectrons to their escape angle. The intensity I_i and concentration X_i of an element i are related by

$$I_i = \frac{I_i^0}{\lambda_i} \int_0^{\infty} r_i(z) X_i(z) \exp\left(-\frac{z}{\lambda_i}\right) dz \quad (2.9)$$

where I_i^0 is the intensity for an elemental bulk standard, λ_i is the effective escape depth of the photoelectrons perpendicular to the surface, $X_i(z)$ is the local concentration at depth z and $r_i \geq 1$, is the back scattering factor. The variation of electron intensity with depth is shown schematically in Figure 2.8. If detected electrons have angle of emission θ w. r. t. the normal to the surface, then

$$\lambda_i = \lambda_i^0 \cos \theta \quad (2.10)$$

where λ_i^0 is the Inelastic Mean Free Path (IMFP) of the electrons for a given energy and material. Its value lies between 0.4 and 4 nm [Seah and Dench, 1979]. In angle dependent XPS experiment, spectra collected at each angle still contains a convolution of the entire depth profile, so the data must be inverted to generate an estimate of the depth profile. If λ_i is a continuous variable, then

$$I\left(\frac{1}{\lambda_i}\right) = \text{constant} \times L[X_i(z)] \quad (2.11)$$

And hence,

$$X_i(z) = \text{constant} \times L^{-1}\left[I\left(\frac{1}{\lambda_i}\right)\right] \quad (2.12)$$

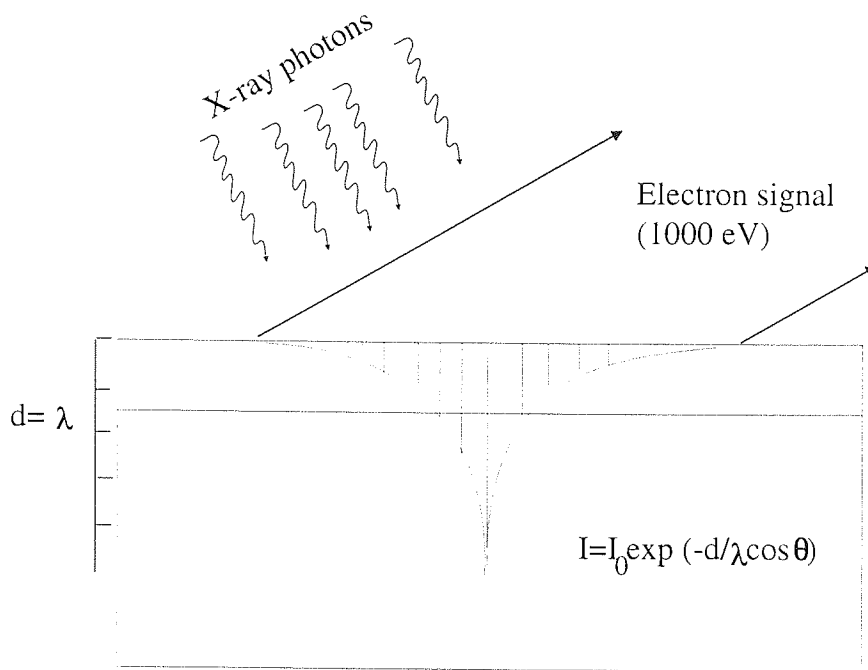


Figure 2.8 Variation of electron intensity with depth.

This method can be used for the determination of the thickness of contamination, implantation, sputtering altered and segregation layers, but because of the limitations in sensitivity, the depth range covered is $< 3\lambda_0$.

The inversion of angle dependent XPS is one of the mathematically "ill-posed problems" so standard numerical techniques can not be used to generate meaningful depth profiles. A variety of algorithms have been proposed for the evaluation of the ARXPS data. The more popular are regularisation method with non-negativity constraints [Tyler et al., 1989], regularisation using a priori information to obtain the most suitable profile [Jisl, 1990], Laplace transform [Holloway and Bussing, 1992] and an algorithm using effects of elastic electron scattering [Jablonski and Powell, 1993]. Nefedov and Baschenko [1988] calculated profile with due allowance for a priori information and have discussed the effects of statistical and systematic input errors on the mathematical results. The systematic input errors include the application of the incorrect values of the photoelectron mean free paths, photoionization cross-section. Baschenko [1992] slightly modified this algorithm by taking into account the compositional dependence of photoelectron mean free path in a sample on the depth z and then, by introducing the photoionization cross-sections, the system is ultimately reduced to solving a set of linear equations. Liversey and Smith [1994] proposed an algorithm based on statistical theory. This algorithm is based on the principle that in ARXPS, the objective is to reconstruct the depth profile from a data set consisting of relatively noisy measurements of intensity or apparent composition. The solution of this problem is the reconstruction that satisfies the data but contains the minimum amount of structure necessary to do so. The required solution is the reconstruction that has the minimum information content i. e. maximum entropy. It is known as maximum entropy algorithm.

Although there are a variety of algorithms proposed for the evaluation of ARXPS data but at present there are no standard algorithms for data analysis. Fulgham [1993] tried to compare three algorithms namely the relative ratio algorithm [Mill et al., 1976], the Laplace transform algorithm [Bussing and Holloway, 1973] and the absolute algorithm [Gries and Wybenga, 1981]. The criteria of comparison included the determination of the (z/λ) values, corrected parameters, experimental requirements, goodness-of-fit and sensitivity to overlayer thickness variation. She considered the relative ratio algorithm to be most accurate and sensitive for overlayer thickness ratio.

In recent years many algorithms have been proposed [Cumpson, 1995], but almost all of them are highly sensitive to the uncertainties in the experimental data and none are simultaneously robust to noise in the data, easy to use, free from parameterization or may be generally applied to a wide range of samples

Chapter 3

Experimental Apparatus and Procedures

3.1 Introduction:

The experimental procedure and details are described in this chapter. The samples chosen for this project consisted of metals and compound semiconductors including aluminium, iron, copper, gold, arsenic, gallium arsenide (GaAs) and aluminium gallium arsenide (AlGaAs). The experimental implantation work for this project is done using two types of instruments

- (a) the VG Scientific ESCALAB 200D system, for monoenergetic ion implantation
- (b) a d. c. plasma cell

3.2 Apparatus:

3.2.1 VGScientific ESCALAB 200D Spectrometer:

The spectrometer used in the project was a VGScientific ESCALAB 200D system. The layout of main components is shown in Figure 3.1 and the directional arrangement of XPS system in ESCALAB is described in Table 3.1. All components for surface analysis are located on the spherical analysis chamber with an inner diameter of about 600 mm. The brief description of system is given in Table 3.1.

Table 3.1 Arrangement of XPS system in VGScientific ESCALAB 200D

Component	φ°	θ°
X-ray Source	60	40
Spectrometer	15	0
Ion Gun EXO5	50	102
S. E. Detector	60	225
Viewport	75	5
CCD Camera	46	0
Sample Manipulator	90	90

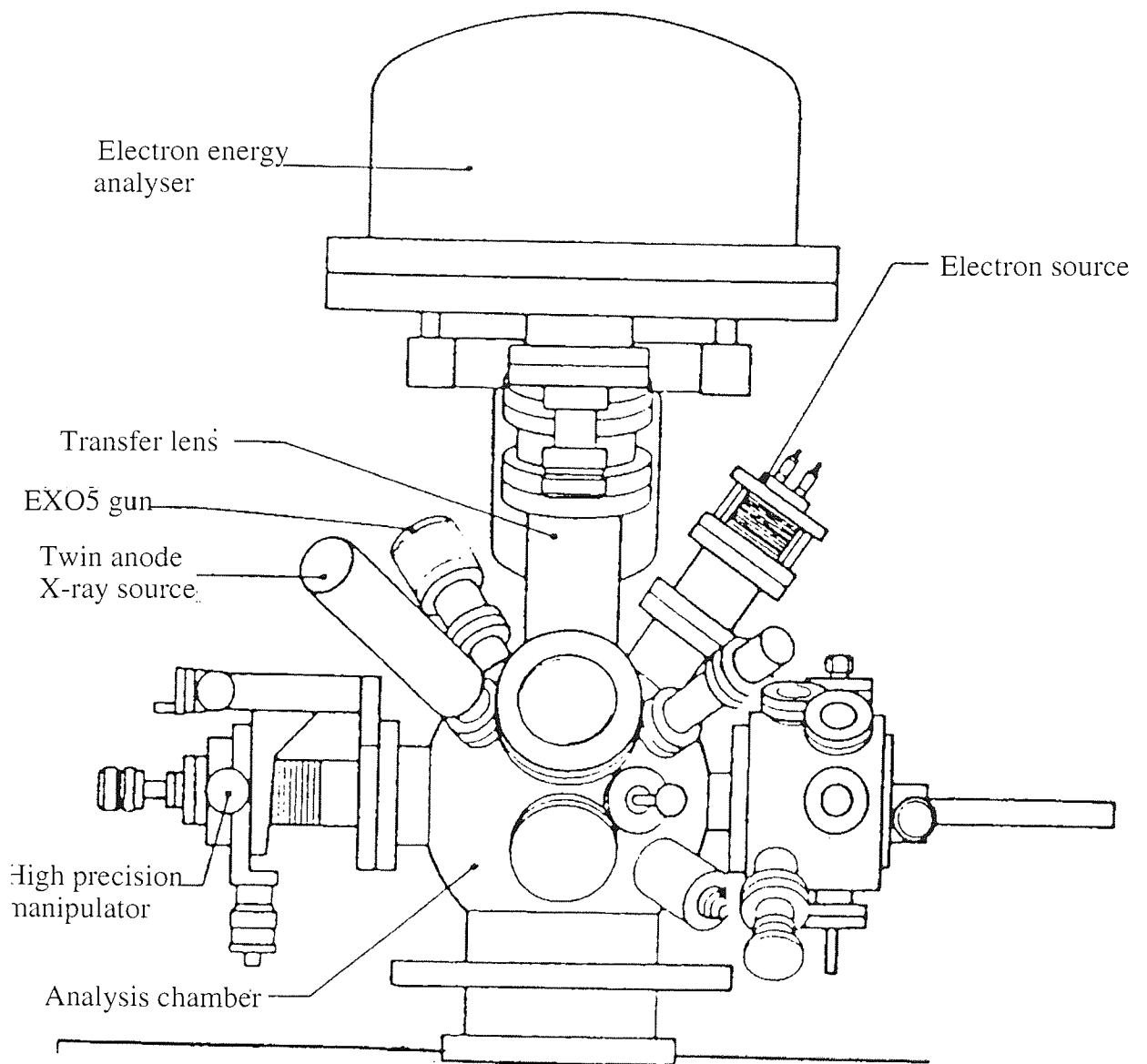


Figure 3.1 Layout of VGScientific ESCALAB 200D

3.2.1.1 Vacuum System:

The system is divided into two sections - the fast entry lock (the preparation chamber) and the analysis chamber. Both chambers have different working pressure, the preparation chamber vacuum is from atmosphere to 10^{-7} mbar and is maintained by a turbo molecular pump while the main analysis chamber pressure is from atmosphere 10^{-7} to 10^{-10} mbar. The main spectrometer vessel is generally pumped by means of a rotary pump and diffusion pump with polyphenyl ether pumping fluid and liquid nitrogen trap. Periodic bake-out of the system is done during the night for about 8-10 hours, at temperature of 200°C .

3.2.1.2 Ion gun:

A VG-EXO5 ion gun was employed in this project. It is an ion source suitable for etching in AES or XPS experiments. It can also be used in SIMS and LEIS experiments. It consists of an electron impact source, and is suitable for use with inert gases like argon and neon and also with nitrogen gas to provide ion beams.

The specification for this gun are given in Table 3.2. The gas is supplied to the source region via the gas inlet valve from a high pressure (1 atm.) volume but during this operation, an analyser chamber vacuum of better than 5×10^{-7} mbar is maintained by differential pumping of the source.

Table 3.2 Specification of EXO5 Ion Gun.

Operating Voltage	100 - 5000 eV
Maximum current	10 μA
Minimum spot size	< 120 μm
Maximum current density	> 5 $\mu\text{A}/\text{cm}^2$
Maximum scanned area	5mmx5mm

The ion energy is adjusted by the potential of the anode. The emission current can be varied from 2 μA to 10 μA continuously by adjusting the extraction voltage (0 to 10 V), by a coarse control to select fixed values in the range 2 μA to 10 μA and a fine control to get a 30% to 100% emission.

The schematics of ion optics of EXO5 ion gun is illustrated in Figure 3.2. When ions are extracted from the extractor, they will be focused by the first triplet lens

which is mainly used to change ion current to form a cross over point at the aperture between two lenses and is further focused by the second lens which principally determines the final spot size to obtain the expected beam spot at a certain distance. The focused ion beam is deflected by two pairs of deflecting plates and rastered over sample surface to give a homogeneous sputtering. A DC bias is applied to the pair of deflecting plates which allows the ion beam to be shifted so that a specific area may be selected. A self bias (12 V) at the sample suppresses the contribution of secondary electrons (from the sample) to the ion current.

3.2.1.3 X-ray source:

The structure of twin anode X-ray source used in this study is illustrated in Figure 3.3. In this system, Mg and Al anodes are fitted and is operated with the filament near earth potential and the anode at a positive potential of up to 15 kV. For Mg and Al anodes the main X-rays come from the transition $2p_{3/2}$ and $2p_{1/2}$ to $1s$, giving $MgK\alpha$ ($h\nu = 1253.6$ eV, FWHM = 0.7 eV) and $AlK\alpha$ ($h\nu = 1486.6$ eV, FWHM = 0.8 eV) lines, respectively. X-rays generated in the anode face pass out through an aperture in the surrounding cylindrical shield, covered with a thin aluminium foil. The aluminium window prevents sample from stray electrons, heat effects and contamination originating in the source. The window also removes other additional X-ray lines, such as $K\beta$, L, M etc. and provides secondary electrons which help in charge compensation.

3.2.1.4 Energy Analyser:

A simplified schematic diagram of 150° Hemispherical Sector Analyser (HSA) is shown in Figure 3.4. HSA is used as a multifunction energy analyser in the system and acts as a narrow pass filter allowing only the electrons with energy $E \pm \Delta E$ to pass. The energy resolution of the analyser is determined by ΔE . Here, $\Delta E = HV$ (eV); where V is the potential difference between inner and outer hemispheres and H is a constant determined by physical measurements of analyser, like the inner and outer radius of the two hemispherical electrodes and slits etc.. The electrostatic lens (in front of input entrance of analyser) improves the transmission characteristics of the analyser.

The energy level scheme of analyser is shown in Figure 3.5. The sample is normally at earth potential and electrons are transmitted from the sample to the analyser by the electrostatic lens and retarded in energy by an amount R (eV) immediately before entering to the analyser.

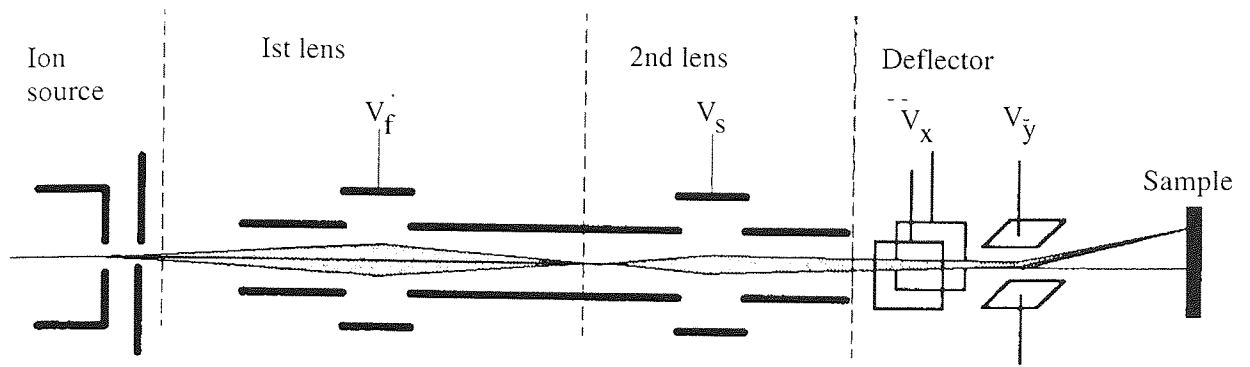


Figure 3.2 Schematics of ion optics in EXO5 ion gun system

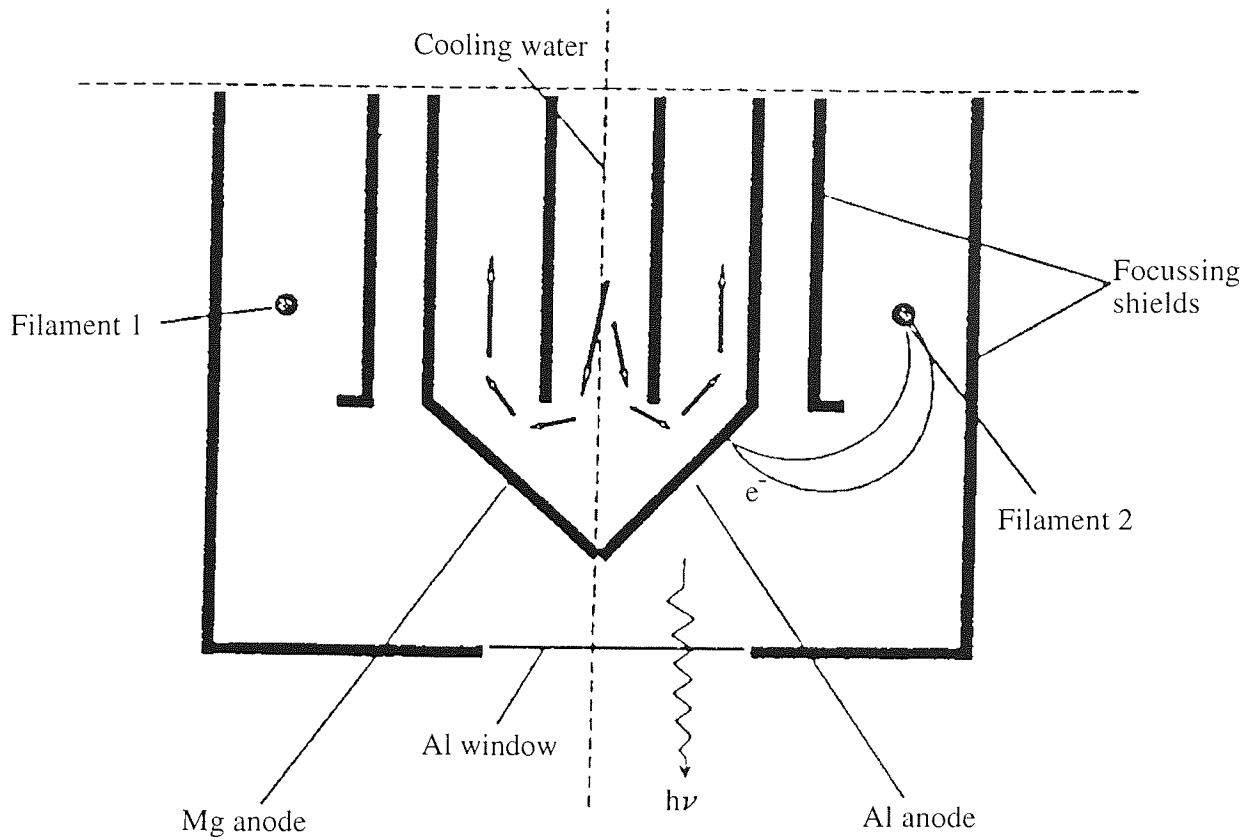


Figure 3.3 Structure of twin anode X-ray source

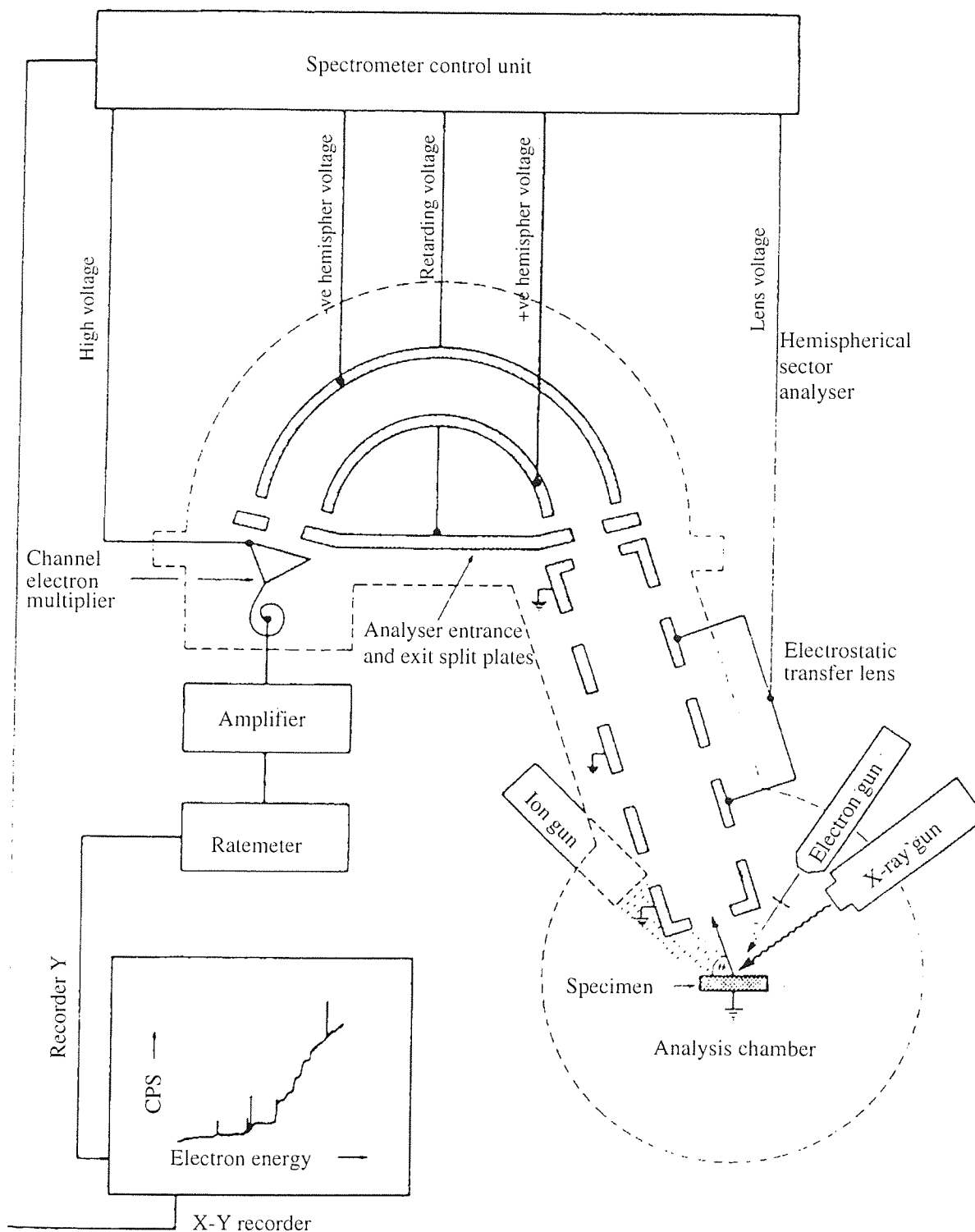


Figure 3.4 Schematic of a 150° Hemispherical sector analyser

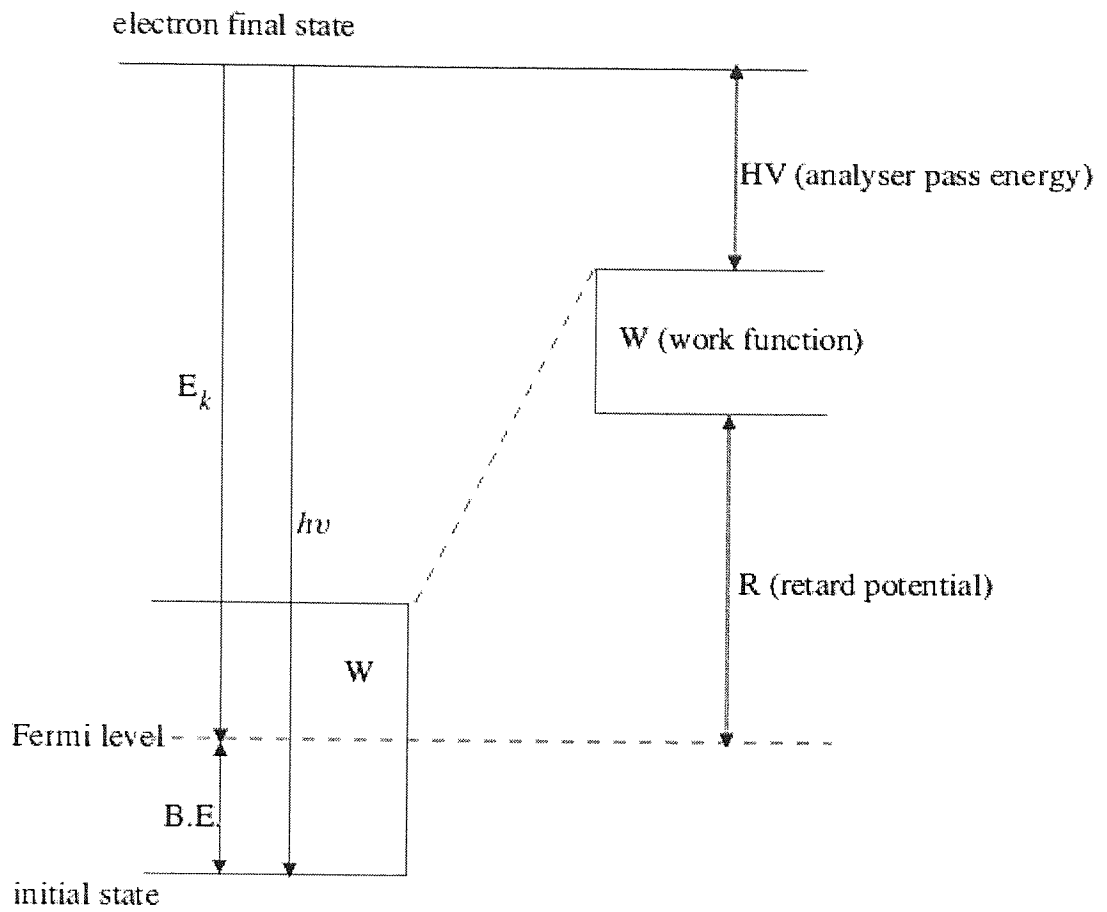


Figure 3.5 A schematic of energy levels of a hemispherical sector analyser

Then, the kinetic energy of electrons leaving the sample (with respect to the Fermi level) is

$$E_k = R + HV + W \quad (3.1)$$

where W is the work function of the spectrometer. The analyser may be operated either in constant energy, CAE mode or constant retard ratio, CRR mode. However, CAE mode is generally preferred in XPS. In CAE mode, HV is kept constant during the acquisition of a spectrum and hence the resolution of electrons with different kinetic energy is fixed.

The analyser has inlet and exit apertures, used to control the sample area by a rotary drive mechanism. The dimensions of the aperture can be changed from 3000 to 150 μm , Table 3.3. These also determine the resolution through the geometric parameter H . The electrons out of analyser are detected by five channeltrons and transmitted into an electronic signal by a set of proper electronics.

Table 3.3 Inlet and exit apertures used in the analyser

Code	Size (μm)	Purpose
A1	3000	Large area XPS
A3	1000	Small area XPS
B1	600	Small area XPS
B3	300	Small area XPS
C1	150	Small area XPS

3.2.1.5 Data System:

The data acquisition and processing are carried initially using a VGScientific 5250 DATA SYSTEM, and latterly using VG Eclipse DATA SYSTEM in which all functions for XPS spectrum analysis such as smoothing, satellite subtraction, charge correction, peak synthesis, quantification and profile are available. A frame store system together with colour graphic copiers is available for image-processing and to get hard copies of images.

3.2.2 Plasma cell (Glow discharge chamber):

A simple and cheap way to excite plasma is by placing a dc potential across two electrodes in a chamber, placed in a low pressure gaseous environment. The charged particles are formed by the interaction of the initially introduced gas with an applied electric field. The plasma cell

used for this project has a planar diode geometry, Figure 3.6, which means the cathode (sample) and anode are in parallel configuration and are placed inside a glass tube. This type of geometry is suitable for analysing samples in the disk form. The only drawback of this type of system is it can be used only for conducting samples.

Inside the glass tube, some steel plates are placed to focus the plasma. This whole arrangement is placed inside an aluminium vessel, with a window on one side to observe discharge. The vessel is pumped by a rotary and a diffusion pump. Both argon and nitrogen gases can be used inside the chamber.

Voltages applied to electrodes are typically of the order of 500-3000 V, yielding currents of a few mA. The pressure inside the chamber is kept at 0.1-0.2 torr.

3.3 Selection of experimental materials:

The samples were selected very carefully to gain an insight into the physics and chemistry of ion implantation process, through a study of effect of mass and binding energy of target and chemical affinity between the ion and target. In terms of enthalpy of formation of nitrides, Table 3.4, Aluminium has a strong chemical interaction with nitrogen, while iron has an intermediate chemical interaction with nitrogen, copper has a small chemical interaction with nitrogen and gold has no chemical interaction with nitrogen. One thus expects to be able to understand the chemistry of implantation by studying this range of metals. The choice of GaAs was on the basis that the Ga and As atoms have very small difference in mass and hence the mass effects will not be dominant, and the other effects like chemical reactivity and surface binding energy effects may be studied, while in case of AlGaAs, because of the mass and chemical reactivity differences between the target elements, the effect of mass can also be studied. Nitridation of GaAs surfaces is of great interest to the device technology of III-V semiconductors. Group III-nitrides, especially GaN, are attractive for opto-electronic devices emitting in the blue and UV spectral ranges. For the growth of such devices, AlGaN/GaN/InGaN type heterostructures are required. This makes study of nitrogen implantation in GaAs and AlGaAs very important.

Table 3.4 Values of heat of formation of nitrides (eV/atom), at 25° C [Lide 1991].

	AlN	Fe ₄ N	Cu ₃ N	AuN	GaN	AsN
Heat of formation	-3.30	-0.11	+0.77	no data	-1.15	no data

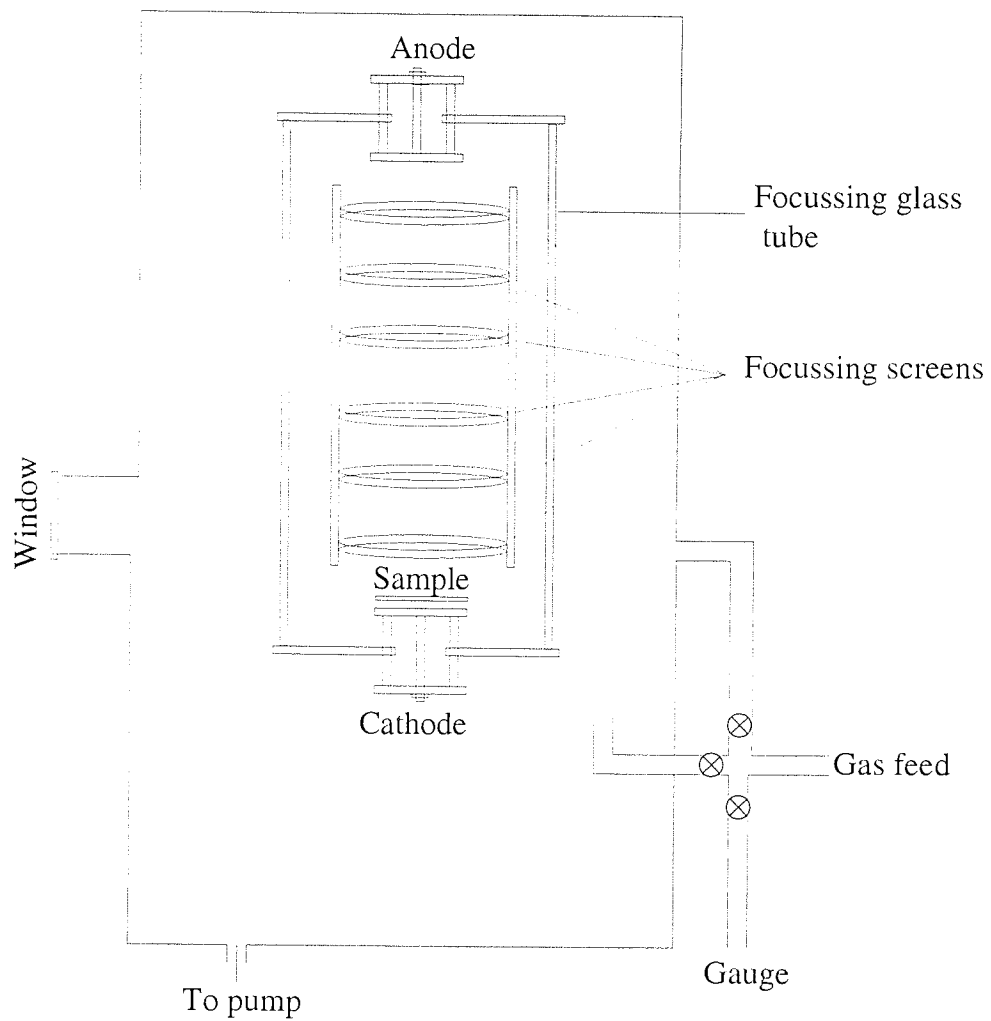


Figure 3.6 Schematics of the apparatus used for generating dc plasma.

Nitrogen: The ions chosen for this work are energetic nitrogen ions. Nitrogen has two stable isotopes ^{14}N (relative atomic mass 14.003, abundance 99.634%) and ^{15}N (relative atomic mass 15.000, abundance 0.366%). Gaseous N_2 is rather inert at room temperature, but the reactivity is considerably enhanced with increasing temperature and nitrogen forms bonds with almost all elements in the periodic table, except noble gases (other than Xe). The excited nitrogen molecules are highly reactive and as a result AlN , $\text{Fe}_{2,3,4}\text{N}$, Fe_{16}N_2 , Cu_3N , $\text{Cu}(\text{N}_3)_2$, GaN and As_4N_4 might be expected to be formed in the various experiments.

Aluminium: For this purpose, aluminium bulk samples of about 3 mm thick cut from a 5 mm diameter rod of 99.99% purity Al, supplied by Goodfellow Cambridge Ltd. were used.

Iron: The samples used in these experiments consisted of 0.125 mm thick iron foils of 99.95% purity, supplied by Advert Research Material Ltd.

Copper: The samples used in these project consisted of copper bulk samples of 3 mm thickness and 8 mm diameter, with 99.95% purity, supplied by Goodfellow Cambridge Ltd..

Gold: Gold samples of 0.0125 mm thick foils, with 99.99% purity, were supplied by Advert Research Material Ltd. .

GaAs: The (100) GaAs samples were supplied by GEC Marconi Technology, Caswell.

As: As samples, with 99.95% purity, in the form of lumps, were supplied by Alfa, Johnsons Matthey Plc..

AlGaAs: The AlGaAs samples used in this project consisted of wafers of 40 nm GaAs, with a layer of 30 nm AlGaAs on the top. These samples were supplied by GEC Marconi Technology, Caswell. The AlGaAs compound is with a configuration $\text{Al}_x\text{Ga}_{1-x}\text{As}_y$; here $x = 0.3$ and $y = 0.7$.

Cu_3N : A standard Copper nitride (Cu_3N) sample was received from Alfa, Johnsons Matthey Plc., in the powdered form and the XPS analysis of standard sample was performed for as received, and then Ar^+ etched for half an hour.

$\text{Fe}_{2,3,4}\text{N}$: A standard iron nitride (mixture of $\text{Fe}_{2,3,4}\text{N}$) sample was supplied by Alfa, Johnsons Matthey Plc., in the powdered form and the XPS analysis of standard sample was performed for as received, and then Ar^+ etched for half an hour.

3.4 Determination of Current Density:

In ion optics, the current density is defined as the magnitude of current per unit area at a time, which is measured by the ratio of the current to the ion beam rastered area. The accurate determination of current density is important but this is a difficult task. The determination of current density is not trivial since the areal coverage of the beam from the EXO5 varies with ion energy, intensity and conditions of focussing and hence the current density.

In this project, current density was chosen as one of the parameters and so accurate determination of current density was very important. For this purpose, ion beam rastered area was determined for different ion energies for known conditions of focussing. To achieve this, copper foil samples of 99.9% purity were chemically cleaned with acetone and then etched by ion beam at various ion energies for known conditions of focussing. The samples were then taken out and the areas etched by beam were measured. These measurements were performed at $E = 2, 3, 4$ and 5 keV, each for magnification of 1, 2 and 5 and at electron take-off angle of 0° and 25° . The measured areas are tabulated in Table 3.5, for electron take-off angle of 0° and in Table 3.6, for electron take-off angle of 25° . In all these measurements and for all the implantation experiments performed for this project, the fine focus control was kept at 0 and the coarse control for focus was kept at 6, while the spot size controls were fixed at 7.2 and 7 for fine and coarse controls.

3.5 Experimental procedure and measurements:

3.5.1 Sample preparation:

The sample surfaces for both, monoenergetic and glow discharge implantation, were prepared by following procedures:

Polishing: The bulk samples such as aluminium and copper were polished with emery paper and then with successively finer grades of alumina powder and then were rinsed in distilled water. However, the gold and iron samples were in the form of foils and hence polishing was not necessary. Arsenic was in the form of lumps of irregular shapes and hence, it was impossible to find a base for polishing, while GaAs and AlGaAs were received in the polished form.

Table 3.5 Determination of current density values for electron take-off angle of 0°.

Magnification	Energy (keV)	Focus		Spot size		Etched area (cm ²)
		Fine	Coarse	Fine	Coarse	
1	5	0	6	7.2	7	0.74
	4					0.94
	3					1.63
	2					3.27
2	5	0	6	7.2	7	0.24
	4					0.31
	3					0.59
	2					1.15
5	5	0	6	7.2	7	0.06
	4					0.12
	3					0.16
	2					0.22

Table 3.6 Determination of current density values for electron take-off angle of 25°.

Magnification	Energy (keV)	Focus		Spot size		Etched area (cm ²)
		Fine	Coarse	Fine	Coarse	
1	5	0	6	7.2	7	0.74
	4					0.94
	3					1.65
	2					3.33
2	5	0	6	7.2	7	0.4
	4					0.5
	3					0.57
	2					1.28
5	5	0	6	7.2	7	0.06
	4					0.15
	3					0.17
	2					0.42

Chemical and ultrasonic cleaning: In order to remove hydrocarbon contamination, the samples were rinsed in hexane and then ultrasonically cleaned in hexane solution for about 15 minutes.

When the samples, with the exception of gold, are exposed to air, native oxide layers are formed on the sample surfaces.

3.5.2 Monoenergetic implantation:

After sample preparation, the monoenergetic ion implantation was performed according to the following procedure:

3.5.2.1 Sample mounting and transport :

Samples to be analysed were placed on sample mounting stub using double side tape, with aluminium foil contacts between sample and stub to make good electrical ground contact and to avoid surface charging. A CCD camera on the spectrometer is alligned to the X-ray source using a standard sample for selecting the analysed area in XPS experiments. A secondary electron detector, consisting of a scintillator and a photomultiplier, is used for collecting secondary electrons in order to obtain a physical image which is displayed on a TV monitor. This assembly is very useful for aligning the ion beam and chosing the analysed area and hence ensuring that the analysed area is same as the bombarded area.

3.5.2.2 General procedure:

- (a) **Initial analysis:** The samples, prepared by the procedure described in section 3.5 (before any ion bombardment), were analysed by XPS by taking a wide scan spectra to find out all elements at the initial surfaces.
- (b) **Ar⁺ cleaning:** After the initial analysis, all the samples with the exception of gold, were found to be oxidised and these samples were cleaned using Ar⁺ beam to remove surface contaminants. This was monitored by narrow scan XPS measurements between successive periods of ion bombardment until the amount of contaminants detected was less than 5%. Due to strong chemical interaction between oxygen and aluminium, it was very difficult to remove oxide. The samples was generally Ar⁺ etched for more than 6 hours to remove the oxide layer, which seemed to be continously reformed. For the other samples, the Ar⁺ etch for about 1-2 hours was sufficient to remove surface contaminants to less than 5%. After cleaning, a wide scan XPS spectra of Ar⁺ beam bombarded samples was taken.
- (c) **N₂⁺ bombardment:** The samples were then bombarded with N₂⁺ beam of required energy and current density and the surface compositional changes were monitored by narrow scan XPS measurements. For a typical experiment, the spectra were collected in the time scale given in Table 3.7, here bombardment time is measured in minutes. At the end of nitrogen ion bombardment, a wide scan XPS spectra of N₂⁺ bombarded samples was taken.

(d) **ARXPS:** The bombarded samples were re-examined by ARXPS.

(e) **Depth profiling:** After each complete implantation, XPS depth profiles were created using Ar⁺ beam at energy 2 keV and current density 2 $\mu\text{A}/\text{cm}^2$ and narrow scan XPS measurements were used to monitor the surface compositional changes and using this information, depth profiles were created. The total time for Ar⁺ depth profiling was slightly different in different experiment (because the time taken to remove the implanted nitrogen was found to be slightly different for different N₂⁺ bombardment condition), but the time scale was same as described in Table 3.7. On the completion of the experiment, a wide scan XPS spectra of Ar⁺ beam bombarded samples was taken.

Table 3.7 Time scale for a typical ion bombardment experiment.

Level of bombardment	1	2	3	4	5	6	7	8	9-12
Bombardment time (min)	0	1	2	2	5	5	10	10	15

3.5.2.3 Experimental conditions for ion bombardment:

For the implantation of nitrogen, eight sets of successful experiments were performed on each sample, using a rastered N₂⁺ ion beam of energy of 2, 3, 4 and 5 keV with current densities of 1 $\mu\text{A}/\text{cm}^2$ and 5 $\mu\text{A}/\text{cm}^2$ for each energy. These current densities correspond to N₂⁺ ions fluxes of 1.25×10^{13} and 6.25×10^{13} ions/cm²/s respectively. For depth profiling, an Ar⁺ beam at energy 2 keV and current density 2 $\mu\text{A}/\text{cm}^2$ was used. In all experiments, the ions were incident on the sample at an angle of 51.6°.

3.5.2.4 XPS measurements:

For this project, the XPS analysis was carried out using both MgK α ($h\nu = 1253.6$ eV, FWHM = 0.7 eV) and AlK α ($h\nu = 1486.6$ eV, FWHM = 0.8 eV) X-ray lines, operated at anode voltage of 15 kV at filament current of 20 mA. The choice of X-ray source was made depending on the requirements of the experiment. The sample was positioned at 0° TOA, here TOA is the electron-take-off angle, measured w. r. t. the surface normal.

For the wide scan, a pass energy of 50 eV, step size of 0.2 eV and the dwell time of 50 ms

were selected, while for the narrow scan, these parameters were chosen as 20 eV, 0.1 eV and 200 ms for photoelectron peaks and 100 eV, 0.2 eV and 100 ms for Auger and valence band peaks. An aperture of 1000 μm was selected. In ARXPS, the electron take-off-angles (TOA) were chosen as 0°, 33°, 45°, 54° and 60°, for all the samples, except for aluminium for which the TOAs were 0°, 25°, 50°, 60° and 75°. For the ARXPS, the small area analysis facility of the ESCALAB 200D was employed at a 1000 μm diameter analysis area and with the iris at the nose of the input lens set to restrict the acceptance angle to less than 8°, that is, below the 10° acceptance angle required for the collection of meaningful ARXPS data. During these experiments, the base pressure was always better than 7×10^{-10} mbar and during ion bombardment experiments, the working vacuum was always better than 5×10^{-7} mbar.

3.5.2.4.1 Spectra collection and calibration:

Aluminium: XPS spectra of Al 2p, Al KLL, Al Valence, C 1s, N 1s and O 1s lines were collected after successive periods of N_2^+ bombardment during the implantation, using Al $\text{K}\alpha$ X-ray radiation. The Al $\text{K}\alpha$ X-ray radiation was chosen in order to collect low kinetic energy Auger lines of aluminum. Binding energy measurements of all the pre-implanted samples were referenced to the C 1s line of the residual carbon set at 284.6 eV. After relatively short periods of ion bombardment the adventitious carbon signals fell to levels which rendered their use as calibrants unreliable. In this case secondary standards were employed, notably the N 1s signal taken from very many measurements of photoelectron emission from the stoichiometric AlN standard to be 396.7 ± 0.1 eV (FWHM = 1.6 eV). For these samples the energy of the well defined Al 2p signal was 73.6 ± 0.1 eV and the separation between the Al 2p and N 1s is 323.1 ± 0.2 eV.

Iron and iron nitride: Using Mg $\text{K}\alpha$ X-ray radiation, XPS spectra of Fe 2p, Fe LMM, Fe Valence, C 1s, N 1s, N KLL and O 1s lines were collected after successive periods of N_2^+ bombardment. In this case, it was possible to choose even Al $\text{K}\alpha$ X-ray source, but the use of Mg $\text{K}\alpha$ X-ray radiation was just by choice. After Ar^+ cleaning most of the carbon was removed, but the peak position of C 1s from the small amount of carbon left in the surface shifted from 284.6 eV to 283.4 eV, for Fe 2p_{3/2} positioned at 707.0 eV. This indicates the formation of iron carbide. As the Ar^+ bombardment changes the carbon to iron carbide, so the C 1s line could not be used for the charge referencing. The binding energy measurements of all the ion bombarded samples were referenced to the differential Fe Valence Band spectra set at 0 eV. For iron nitride sample, the spectral peaks collected were the same as above, but the binding energy measurements were referenced to the C 1s peak set at 284.6 eV.

Copper and copper nitride: During N_2^+ implantation, XPS spectra of Cu 2p, Cu LMM, Cu Valence, C 1s, N 1s, N KLL and O 1s lines were collected after successive periods of ion bombardment until steady state saturation of nitrogen had been reached. These measurements were made using, Mg K_α X-ray radiation. Again in this case, it was possible to use Al K_α X-ray radiation. As the Ar^+ bombardment changes the carbon concentrations to a low value, so the C 1s line could not be used for the charge referencing. The binding energy measurements of all the ion bombarded samples were referenced to the differential Cu Valence Band spectra set at 0 eV. For standard copper nitride sample, the spectral peaks collected were the same as above, but the binding energy measurements were referenced to the C 1s peak set at 284.6 eV.

Gold: After successive periods of N_2^+ bombardment, XPS spectra of Au 4d, Au 4f, Au LMM, Au Valence, C 1s, N 1s, N KLL and O 1s lines were collected using, Mg K_α X-ray radiation. However, the use of Al K_α X-ray radiation will be equally informative. The Au 4f7 peak, positioned at 85.0 eV was used as calibrant. The binding energy measurements were also referenced to the differential Au Valence Band spectra set at 0 eV.

GaAs: During N_2^+ bombardment, XPS spectra of Ga 3d, As 3d, Ga 2p_{3/2}, Ga LMM, As LMM, GaAs Valence, N 1s, and O 1s lines were taken after successive periods of bombardment using Mg K_α X-ray radiation. In addition to this wide scan spectra, ranging from -10 to 1200 eV were also collected for chemically cleaned, Ar^+ cleaned and nitrogen ion implanted samples using the same X-ray source. The Al K_α X-ray radiation could not be used for this purpose because of interference between Ga $L_{2,3}M_{4,5}M_{4,5}$ peak (positioned at 396 eV) and N 1s peak, however, a wide scan spectra, ranging from -10 to 1400 eV were also collected for chemically cleaned, Ar^+ cleaned and nitrogen ion implanted samples using, Al K_α X-ray source, to get information about Ga 2p and As 2p peaks. The binding energy measurements of all the ion bombarded samples were referenced to the As 3d spectra set at 41.1 eV.

AlGaAs: Using Mg K_α X-ray radiation, XPS spectra of Al 2p, Ga 3d, As 3d, Ga 2p_{3/2}, Al KLL, Ga LMM, As LMM, AlGaAs Valence, N 1s, and N KLL were taken after successive periods of N_2^+ bombardment during the implantation until steady state saturation of nitrogen concentration were observed. Using the same X-ray source, wide scan spectra, ranging from -10 to 1200 eV were also collected for chemically cleaned, Ar^+ cleaned and nitrogen ion implanted samples. The Al K_α X-ray radiation could not be used for this purpose because of interference between Ga $L_{2,3}M_{4,5}M_{4,5}$ peak (positioned at 396 eV) and N 1s peak, however, a wide scan spectra, ranging from -10 to 1400 eV were also collected for chemically cleaned, Ar^+ cleaned and nitrogen ion implanted samples using Al K_α X-ray radiation, to get information about Ga 2p and As 2p peaks and hence the sample surface. The binding energy

measurements of all the ion bombarded samples were referenced to the As 3d spectra set at 41.0 eV.

As: During N_2^+ bombardment, XPS spectra of As 3d, As LMM, As Valence, N 1s, and O 1s lines were taken after successive periods of bombardment using Al K_α X-ray radiation. In addition to this wide scan spectra, ranging from -10 to 1400 eV were also collected for chemically cleaned, Ar^+ cleaned and nitrogen ion implanted samples using the same X-ray source. The binding energy measurements of all the ion bombarded samples were referenced to C 1s peak set at 284.6 eV and when the amount of carbon was low, the As 3d peak set at 41.5 eV, was used as a reference peak.

3.5.2.4.2 Data processing:

As described in Chapter 2, to get maximum information, all the XPS spectra mentioned above were processed in the order of smoothing, energy calibration, background removal and quantification. The relative sensitivity factors used for quantification of data are listed in Table 3.8 for both Al K_α and Mg K_α X-ray sources. In case of Fe 2p3 and Cu 2p3, only one value is reported as only one type of X-ray source was used for the quantification of the data.

Table 3.8 Values of Relative Sensitivity Factor used with Al K_α and Mg K_α X-ray sources

Peak	Al 2p	Fe 2p3	Cu 2p3	Ga 3d	As 3d	N 1s	O 1s	C 1s
RSF (Al)	0.54	-----	-----	1.09	1.82	1.80	2.93	1.00
RSF (Mg)	0.57	6.50	16.73	1.19	1.97	1.77	2.85	1.00

3.5.3 Glow discharge chamber:

The samples were prepared by following the procedure described in section 3.5.1 and were transferred to glow discharge chamber. Then, the plasma deposition experiments were performed according to the following procedure:

3.5.3.1 Routine Operation:

- (1) **Ar cleaning:** As mentioned before, all the samples get oxidised on exposure to air. So the samples were cleaned with argon plasma for about 2 hours.

- (2) **Nitrogen plasma deposition:** The samples were exposed to nitrogen plasma for about $\frac{1}{2}$ hour.
- (3) **Cooling of the samples:** After step (2), the samples were cooled with argon gas for about $\frac{1}{2}$ hour.
- (4) **Transfer of samples:** After cooling, the samples were immediately transferred to the preparation chamber of VGScientific ESCALAB 200D system.
- (5) **ARXPS:** In ESCALAB, the plasma deposited samples were examined by ARXPS, exactly in the same way as the monoenergetically ion implanted samples.

3.5.3.2 Experimental conditions:

In each case, two sets of successful experiments were performed, by exposing the samples to nitrogen plasma for the following two conditions:

- at low pressure and high voltage
- at high pressure and low voltage

The exact value of the pressure inside the glow discharge chamber and voltage applied across the electrodes for different samples are given in Table 3.9. Because of the designing of the chamber, it was not possible to perform experiments with gold, GaAs and AlGaAs samples.

Table 3.9 The experimental conditions for exposure of nitrogen plasama, for various samples

Sample	Voltage (kV)	Pressure (torr)
Aluminium	3.0	0.05
	0.6	0.2
Iron	3.0	0.05
	0.6	0.2
Copper	3.0	0.07
	1.6	0.2

From this table, it can be seen that the exact value of pressure and voltage were slightly different for different samples as different cathode material (here samples, acting as cathode) have different secondary electron emission efficiency.

Chapter 4

Experimental Results

4.1 Monoenergetic implantation:

In this section, the results obtained from all ion implantation experiments carried in ESCALAB 200D are reported.

4.1.1 Aluminium:

4.1.1.1 Nitrogen implantation:

The changes in the atomic concentration of aluminium, nitrogen and oxygen were calculated at successive intervals of sputtering. The concentration profiles at all the energies and current densities $1\mu\text{A}/\text{cm}^2$ and $5\mu\text{A}/\text{cm}^2$ are shown in Figures 4.1 and 4.2 respectively. From these figures it may be seen that as the implantation proceeds, the nitrogen concentration increases and eventually reaches a saturation value. The concentration of oxygen falls slightly and then remains almost constant. The relative concentration profiles of (N/Al) atomic ratios at all the energies and current densities $1\mu\text{A}/\text{cm}^2$ and $5\mu\text{A}/\text{cm}^2$, Figures 4.3, show that saturation occurs earlier for higher current density implantation. The (N/Al) saturation ratios at various energies and current densities are shown in Table 4.1.

Table 4.1 Tabulation of measured (N / Al) saturation ratios.

Energy (keV)	Current density ($\mu\text{A}/\text{cm}^2$)	(N/Al)saturation ratio
5	5	0.45 ± 0.07
4		0.47 ± 0.07
3		0.46 ± 0.07
2		0.49 ± 0.07
5	1	0.47 ± 0.07
4		0.54 ± 0.07
3		0.50 ± 0.07
2		0.43 ± 0.07

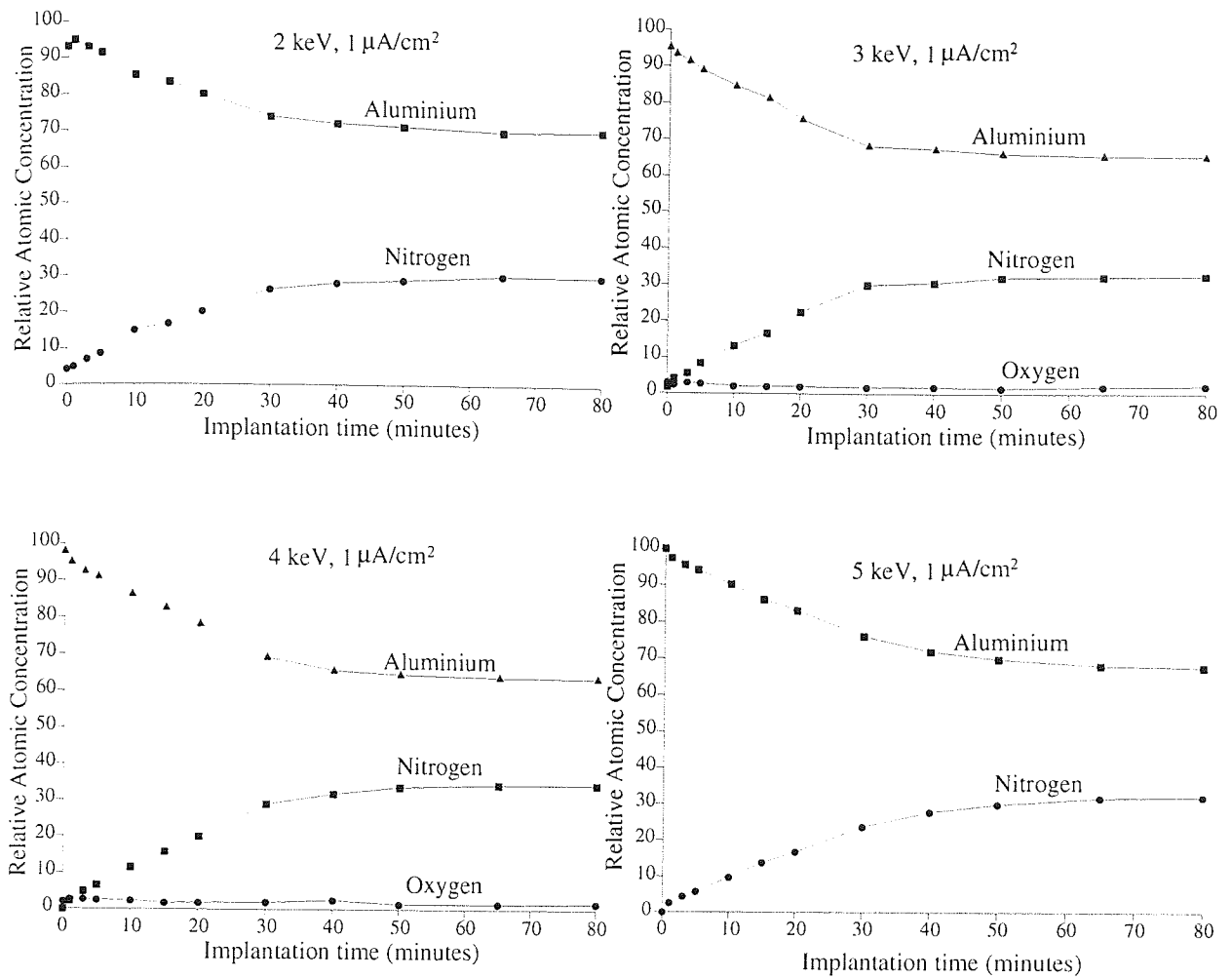


Figure 4.1 XPS time profile of nitrogen implantation in aluminium at $E = 2, 3, 4$ and 5 keV ; $\mu = 1 \mu\text{A}/\text{cm}^2$.

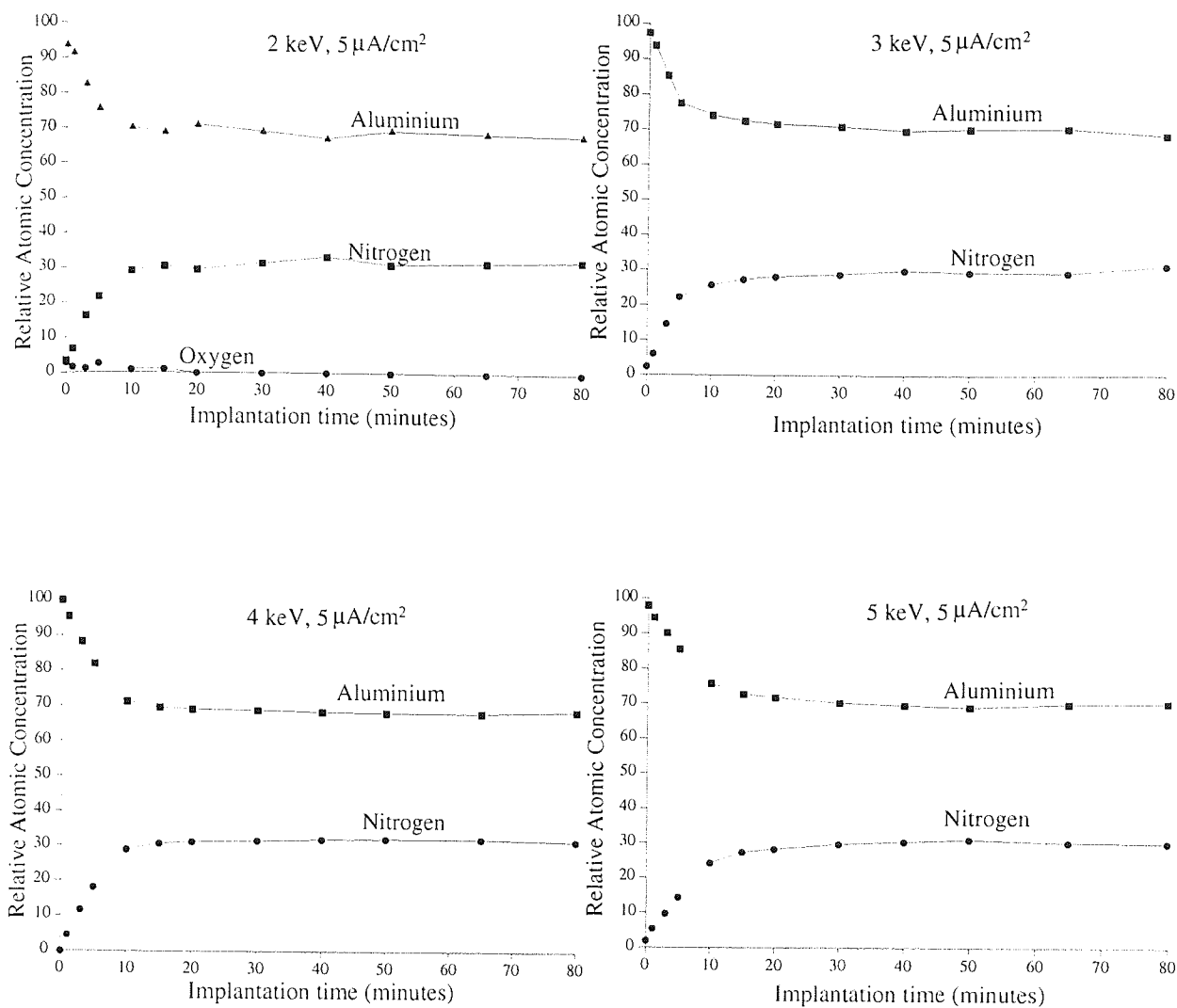


Figure 4.2 XPS time profile of nitrogen implantation in aluminium at $E = 2, 3, 4$ and 5 keV; $\mu = 5 \mu\text{A}/\text{cm}^2$.

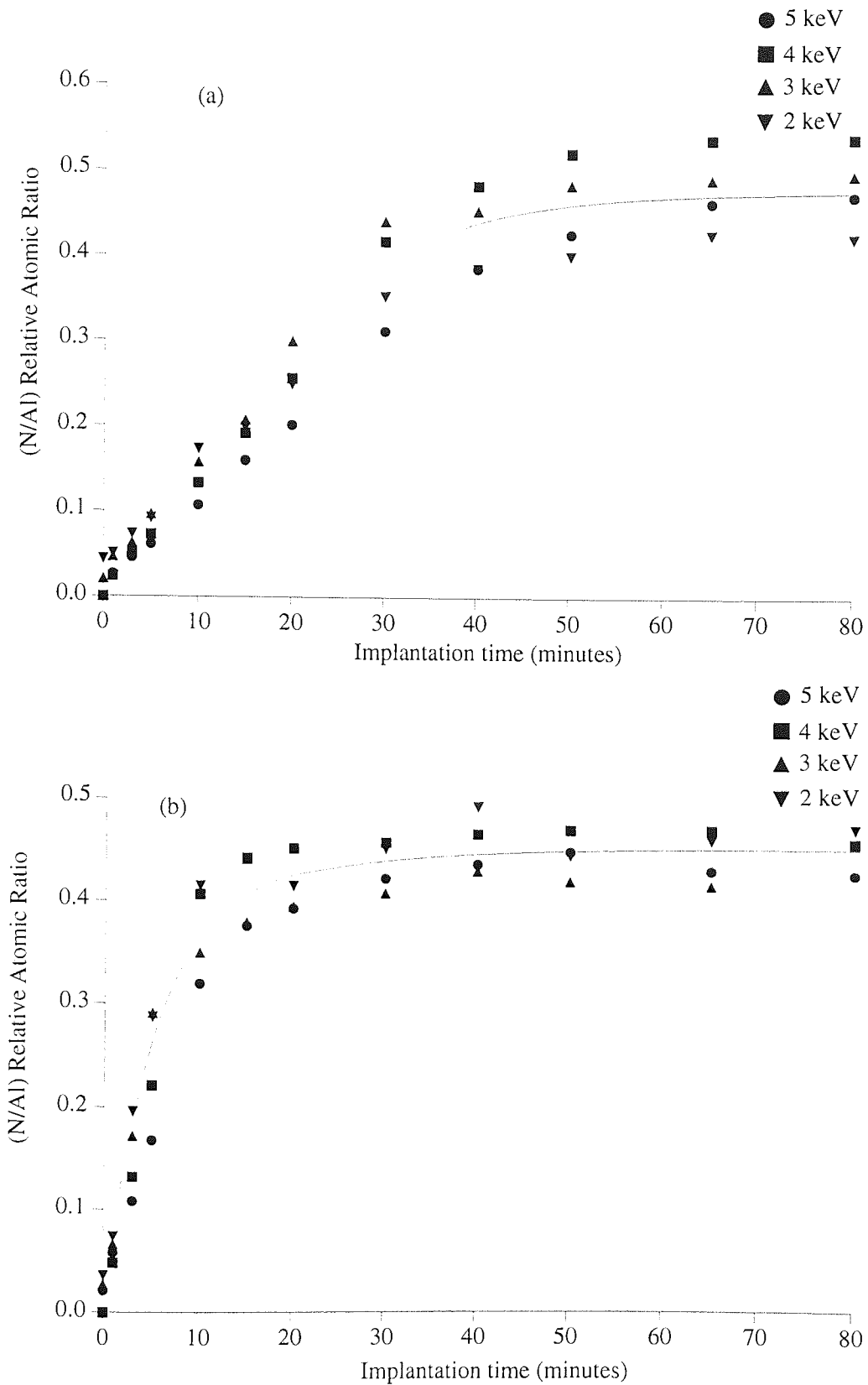


Figure 4.3 XPS time profile of nitrogen to aluminium relative atomic concentration ratios for implantation in aluminium at $E = 2, 3, 4$ and 5 keV; and current densities of (a) $\mu = 1 \mu\text{A}/\text{cm}^2$ and (b) $\mu = 5 \mu\text{A}/\text{cm}^2$.

To further investigate the effect of current density, (N/Al) relative atomic concentration ratios were plotted as a function of ion dose for 2, 3, 4 and 5 keV ions for the implantation at $1 \mu\text{A}/\text{cm}^2$ and $5 \mu\text{A}/\text{cm}^2$, Figure 4.4. No difference in concentration was found for 2 keV experiment, 4.4(a), but from Figures 4.4(b), 4.4(c) and 4.4(d), for ion implantation at ion energies of 3, 4 and 5 keV, the nitrogen concentration is higher for a given dose for implantation carried out at current density of $1 \mu\text{A}/\text{cm}^2$ compared to the same for $5 \mu\text{A}/\text{cm}^2$.

4.1.1.2 Argon ion bombardment:

After implantation Ar^+ bombardment was used to gain depth profile information on the relative atomic concentration of N and Al in the sample surfaces. These profiles are shown in Figures 4.5(a) and 4.5(b) for implantation current densities of 1 and $5 \mu\text{A}/\text{cm}^2$ respectively. Relative atomic concentrations in these profiles are actually measured as a function of time. The time axis is converted into depth scale using the etch rate value of 0.055 nm/s, calculated from SUSPRE [Webb, 1992]. It should be noted, however, that the absolute depth values will be different from the depth values calculated in this manner, as the sputter yield is matrix dependent. The error in the calculated depth could be up to 3, however the differences in the error for profiles at different implantation energies will be small. Hence one can still use this for the purpose of comparison of profiles. As expected, the implantation profiles show greater persistence of N with depth at higher ion impact energies. The profiles consist of a high concentration of nitrogen from surface to a few nm depth followed by a region of much lower concentration of nitrogen. They then follow the expected trend and show that the nitrogen implantation is shallower at lower ion energies.

4.1.1.3 Al spectra:

Figure 4.6 shows the N 1s spectra for nitrogen implanted in aluminium. Figure 4.7 shows the changes in the Al 2p and Al KLL Auger peaks after relatively short periods of nitrogen ion bombardment. The values of binding energy of Al 2p, the kinetic energy of the Al KLL line and Auger parameter are shown in Table 4.2, for pure aluminium, after N_2^+ bombardment and then Ar^+ bombardment. The values for pure Al and standard AlN are also reported [Wagner, 1990]. The comparison of Valence Band spectra of aluminium, before and after N_2^+ bombardment, is shown in Figure 2.5. The synthesised Al 2p spectra, Figure 4.8, show the presence of metallic aluminium, AlN and Al_2O_3 . Al_2O_3 is present due to oxidation of aluminium sample on exposure to the atmosphere before transferring to the vacuum chamber but this peak was rarely completely removed even after prolonged periods of bombardment at base pressures better than 7×10^{-10} mbar.

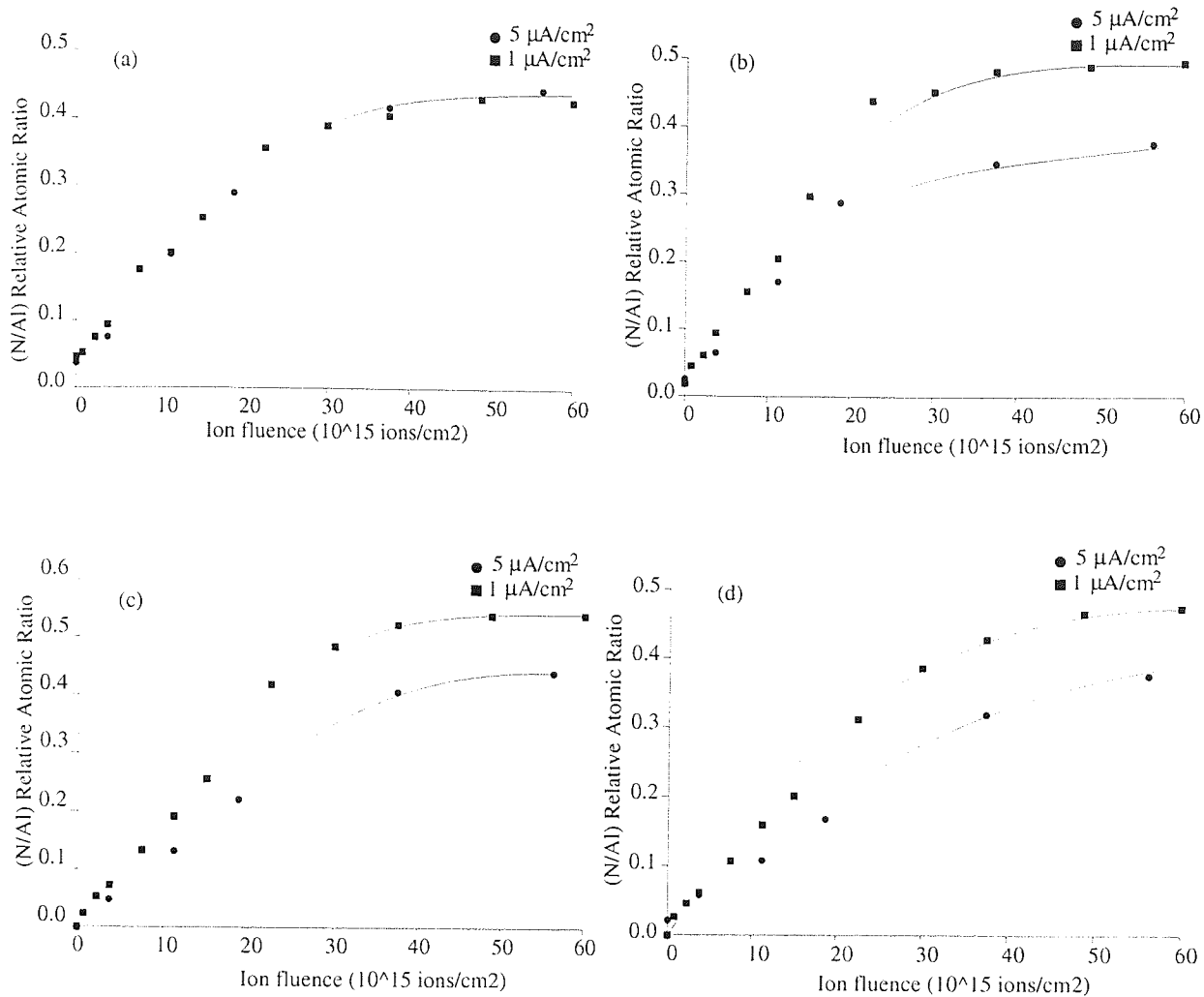


Figure 4.4 XPS time profile of nitrogen ion implantation at (a) 2 keV, (b) 3 keV, (c) 4 keV and (d) 5 keV at current densities of $1 \mu\text{A}/\text{cm}^2$ and $5 \mu\text{A}/\text{cm}^2$.

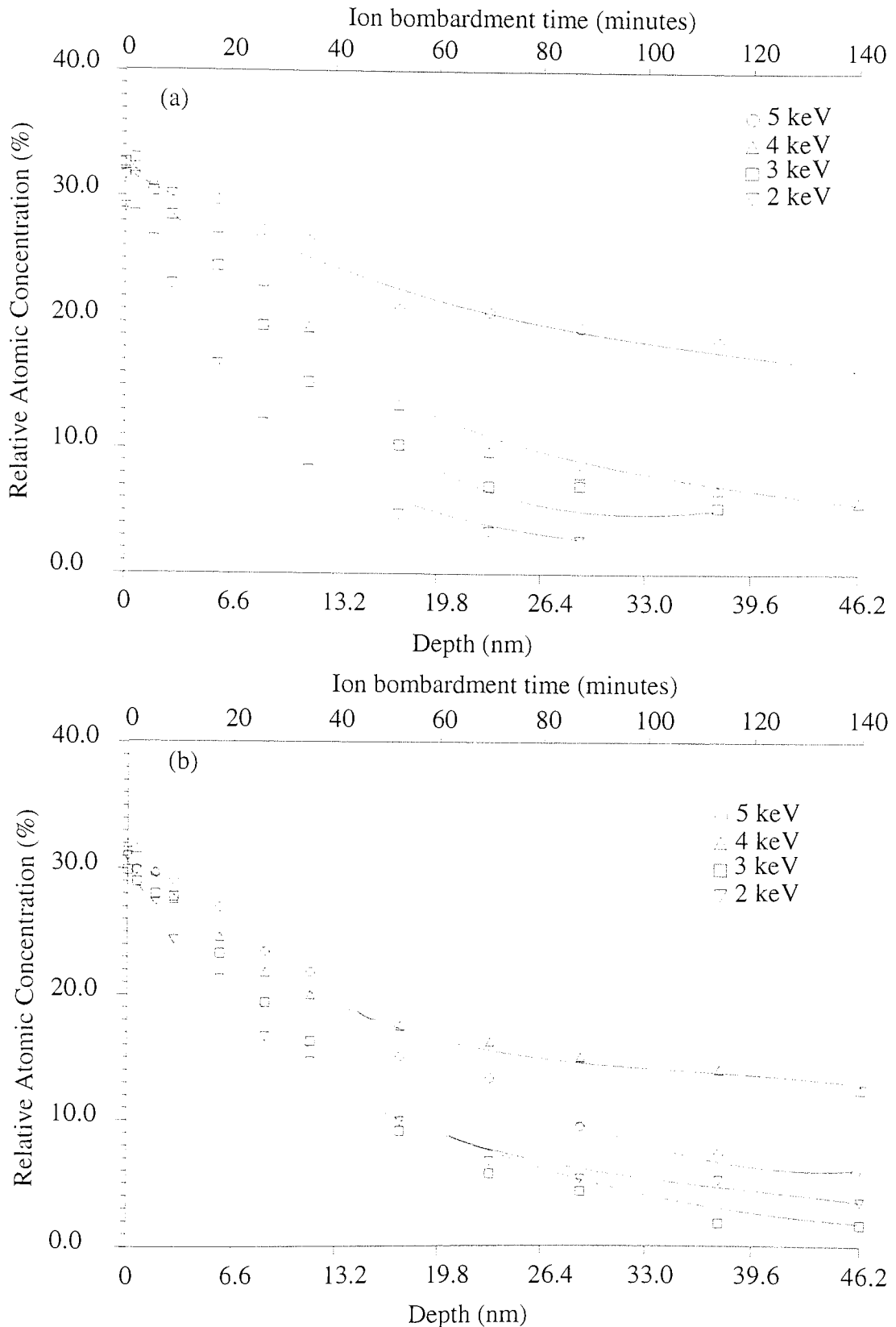


Figure 4.5 Nitrogen depth and time profile using Ar^+ of energy 2 keV and $2 \mu\text{A}/\text{cm}^2$ after nitrogen implantation on aluminium at $E = 2, 3, 4$ and 5 keV and current densities of (a) $\mu = 1 \mu\text{A}/\text{cm}^2$ and (b) $\mu = 5 \mu\text{A}/\text{cm}^2$. The time scale is converted to the depth scale using the etch rate value calculated from SUSPRE.

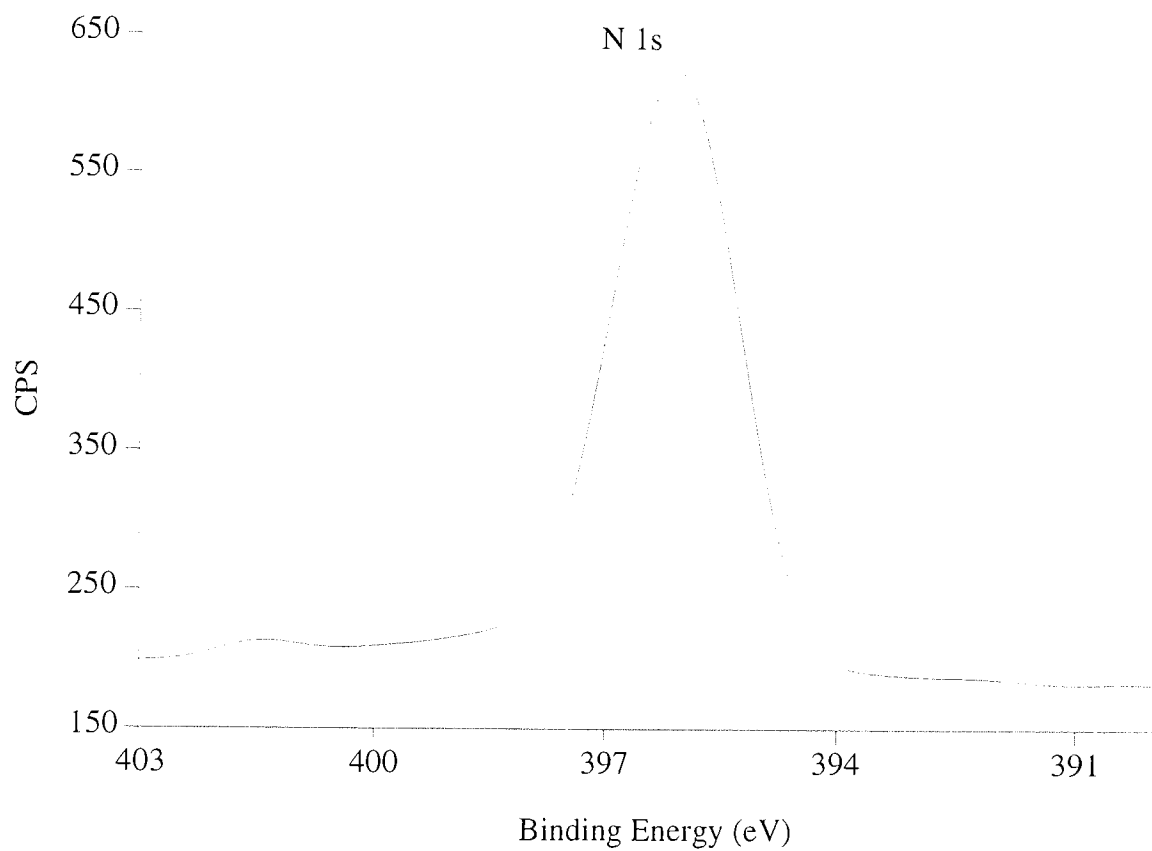


Figure 4.6 Photoelectron spectra of N 1s.

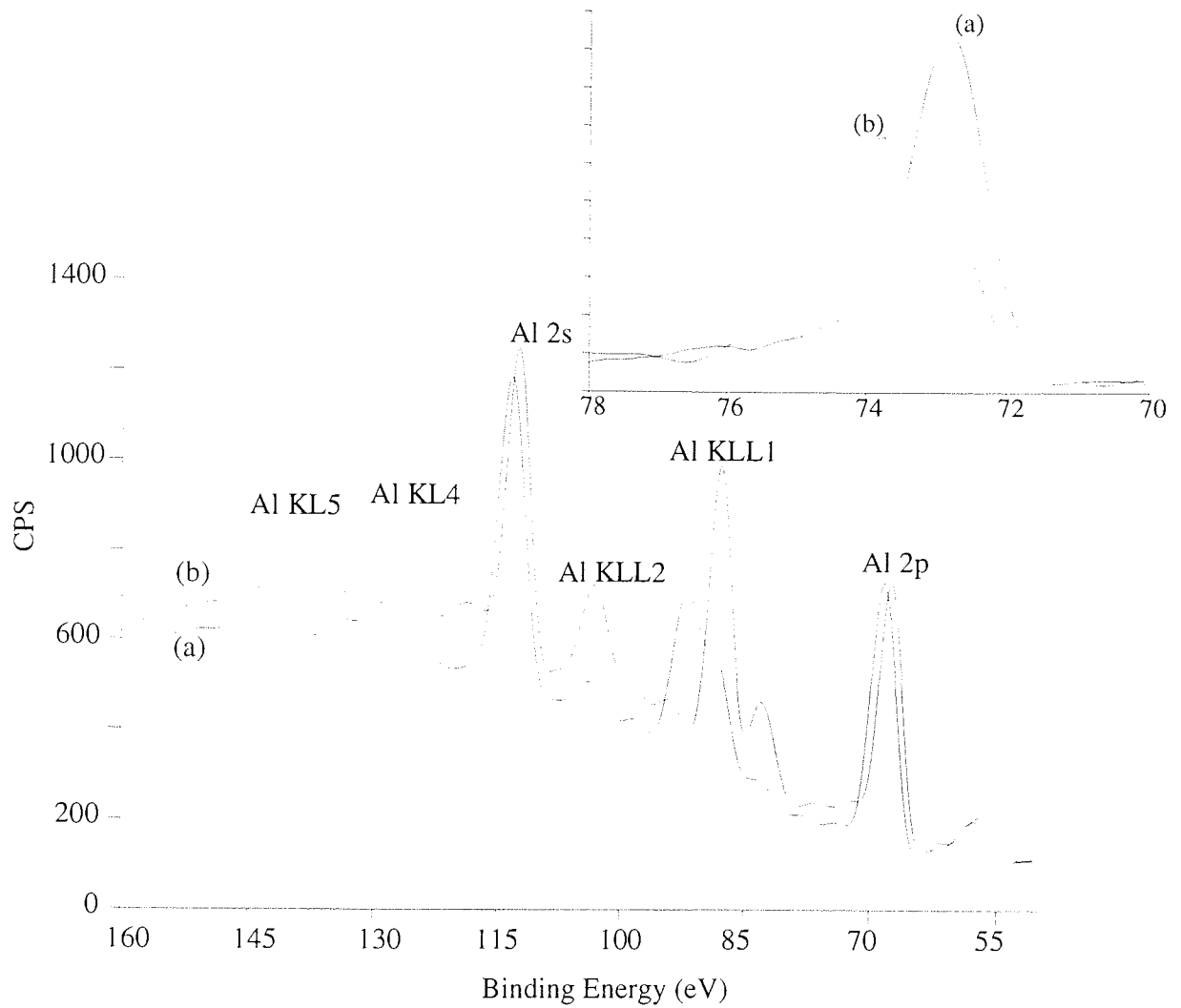
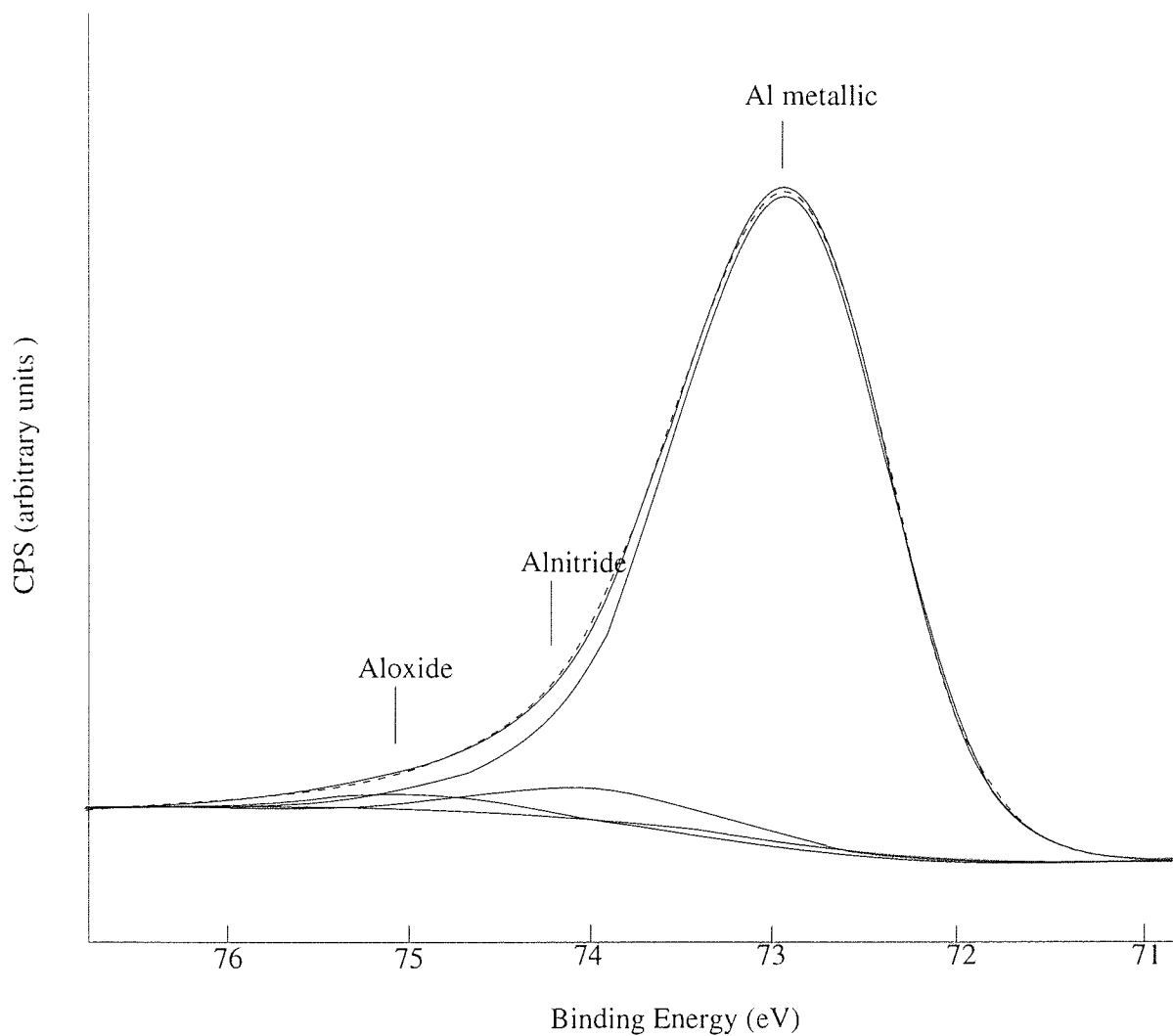
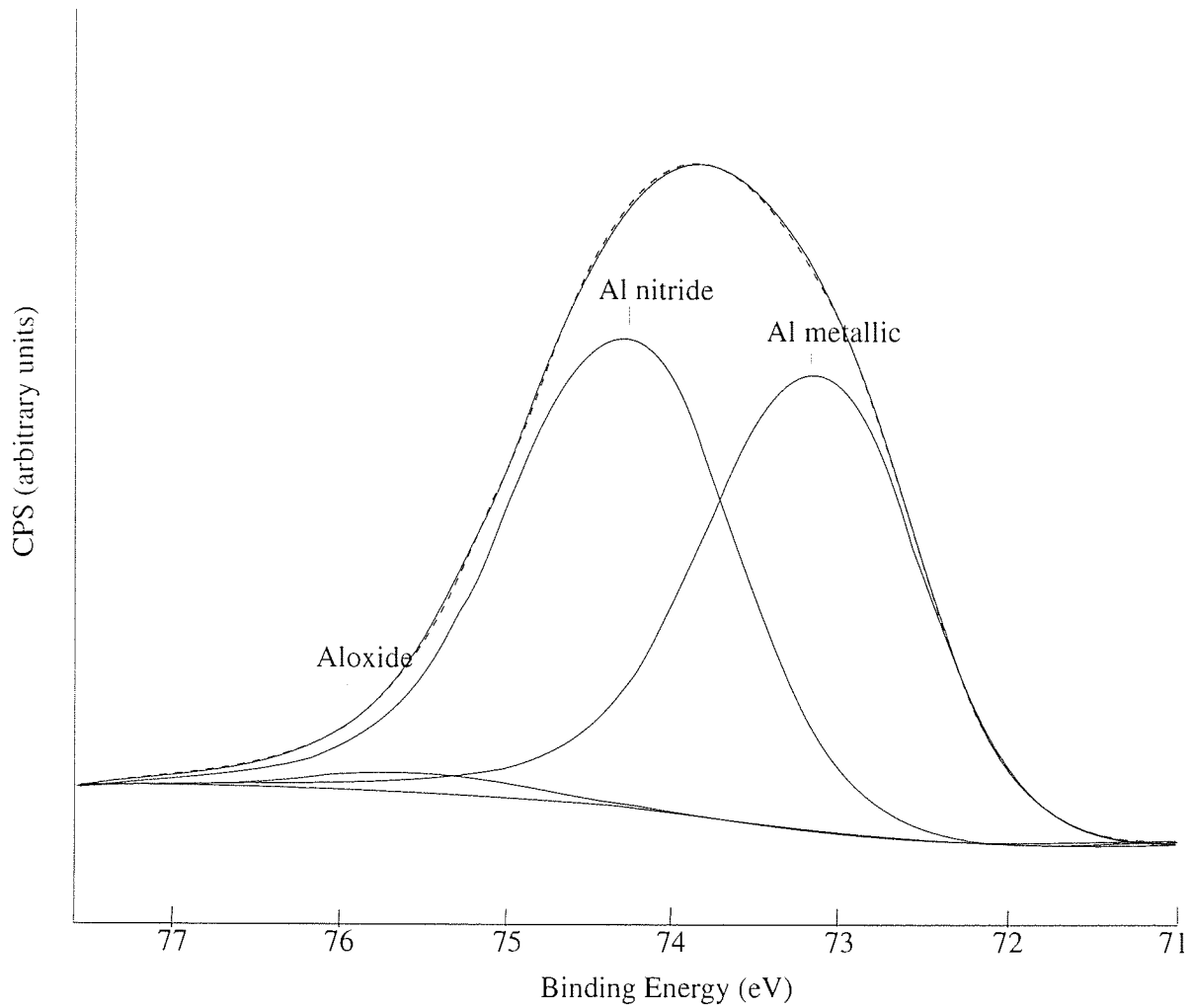


Figure 4.7 Auger spectrum of (a) pure aluminium and (b) nitrated aluminium (Al 2p peak is shown inset).



Peak	Centre (eV)	FWHM (eV)	Height (%)	G/L (%)	Area (%)
Al metallic	72.9	1.19	84.4	30	94.2
Al nitride	74.0	1.29	4.2	30	4.8
Al oxide	75.1	1.33	1.0	30	1.0

Figure 4.8(a) Deconvolution of various chemical states in Al 2p spectra, after 1 minute of nitrogen ion bombardment (uncalibrated spectra).



Peak	Centre (eV)	FWHM (eV)	Height (%)	G/L (%)	Area (%)
Al metallic	73.1	1.37	56.4	30	47.3
Al nitride	74.2	1.47	57.9	30	50.9
Al oxide	75.4	1.52	2.1	30	1.8

Figure 4.8 (b) Deconvolution of various chemical states in Al 2p spectra, after 80 minutes of nitrogen ion bombardment at 4 keV and 1 $\mu\text{A}/\text{cm}^2$ (uncalibrated spectra).

Table 4.2 The values of Al 2p binding energies (eV) and KLL kinetic energies (eV) for clean, N₂⁺ bombarded, and then Ar⁺ bombarded are tabulated in first three rows. The last two rows show the value of the above mentioned parameters for pure aluminium and standard AlN.

	Al 2p	Al KLL	Auger parameter
Al metal	72.9±0.1	1393.3±0.1	1466.2±0.2
N ₂ ⁺ bombarded aluminium	73.8±0.1	1389.4±0.1	1463.2±0.2
First N ₂ ⁺ and then, Ar ⁺ bombardment	73.0±0.1	1393.0±0.1	1466.0±0.2
Al [Wagner, 1990]	72.9	1393.3	1466.2
AlN [Wagner, 1990]	74.0	1388.9	1462.9

After quantification of the XPS spectra and synthesis of Al 2p peaks, the relative atomic concentration of Al present in the pure metallic form and in the form of nitride were determined and the ratios N/Al_{total} and $N/Al_{nitride}$ were plotted against the implantation time. Figure 4.9(a) and 4.9(b) shows the variation of these ratios at a current density of 1 $\mu A/cm^2$ and 5 $\mu A/cm^2$ respectively.

4.1.1.4 ARXPS results:

The ARXPS results for the nitrogen ion implantation are shown in Table 4.3. For 5 $\mu A/cm^2$ implantation, the relative atomic concentration ratio of nitrogen at shallow angles (50° and 75° TOA) is higher compared to the same at 1 $\mu A/cm^2$ implantation. This may suggest the presence of segregation at higher doses. However considering the uncertainties in the data it is difficult to say if the trend is real. From these results it may be seen that the concentration of nitrogen present at the surface (75° TOA, Table 4.3) is either very small or no nitrogen is present at all. On the other hand, the concentration of oxygen at the surface is relatively high. Even after long periods of Ar⁺ bombardment, when the concentration of oxygen from the bulk is only 5%, oxygen concentration in the outer layers can be as high as 50 atomic %. Figure 4.10 shows the Al 2p spectra at various values of electron take-off-angles. Clearly at large take-off angles the aluminium is mainly in the form of oxide.

4.1.2 Iron:

Table 4.3 Tabulation of ARXPS data at various energies and current densities

Energy (keV)	Current Density ($\mu\text{A}/\text{cm}^2$)	TOA	Relative atomic Concentration		
			O (%)	N (%)	Al (%)
5	5	0	0	31	69
		25	2	30.4	67.6
		50	6.9	19.8	73.3
		60	27	10.1	62.9
		75	34.1	8.1	57.8
4	5	0	0	31.3	68.7
		25	1.9	31.2	66.7
		50	7.4	19.8	72.8
		60	16.8	11.5	71.7
		75	30.5	9.7	59.8
3	5	0	0	29.7	70.3
		25	1.2	26.3	72.5
		50	16.5	18.3	65.2
		60	34	10.8	55.2
		75	48.6	4.6	46.8
2	5	0	0	31.6	68.4
		25	2	32.9	65.1
		50	12.3	27.7	60
		60	33.7	12.3	54
		75	51.1	2.8	46.1
5	1	0	1	31.1	67.9
		25	1.2	32	66.8
		50	8.5	22.8	68.7
		60	21.5	12.7	65.8
		75	35.4	7.1	57.5
4	1	0	5.8	30.8	63.4
		25	7.2	29.1	63.7
		50	19.1	4.8	76.1
		60	34.3	0	65.7
		75	48.4	0	51.5
3	1	0	2.5	32	65.5
		25	3.4	33.2	63.4
		50	22.1	16.3	61.6
		60	40.4	4.3	55.3
		75	54.4	0.3	45.3
2	1	0	1.4	29.4	69.2
		25	1.5	29.8	68.7
		50	15	21.5	63.5
		60	33.2	12	54.8
		75	49	4.7	46.3

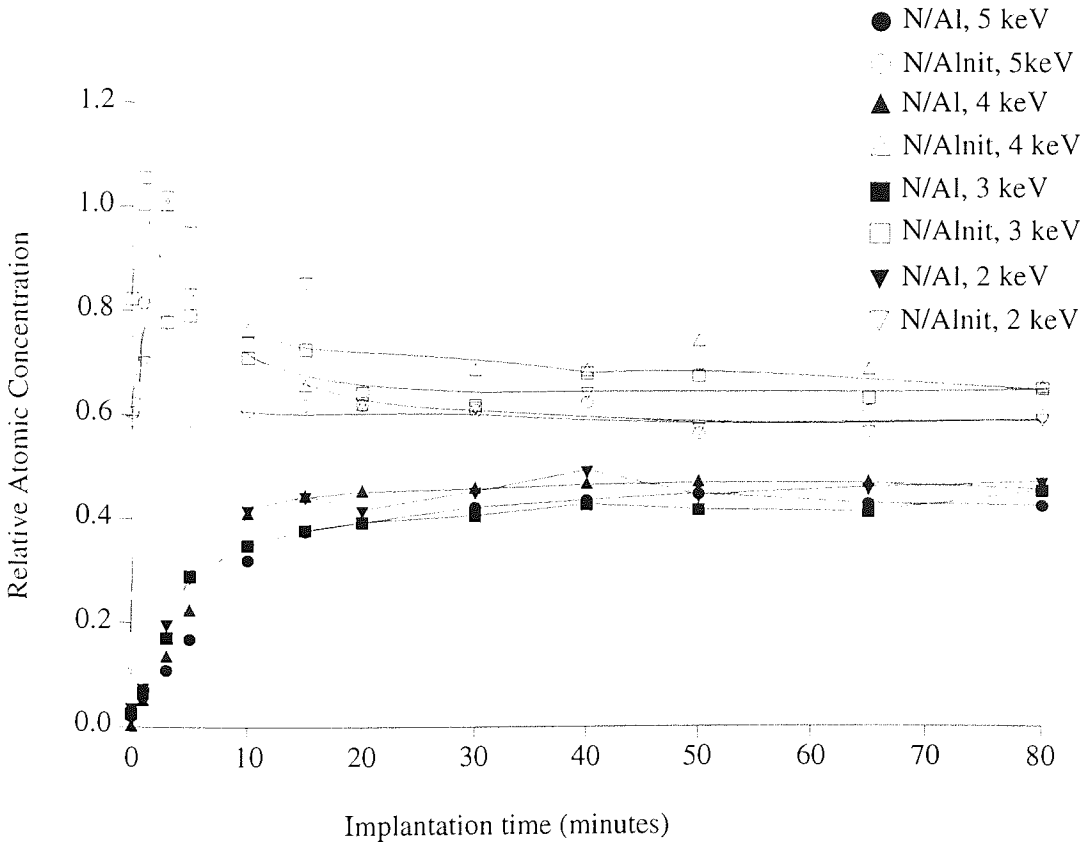
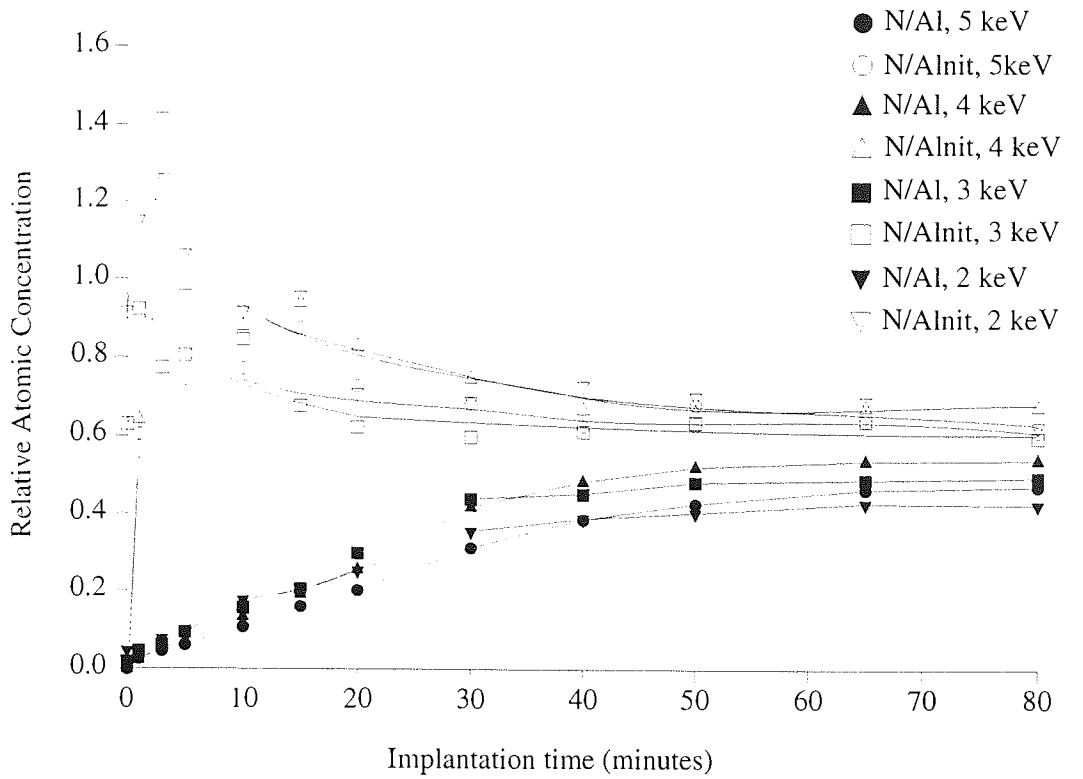


Figure 4.9 Variation of N/Al_{Nit} and N/Al_{tot} with the implantation time at $E = 2, 3, 4$ and 5keV ; (a) $\mu = 1 \mu\text{A}/\text{cm}^2$ and (b) $\mu = 5 \mu\text{A}/\text{cm}^2$.

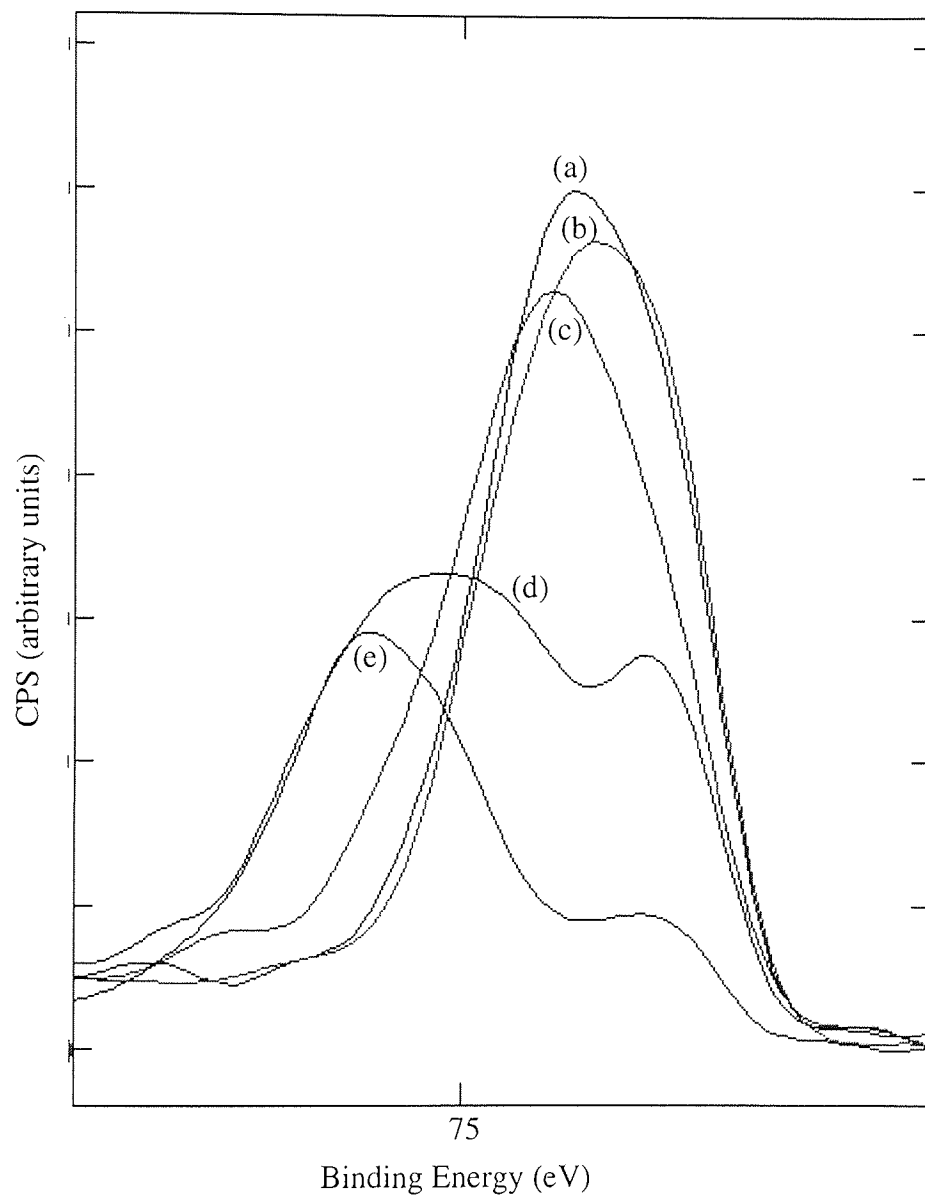


Figure 4.10 Al 2p photoelectron spectrum of nitrated aluminium, at different take-off-angles, (a) 0°, (b) 25°, (c) 50°, (d) 60° and (e) 75°, here angle is measured w.r.t. the normal to the sample surface.

4.1.2.1 Nitrogen implantation:

During N_2^+ bombardment, the changes in the relative atomic concentration of iron, nitrogen, carbon and oxygen were determined at successive intervals of sputtering and are shown as a function of implantation time in Figures 4.11 and 4.12 for implantation at current densities of $1 \mu A/cm^2$ and $5 \mu A/cm^2$ respectively. These figures indicate that as the implantation proceeds, the nitrogen concentration increases to a saturation value and the concentrations of oxygen and carbon fall slightly and then remain almost constant. As the concentration of impurities (carbon and oxygen) was slightly different in all experiments, the relative atomic concentration ratios of iron and nitrogen are plotted in Figure 4.13, in order to study the effect of ion energy and current density on the nitrogen relative atomic concentration. The saturation values at various energies and current densities are shown in Table 4.4

Table 4.4 Tabulation of (N/Fe)saturation values.

Energy (keV)	Current density ($\mu A/cm^2$)	(N/Fe)saturation ratio
5	1	0.12 ± 0.02
4		0.10 ± 0.02
3		0.08 ± 0.02
2		0.08 ± 0.02
5	5	0.10 ± 0.02
4		0.10 ± 0.02
3		0.09 ± 0.02
2		0.10 ± 0.02

To study the effect of ion dose on the nitrogen concentration values, the concentration profiles of nitrogen implantation are plotted as a function of ion dose for ion energies of 2, 3, 4 and 5 keV at both current densities, in Figure 4.14 (a), (b), (c) and (d) respectively. From Figure 4.14(a), it can be seen that the effect of current density is not important, as for a given dose, the relative atomic concentration of nitrogen is same at both current densities. However, from Figures 4.14(b), 4.14(c) and 4.14(d), for ion implantation carried out at 3, 4 and 5 keV, for a given dose, the value of nitrogen concentration is higher for implantation performed at $1 \mu A/cm^2$ as compared to the same at $5 \mu A/cm^2$.

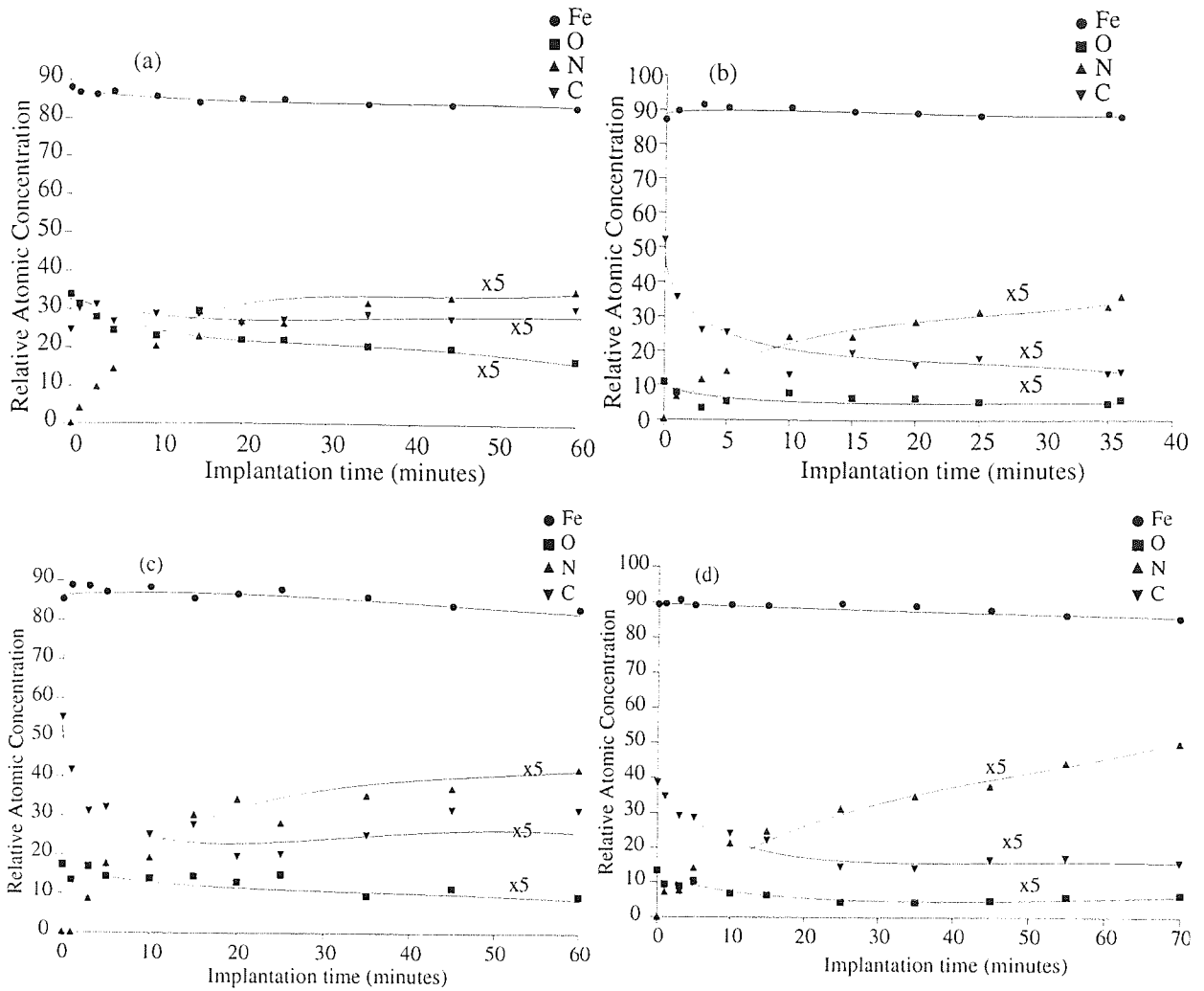


Figure 4.11 XPS time profiles of nitrogen ion implantation in iron at 2, 3, 4 and 5 keV at a current density of $1 \mu\text{A}/\text{cm}^2$. The relative atomic concentrations of oxygen, nitrogen and carbon are multiplied by 5 for clarity.

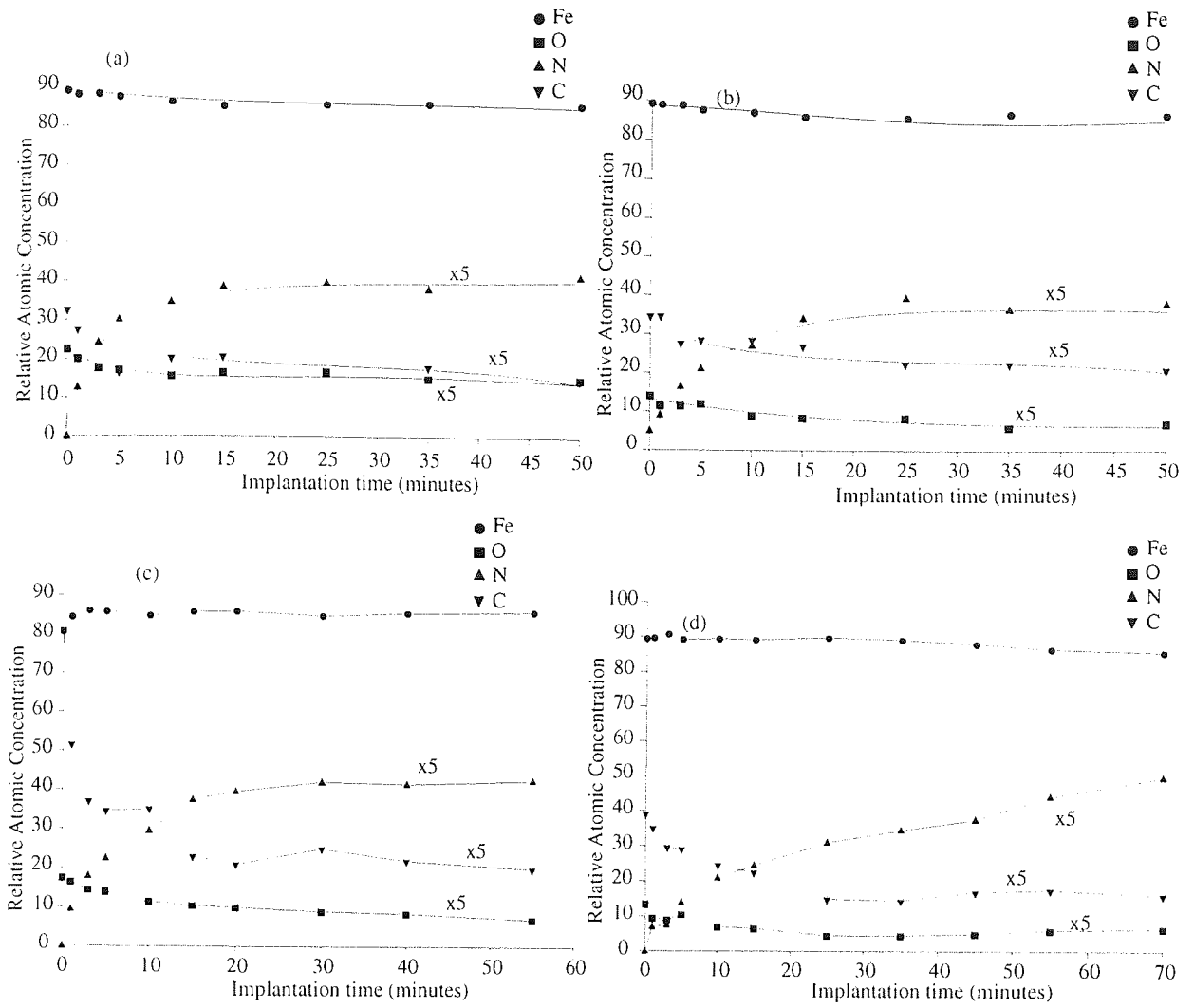


Figure 4.12 XPS time profiles of nitrogen ion implantation in iron at 2, 3, 4 and 5 keV at a current density of $5 \mu\text{A}/\text{cm}^2$. The relative atomic concentrations of oxygen, nitrogen and carbon are multiplied by 5 for clarity.

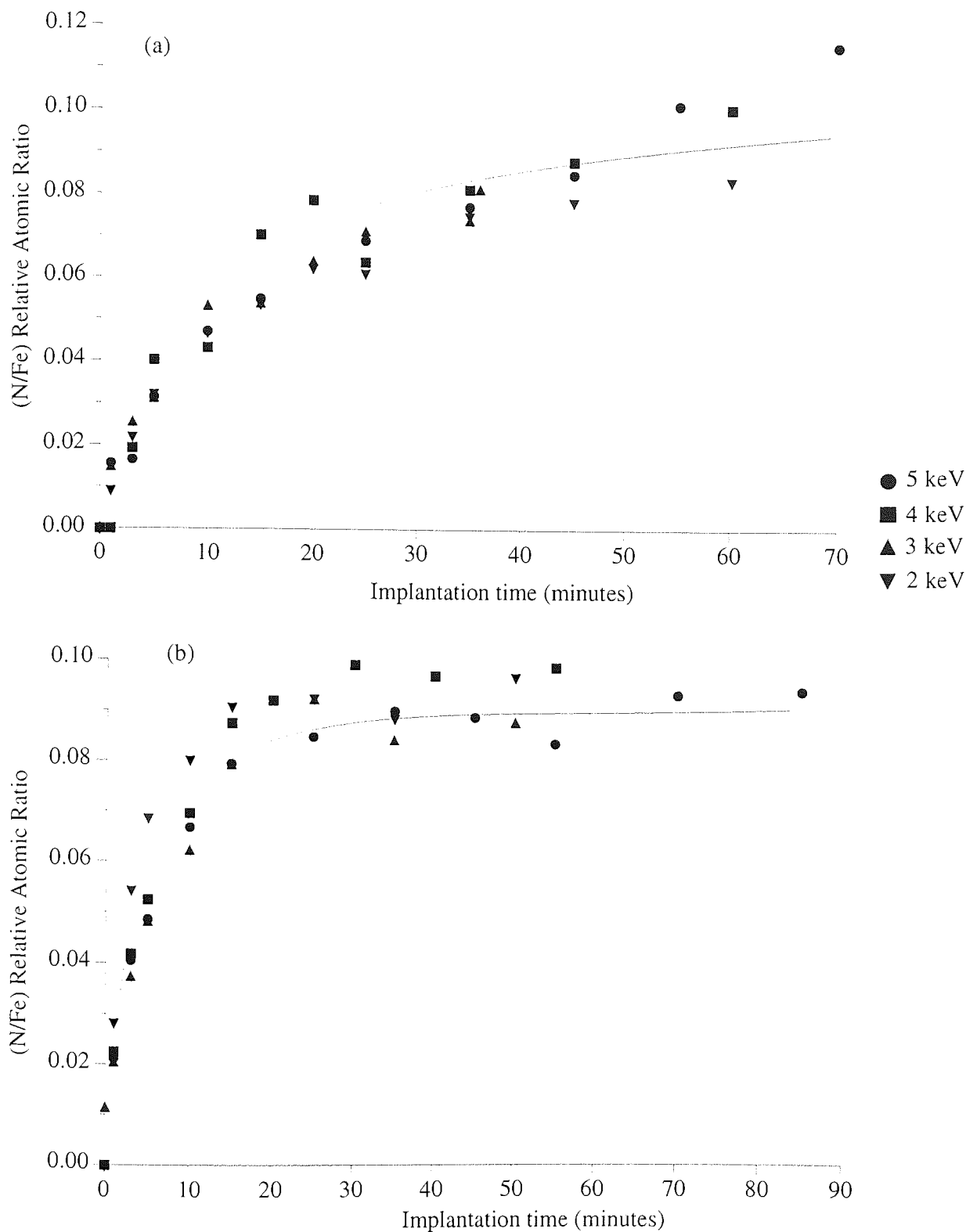


Figure 4.13 XPS time profile of nitrogen to iron relative atomic concentration ratio for implantation in iron at $E = 2, 3, 4$ and 5 keV ; and current densities of (a) $\mu = 1 \mu\text{A}/\text{cm}^2$ and (b) $\mu = 5 \mu\text{A}/\text{cm}^2$.

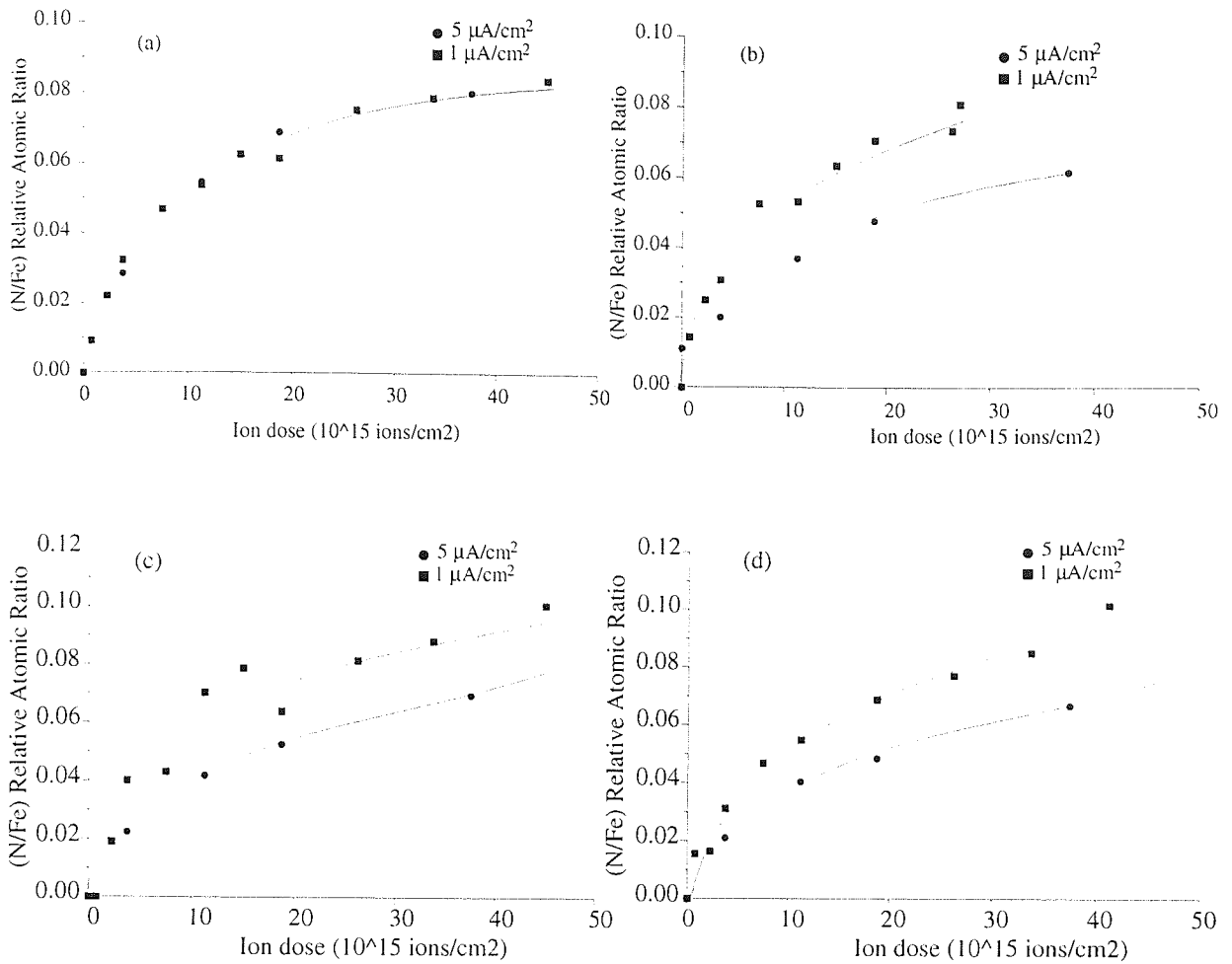


Figure 4.14 XPS profile of nitrogen to iron relative atomic concentrations, as a function of ion dose, at ion energies of (a) 2 keV, (b) 3 keV, (c) 4 keV and (d) 5 keV at current densities of 1 $\mu\text{A}/\text{cm}^2$ and 5 $\mu\text{A}/\text{cm}^2$.

4.1.2.2 Argon ion bombardment:

The Ar⁺ bombardment profiles are shown in Figures 4.15(a) and 4.15(b) for implantation current densities of 1 and 5 $\mu\text{A}/\text{cm}^2$ respectively. Relative atomic concentrations in these profiles are actually measured as a function of time. The time axis may be converted into depth scale using an etch rate value of 0.0042 nm/s, calculated from SUSPRE [Webb, 1992]. The error in the calculated depth could be upto 3, however the differences in the error for profiles at different implantation energies will be small. Hence one can still use this for the purpose of comparison of profiles. The profiles follow the expected trend and show that the nitrogen implantation is shallower at lower ion energies.

4.1.2.3 Fe spectra:

Figure 4.16 shows the Fe 2p, Valence band spectra and Auger spectra before and after nitrogen ion bombardment. The peak position of Fe 2p remains unchanged, however, the peak becomes slightly broadened (FWHM of Fe 2p_{1/2} increases from 2.71 to 2.83 eV and that of Fe 2p_{3/2} increases from 2.55 to 2.61 eV), after the nitrogen implantation. The separation between Fe 2p_{1/2} and Fe 2p_{3/2} peaks is 13.0, before and after nitrogen ion implantation. The XPS valence band spectrum and Auger spectra of iron did not change on nitrogen ion bombardment. The values of binding energy of Fe 2p_{3/2}, the kinetic energy of the Fe L₃VV line and Auger parameter are shown in Table 4.5, for iron sample prior to treatment, after Ar⁺ cleaning, after nitrogen ion bombardment and then Ar⁺ bombardment. The values of the same for pure Fe and standard mixture of Fe_{2,3,4}N are also reported. However, the analysis of standard sample, mixture of Fe_{2,3,4}N, was not very helpful as the sample was oxidised.

The spectra of N 1s and the Auger spectra of nitrogen are shown in Figure 4.17. The N 1s peak position is found at $397.9 \pm 0.1 \text{ eV}$, FWHM = 2.2 eV and the position of Auger peaks KL₁L₂₃, KL₂₃L₂₃ is at 369.0 ± 0.2 and $383.0 \pm 0.2 \text{ eV}$. The KL₁L₂₃ peak intensity was small and hence peak position can not be very accurately assigned. The Auger peak KL₁L₁ was not clear and this was almost absent in most of the cases. However when it appeared, it was with a small peak intensity and its position was found to be at 353.3 ± 0.2 . The values of N 1s binding energies (eV) and KL₂₃L₂₃ kinetic energies (eV) for N₂⁺ bombarded, standard mixture of Fe_{2,3,4}N, and nitrogen present in C-N bonding, along with the Auger parameter values are given in Table 4.6.

4.1.2.4 ARXPS results:

The ARXPS results for the nitrogen ion implantation are shown in Table 4.7. The N 1s peak

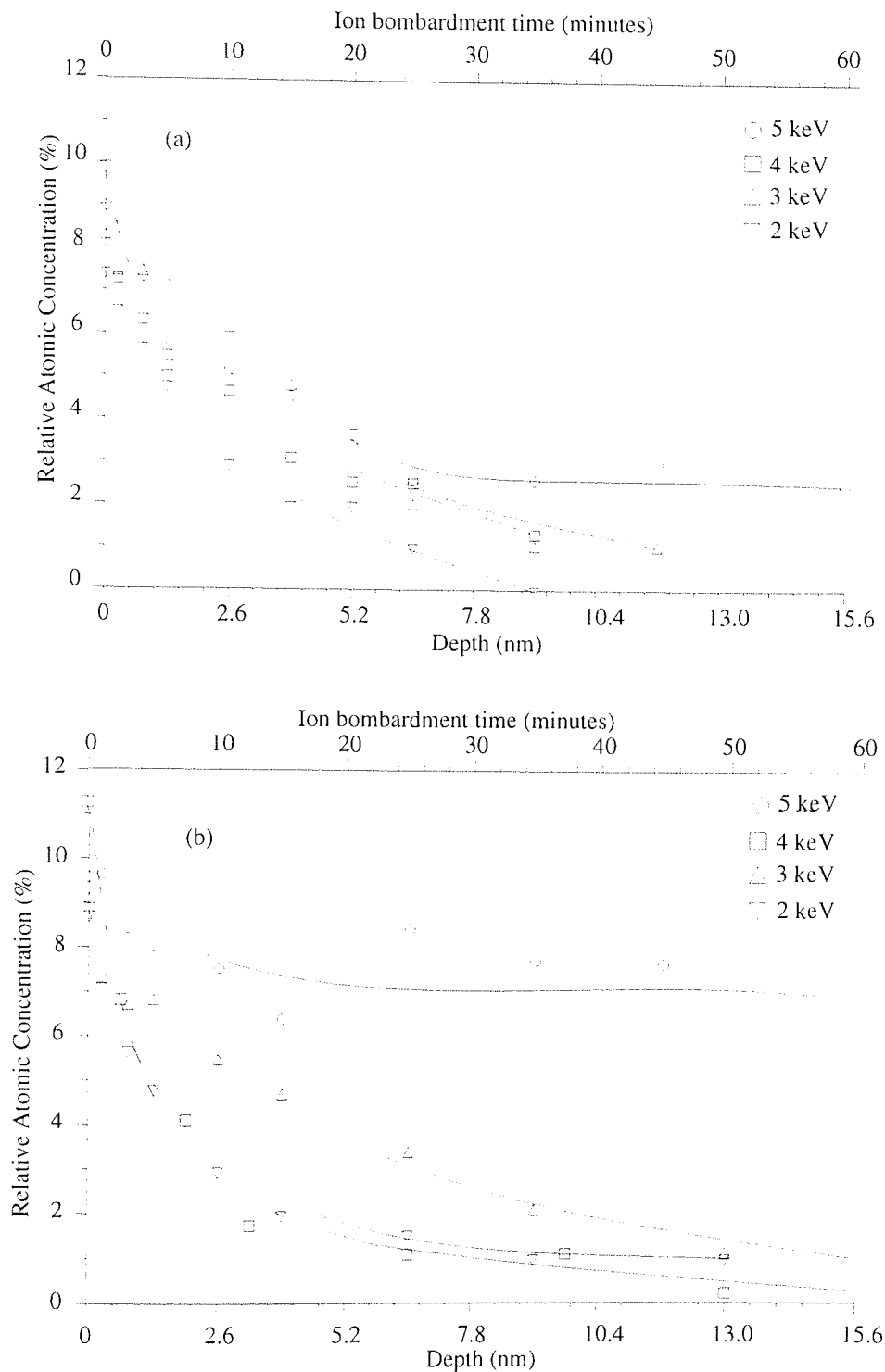


Figure 4.15 Depth and time profile of nitrogen implanted in iron, using Ar^+ of energy 2 keV and $2 \mu\text{A}/\text{cm}^2$ after nitrogen implantation on iron at $E = 2, 3, 4$ and 5 keV and (a) $1 \mu\text{A}/\text{cm}^2$ and (b) $5 \mu\text{A}/\text{cm}^2$. The time scale is converted to the depth scale using the etch rate value calculated from SUSPRE.

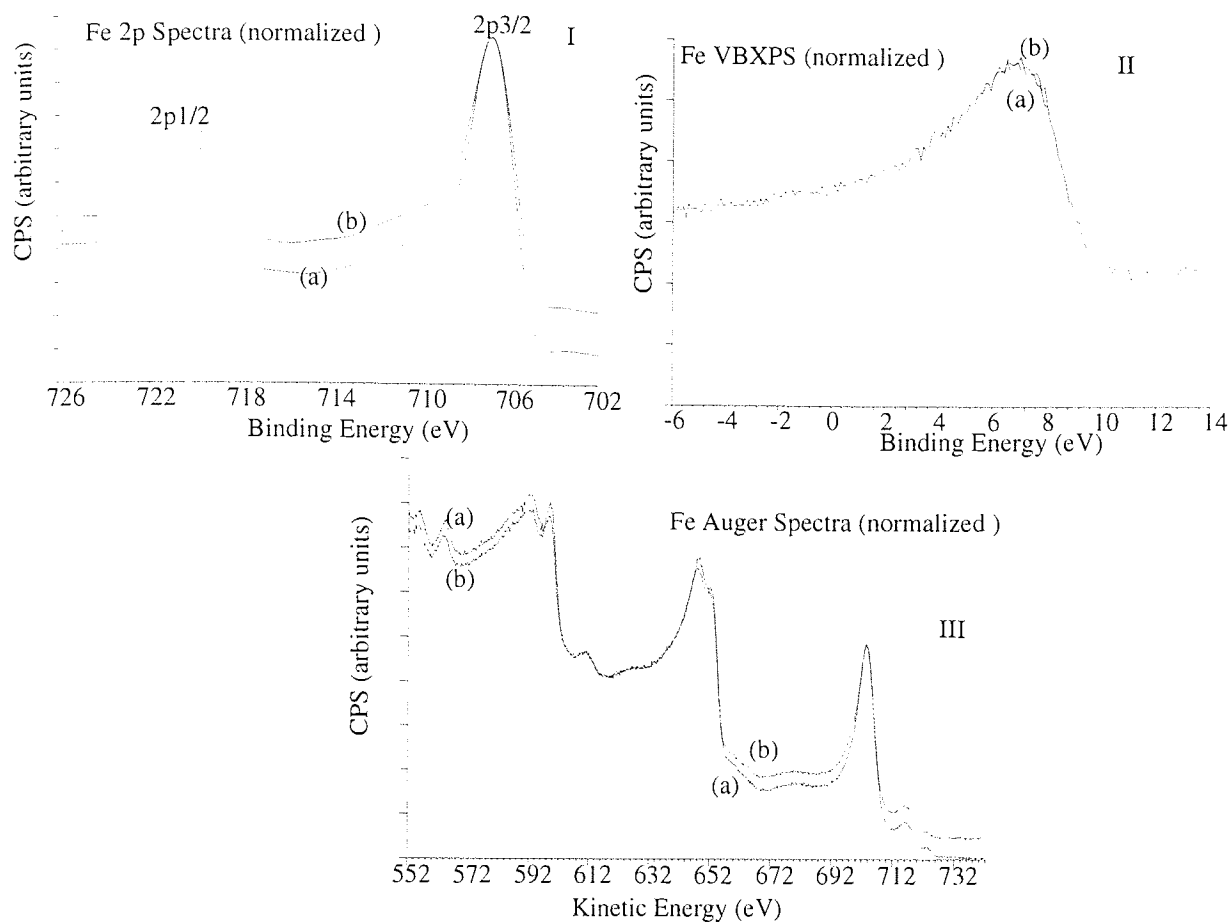


Figure 4.16 Fe 2p, Valence Band X-ray Photoelectron Spectra (VBXPS) and Auger spectra of (a) before and (b) after N_2^+ ion bombardment of iron sample. In all these figures, the spectras are normalized for comparison.

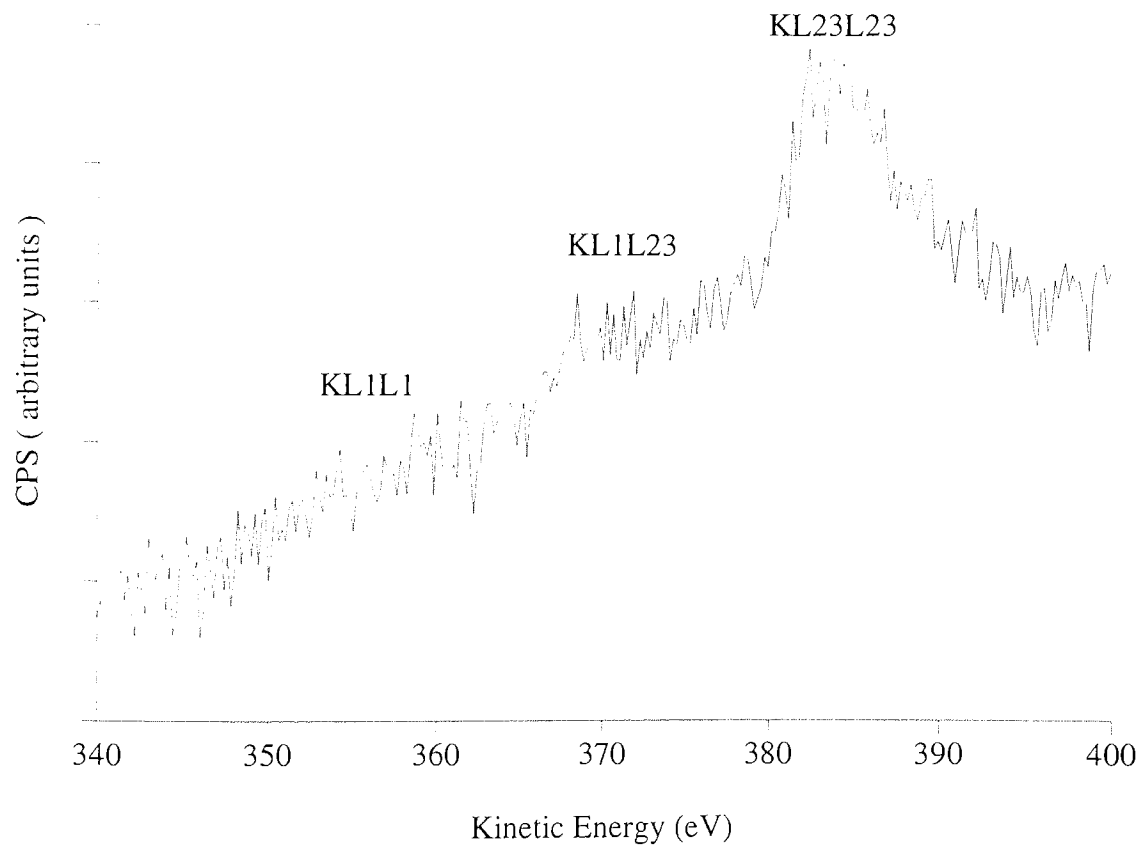
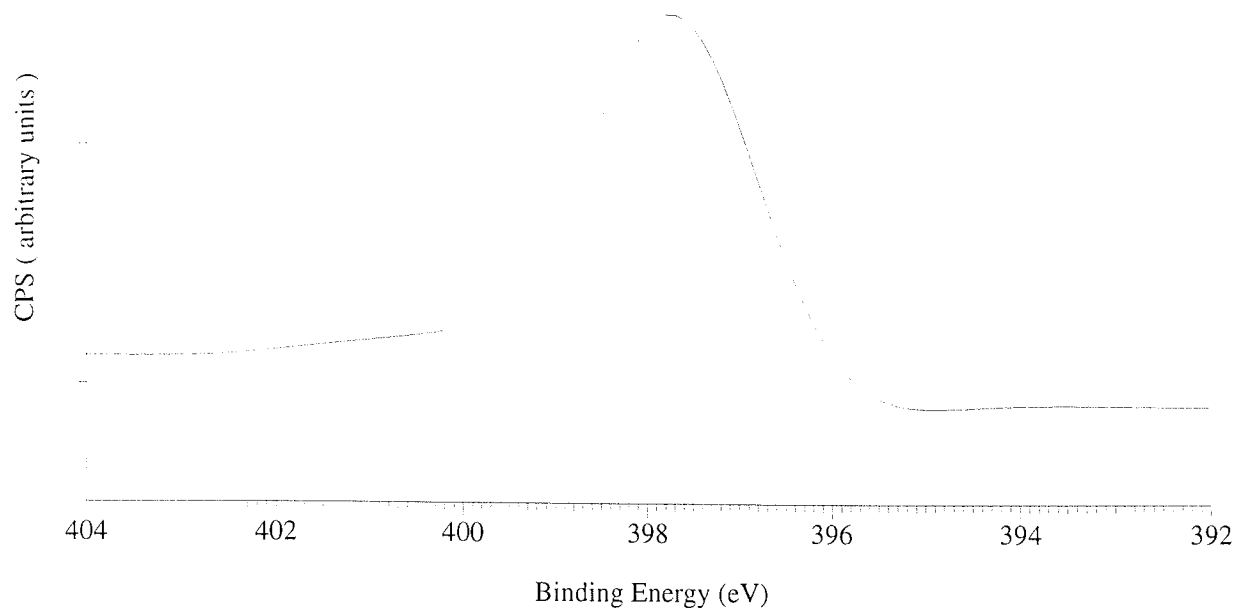


Figure 4.17 N 1s and Auger spectra of nitrogen ion bombarded iron sample, using XPS.

Table 4.5 The values of Fe 2p_{3/2} binding energies (eV) and L₃VV kinetic energies (eV) for as received, Ar⁺ ion cleaned, N₂⁺ bombarded, and then Ar⁺ bombarded are tabulated in first four rows. The last two rows show the value of the above mentioned parameters for pure iron and standard mixture of Fe_{2,3,4}N. The values inside the brackets are the FWHM of the peak.

	Fe 2p ₃	Fe L ₃ VV	Auger parameter
Fe metal (as received)	709.0±0.1 (3.3)	704.1±0.2	1413.1±0.3
Fe metal (after Ar ⁺ cleaning)	707.1±0.1 (2.5)	703.2±0.2	1410.3±0.3
N ₂ ⁺ bombarded iron	707.5±0.1 (2.6)	702.9±0.2	1410.4±0.3
First N ₂ ⁺ and then, Ar ⁺ bombardment	707.0±0.1	703.3±0.2	1410.3±0.3
Fe [Wagner, 1990]	706.95	702.4	1409.35
Mixture of Fe _(2,3,4) N	710.7±0.1 (3.7)	723.6±0.2	1434.3±0.3

Table 4.6 The values of N 1s binding energies (eV) and KL₂₃L₂₃ kinetic energies (eV) for N₂⁺ bombarded, standard mixture of Fe_{2,3,4}N, nitrogen present in C-N bonding, along with the values of Auger parameter.

	N 1s	N KL ₂₃ L ₂₃	Auger parameter
N ₂ ⁺ bombarded iron	397.9±0.1	383.1±0.2	781.0±0.3
Mixture of Fe _(2,3,4) N	397.2±0.1	no auger lines	-
Mixture of Fe _(2,3,4) N [Biwer and Bernasek, 1986]	397.3	383.0	780.3
Iron nitride [Diekmann et al., 1989]	398.1	381.9	780.0
N segregated on iron [Diekmann et al., 1989]	397.2	384.3	781.5
Nitrogen in C-N bonding [Boyd et al., 1995]	397.0	382.0	779.0

position remains the same at all the angles, suggesting that the nitrogen is present in the same chemical state at all the analysed depths. After the Ar⁺ cleaning, the C 1s signal from bulk was found at 283.4 eV, but ARXPS at 60° showed the C 1s at 284.6 eV, suggesting that the iron carbide is formed below a layer of adventitious carbon. (It should be remembered, however, that the total carbon concentration was low).

4.1.3 Copper:

Table 4.7 ARXPS data of nitrogen ion implantation in iron, at various ion energies and current densities.

Energy (keV)	Current Density (micA/cm ²)	TOA	Relative atomic Concentration				N/Fe
			Fe (%)	O (%)	N (%)	C (%)	
2	1	0	80.8	4	6.9	8.3	0.09
		33	79.9	4.1	8.1	7.9	0.1
		45	76.9	4.4	7.4	11.3	0.1
		54	68.9	7.3	7.4	16.4	0.11
		60	58.6	10.5	6.7	24.2	0.11
3	1	0	86.4	1.3	7.4	4.9	0.09
		33	85.1	1.8	7.8	5.3	0.09
		45	83.2	1.8	8.5	6.5	0.1
		54	78.5	1.5	8.6	11.4	0.11
		60	76.1	2	8.5	13.3	0.11
4	1	0	71	2.2	7.5	19.3	0.11
		33	66.3	2.5	8.5	22.7	0.13
		45	63.3	3.8	8	24.9	0.13
		54	59.7	4.9	8	27.4	0.13
		60	55.7	4.6	8.6	31.1	0.15
5	1	0	83.8	0.6	10.5	5.1	0.13
		33	82.8	0.7	10.5	5.9	0.13
		45	79.7	1	10.7	8.7	0.13
		54	78.4	1.2	10.1	10.3	0.13
		60	74.5	3.1	10.2	12.2	0.14
2	5	0	80.9	3	8.8	7.2	0.11
		33	79.9	2.6	8.7	8.8	0.11
		45	78.1	2.2	9	10.7	0.12
		54	75.7	2.1	9.9	12.3	0.13
		60	70.7	2.6	9.8	16.8	0.14
3	5	0	86.8	1.4	7.6	4.2	0.09
		33	81.8	1.7	8.1	8.4	0.1
		45	77	2.6	7.3	13	0.1
		54	68.5	4.2	7.1	20.2	0.1
		60	59.1	5.8	5.7	29.4	0.1
4	5	0	86.1	1.4	8.5	4	0.1
		33	80.6	1.6	8.6	9.2	0.11
		45	76.5	1.8	9.1	12.5	0.12
		54	70	1.9	9.6	18.5	0.14
		60	63.4	2.3	8.6	25.6	0.14
5	5	0	70.1	1.2	7.9	20.8	0.11
		33	67.3	1.7	8	23	0.1
		45	63.2	1.7	9.1	25.9	0.14
		54	60.6	2.2	8	29.2	0.13
		60	54.6	2.8	8.4	34.2	0.15

4.1.3.1 Nitrogen implantation:

For implantation at current densities of 1 and 5 $\mu\text{A}/\text{cm}^2$, the relative atomic concentrations of copper, nitrogen, carbon and oxygen were determined after successive periods of ion

bombardment and the changes in these concentrations are plotted in Figures 4.18 and 4.19, respectively. For clarity, the nitrogen, carbon and oxygen atomic concentration values are multiplied by 5. From these figures, it may be seen that as the implantation proceeds, the nitrogen concentration increases and reaches some saturation value and the concentrations of oxygen and carbon fall slightly and then remain almost constant. As the impurity level (the concentration of carbon and oxygen contaminants) was slightly different in all experiments, so the relative atomic concentrations ratios of nitrogen to copper were plotted as a function of bombardment time, at all the energies and current densities $1 \mu\text{A}/\text{cm}^2$ and $5 \mu\text{A}/\text{cm}^2$, Figure 4.20. From the figures, there is no evidence of significant variation in N saturation values with energy and current density and Table 4.8 confirms this.

Table 4.8 Tabulation of (N/Cu)saturation values.

Energy (keV)	Current density ($\mu\text{A}/\text{cm}^2$)	(N/Cu)saturation ratio
5	1	0.06 ± 0.02
4		0.05 ± 0.02
3		0.06 ± 0.02
2		0.06 ± 0.02
5	5	0.06 ± 0.02
4		0.07 ± 0.02
3		0.06 ± 0.02
2		0.06 ± 0.02

4.1.3.2 Argon ion bombardment:

The Ar^+ bombardment profiles of nitrogen to copper relative atomic concentration ratios are shown in Figure 4.21 for implantation at all ion energies and current densities. Relative atomic concentrations in these profiles are actually measured as a function of time. The time axis is converted into depth scale using the etch rate value of 0.0062 nm/s , calculated from SUSPRE [Webb, 1992]. As discussed in the case of aluminium and iron, the error in the calculated depth could be upto 3, however one can still use this for the purpose of comparison of profiles.

4.1.3.3 Cu spectra:

Figure 4.22 shows the Cu 2p, Auger spectra and Valence band spectra before and after

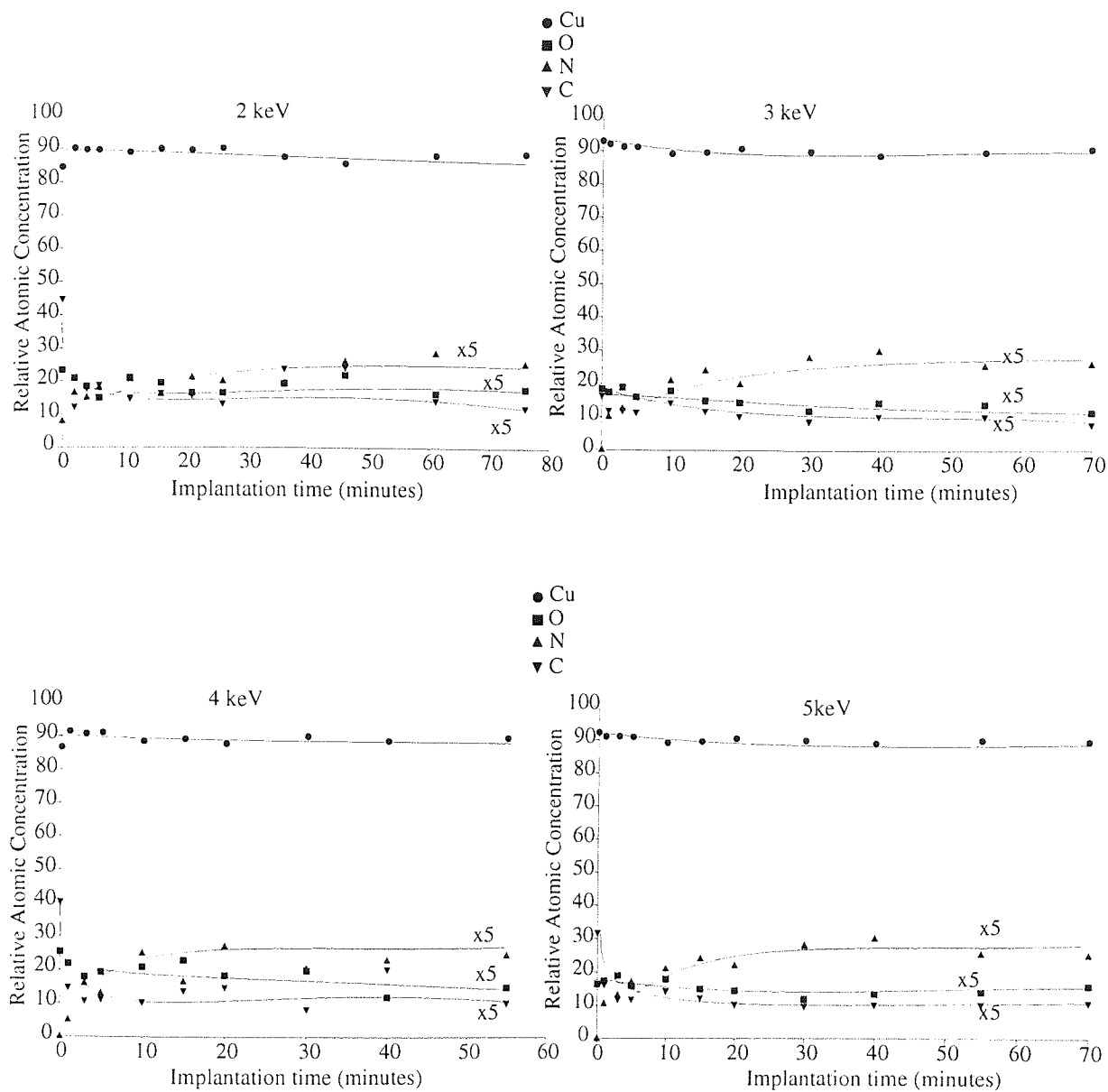


Figure 4.18 XPS time profiles of nitrogen ion implantation in copper at 2, 3, 4 and 5 keV at a current density of $1 \mu\text{A}/\text{cm}^2$. For clarity, the nitrogen, carbon and oxygen atomic concentration values are multiplied by 5.

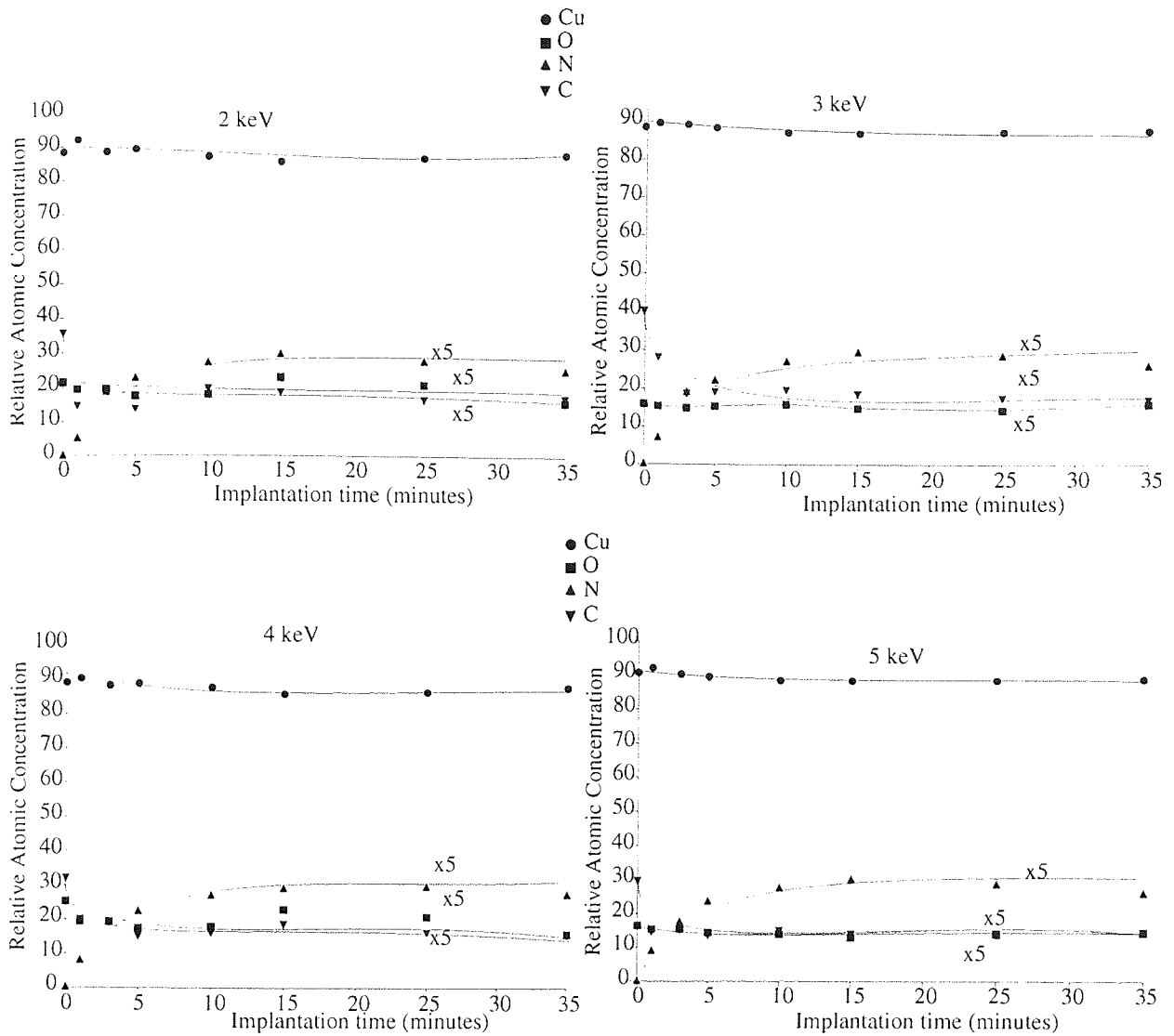


Figure 4.19 XPS time profiles of nitrogen ion implantation in copper at 2, 3, 4 and 5 keV at a current density of $5 \mu\text{A}/\text{cm}^2$. For clarity, the nitrogen, carbon and oxygen atomic concentration values are multiplied by 5.

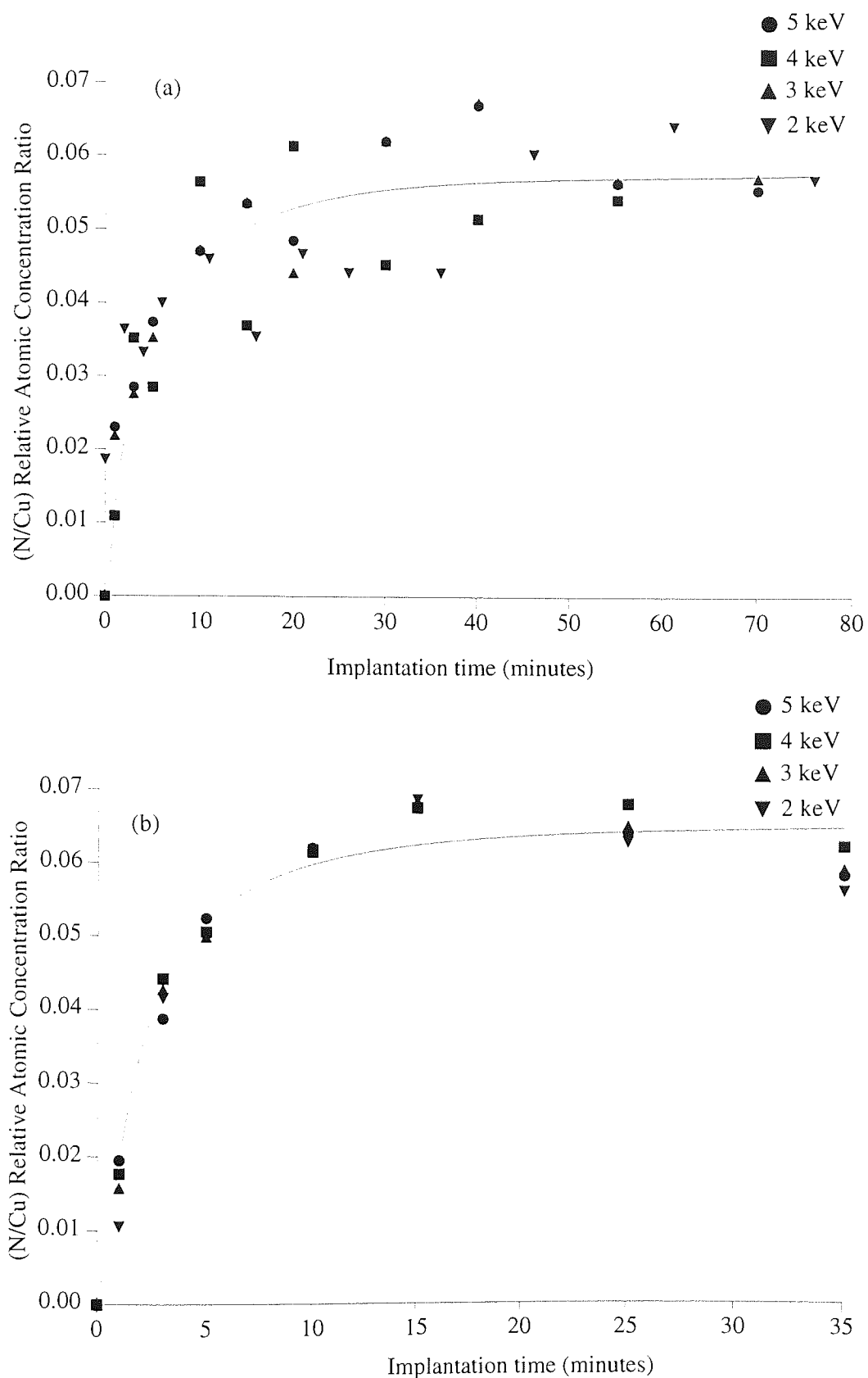


Figure 4.20 XPS profile of nitrogen to copper relative atomic concentration ratios for ion implantation in copper at 2, 3, 4 and 5 keV at current densities of (a) $1 \mu\text{A}/\text{cm}^2$ and (b) $5 \mu\text{A}/\text{cm}^2$.

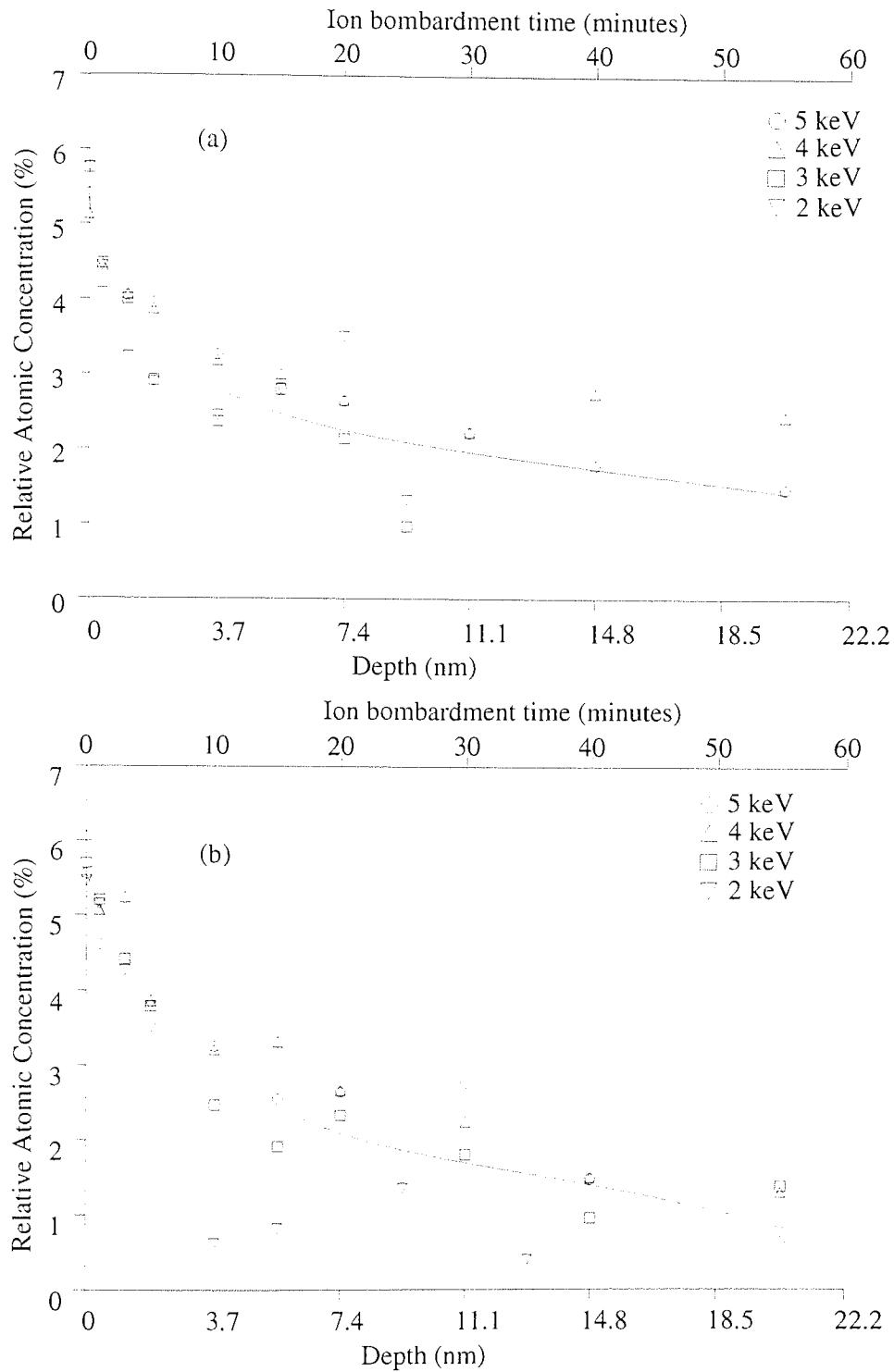


Figure 4.21 XPS Ar⁺ depth and time profile of nitrogen implanted in copper, using Ar⁺ of energy 2 keV and $2 \mu\text{A}/\text{cm}^2$ after nitrogen implantation on iron at $E = 2, 3, 4$ and 5 keV and (a) $1 \mu\text{A}/\text{cm}^2$ and (b) $\mu = 5 \mu\text{A}/\text{cm}^2$. The time scale is converted to the depth scale using the etch rate value calculated from SUSPRE.

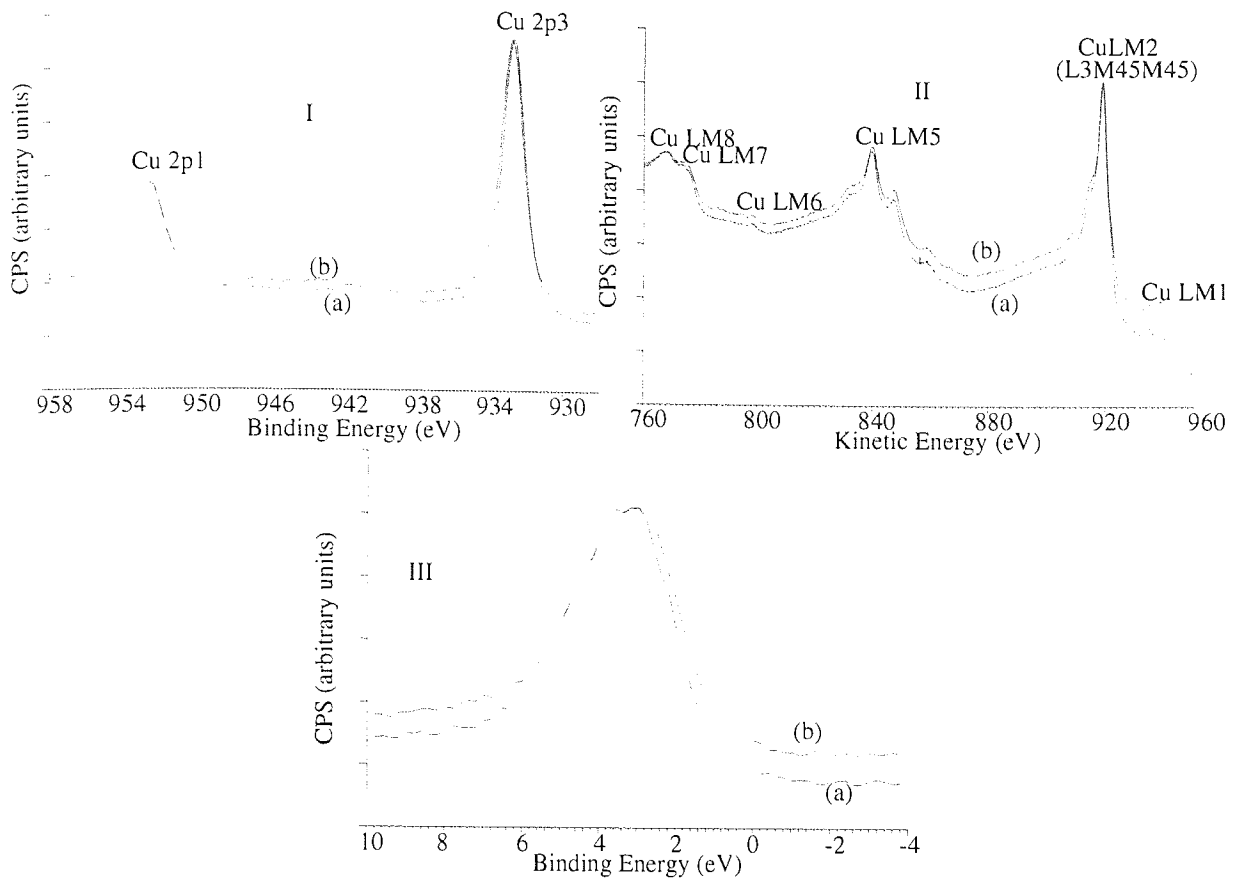


Figure 4.22 The normalized Cu 2p, Auger spectra and Valence Band X-ray Photoelectron Spectra (VBXPS) of (a) before and (b) after N₂⁺ ion bombardment of copper sample.

nitrogen ion bombardment. The peak position of Cu 2p remains unchanged, however, the peak becomes slightly broadened, after the nitrogen implantation. The energy gap between Cu 2p_{1/2} and Cu 2p_{3/2} peaks remains same, 19.9±0.2 eV, before and after nitrogen ion implantation. The analysis of standard Cu₃N sample shows this gap to be 19.7±0.2 eV. The XPS valence band and Auger spectra of copper did not change on nitrogen ion bombardment. Hence, it is not possible to conclude from this evidence that chemical interaction has taken place. The values of binding energy of Cu 2p_{3/2}, the kinetic energy of the Cu L₃VV line and Auger parameter are shown in Table 4.9, for copper sample prior to treatment, after Ar⁺ ion cleaning, after nitrogen ion bombardment and then Ar⁺ bombardment. The values of the same for pure copper and standard mixture of Cu₃N are also reported, however, for standard copper nitride sample the Auger lines could not be observed due to carbon and oxygen contamination on the surface.

Table 4.9 The values of Cu 2p_{3/2} binding energies (eV) and L₃VV kinetic energies (eV) for as received, Ar⁺ ion cleaned, N₂⁺ bombarded, and then Ar⁺ bombarded are tabulated in first four rows. The last two rows show the value of the above mentioned parameters for pure copper and standard Cu₃N. The values inside the brackets are the FWHM of the peak.

	Cu 2p ₃	CuL ₃ VV	Auger parameter
Cu metal (as received)	932.0±0.1 (1.88)	931.7±0.2	1863.7±0.3
Cu metal (after Ar ⁺ cleaning)	932.3±0.1 (1.96)	919.0±0.2	1851.3±0.3
N ₂ ⁺ bombarded copper	932.4±0.1 (1.97)	919.1±0.2	1851.5±0.3
First N ₂ ⁺ and then, Ar ⁺ bombardment	932.6±0.1 (1.97)	919.0±0.2	1851.6±0.3
Cu [Wagner, 1990]	932.67	918.65	1851.32
Standard Cu ₃ N	933.0±0.1 (2.4)	no auger lines	--

The spectra of N 1s of nitrogen implanted in copper and standard copper nitride is shown in Figures 4.23. For nitrogen ion implanted copper, there are two peaks of nitrogen at peak position 396.8±0.1 eV, FWHM = 2.12 eV (approximately 50 % of the total nitrogen) and 403.3±0.1 eV, FWHM = 2.41 eV. The binding energy gap between Cu 2p_{3/2} and N 1s peak is found to be 535.6±0.2 and 529.2±0.2 eV, for both peaks of nitrogen. For standard copper nitride, there was only a single peak of nitrogen at 397.6 eV. The energy gap between Cu 2p_{3/2} and N 1s peak for standard copper nitride sample is found to be 535.4±0.2, which suggests that for nitrogen ion bombarded copper sample, the N 1s peak at 396.8±0.1 eV is due to copper nitride.

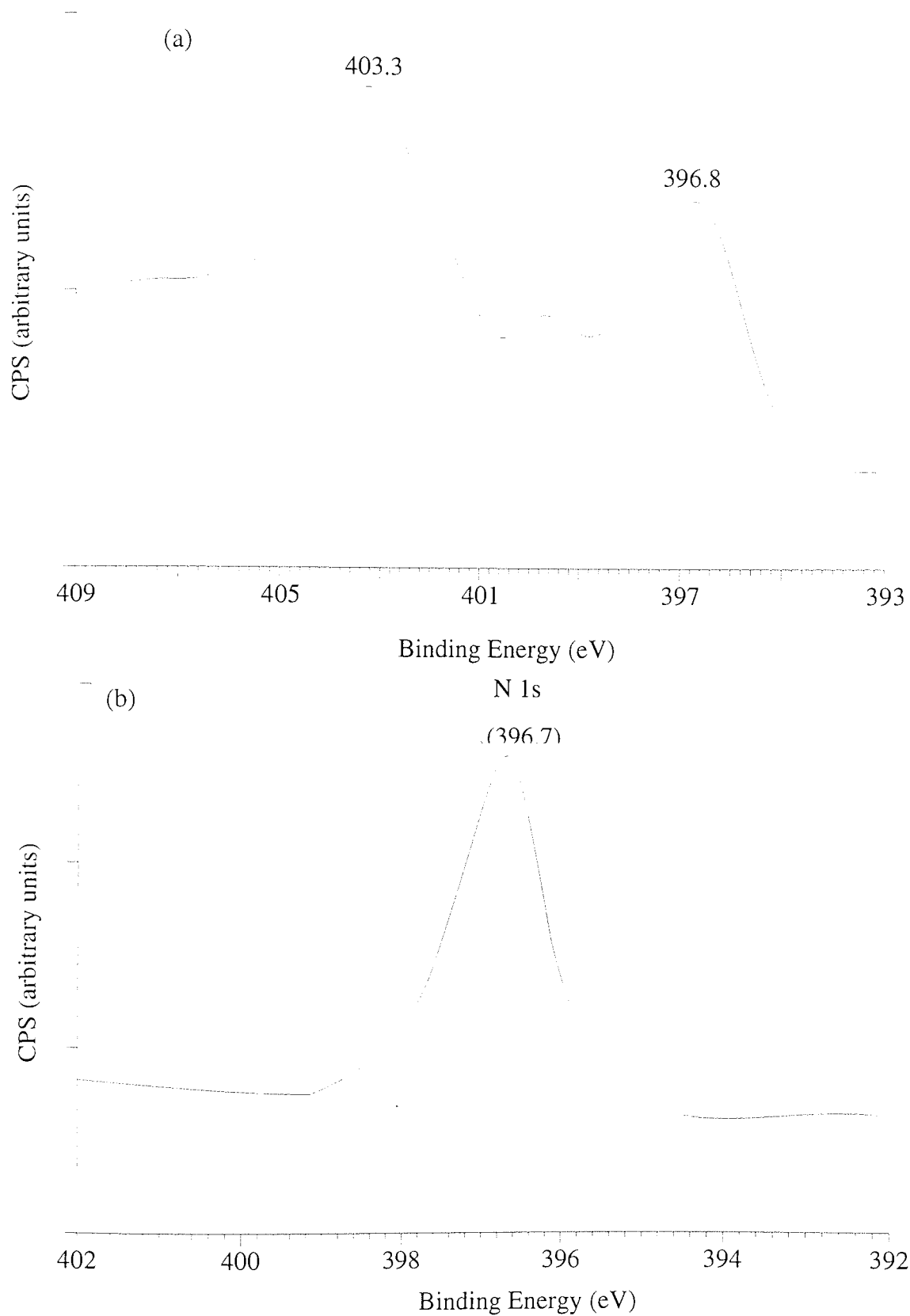


Figure 4.23 N 1s spectra obtained from (a) nitrogen ion bombarded copper sample (b) Cu_3N standard sample.

4.1.3.3 ARXPS results:

The ARXPS results for the nitrogen ion implantation are shown in Table 4.10. The N 1s peak position remains the same at all the angles, suggesting that the nitrogen is present in the same chemical state at all the analysed depths.

4.1.4 Gold:

4.1.4.1 Nitrogen implantation:

The nitrogen ion bombardment of gold did not result in implantation of nitrogen. The nitrogen photoelectron signal was very rarely observed and whenever it was, it was very small.

4.1.4.2 Au spectra:

Figure 4.24 shows the comparison of Au 4d, Au 4f spectra and Valence band spectra before and after N_2^+ bombardment. Clearly, the spectra of gold show no change. The spectra of highest available nitrogen is shown in Figure 4.25.

4.1.5 GaAs:

4.1.5.1 Nitrogen implantation:

The changes in the atomic concentration of gallium, arsenic and nitrogen were determined at successive intervals of implantation. Figures 4.26 and 4.27 show the relative atomic concentrations of gallium, arsenic and nitrogen as a function of time of implantation, for implantation at current densities of $1 \mu A/cm^2$ and $5 \mu A/cm^2$ respectively. From these figures, it may be seen that as the implantation proceeds, the nitrogen concentration increases to a saturation value and the concentrations of gallium and arsenic fall slightly and then remain constant. In Figure 4.28, the ratio of relative atomic concentrations of nitrogen and sum of gallium and arsenic concentrations; $[N/(Ga+As)]$, are plotted as a function of implantation time. The As/Ga ratios were found to decrease upon ion bombardment. Figure 4.29 shows that the extent of As depletion is not a function of ion energy but depends on ion bombardment time.

Table 4.10 ARXPS data of nitrogen ion implantation in copper, at various ion energies and current densities.

Energy (keV)	Current Density (micA/cm ²)	TOA	Relative atomic Concentration				N/Cu
			Cu (%)	O (%)	N (%)	C (%)	
2	1	0	84.4	3.2	5	7.4	0.06
		33	81.2	4	5.2	9.6	0.06
		45	76.8	4.4	5.5	13.3	0.07
		54	72.4	4.1	6.2	17.3	0.09
		60	64.3	6.7	5	24	0.08
3	1	0	86.5	3	4.8	5.7	0.06
		33	76.1	3.2	5	15.7	0.07
		45	84	3.3	4.9	7.8	0.06
		54	78.1	3.9	4.7	13.2	0.06
		60	74.6	4.1	4.5	16.8	0.06
4	1	0	86.2	3.8	5	5	0.06
		33	84	3.4	5.3	7.3	0.06
		45	82.4	4.4	4.2	9	0.05
		54	77.1	5.1	6	11.8	0.08
		60	72	5.7	4.7	17.6	0.07
5	1	0	86.5	3.2	4.8	5.5	0.06
		33	84.5	3.4	5.1	7	0.06
		45	82	3.7	5.1	9.2	0.06
		54	77.9	3.9	4.7	13.5	0.06
		60	74.2	4.1	4.5	17.2	0.06
2	5	0	88.3	3.2	5	3.5	0.06
		33	83.3	3.4	6.2	7.1	0.07
		45	80.4	3.3	6.2	10.1	0.08
		54	75.3	4.6	5.6	14.5	0.07
		60	56.1	14.5	5	24.4	0.09
3	5	0	85.9	3	5.1	6	0.06
		33	82.8	3.3	5	8.9	0.06
		45	80.2	3.4	5.1	11.3	0.06
		54	77.6	3.7	4.9	13.8	0.06
		60	74.1	4.1	4.7	17.1	0.06
4	5	0	86.3	3.7	5.2	4.8	0.06
		33	83.8	3.4	5.3	7.5	0.06
		45	81.7	4.4	4.2	9.7	0.05
		54	77.2	4.9	5.9	12	0.08
		60	71.7	5.6	5.1	17.6	0.07
5	5	0	86	3	5	6	0.06
		33	82.1	3.4	6.2	8.3	0.08
		45	80.3	3.4	6.2	10.1	0.08
		54	75.3	4.6	5.6	14.5	0.07
		60	56.6	14.4	5	24	0.09

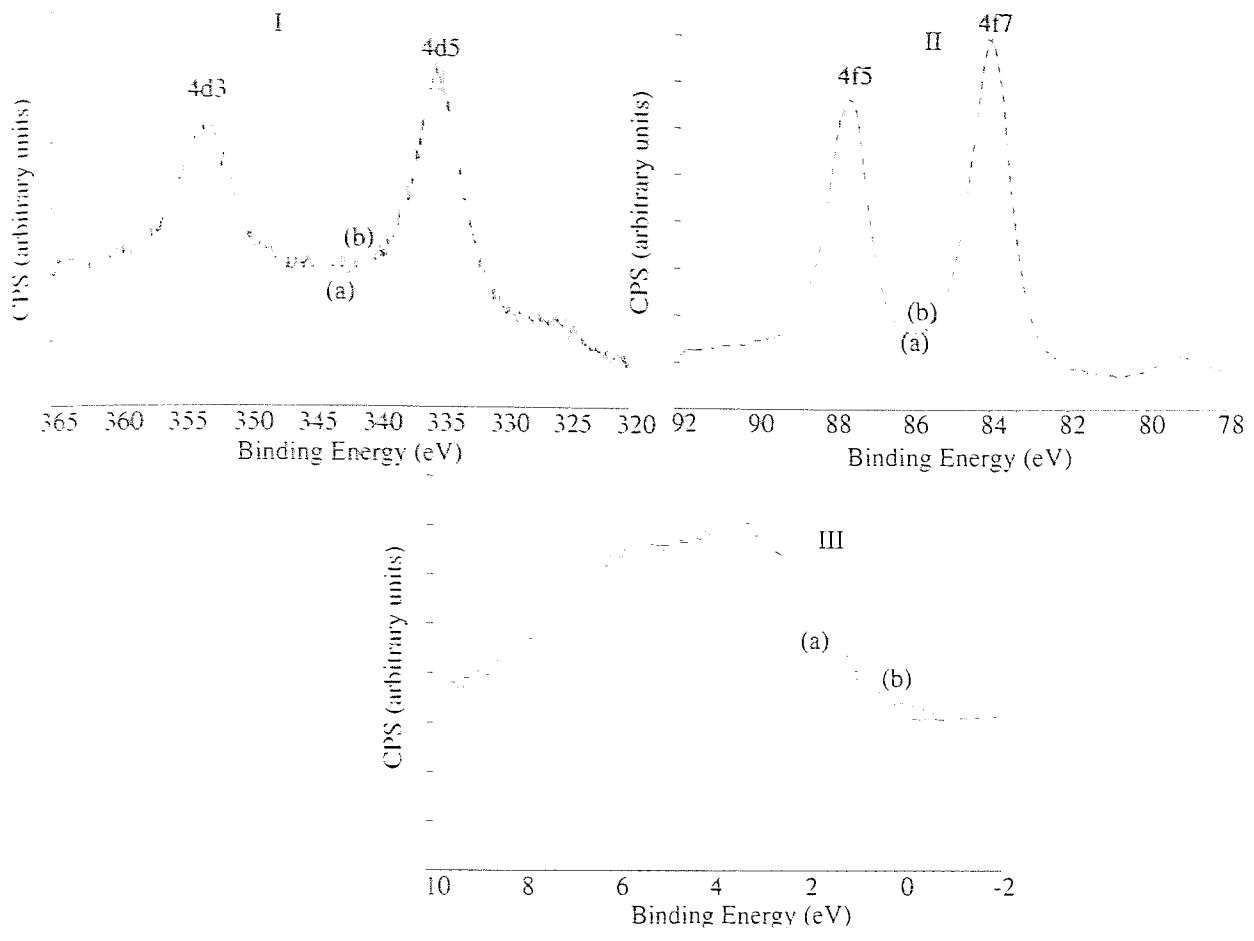


Figure 4.24 Au 4d, 4f and Valence band spectra of (a) before and (b) after N_2^+ ion bombardment of gold sample.

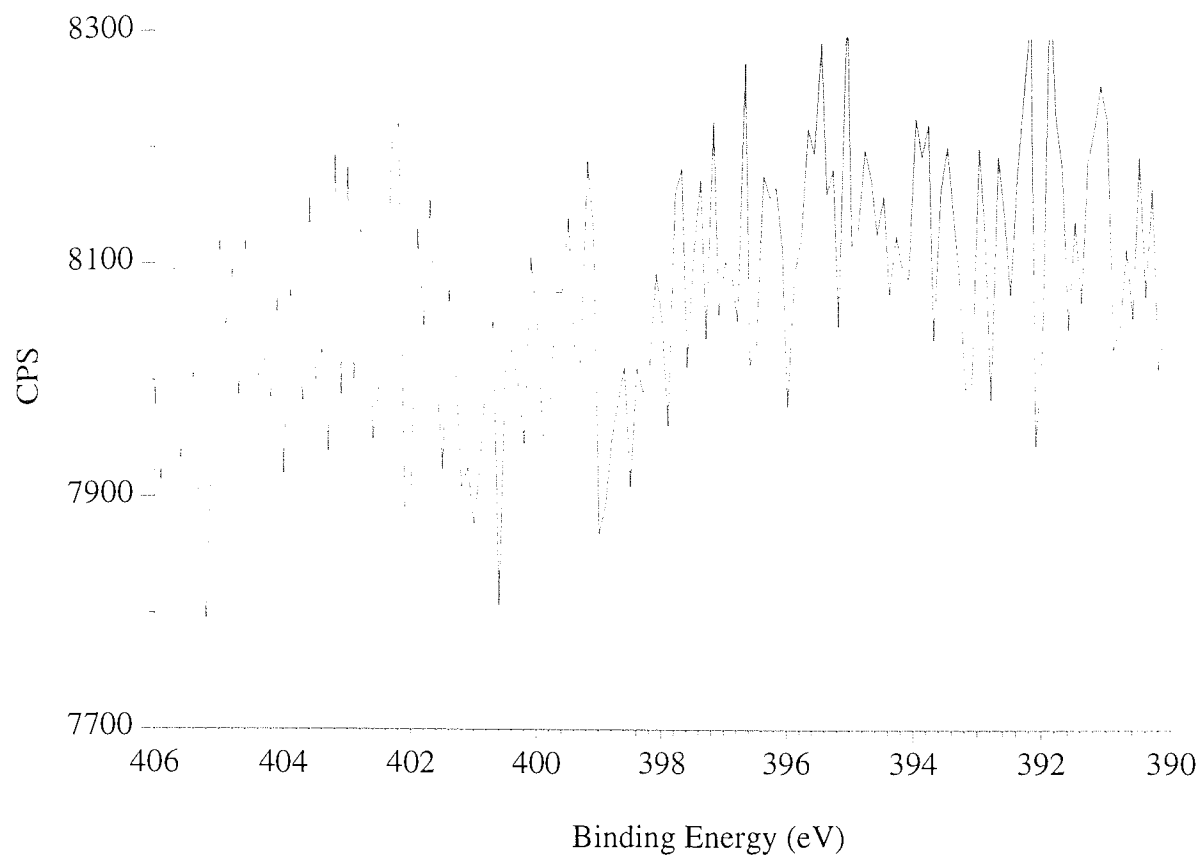


Figure 4.25 N 1s spectra of nitrogen obtained from nitrogen ion bombarded gold sample.

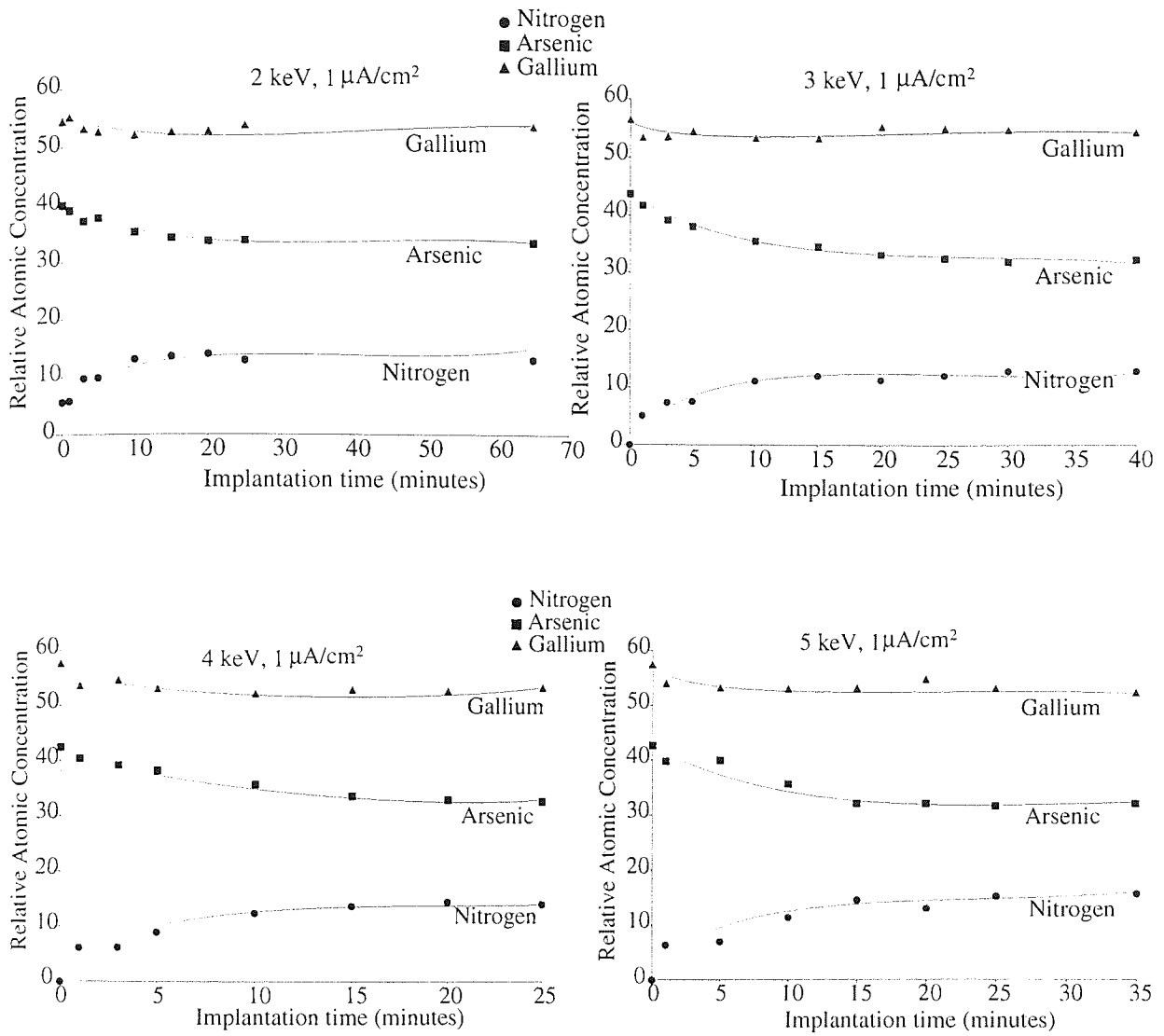


Figure 4.26 XPS time profile of nitrogen ion implantation in GaAs at 2, 3, 4 and 5 keV at a current density of $1 \mu\text{A}/\text{cm}^2$.

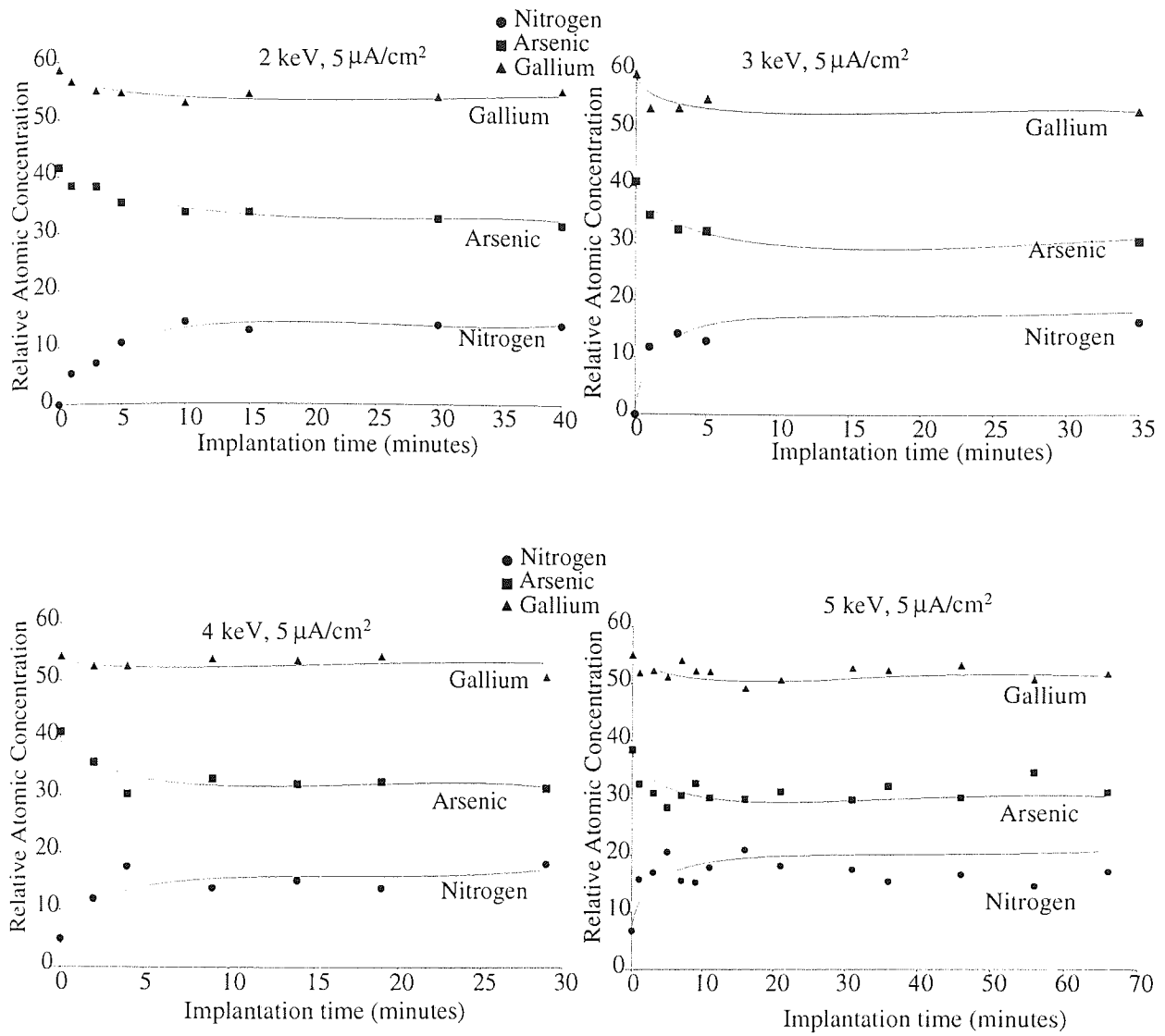


Figure 4.27 XPS time profile of nitrogen ion implantation in GaAs at 2, 3, 4 and 5 keV at a current density of $5 \mu\text{A}/\text{cm}^2$.

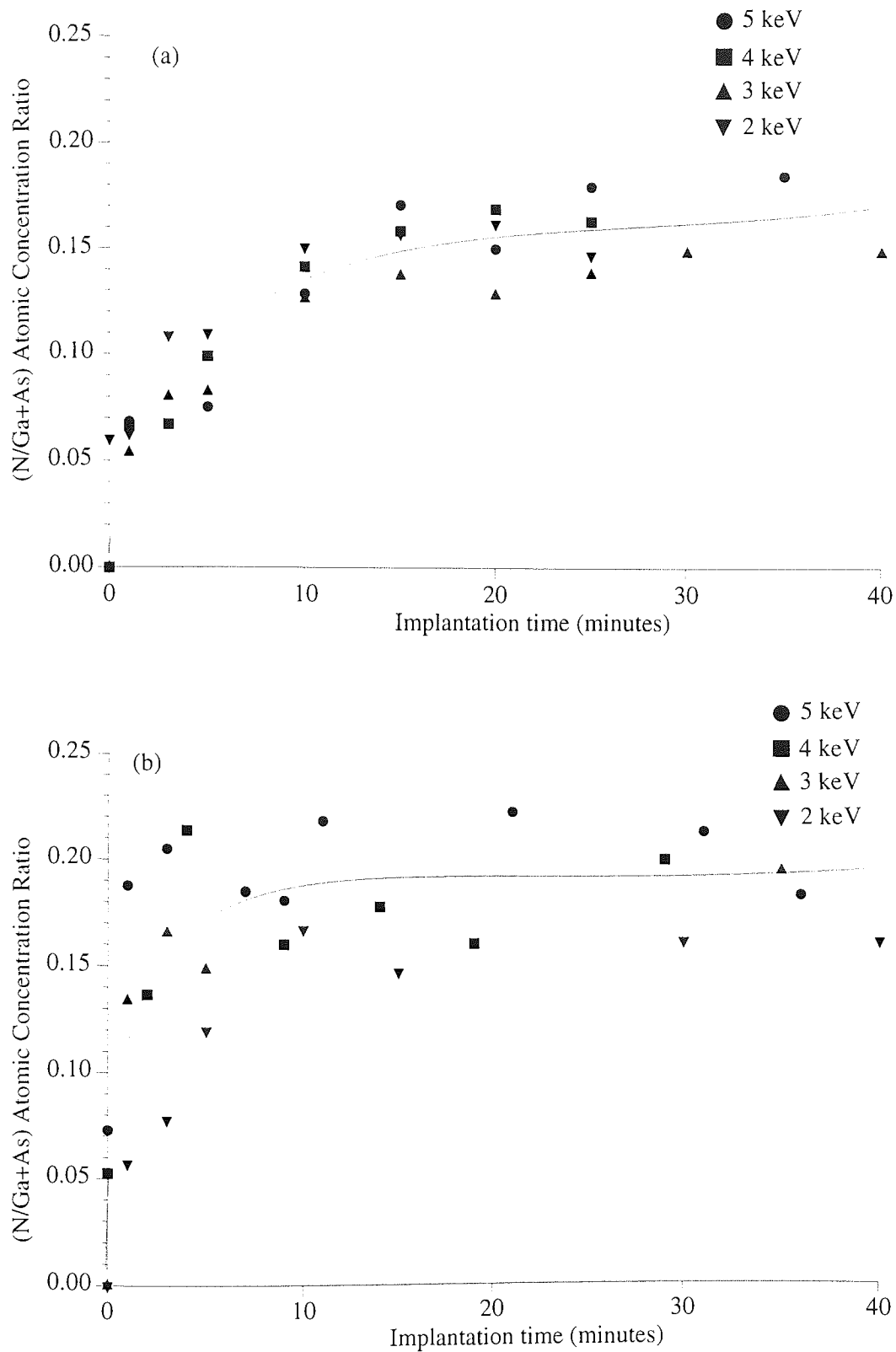


Figure 4.28 Variation of ratio of relative atomic concentration of nitrogen to target, $N/(Ga+As)$, as a function of implantation time, for implantation at 2, 3, 4 and 5 keV at current densities of (a) $1 \mu A/cm^2$ and (b) $5 \mu A/cm^2$.

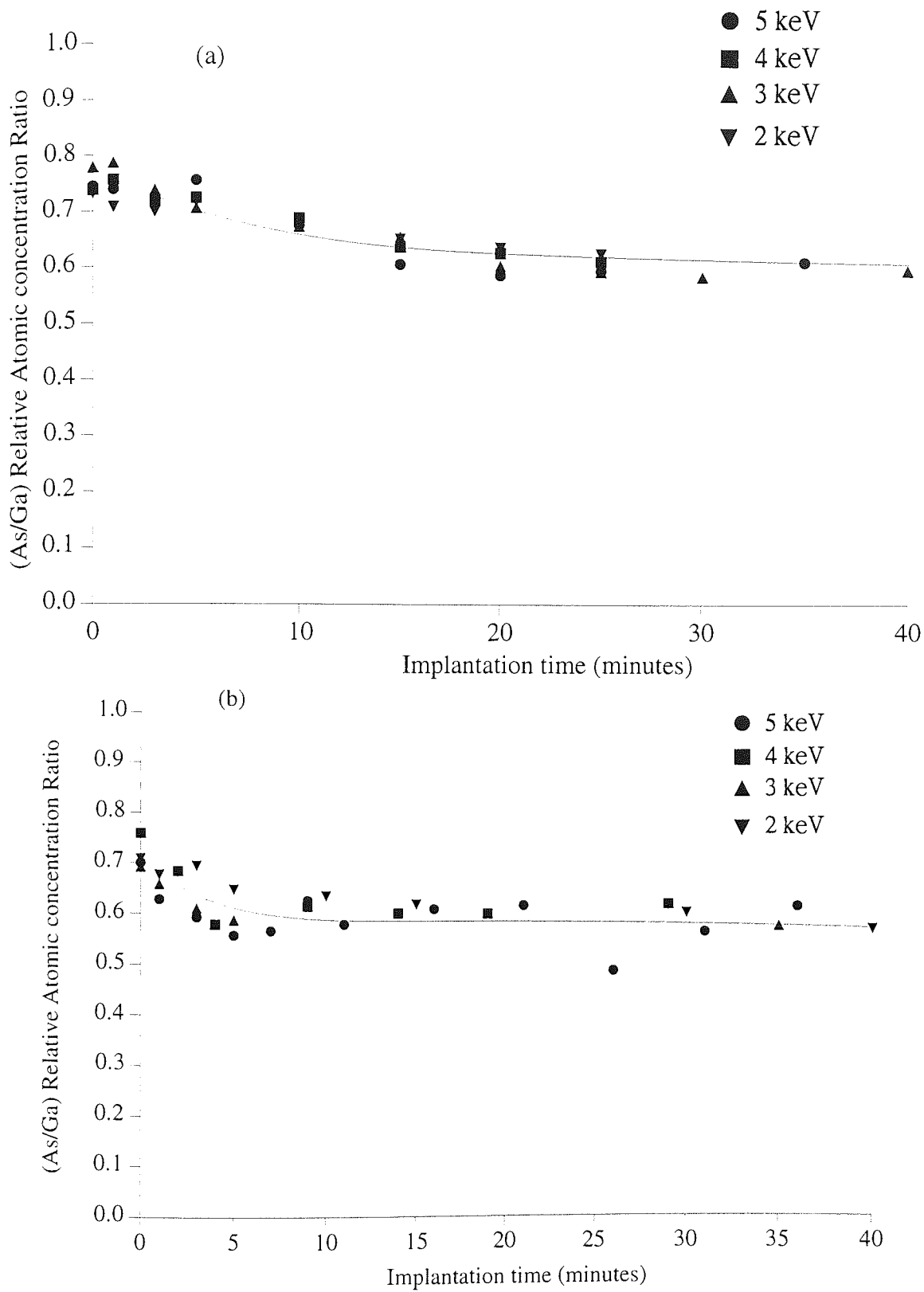


Figure 4.29 Variation of ratio of relative atomic concentration of arsenic and gallium, (As/Ga), as a function of implantation time at 2, 3, 4 and 5 keV at current densities of (a) $1 \mu\text{A}/\text{cm}^2$ and (b) $5 \mu\text{A}/\text{cm}^2$.

4.1.5.2 Argon ion bombardment:

The Ar⁺ bombardment profiles of relative atomic concentration of N, Ga and As in the sample surfaces are shown in Figure 4.30. Relative atomic concentrations in these profiles are actually measured as a function of time. The time axis is converted into depth scale using the etch rate value of 0.019 nm/s, calculated from SUSPRE [Webb, 1992]. The error in the calculated depth could be upto 3, however the differences in the error for profiles at different implantation energies will be small. Hence one can still use this for the purpose of comparison of profiles. In Figure 4.32, the As/Ga relative atomic concentration ratios are plotted as a function of Ar⁺ bombardment time, showing that the As/Ga ratios increase during the first few minutes of Ar⁺ bombardment and then they show a steady increase towards but never quite reaching the pre-bombardment condition.

4.1.5.3 GaAs spectra:

Figure 4.32 shows the comparison of GaAs 3d, As L₃M₄₅M₄₅ and Ga L₃M₄₅M₄₅ spectra, before and after nitrogen ion bombardment. The Ga 3d peak broadens and shifts to higher binding energy while the As 3d peak width remains almost unchanged. The separation between Ga and As 3d changes from 22.0±0.2 eV to 21.8±0.2 eV. The Auger spectra of Ga and As did not show any appreciable change in peak position or peak shape. The values of binding energy of Ga 3d, the kinetic energy of the Ga L₃M₄₅M₄₅ line and Auger parameter are shown in Table 4.11, for GaAs sample as received, after Ar⁺ cleaning, after nitrogen ion bombardment and then Ar⁺ bombardment. The values of the same for pure Ga, GaAs and standard mixture of GaN are also reported. The values of binding energy of As 3d, the kinetic energy of the As L₃M₄₅M₄₅ line and Auger parameter are shown in Table 4.12, for GaAs sample as received, after Ar⁺ cleaning, after nitrogen ion bombardment and then Ar⁺ bombardment. The values of the same for pure As and GaAs are also reported.

The synthesised Ga 3d spectra, Figure 4.33, shows the presence of Ga atoms in the form of GaAs and GaN. The relative atomic concentration ratio of N to Ga in the form of GaN is plotted in Figure 4.34 for implantation at all ion energies and current densities. As expected, this ratio increases with implantation time and eventually saturates.

Since Ga 3d and As 3d are doublets, so the identification of chemical states is expected to be difficult using these peaks, however, the higher binding energy peaks Ga 2p and As 2p are single peaks and so the analysis of these peaks may be helpful in identifying the different chemical states of Ga and As. The comparison of these spectra is shown in Figure 4.35.

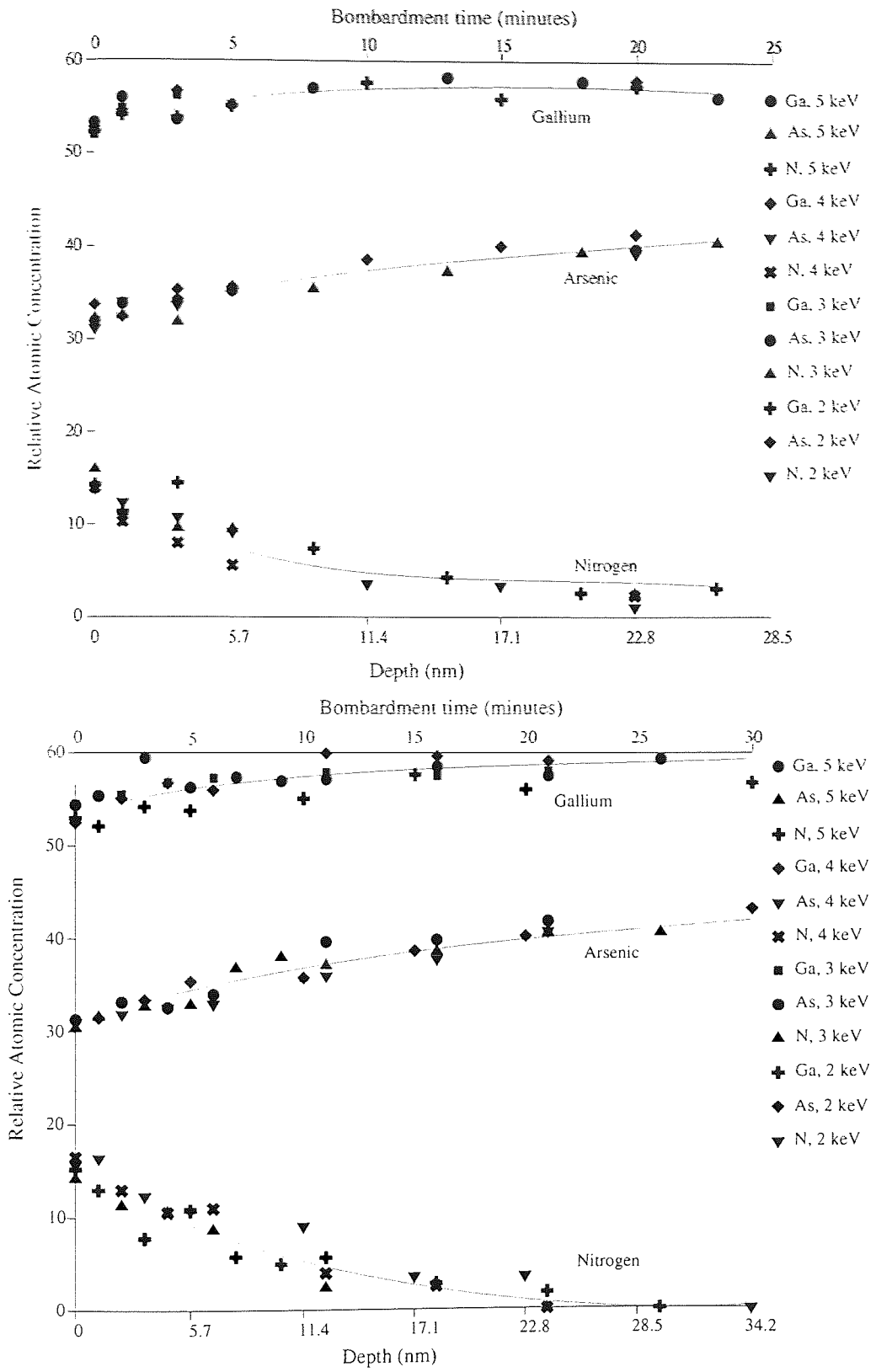


Figure 4.30 Nitrogen depth and time profile using Ar⁺ of energy 2keV and 2 μA/cm² after nitrogen implantation on GaAs at E = 2, 3, 4 and 5 keV at current densities of (a) μ = 1 μA/cm² and (b) μ = 5 μA/cm². The time scale is converted to the depth scale using the etch rate value calculated from SUSPRE.

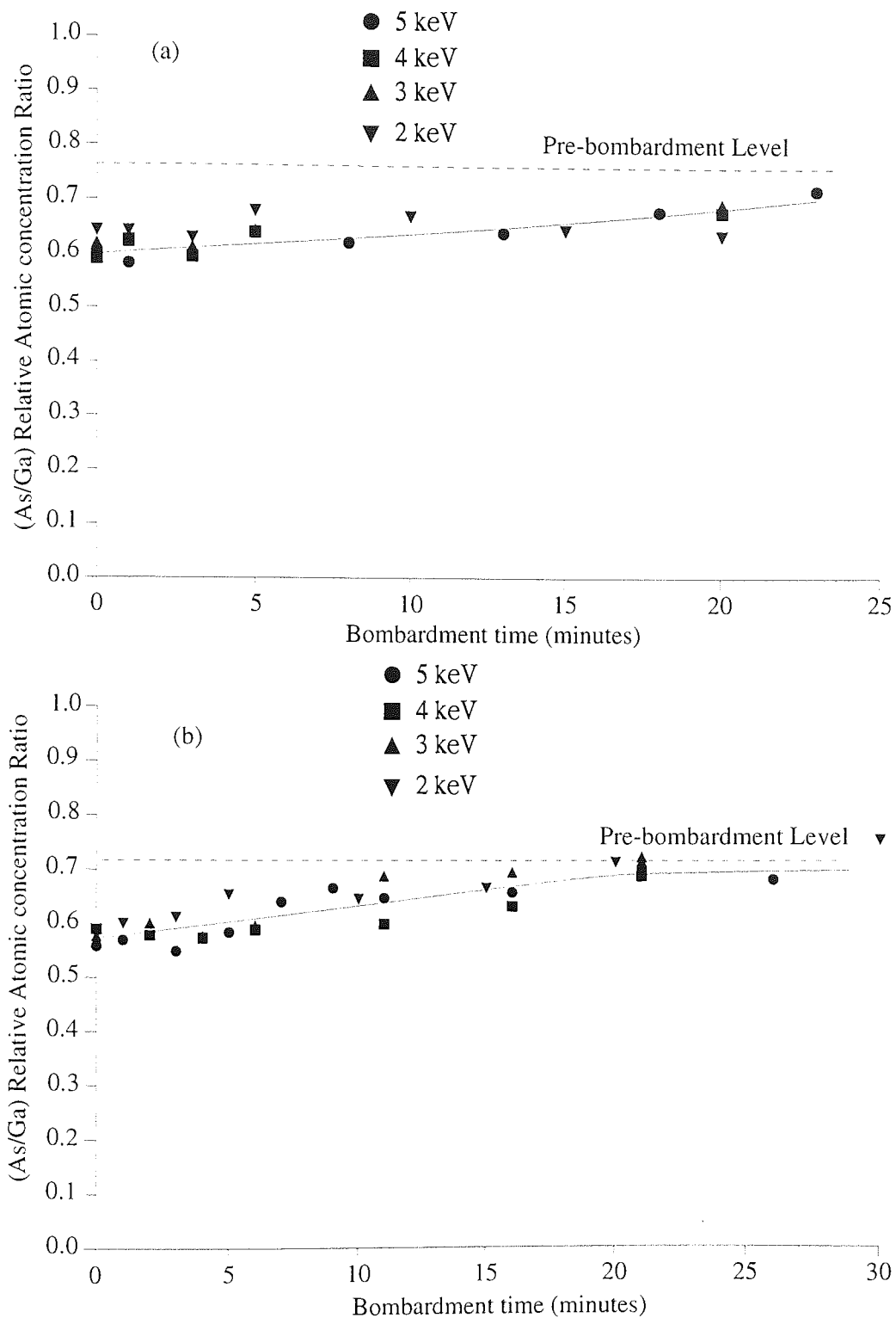


Figure 4.31 Variation of ratio of relative atomic concentration of arsenic and gallium, (As/Ga), as a function of Ar^+ bombardment time after N_2^+ implantation at 2, 3, 4 and 5 keV at current densities of (a) $1 \mu\text{A}/\text{cm}^2$ and (b) $5 \mu\text{A}/\text{cm}^2$.

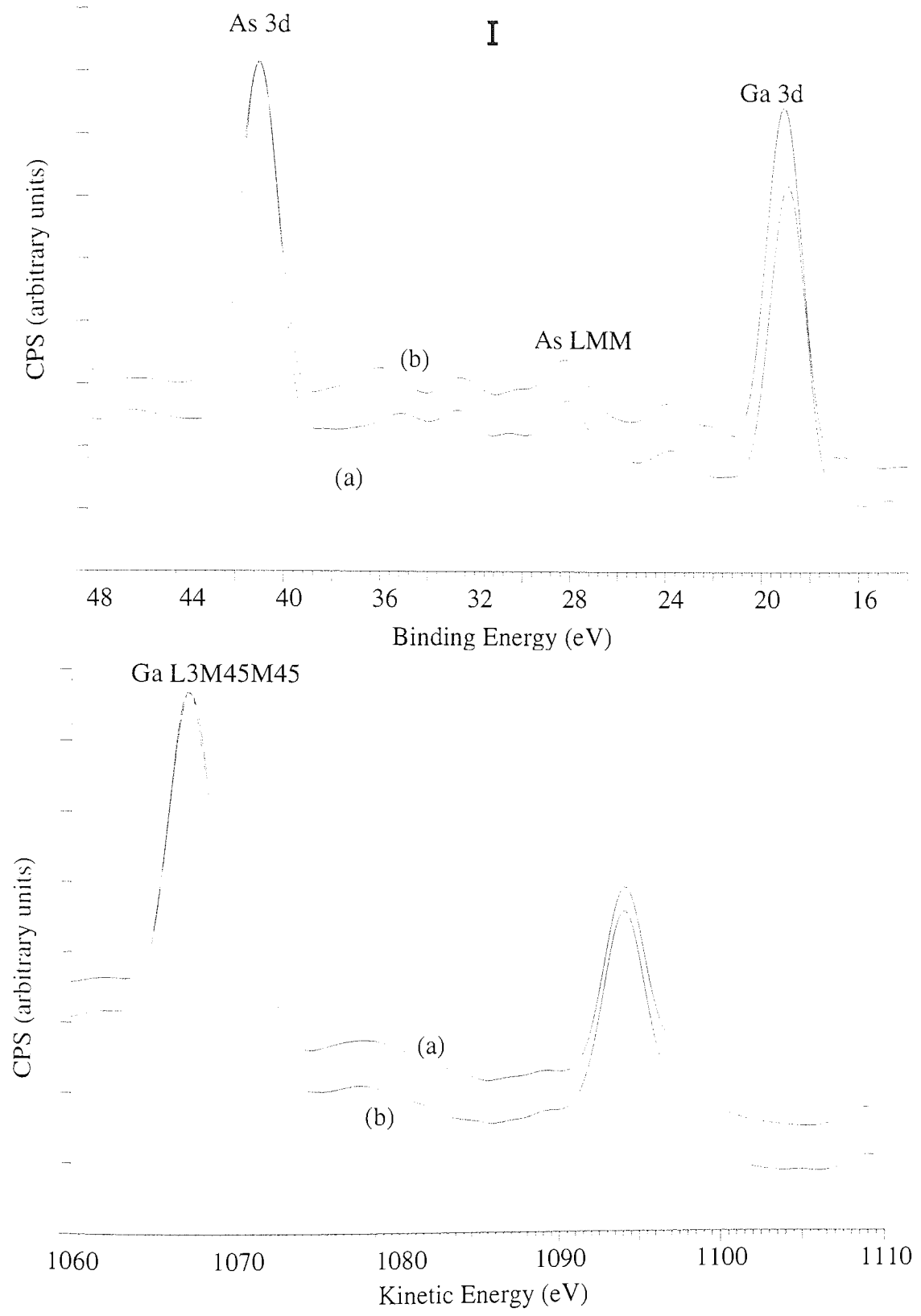
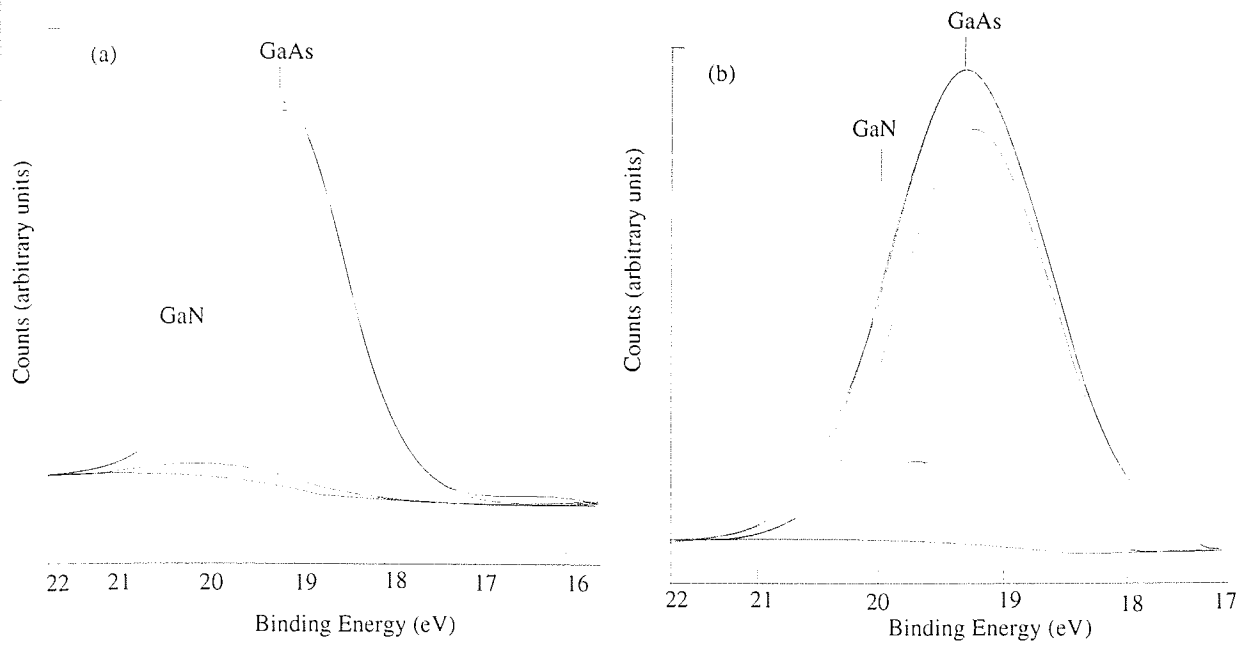


Figure 4.32 GaAs 3d and Auger spectra of (a) before and (b) after N_2^+ bombardment of GaAs sample. The spectra are normalized for comparison.



Peak	Centre (eV)	FWHM (eV)	Height (%)	G/L (%)	Area (%)
GaAs	19.0(19.2)	1.56(1.48)	78.3(69.3)	30	96.8(83.7)
GaN	19.5(19.7)	1.46(1.48)	2.8(19.7)	30	3.2(16.3)

Figure 4.33 Deconvolution of various chemical states in Ga 3d spectra, after (a) 1 minute and (b) 40 minutes of nitrogen ion bombardment at 2 keV and 5 $\mu\text{A}/\text{cm}^2$. The table gives the parameters chosen for peak fitting. The values outside the brackets are for case (a) and those inside the brackets are for case (b). The G/L ratio was same for both cases.

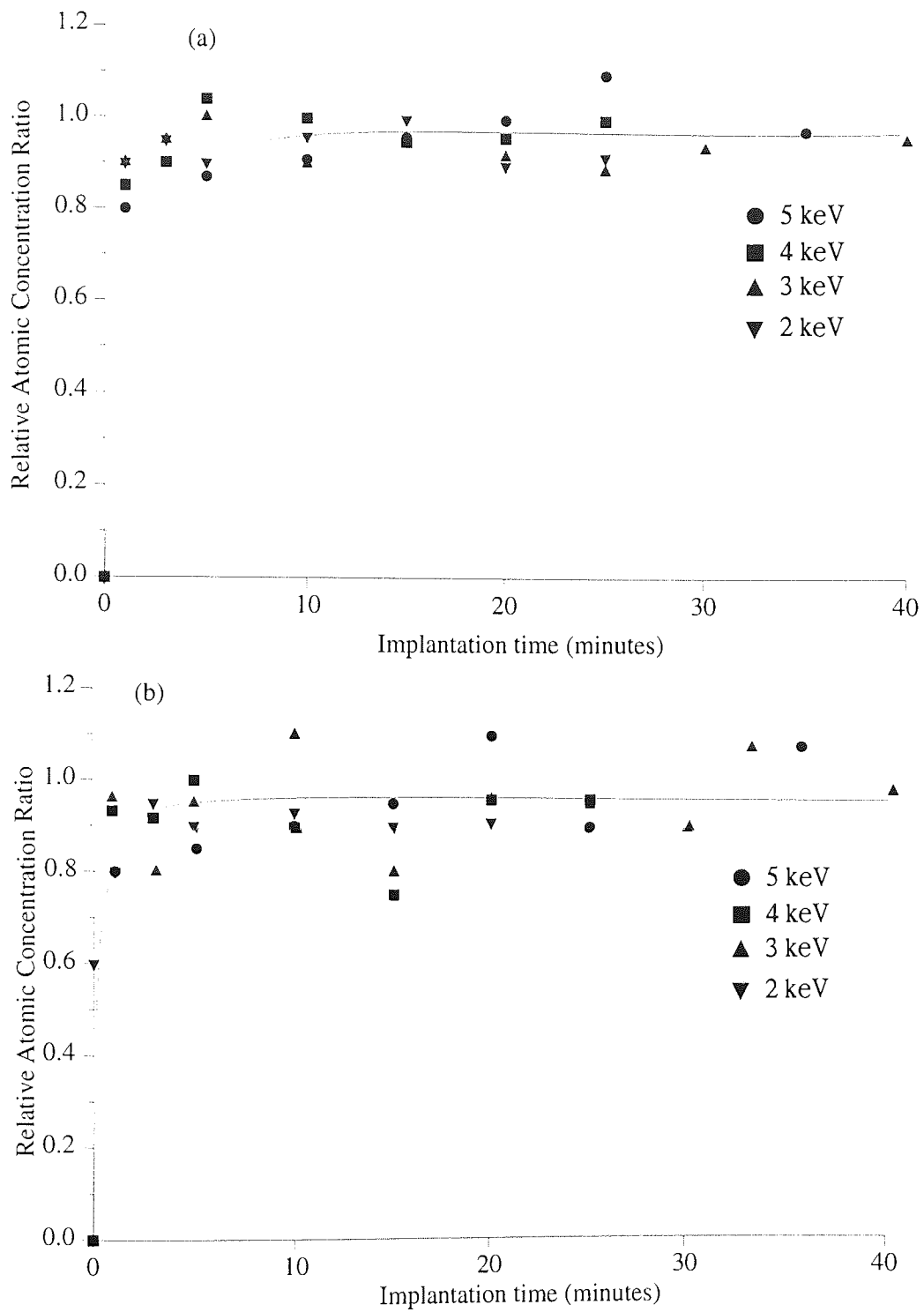


Figure 4.34 Variation of N/Ga(GaN) with the implantation time at 2, 3, 4 and 5 keV at current densities of (a) 1 $\mu\text{A}/\text{cm}^2$ and (b) 5 $\mu\text{A}/\text{cm}^2$.

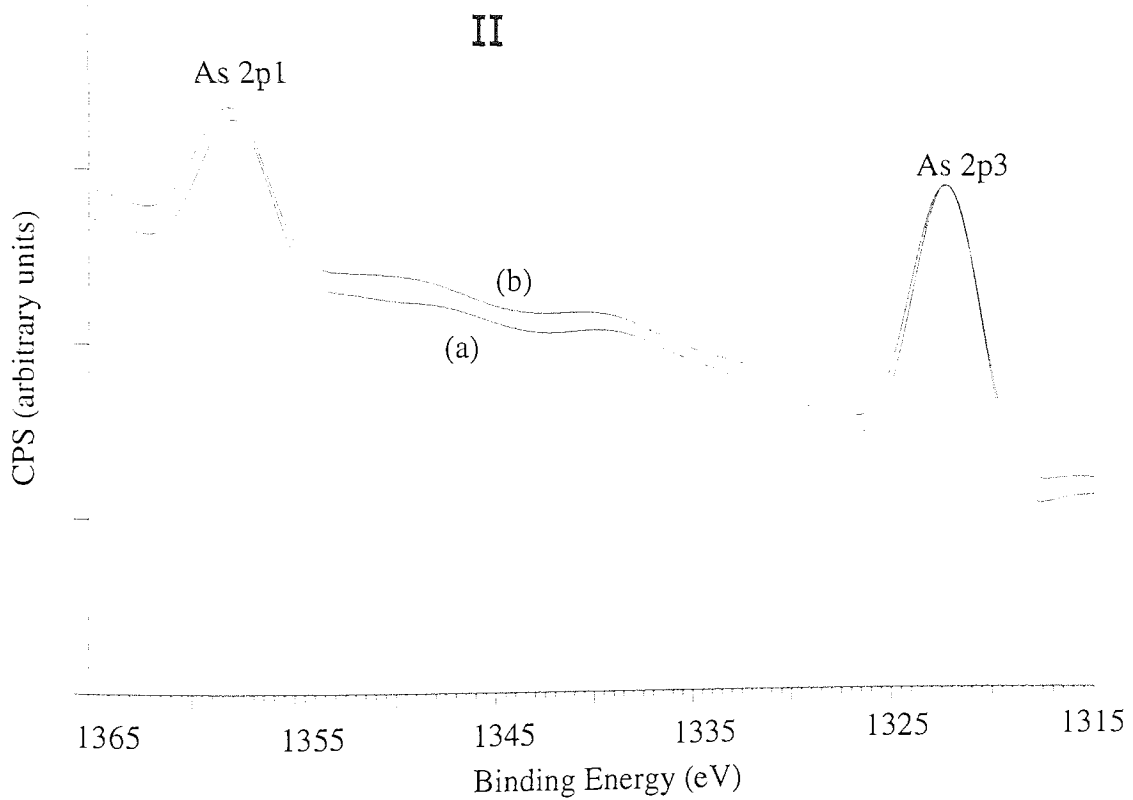
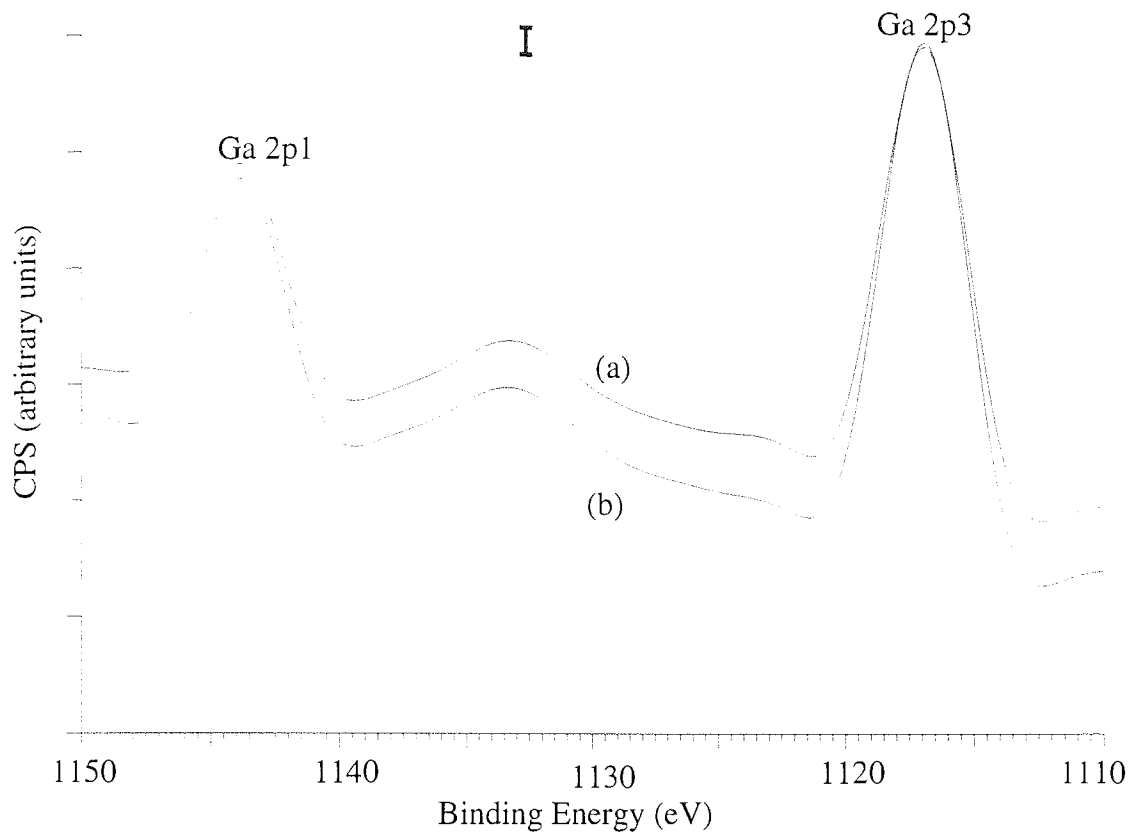


Figure 4.35 Ga 2p and As2p spectra of (a) before and (b) after N_2^+ ion bombardment of GaAs sample. The spectra are normalized for comparison.

The N 1s and Auger spectra of nitrogen is shown in Figure 4.36 and the values of binding energy of N 1s, the kinetic energy of the N KL₂₃L₂₃ line and Auger parameter are listed in Table 4.13. The value of Auger parameter reported for GaN [Hedman and Martesson, 1980] is higher than the same for nitrogen implanted in GaAs. The comparison of Valence band X-ray Photoelectron Spectra (VBXPS), before and after nitrogen ion bombardment is shown in Figure 4.37.

Table 4.11 The values of Ga 3d binding energies (eV) and Ga L₃M₄₅M₄₅ kinetic energies (eV) for as received, Ar⁺ ion cleaned, N₂⁺ bombarded, and then Ar⁺ bombarded GaAs are tabulated in first four rows. The last three rows show the value of the above mentioned parameters for pure Ga, GaAs and GaN.

	Ga 3d	Ga L ₃ M ₄₅ M ₄₅	Auger parameter
As received GaAs	19.3±0.1	1066.9±0.2	1086.2±0.3
After Ar ⁺ cleaning	19.1±0.1	1066.7±0.2	1085.8±0.3
N ₂ ⁺ bombarded GaAs	19.3±0.1	1066.6±0.2	1085.9±0.3
First N ₂ ⁺ and then, Ar ⁺ bombarded GaAs	18.9±0.1	1067.1±0.2	1086.0±0.3
Ga [Wagner, 1992]	18.67	1068.1	1086.8
GaAs [Wagner, 1992]	19.3	1066.3	1085.6
GaN [Wagner, 1992]	19.5	1064.5	1084.0

Table 4.12 The values of As 3d binding energies (eV) and As L₃M₄₅M₄₅ kinetic energies (eV) for as received, Ar⁺ ion cleaned, N₂⁺ bombarded, and then Ar⁺ bombarded GaAs are tabulated in first four rows. The last two rows show the value of the above mentioned parameters for pure As, and GaAs.

	As3d	As L ₃ M ₄₅ M ₄₅	Auger parameter
As received GaAs	41.1±0.1	1225.3±0.2	1266.4±0.3
After Ar ⁺ cleaning	41.1±0.1	1224.6±0.2	1265.7±0.3
N ₂ ⁺ bombarded GaAs	41.1±0.1	1224.9±0.2	1266.0±0.3
First N ₂ ⁺ and then, Ar ⁺ bombarded GaAs	41.0±0.1	1225.5±0.2	1265.5±0.3
As [Wagner, 1992]	41.5	1225.0	1266.5
GaAs [Wagner, 1992]	41.2	1225.0	1266.2

Table 4.13 The values of N 1s binding energies (eV) and KL₂₃L₂₃ kinetic energies (eV) for N₂⁺ bombarded GaAs, along with the values of Auger parameter.

	N 1s	N KL ₂₃ L ₂₃	Auger parameter
N ₂ ⁺ bombarded GaAs	396.9±0.2	383.9±0.2	780.8±0.4
GaN [Hedman and Martesson, 1980]	397	385	782

4.1.5.4 ARXPS results:

The ARXPS results for the nitrogen ion implantation are shown in Table 4.14. The relative concentration of nitrogen on the surface, is lower in almost all the cases as compared to the same measured from the bulk. The N 1s peak position was same at all angles, suggesting the presence of nitrogen in the same chemical state at the analysed depths.

4.1.6 AlGaAs:

4.1.6.1 Nitrogen implantation:

Figures 4.38 and 4.39 show the concentration profiles of relative atomic concentrations of aluminium, gallium, arsenic and nitrogen as a function of time of implantation, for implantation at current densities of 1 μA/cm² and 5 μA/cm², respectively. From this figure, it may be seen that as the implantation proceeds, the nitrogen concentration increases to a saturation value and the concentrations of gallium, arsenic and aluminium fall slightly and then remain almost constant. The ratio of relative atomic concentration of nitrogen and the sum of that for aluminium, gallium and arsenic is plotted as a function of implantation time in Figure 4.40. The relative atomic concentration ratios of nitrogen to aluminium, gallium and arsenic is shown in Figure 4.41 for implantation at 5 μA/cm². The general trend is an increase in all the considered relative atomic ratios with increase in implantation time and eventual saturation, as expected. Figure 4.42 shows that the extent of As depletion is not a function of ion energy. However As depletion increases with increasing ion bombardment time.

4.1.6.2 Argon ion bombardment:

The Ar⁺ bombardment profiles of relative atomic concentration of N, Ga and As in the sample

surfaces are shown in Figure 4.43 for implantation at current densities of 1 $\mu\text{A}/\text{cm}^2$ and 5 $\mu\text{A}/\text{cm}^2$

Table 4.14 ARXPS data of nitrogen ion implantation in GaAs, at various ion energies and current densities.

Energy (keV)	Current Density ($\mu\text{A}/\text{cm}^2$)	TOA	Relative atomic Concentration			N/(Ga+As)
			N (%)	As (%)	Ga (%)	
5	5	0	17.2	31.1	51.7	0.21
		33	13.1	32.1	54.8	0.15
		45	14.6	30.3	55.1	0.17
		54	14.8	31	54.2	0.17
		60	13.7	31.8	54.5	0.16
4	5	0	16.8	31.1	52.1	0.20
		33	14.8	31.1	54.1	0.17
		45	13.3	32.1	54.6	0.15
		54	13.7	31.8	54.5	0.16
		60	13.1	32.2	54.7	0.15
3	5	0	16.3	30.5	53.2	0.19
		33	14.2	31.2	54.6	0.17
		45	13.7	31.4	54.9	0.16
		54	10.8	32.5	56.7	0.12
		60	10.2	32.7	57.1	0.11
2	5	0	13.9	31.4	54.7	0.16
		33	15.6	30.8	53.6	0.18
		45	14.4	30.8	54.8	0.17
		54	14.6	31.6	53.8	0.17
		60	13.7	32	54.3	0.16
5	1	0	15.7	32.1	52.2	0.19
		33	10.9	32.4	56.7	0.12
		45	14.2	32	53.7	0.17
		54	15.3	31.4	53.3	0.18
		60	12.2	31.9	55.9	0.14
4	1	0	14.1	32.7	53.2	0.16
		33	12	31.8	56.2	0.14
		45	13.4	31.9	54.7	0.15
		54	12.9	32.1	55	0.15
		60	10.8	32.2	57	0.12
3	1	0	13	32.5	54.5	0.15
		33	12.8	31.2	56	0.15
		45	9.5	32.4	58.1	0.10
		54	11.7	31.6	56.7	0.13
		60	11.2	31.6	57.2	0.13
2	1	0	13.1	33.5	53.4	0.15
		33	13.2	32.6	54.2	0.15
		45	12.2	32.9	54.9	0.14
		54	13.8	33.1	53.1	0.16
		60	9.9	35	55.1	0.11

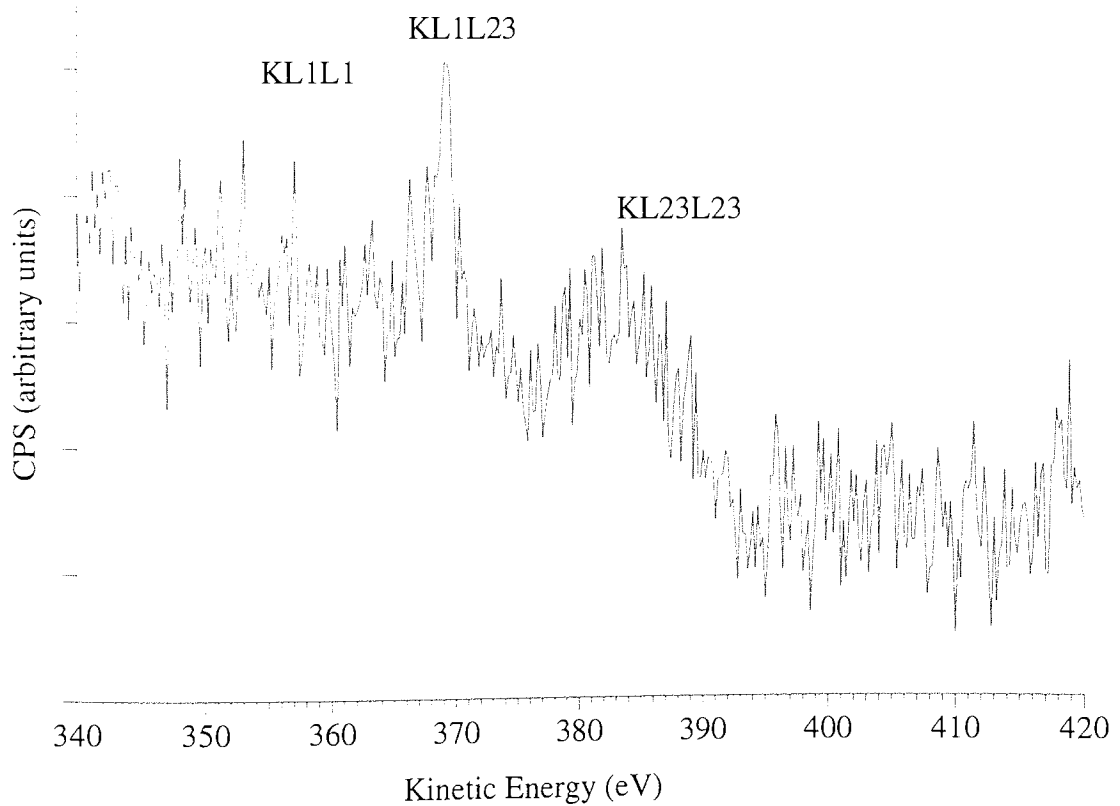
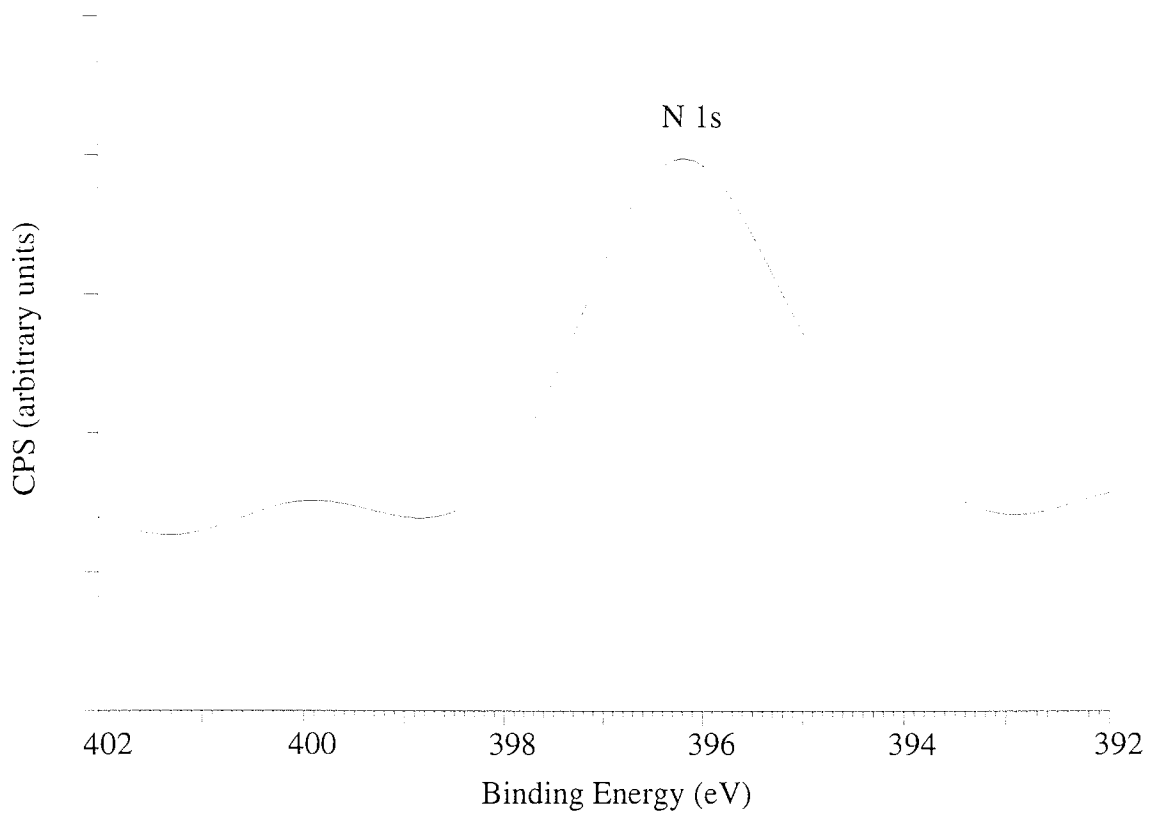


Figure 4.36 N 1s and Auger spectra of nitrogen obtained from nitrogen ion bombarded GaAs sample.

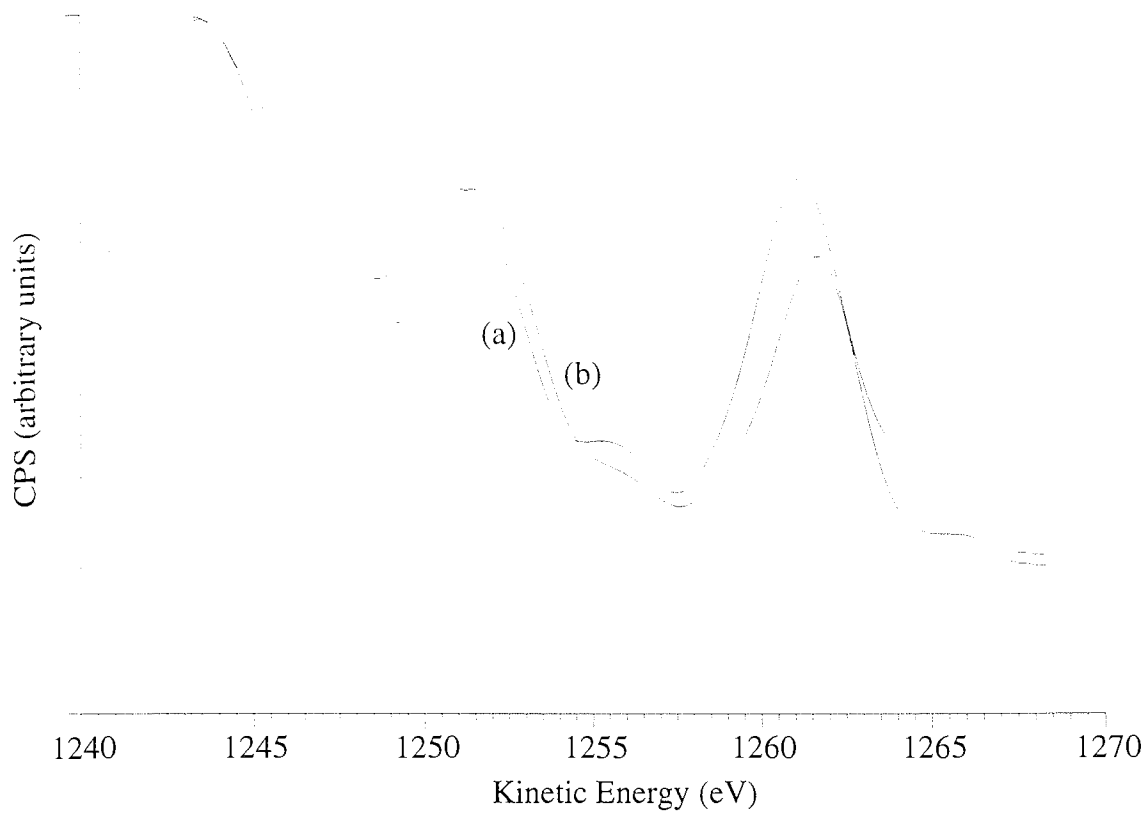


Figure 4.37 GaAs Valence Band X-ray Photoelectron Spectra (VBXPS) of (a) before and (b) after N_2^+ ion bombardment of GaAs sample. The spectra are normalized for comparison.

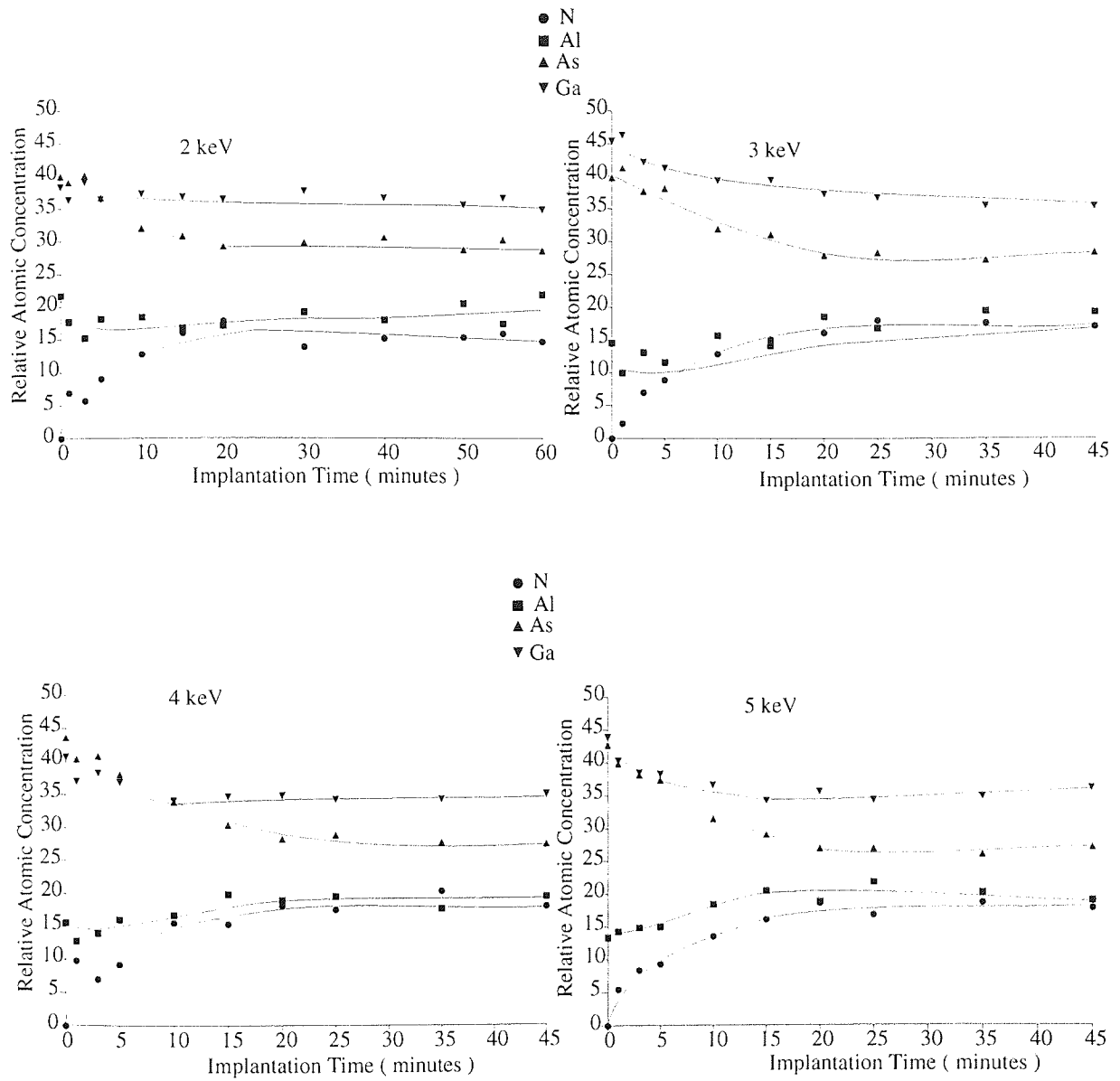


Figure 4.38 XPS time profile of nitrogen ion implantation in AlGaAs at 2, 3, 4 and 5 keV at a current density of $1 \mu\text{A}/\text{cm}^2$.

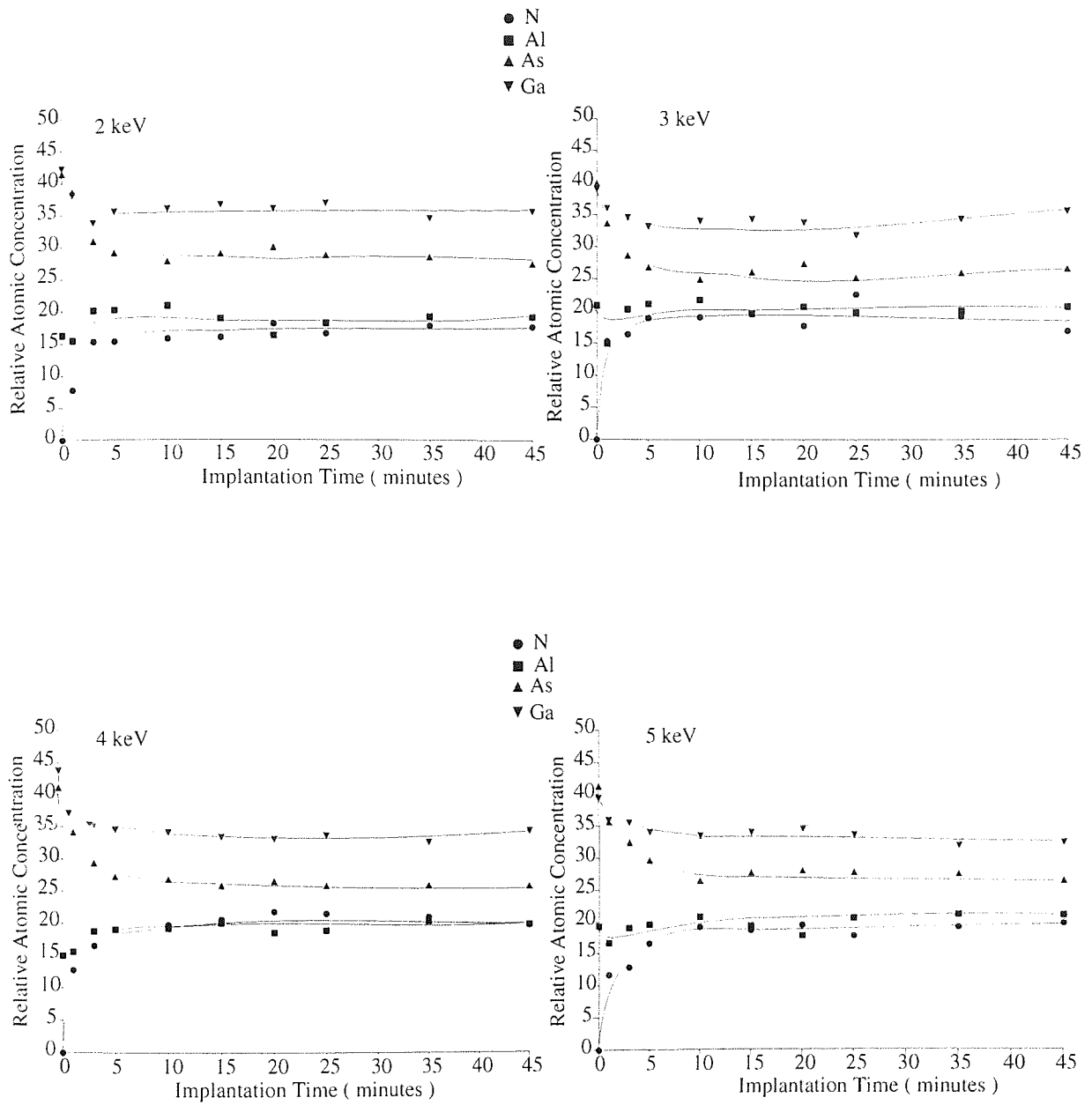


Figure 4.39 XPS time profile of nitrogen ion implantation in AlGaAs at 2, 3, 4 and 5 keV at a current density of $5 \mu\text{A}/\text{cm}^2$.

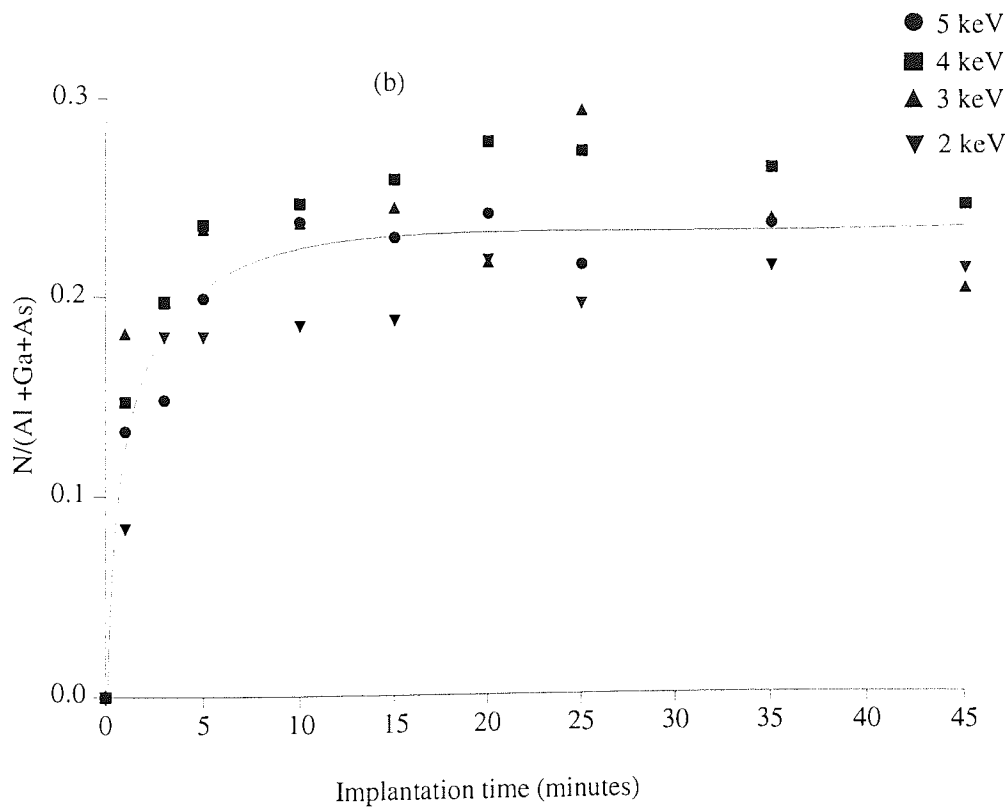
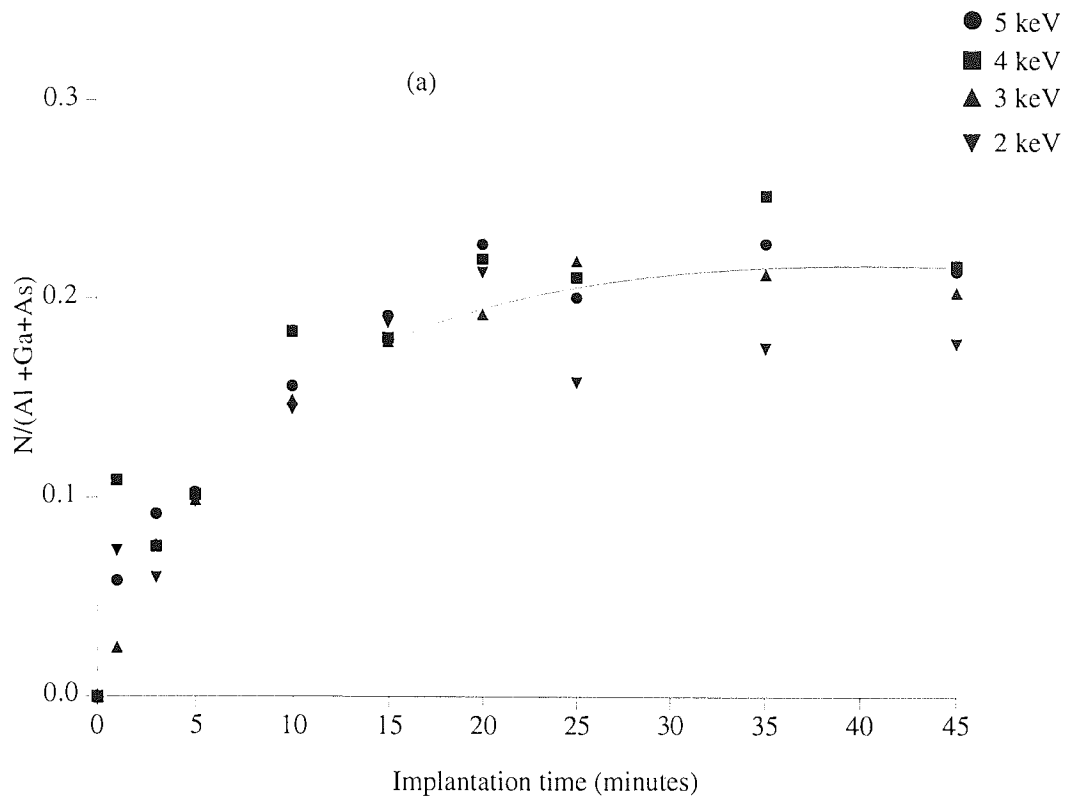


Figure 4.40 Variation of ratio of relative atomic concentration of nitrogen and the sum of that for aluminium, gallium and arsenic $[N/(Al+Ga+As)]$ as a function of implantation time at 2, 3, 4 and 5 keV at current densities of (a) $1 \mu A/cm^2$ and (b) $5 \mu A/cm^2$.

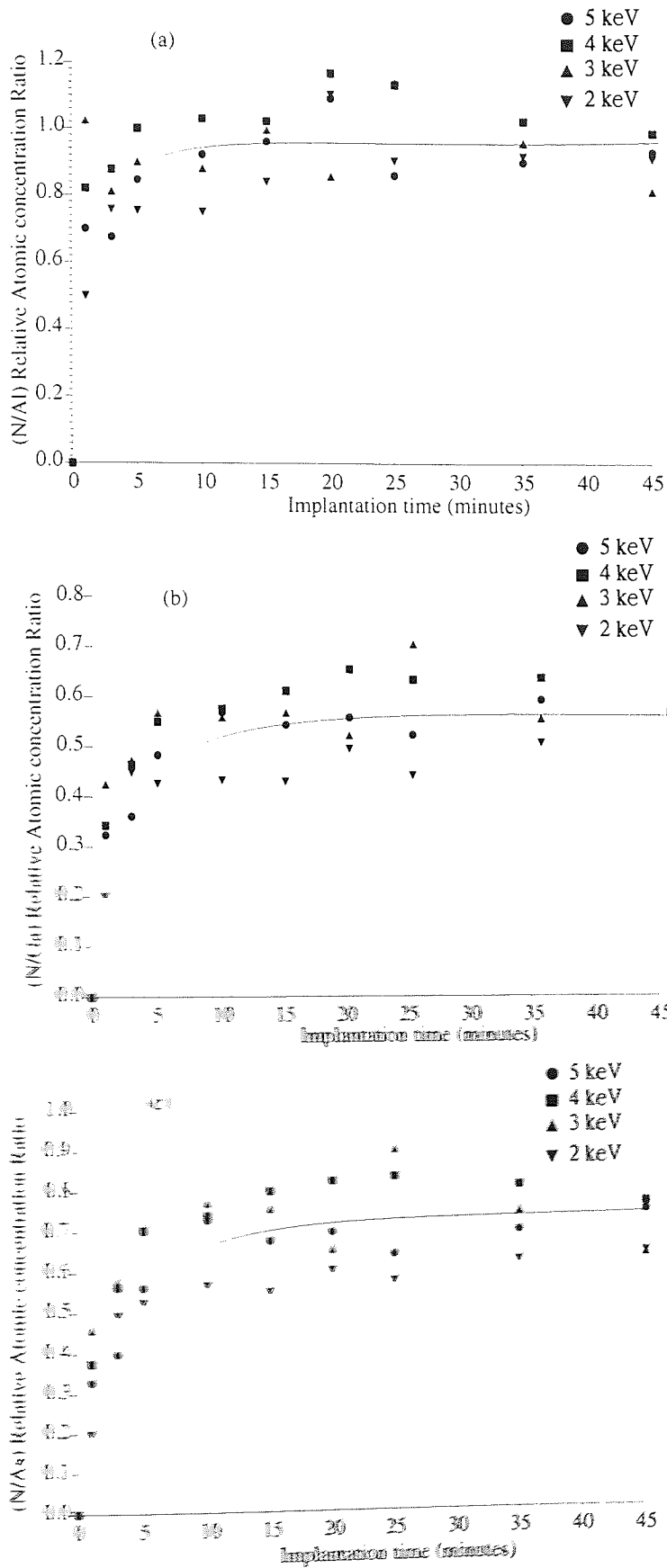


Figure 4.41 Variation of ratio of relative atomic concentration ratio of implantant and target atoms, as a function of N_2^- bombardment time, for implantation at $\mu = 5 \mu A/cm^2$.

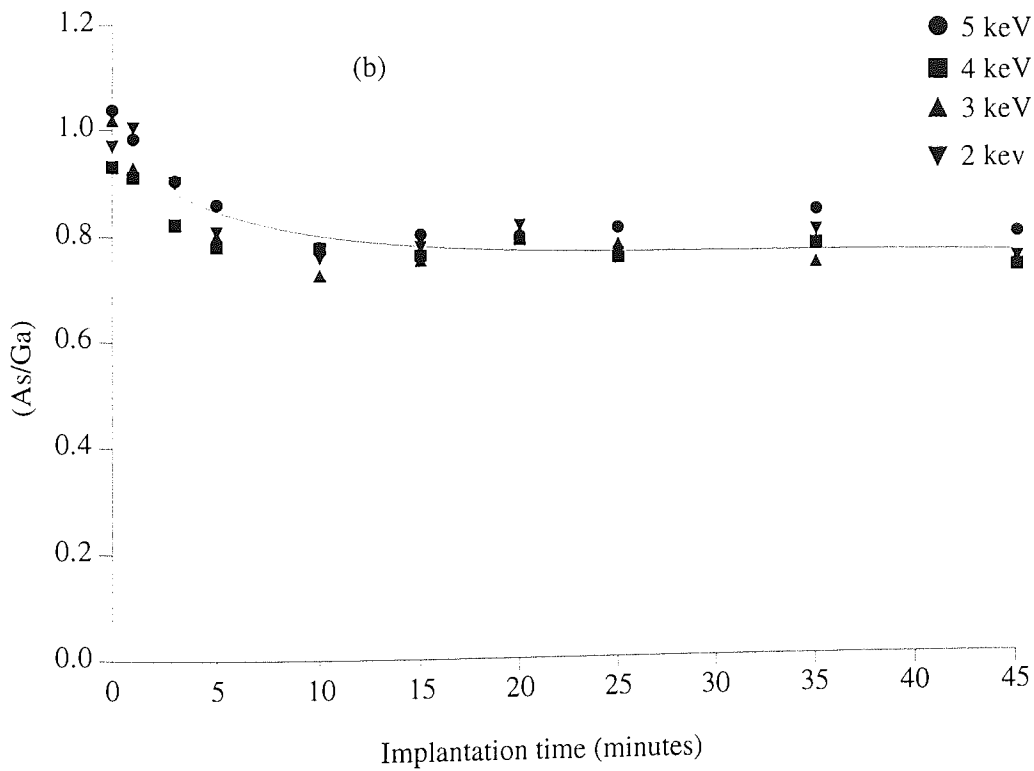
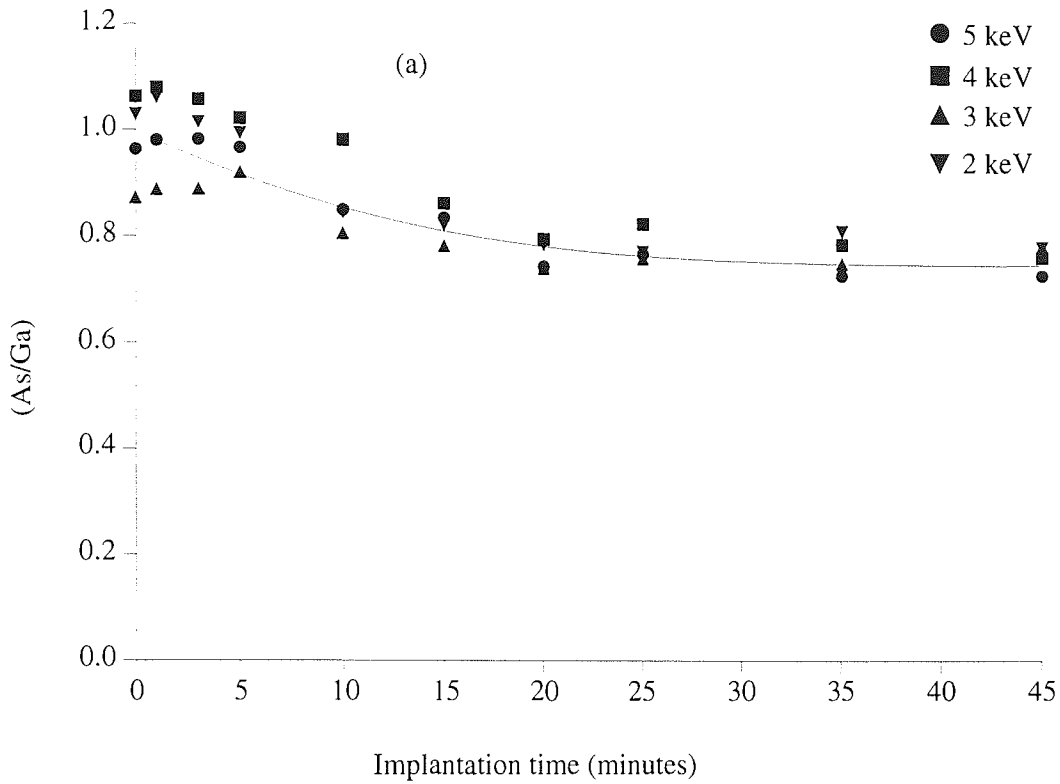


Figure 4.42 Variation of ratio of relative atomic concentration of arsenic and gallium, (As/Ga), as a function of implantation time at 2, 3, 4 and 5 keV at current densities of (a) $1 \mu\text{A}/\text{cm}^2$ and (b) $5 \mu\text{A}/\text{cm}^2$.

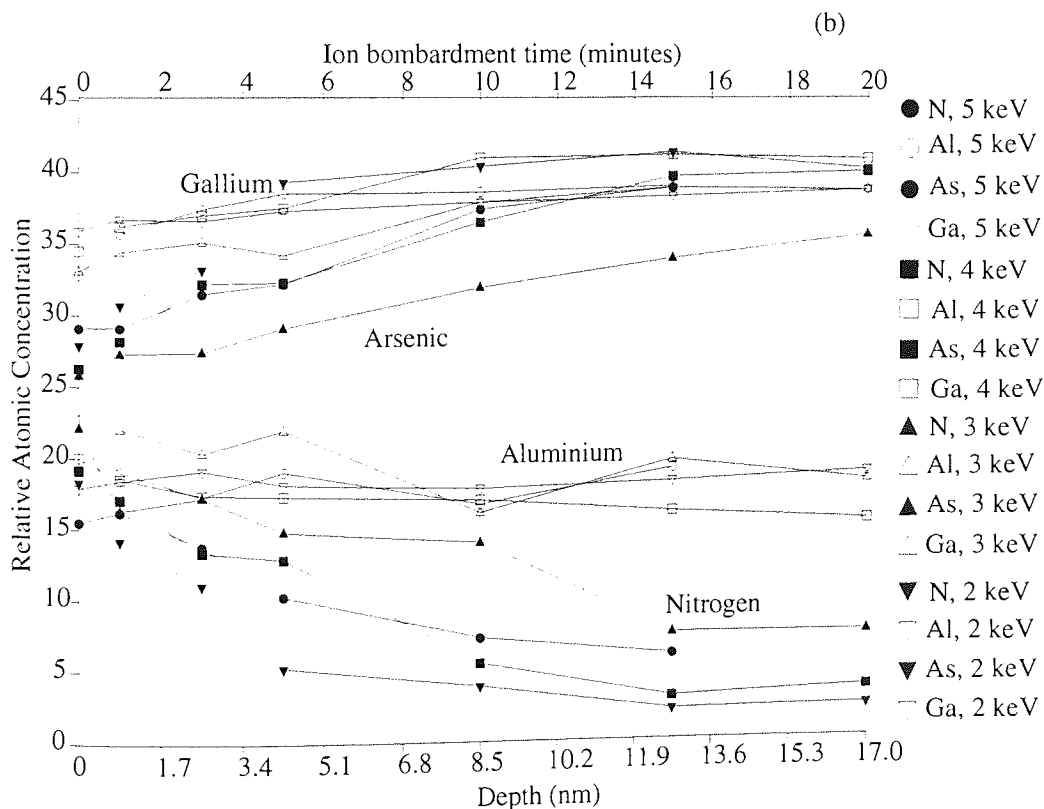
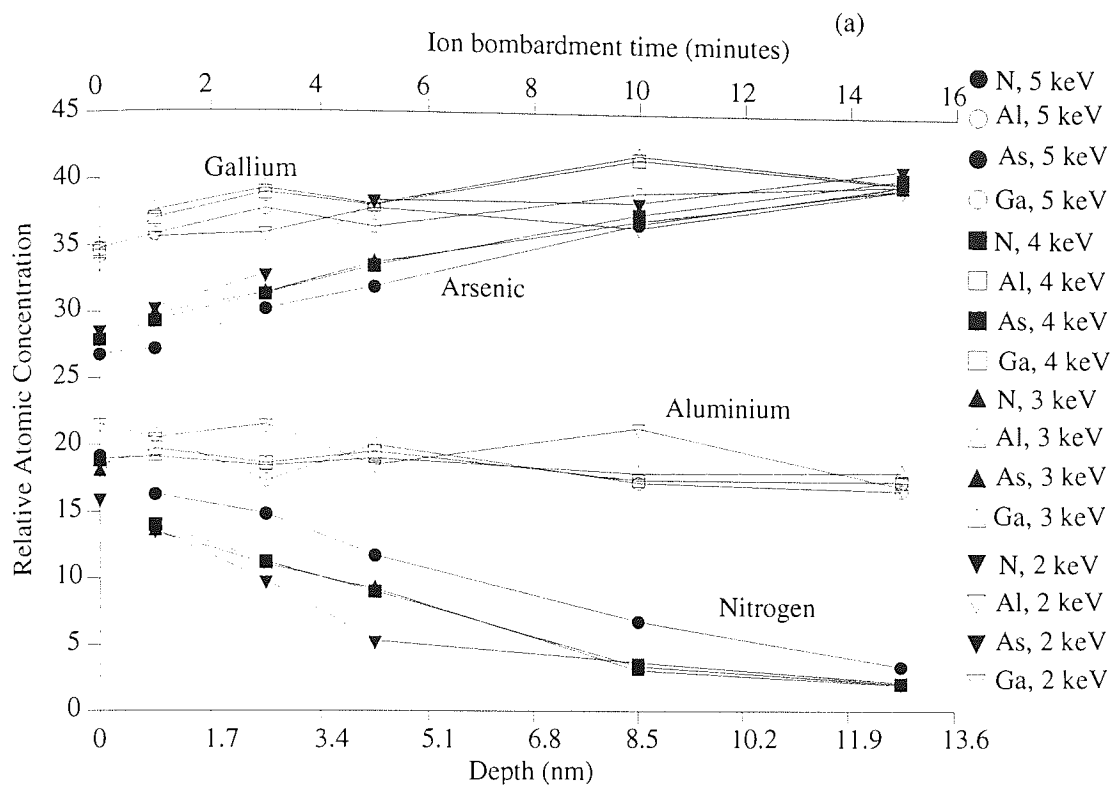


Figure 4.43 Nitrogen depth and time profile using Ar^+ of energy 2 keV and $2 \mu\text{A}/\text{cm}^2$ after nitrogen implantation on AlGaAs at $E = 2, 3, 4$ and 5 keV and current densities of (a) $\mu = 1 \mu\text{A}/\text{cm}^2$ and (b) $\mu = 5 \mu\text{A}/\text{cm}^2$. The time scale is converted to the depth scale using the etch rate value calculated from SUSPRE.

cm², respectively. Relative atomic concentrations in these profiles are actually measured as a function of time. The time axis is converted into depth scale using the etch rate value of 0.014nm/s, calculated from SUSPRE [Webb, 1992]. The error in the calculated depth could be upto 3. However the differences in the error for profiles at different implantation energies will be smaller. Hence one can still use this for the purpose of comparison of profiles. Figure 4.44 shows the target to implantant ratio, $[N/(Al+Ga+As)]$, as a function of bombardment time. The As/Ga relative atomic concentration ratios are plotted as a function of bombardment time for N₂⁺ implantation at current densities of 1 μA/cm² and 5 μA/cm², in Figure 4.45. Clearly the As/Ga ratios increase with the increase in ion bombardment time.

4.1.6.3 AlGaAs spectra:

Figure 4.46 shows a comparison of Al 2p, GaAs 3d and As L₃M₄₅M₄₅, before and after nitrogen ion bombardment. The comparison of Valence band X-ray Photoelectron Spectra (VBXPS) and Ga L₃M₄₅M₄₅ spectra, before and after nitrogen ion bombardment is shown in Figure 4.47. The Ga 3d peak broadens and shifts to higher binding energy, while the As 3d peak position and width remains almost unchanged. The separation between Ga and As 3d changes from 22.0 eV to 21.7 eV. The Auger spectra of Ga and As did not show any appreciable change in peak position or peak shape.

The values of binding energy of Ga 3d, the kinetic energy of the Ga L₃M₄₅M₄₅ line and Auger parameter are shown in Table 4.15, for AlGaAs sample, after Ar⁺ ion cleaning, after nitrogen ion bombardment and then Ar⁺ bombardment. The values of the same for pure Ga, GaAs, AlGaAs and standard mixture of GaN are also reported. The values of binding energy of As 3d, the kinetic energy of the As L₃M₄₅M₄₅ line and Auger parameter are shown in Table 4.16, for AlGaAs sample, after Ar⁺ ion cleaning, after nitrogen ion bombardment and then Ar⁺ bombardment. Table 4.17 enlists the values of binding energy of Al 2p, the kinetic energy of the Al KLL line and Auger parameter, for AlGaAs sample after Ar⁺ ion cleaning, after nitrogen ion bombardment and then Ar⁺ bombardment. The same for Al, AlGaAs and AlN are also reported.

The N 1s and Auger spectra of nitrogen is shown in Figure 4.48 and the values of binding energy of N 1s, the kinetic energy of the N KL₂₃L₂₃ line and Auger parameter are listed in Table 4.18. ARXPS results show that the peak positions for all the above mentioned peaks, at all values of electron take-off-angles, were same, hence suggesting the nitrogen was in same chemical state at all the depths.

4.1.6.4 ARXPS results:

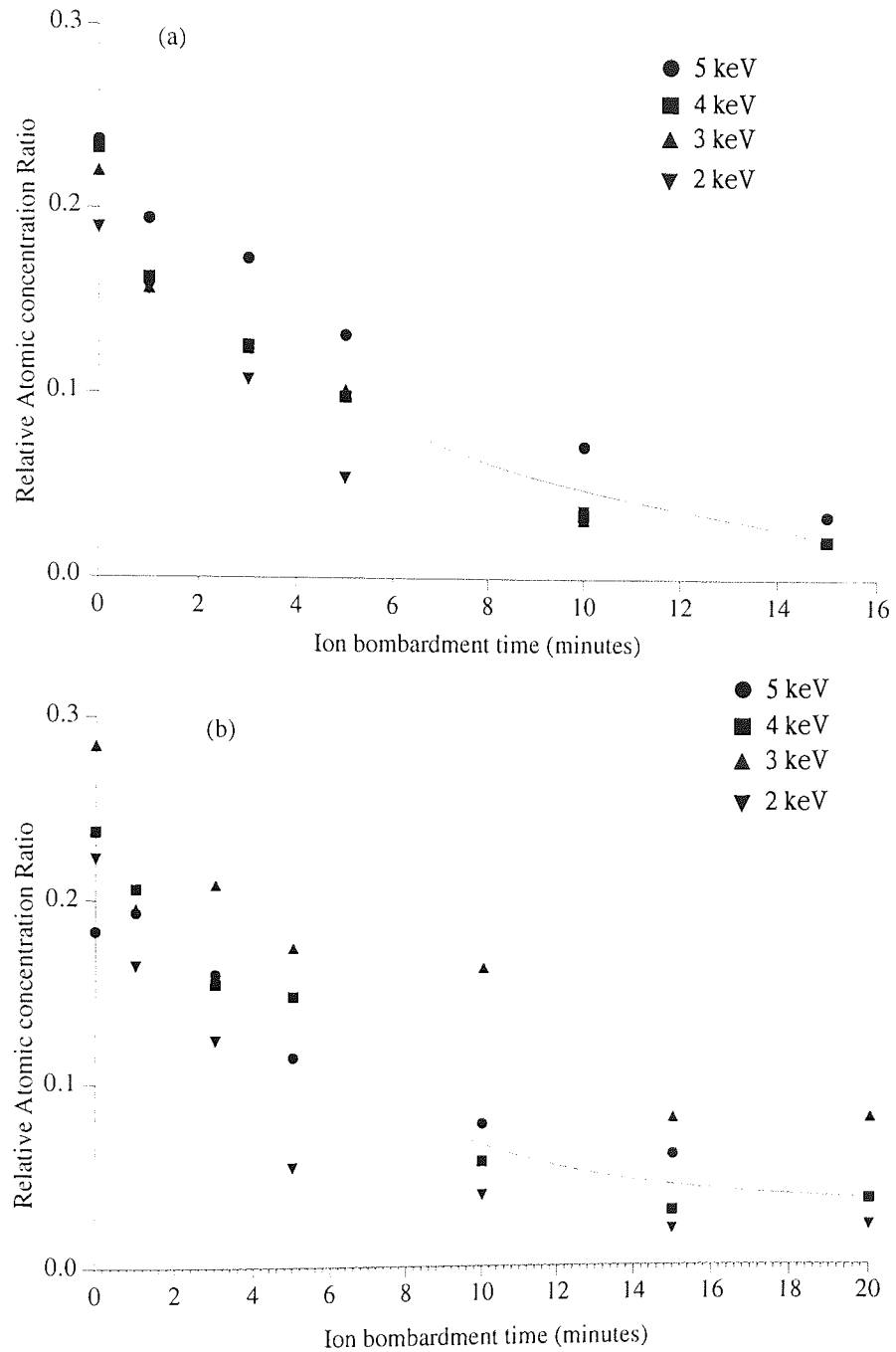


Figure 4.44 Variation of ratio of relative atomic concentration ratio of implantant and target, $N/(Al+Ga+As)$, as a function of Ar^+ bombardment time, after nitrogen implantation on AlGaAs at $E = 2, 3, 4$ and 5 keV and current densities of (a) $\mu = 1 \mu A/cm^2$ and (b) $\mu = 5 \mu A/cm^2$.

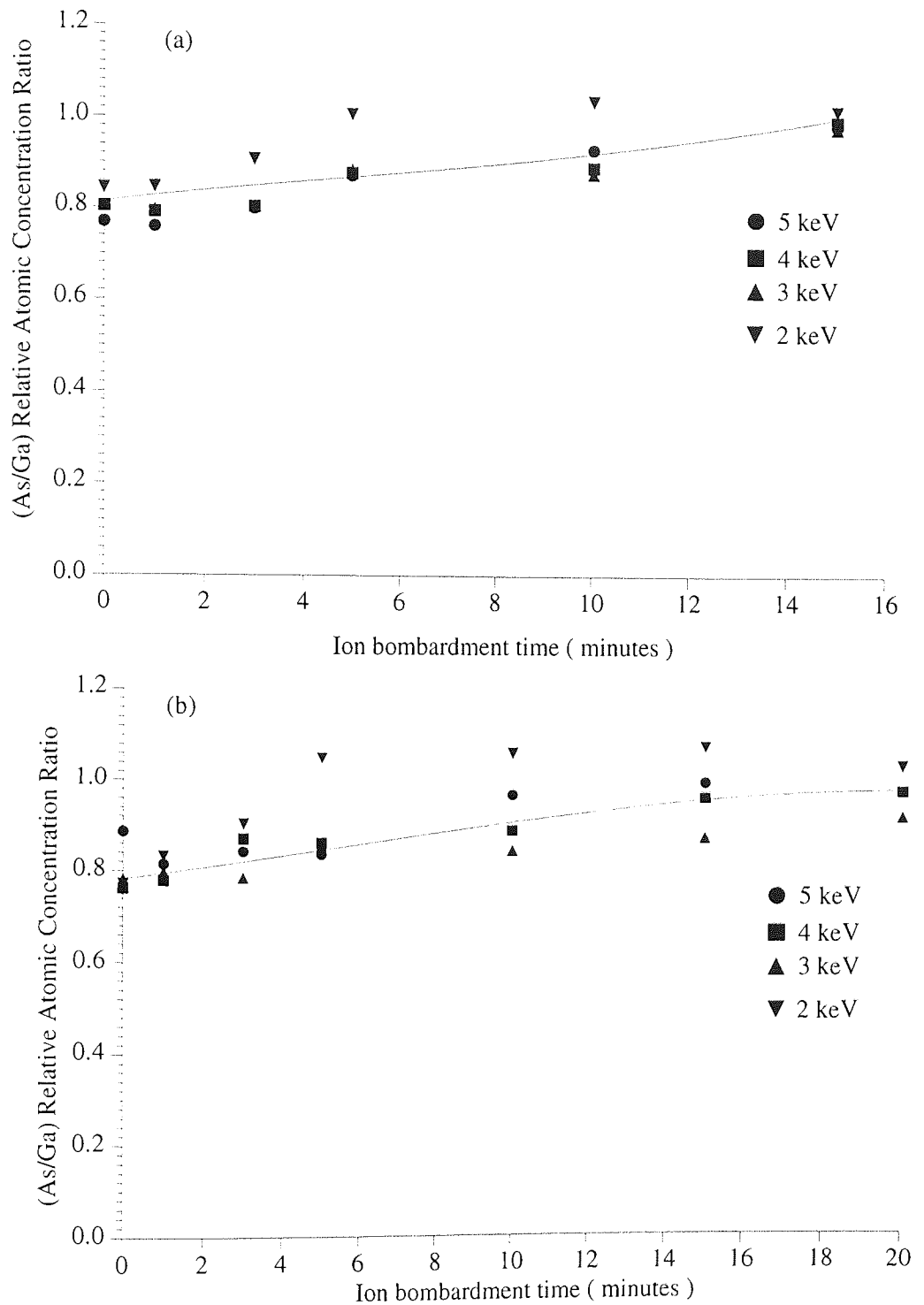


Figure 4.45 Variation of ratio of relative atomic concentration of arsenic and gallium, (As/Ga) , as a function of Ar^+ bombardment time, after nitrogen implantation at 2, 3, 4 and 5 keV at current densities of (a) $1 \mu A/cm^2$ and (b) $5 \mu A/cm^2$.

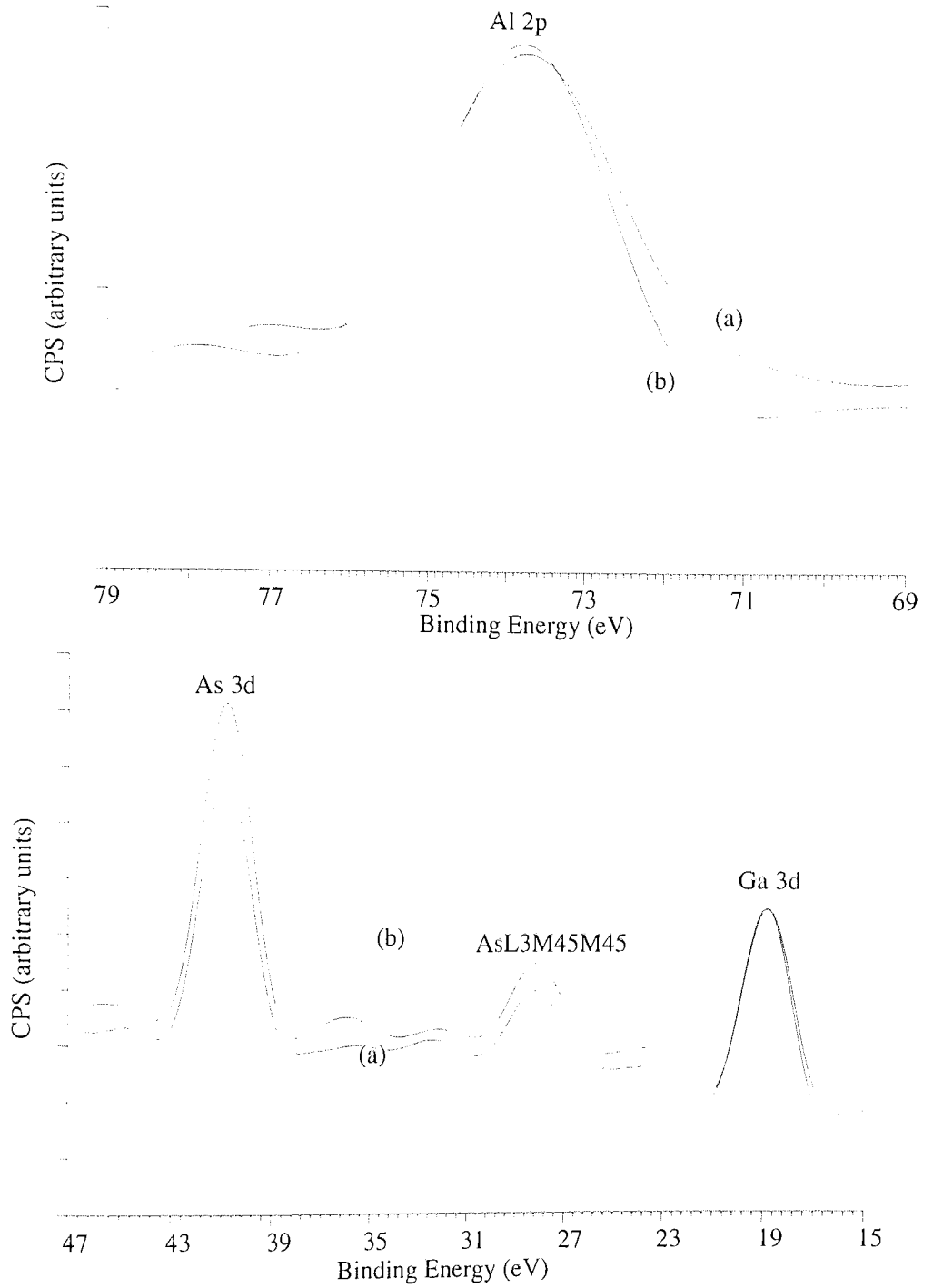


Figure 4.46 Comparison of Al 2p, GaAs 3d and As $L_3M_{45}M_{45}$ spectra of (a) before and (b) after N_2^+ ion bombardment of AlGaAs sample.

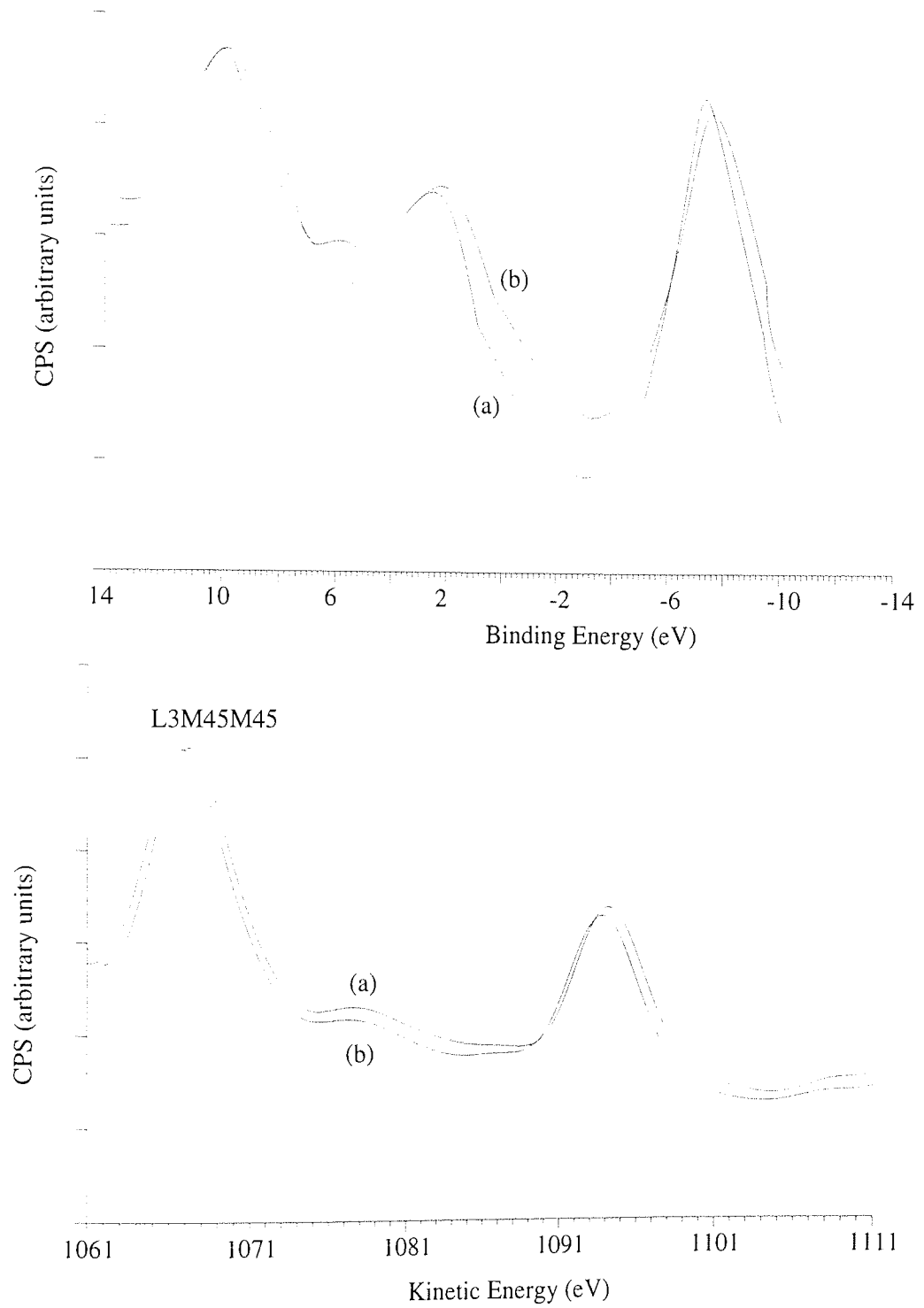


Figure 4.47 Comparison of AlGaAs Valence band and Ga Auger spectra of (a) before and (b) after N_2^+ ion bombardment of AlGaAs sample.

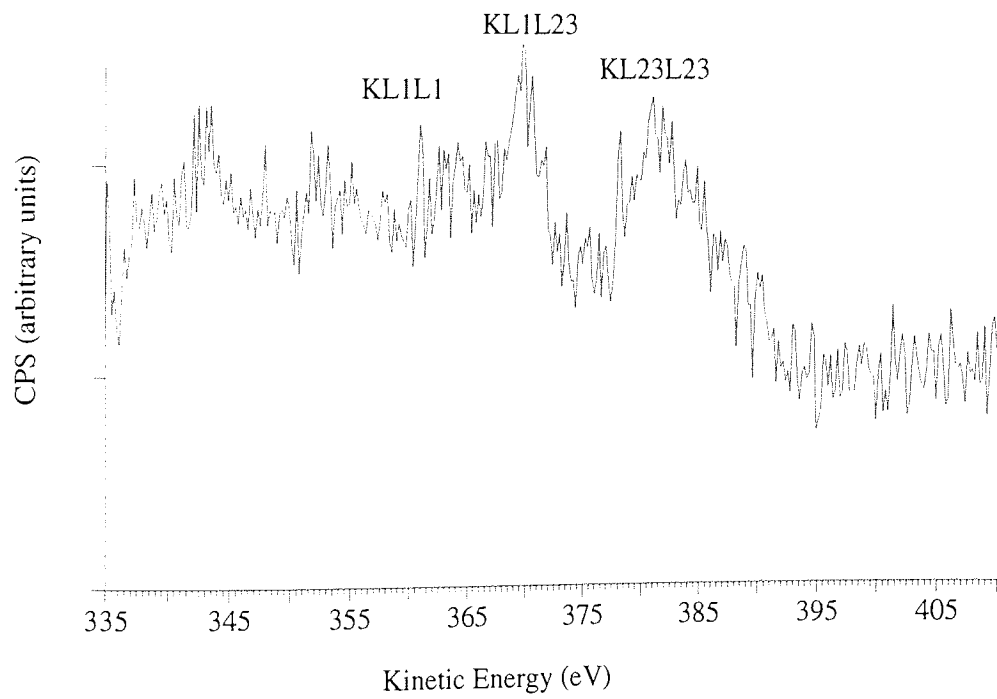
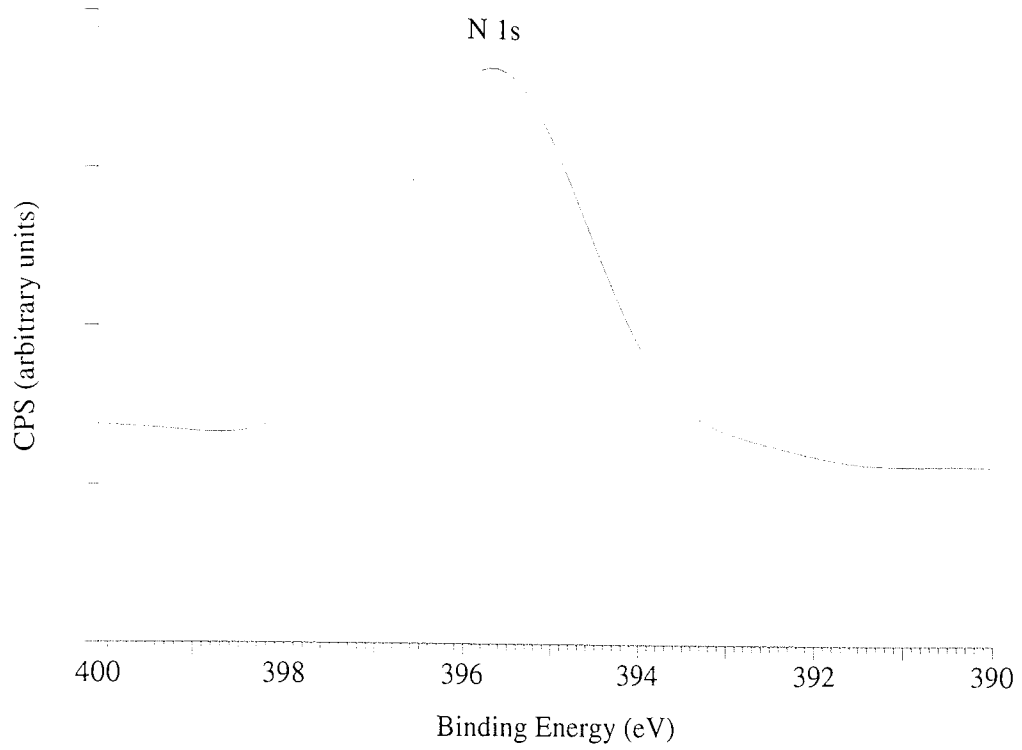


Figure 4.48 N 1s and Auger spectra of nitrogen obtained from nitrogen ion bombarded AlGaAs sample.

Table 4.15 The values of Ga 3d binding energies (eV) and Ga $L_3M_{45}M_{45}$ kinetic energies (eV) for Ar⁺ ion cleaned, N₂⁺ bombarded, and then Ar⁺ bombarded AlGaAs are tabulated in first four rows. The last three rows show the value of the above mentioned parameters for pure Ga, GaAs and AlGaAs and GaN.

	Ga 3d	Ga $L_3M_{45}M_{45}$	Auger parameter
As received AlGaAs	19.1±0.1	1066.5±0.2	1085.6±0.3
N ₂ ⁺ bombarded AlGaAs	19.3±0.1	1066.7±0.2	1086.0±0.3
First N ₂ ⁺ and then, Ar ⁺ bombarded AlGaAs	19.2±0.1	1066.7±0.2	1085.9±0.3
Ga [Wagner, 1992]	18.7	1068.1	1086.8
GaAs [Wagner, 1992]	19.3	1066.3	1085.6
AlGaAs [Wagner, 1992]	19.0	no data	no data
GaN [Wagner, 1992]	19.5	1064.5	1084.0

Table 4.16 The values of As 3d binding energies (eV) and As $L_3M_{45}M_{45}$ kinetic energies (eV) for Ar⁺ ion cleaned, N₂⁺ bombarded, and then Ar⁺ bombarded AlGaAs are tabulated in first four rows. The last two rows show the value of the above mentioned parameters for pure As, GaAs and AlGaAs.

	As3d	As $L_3M_{45}M_{45}$	Auger parameter
After Ar ⁺ cleaning	41.0±0.1	1225.1±0.2	1266.1±0.3
N ₂ ⁺ bombarded AlGaAs	41.0±0.1	1225.0±0.2	1266.0±0.3
First N ₂ ⁺ and then, Ar ⁺ bombarded AlGaAs	41.0±0.1	1225.1±0.2	1266.1±0.3
As [Wagner, 1992]	41.5	1225.0	1266.5
GaAs [Wagner, 1992]	41.2	1225.0	1266.2
AlGaAs [Wagner, 1992]	41.0	no data	no data

The ARXPS results for the nitrogen ion implantation are shown in Table 4.19. The relative concentration of nitrogen on the surface, is lower in almost all the cases compared to the same measured from the bulk. However considering the experimental uncertainties it is difficult to say if the trend is real.

4.1.7 Arsenic:

The nitrogen ion bombardment of arsenic did not result in implantation of nitrogen or any change in the spectra of As. The nitrogen photoelectron signal was very rarely observed and whenever it was, it was very small.

Table 4.17 The values of Al 2p binding energies (eV) and KLL kinetic energies (eV) for clean, N₂⁺ bombarded, and then Ar⁺ bombarded AlGaAs are tabulated in first three rows. The last two rows show the value of the above mentioned parameters for pure aluminium and standard AlN.

	Al 2p	Al KLL	Auger parameter
AlGaAs, after Ar ⁺ cleaning	73.5±0.2	1392.1±0.2	1465.6±0.4
N ₂ ⁺ bombarded AlGaAs	73.7±0.2	1391.2±0.2	1464.9±0.4
First N ₂ ⁺ and then, Ar ⁺ bombarded AlGaAs	73.2±0.2	1392.8±0.2	1466.0±0.4
Al [Wagner, 1990]	72.9	1393.3	1466.2
AlGaAs [Wagner, 1990]	73.6	no data	no data
AlN [Wagner, 1990]	74.0	1388.9	1462.9

Table 4.18 The values of N 1s binding energies (eV) and KL₂₃L₂₃ kinetic energies (eV), along with the values of Auger parameter, for N₂⁺ bombarded AlGaAs and Al and for standard GaN are also reported.

	N 1s	N KL ₂₃ L ₂₃	Auger parameter
N ₂ ⁺ bombarded AlGaAs	396.6±0.2	381.0±0.2	777.6±0.4
N ₂ ⁺ bombarded Al	396.7±0.1	380.3±0.2	777.0±0.3
GaN [Hedman and Martesson, 1980]	397	385	782

4.2 Plasma implantation:

The ions in glow discharge consist of an energy distribution and hence, the average energy of the ions was determined using a model developed by Wronski [1990].

4.2.1 Aluminium:

The ARXPS results for the nitrogen ion glow discharge exposure are shown in Table 4.20.

The N 1s spectra, Figure 4.49 (a), shows that nitrogen exists in two forms: strongly bound to aluminium (binding energy, 396.0 eV) and weakly bound or bound with oxygen (binding

Table 4.19 ARXPS data of nitrogen ion implantation in AlGaAs, at various ion energies and current densities.

Energy (keV)	Current Density (micA/cm ²)	TOA	Relative atomic Concentration				N/(Al+As+Ga)
			N (%)	Al (%)	As (%)	Ga (%)	
5	5	0	17.6	22.5	26.6	33.3	0.21
		33	17.5	22.1	26.2	34.2	0.21
		45	19.1	21.5	25.8	33.6	0.24
		54	19	23.1	26	31.9	0.23
		60	16.3	26.2	25.7	31.8	0.19
4	5	0	18.7	21.1	26.4	33.8	0.23
		33	22.2	20.2	24.8	32.8	0.29
		45	19.1	20	25.4	35.5	0.24
		54	15.6	17.8	28.8	37.8	0.18
		60	16.4	16.3	29.4	37.9	0.20
3	5	0	19.3	20.2	26.7	33.8	0.24
		33	18.4	21.2	26.2	34.2	0.23
		45	18	18.8	27.5	35.7	0.22
		54	13.4	13.2	33	40.4	0.15
		60	9.2	10.4	35.2	45.2	0.10
2	5	0	17.4	19.5	27.8	35.3	0.21
		33	17.7	19.8	27.4	35.1	0.22
		45	17.8	18.4	27	36.8	0.22
		54	15.3	15.4	29.4	39.9	0.18
		60	11.9	11.3	33.2	43.6	0.14
5	1	0	18.5	19.4	26.2	35.9	0.23
		33	19	19.6	26.8	34.6	0.23
		45	19	20.3	25.5	35.2	0.23
		54	17.7	21.8	26	34.4	0.22
		60	19.2	21.6	25.3	33.9	0.24
4	1	0	18.9	20.2	26.7	34.2	0.23
		33	14.6	22.9	26.7	35.8	0.17
		45	17.9	22.2	26.4	33.5	0.22
		54	17.5	21.8	26.6	34.1	0.21
		60	19.5	20.9	24.7	34.9	0.24
3	1	0	18.5	18.8	27.3	35.4	0.23
		33	18.3	14.3	26.9	40.5	0.22
		45	17	15.7	26	41.3	0.20
		54	19.9	13	25.6	41.5	0.25
		60	18.3	13.3	27.1	41.3	0.22
2	1	0	15.9	16.1	29.8	38.2	0.19
		33	16.6	16.3	28.4	38.7	0.20
		45	16.9	16.8	26.8	37.5	0.21
		54	15.3	20.4	28.9	35.4	0.18
		60	14.5	21	27.8	36.7	0.17

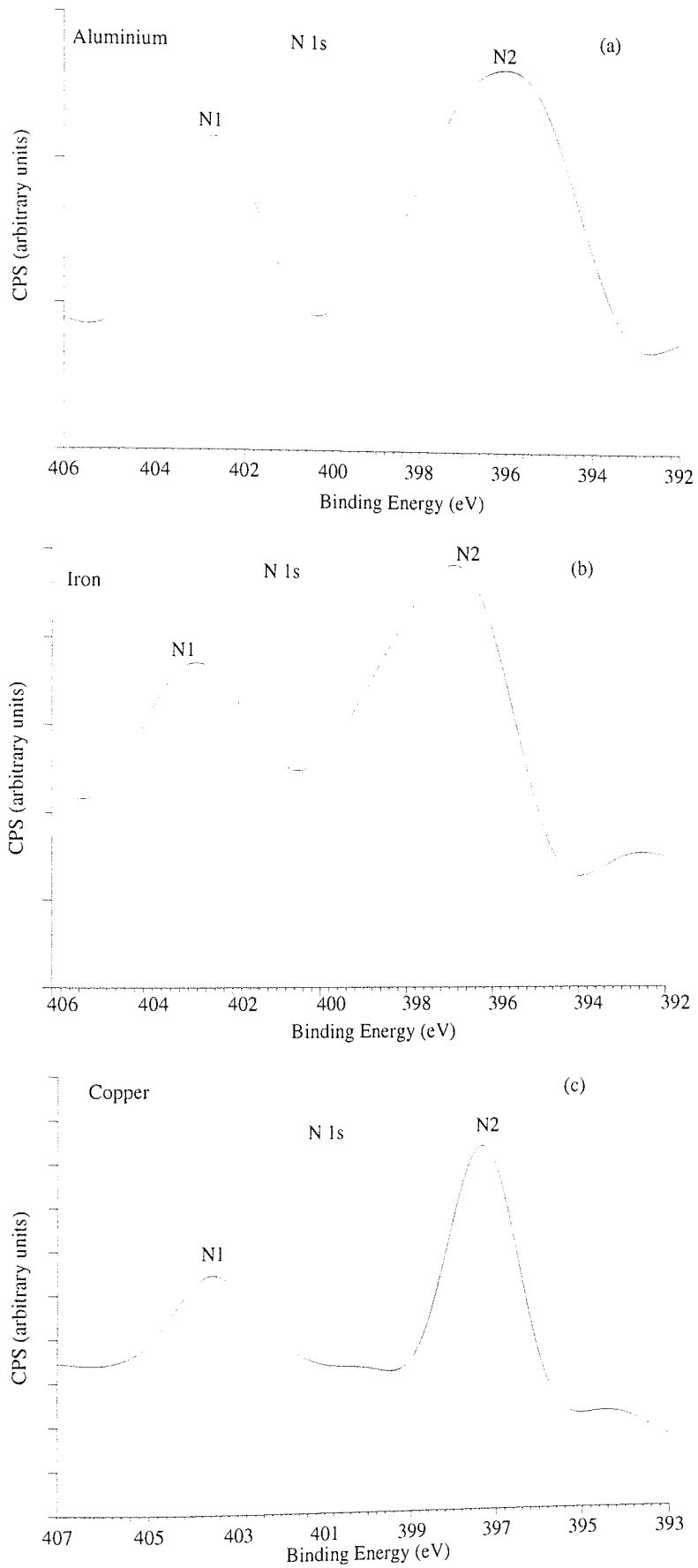


Figure 4.49 N 1s spectra for the target samples (a) aluminium, (b) iron and (c) copper, exposed to nitrogen glow discharge.

energy, 402.7 eV). In the figure and table, these components are marked as N₂ and N₁, respectively. The relative concentration of nitrogen on the surface, (75° take-off angle) is lower. This is probably due to presence of a large amount of surface contaminants.

Table 4.20 ARXPS data of nitrogen glow discharge exposure to aluminium.

Voltage (kV)	Pressure (torr)	Current (mA)	Average energy (keV)	TOA	Relative Atomic Concentration					(N1+N2)/Al
					Al (%)	O (%)	N1 (%)	N2 (%)	C (%)	
0.55	0.21	2.1	0.18	0	35.7	39.2	5.7	7.8	11.7	0.38
				25	34.7	40.5	5.2	7.1	12.5	0.35
				50	41.4	32.1	4.5	8.4	13.7	0.31
				75	32.1	24.9	3.5	6.5	33	0.31
3.00	0.05	1.0	0.88	0	33.2	40.2	5.9	8.6	12.1	0.44
				25	33.2	38.7	5.8	9.6	12.7	0.46
				50	37.5	33.5	4.7	10.2	14.1	0.40
				75	30.7	25.3	3.7	7.5	32.8	0.36

4.2.2 Iron:

After glow discharge exposure, the ARXPS results for iron, are shown in Table 4.21. The sample was highly contaminated with carbon and oxygen and the nitrogen was found to exist in two forms: bound to iron (binding energy, 395.9 eV) and weakly bound with oxygen (binding energy, 402.3 eV, Figure 4.49 (b)). These components are marked as N₂ and N₁ respectively, in the figure and table. The relative concentration of nitrogen on the surface, (75° take-off angle) is lower. This is probably due to presence of a large amount of surface contaminants.

Table 4.21 ARXPS data of nitrogen glow discharge exposure to Iron.

Voltage (kV)	Pressure (torr)	Current (mA)	Average energy (keV)	TOA	Relative Atomic Concentration					(N1+N2)/Fe
					Fe (%)	O (%)	N1 (%)	N2 (%)	C (%)	
0.55	0.21	2.1	0.18	0	30.1	41.3	5.5	4.6	18.6	0.34
				25	29.7	41.4	4.9	4.3	19.7	0.31
				50	28.4	38.4	5.0	5.2	23.0	0.36
				75	18.5	32.9	1.5	2.2	45.0	0.20
3	0.05	1	0.95	0	33.2	39.8	5.7	4.8	16.5	0.32
				25	31.7	39.3	5.2	5.4	18.4	0.33
				50	30.3	38.9	5.4	5.3	20.1	0.35
				75	20.2	39.0	1.7	2.4	36.7	0.20

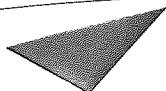
4.2.3 Copper:

The ARXPS data obtained after exposing copper to nitrogen glow discharge, is shown in Table 4.22. Like aluminium and iron, the sample was highly contaminated with carbon and oxygen. The N 1s spectra, Figure 4.49 (c), shows that nitrogen exists in two forms: strongly bound to copper (binding energy, 397.4 eV) and weakly bound or bound with oxygen (binding energy, 403.6 eV). In the figure and table, these components are marked as N₂ and N₁ respectively.

Table 4.22 ARXPS data of nitrogen glow discharge exposure to Copper.

Voltage (kV)	Pressure (torr)	Current (mA)	Average energy (keV)	TOA	Relative Atomic Concentration					(N1+N2)/Cu
					Cu (%)	O (%)	N1 (%)	N2 (%)	C (%)	
1.6	0.20	2.1	0.5	0	65.4	8	3.1	7.9	15.6	0.17
				25	62.9	9.1	2.8	8.4	16.8	0.18
				50	55.6	11.3	2.8	9.1	21.2	0.21
				75	51.7	14.4	2.8	8.9	22.2	0.23
3.0	0.07	1.0	1.2	0	63.4	12.9	1.7	7.6	14.4	0.15
				25	60.4	16	1.9	6.9	14.8	0.15
				50	56.1	21.2	0.9	6.7	15.1	0.14
				75	52.9	19.1	2.1	4.9	18.8	0.13

Chemical and electrochemical treatments of GaAs with Na₂S



Aston University

Content has been removed for copyright reasons

Vac. Sci Technol. A 11(A), Jul./Aug. 1993, pp. 1083-1088

[Return to Abstract List](#)

Chapter 5

Theory and Computer Simulations

5.1 Introduction:

This chapter is divided in two subsections. In the first subsection, theoretical models, especially Sigmund's linear cascade theory and Gibbsian segregation will be discussed. Some aspects of the theoretical models including the scattering parameter, origin of sputtered particles, surface binding energy in Sigmund's theory, the surface energy in crystal solids, the function of ion bombardment in segregation and diffusion etc., are also discussed. In the second subsection, some results of computer simulation models, such as SATVAL, SUSPRE and TRIM are reported. These will be compared with the experimental results.

As N_2^+ molecular ion dissociates and the energy of the molecule is apportioned to the constituent ions such that both constituent ions of the N_2^+ will have half of the energy of primary molecular ion. Hence for all the calculations each ion was assumed to take half of the ion beam energy. Some physical properties of the target material are tabulated in Table 5.1, which will be useful for discussion of some results. Here the density is expressed in units of g/cm^3 , the sublimation energy is assumed to represent surface binding energy (S. B. E.) and is expressed in units of eV. For compound targets, the surface binding energy is assumed to be the average sum of the sublimation energy of component elements.

Table 5.1 Some Physical properties of target materials

Target	Al	Fe	Cu	Au	GaAs	AlGaAs
Atomic No.	13	26	29	79	32	25.7
Atomic Mass	26.98	55.85	63.55	196.97	72.32	57.21
Density	2.6	7.9	8.9	19.3	5.3	5.4
S.B.E.	2.7	4.34	3.52	3.8	2	2.26

5.2 Stopping power:

Figure 5.1 (a) shows the nuclear and electronic stopping powers calculated using SUSPRE code, for nitrogen ions of energy 2, 3, 4 and 5 keV, incident on various target materials at an angle of 51.6° . Both nuclear and electronic stopping powers increase with increase in ion

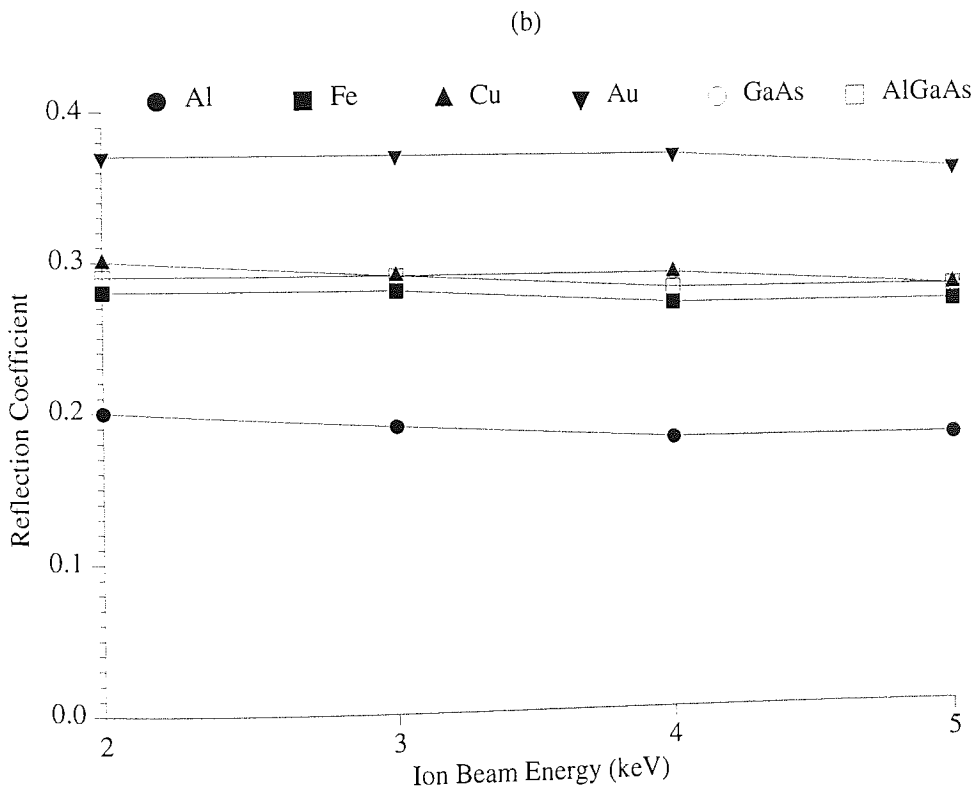
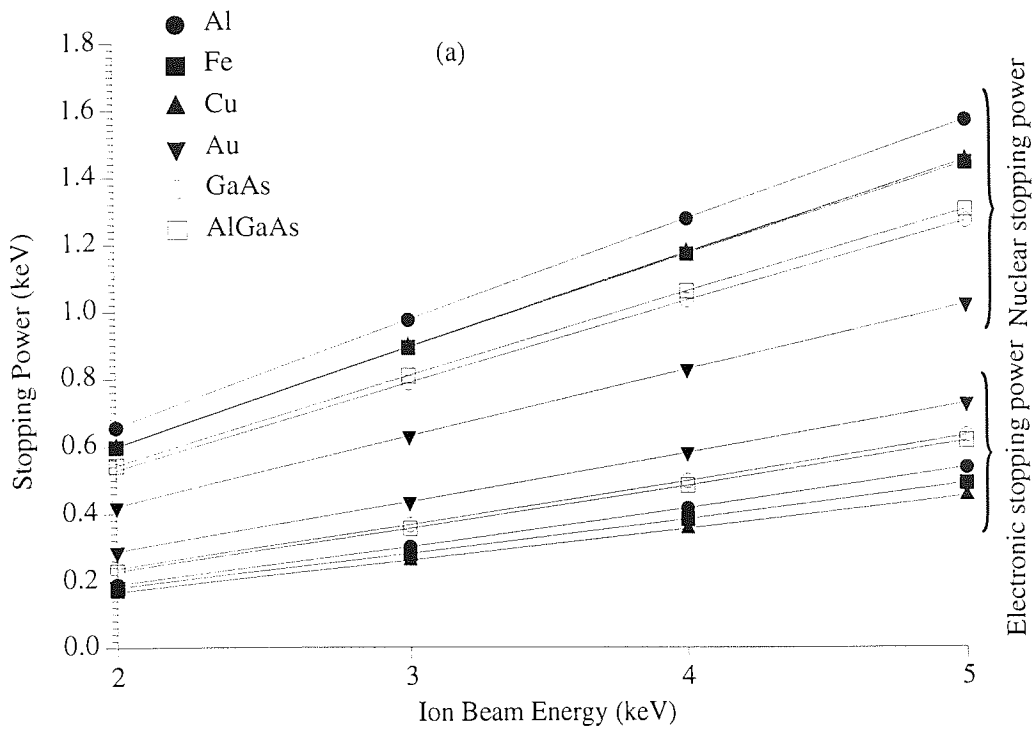


Figure 5.1 Variation of (a) nuclear and electronic stopping powers; and (b) reflection coefficient, with nitrogen ion beam energy, for various target materials. The calculations are made using SUSPRE code, for nitrogen ions incident on a given target at an angle of 51.6° .

beam energy. Clearly, the nuclear stopping power is the main mechanism for energy loss. Although most of ion energy is transferred to nuclei, still an appreciable amount of energy contributes to electronic processes, which seems to depend on density for the metallic targets (Table 5.1), being higher for the target with smaller target density. The smaller the stopping power, the longer the slowing down time and hence greater the weight with which a given atom contributes to the particle flux under steady state conditions. Another interesting point is the sum of nuclear and electronic energy losses is less than the primary ion energy. This is because of the fact the beam is incident at an angle of 51.6° with respect to the surface normal and so some of the incident particles will be reflected, resulting in some of energy loss. However for an ion beam incident normal to the sample surface, all the ion energy would be consumed by collisions with the target nuclei and electrons. The reflection coefficient for various target materials, are plotted as a function of ion beam energy in Figure 5.1 (b). As expected, the reflection coefficient for ions is higher in heavy mass targets [Table 5.1] and reflection seems to be slightly more dominant at lower energies compared to the same at higher ion energies.

5.2 Range of ions in various target materials:

It is important to know the range of ions in the target material, but there is not a convenient experimental method to measure the penetration depth of the energetic ions and the distribution of ions and recoils. As the number of collisions per unit distance and the energy lost per collision are random variables, there will be a spatial distribution of ions having the same mass and same initial energy. The statistical fluctuations in the R_p are called the projected straggle ΔR_p . There is also a statistical fluctuation along the axis perpendicular to the axis of incidence, called the lateral straggle ΔR_\perp . Using TRIM, the range and straggle of ion in all target materials were calculated at various ion energies and are tabulated in Table 5.2. Clearly, the range and straggle values of Al, GaAs and AlGaAs are similar and that of Fe and Cu are similar, while the same for gold lie between the two. The actual range of ions, however, is found to be far more than the predicted range ("long range effect"). The sum of range and straggle is called the ballistic penetration depth. The penetration depth in case of Fe and Cu is almost 40% smaller than the same for Al, GaAs and AlGaAs. For more clarity, the values of longitudinal ion range are plotted as a function of ion beam energy in Figure 5.2. However, the values plotted in this Figure were calculated using SUSPRE. The values calculated using SUSPRE are smaller than the TRIM calculated values. Since the energy transfer from the incoming ions to the lighter target atoms is smaller than that to heavier atoms, the ion projected range is longer in low mass target as compared to high mass ones.

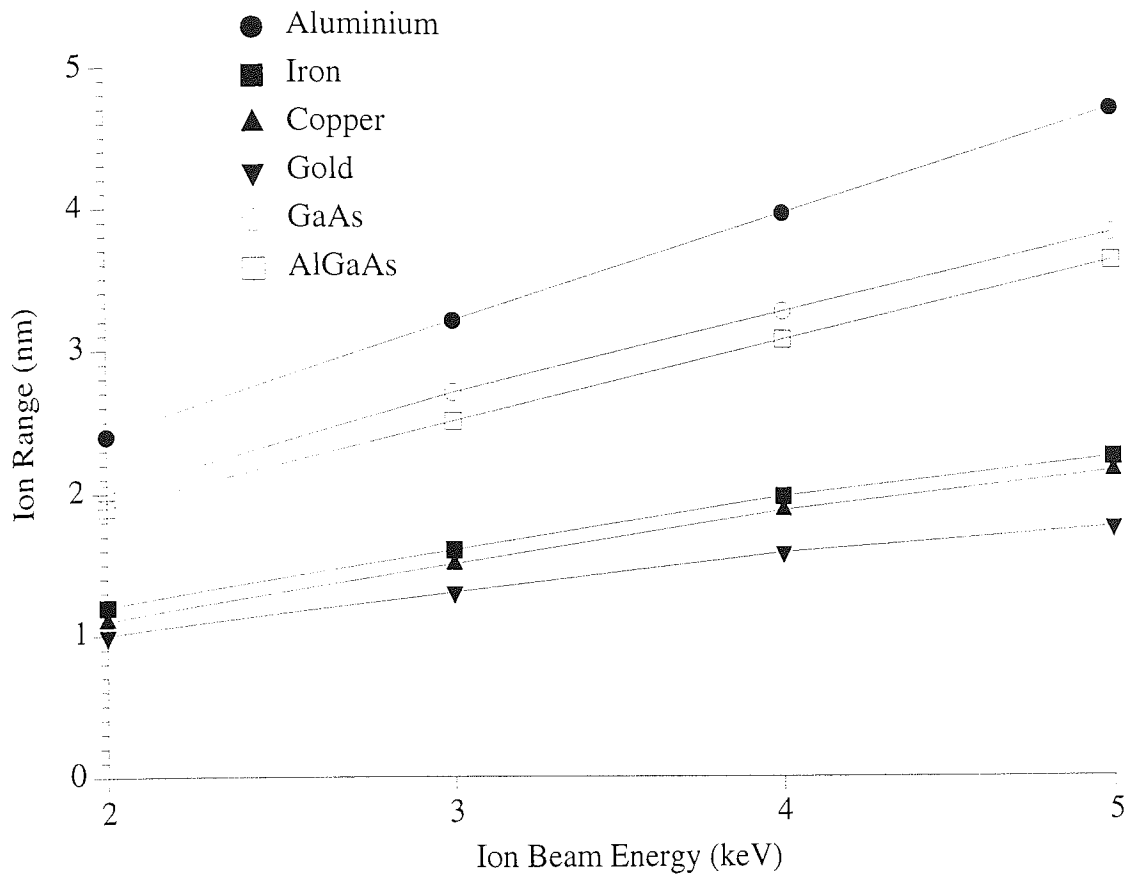


Figure 5.2 Variation of ion range, with nitrogen ion beam energy, for various target materials. The calculations are made using SUSPRE code, for nitrogen ions incident on a given target at an angle of 51.6° .

Table 5.2 Ion range and straggle in different target materials, at various ion energies.

Ion Beam Energy (keV)	Target	Al	Fe	Cu	Au	GaAs	AlGaAs	
2	Longitudinal	Range	33	21	20	28	34	35
		Straggle	20	12	12	16	20	21
	Lateral Proj.	Range	35	19	20	22	32	32
		Straggle	41	23	25	28	40	39
	Radial	Range	43	25	26	32	43	42
		Straggle	22	13	14	17	23	22
3	Longitudinal	Range	43	27	28	36	45	45
		Straggle	26	16	17	20	27	27
	Lateral Proj.	Range	46	25	25	28	40	41
		Straggle	55	31	31	35	48	51
	Radial	Range	57	33	34	41	55	55
		Straggle	29	17	17	22	27	29
4	Longitudinal	Range	53	32	33	42	54	54
		Straggle	32	19	20	24	32	32
	Lateral Proj.	Range	57	31	29	34	49	51
		Straggle	68	37	36	42	60	62
	Radial	Range	70	40	39	49	66	67
		Straggle	35	21	22	26	35	35
5	Longitudinal	Range	63	38	40	48	64	63
		Straggle	37	23	24	28	38	37
	Lateral Proj.	Range	68	36	35	39	57	59
		Straggle	80	44	44	48	69	72
	Radial	Range	82	47	48	56	76	78
		Straggle	41	24	25	29	40	41

5.3 Ion and Recoil distributions:

In the low energy regime, collisional cascades between recoils are major events and so bombardment damage may be more influenced by recoils than primary ions. This can be seen clearly from the ion and recoil distributions, shown in Figure 5.3. These were obtained using TRIM by simulating 99999 nitrogen ions bombarding the target surfaces at an angle of 51.6°. Here the results of only iron and AlGaAs targets are shown, but similar results were obtained from the other target materials. From figures, it is clear that

- ion beam induced damage is limited to a depth of about 10 to 20 nm

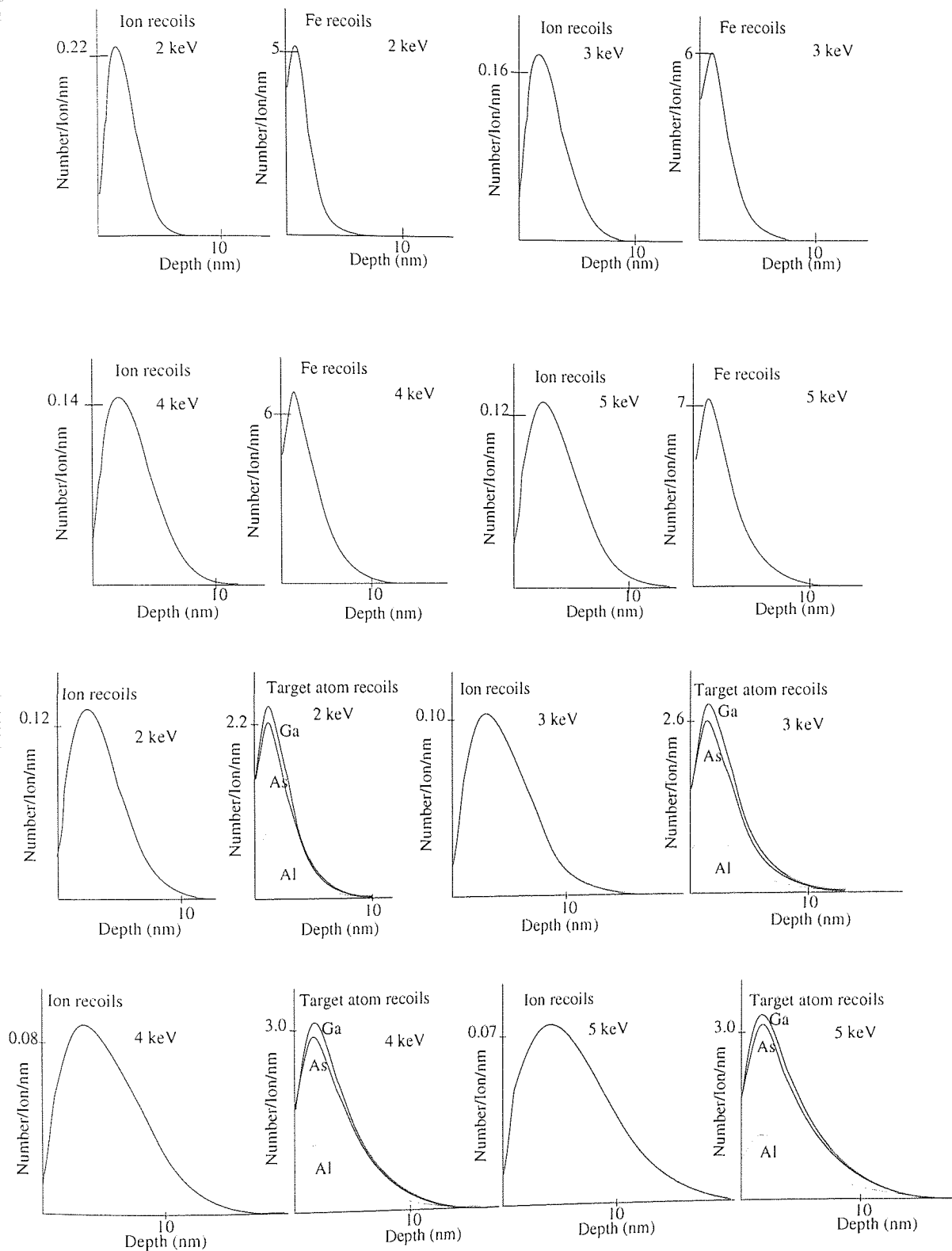


Figure 5.3 Nitrogen ion and target atom recoil distribution for nitrogen ion bombarded iron and AlGaAs targets.

- the number of recoils is much greater than that of incident ions, implying that collision cascade, rather than the direct ion-atom interaction plays a dominant role in surface compositional changes.

From Figure 5.3, it is clear that with an increase in ion energy, the maximum number of ions recoiling per incident ion per unit distance decreases, whereas the same for target atoms increases, implying that in the energy range of 2-5 keV, the dominance of recoiling target atoms increases with increase in ion energy. The recoil depth (depth, beyond which the number of recoils is less than 5% of its maximum value) is greater for higher ion energies.

The energy losses by ions and recoils in the form of ionization, vacancies and phonons are shown in Table 5.3. The calculations were obtained by TRIM by simulating 99999 nitrogen ions striking the target surface at an angle of 51.6°. Clearly, in all the targets, the main energy loss is by recoils in the form of phonons. The general trend of energy loss is:

- For ions, energy loss by ionization > phonons > vacancies
- For recoils, energy loss by phonons > ionization > vacancies

The comparison of energy losses for various targets shows,

For ions,

energy loss by ionization,	Au > GaAs > AlGaAs > Fe > Cu > Al
energy loss by vacancies,	AlGaAs > Au > Cu ≈ Fe ≈ GaAs > Al
energy loss by phonons,	Au > Cu > GaAs > Fe > Al > AlGaAs

For recoils,

energy loss by ionization,	Al > AlGaAs > Au > Fe > Cu > GaAs
energy loss by vacancies,	AlGaAs > Al > Cu ≈ Fe > Au > GaAs
energy loss by phonons,	Al > Cu > Fe > GaAs > AlGaAs > Au

For ions and recoils,

energy loss by ionization,	Au > AlGaAs > GaAs > Fe > Al > Cu
energy loss by vacancies,	AlGaAs > Au ≈ Al ≈ Cu > Fe > GaAs
energy loss by phonons,	Cu > Al > Fe > GaAs > AlGaAs > Au

As the ionization losses are not very important, from the point of view of ion implantation, the important losses are only the energy losses by phonons and vacancies.

Table 5.3 Tabulation of energy losses by ions and recoils in the form of ionization, vacancies and phonons, The calculations are made using TRIM.

Ion Beam Energy (keV)		Target		Al	Fe	Cu	Au	GaAs	AlGaAs
2.0	Energy loss (%)	Ionization	Ions	20.7	25.5	23.3	40.6	30.3	28.6
			Recoils	11.7	8.8	8.7	9.9	7.4	10.2
		Vacancies	Ions	1.2	1.4	1.4	1.5	1.4	1.7
			Recoils	1.3	1.1	1.1	1.0	0.9	2.9
		Phonons	Ions	9.0	10.2	11.1	14.4	10.9	8.1
			Recoils	56.1	53.1	54.4	32.6	49.1	48.6
3.0	Energy loss (%)	Ionization	Ions	22.2	26.4	24.3	41.0	31.3	29.7
			Recoils	12.2	9.4	9.2	11.4	8.0	11.0
		Vacancies	Ions	1.1	1.1	1.2	1.3	1.2	1.4
			Recoils	1.4	1.3	1.3	1.3	1.1	3.1
		Phonons	Ions	7.1	7.9	8.5	11.0	8.3	6.2
			Recoils	56.0	53.9	55.5	34.0	50.2	48.6
4.0	Energy loss (%)	Ionization	Ions	23.6	27.5	24.8	41.4	32.1	30.8
			Recoils	12.5	9.7	9.7	12.4	8.3	11.5
		Vacancies	Ions	0.9	1.0	1.1	1.2	1.0	1.2
			Recoils	1.5	1.4	1.4	1.4	1.2	3.2
		Phonons	Ions	6.0	6.5	7.1	9.1	6.9	5.1
			Recoils	55.5	53.9	55.9	34.5	50.5	48.1
5.0	Energy loss (%)	Ionization	Ions	24.5	28.3	26.0	41.9	33.4	31.6
			Recoils	12.8	9.9	9.8	13.0	8.4	11.9
		Vacancies	Ions	0.9	0.9	0.9	1.1	0.9	1.1
			Recoils	1.6	1.5	1.5	1.5	1.3	3.3
		Phonons	Ions	5.2	5.8	6.2	7.8	6.0	4.4
			Recoils	55.2	53.7	55.5	34.7	49.9	47.7

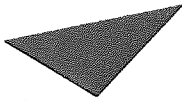
5.4 Surface Binding Energy:

For the calculations taken in the next subsection and simulation work, the value of surface binding energy is required. As discussed in Chapter 1, the determination of correct value of surface binding energy, U , is a difficult problem, especially in the case of alloys and compound semiconductors. There are different models for the estimation of the surface

binding energy, but they all give different values of U . For these calculations, values of some physical parameters, are required. Some of these properties are listed in Tables 5.4 and 5.5. In the case of GaAs, the following estimates of (U_{As}/U_{Ga}) are obtained using different models:

Table 5.4 Some physical properties of the target elements [Lide, 1991]

	Al	Fe	C	As	Ga	As	Ni
--	----	----	---	----	----	----	----



Aston University

Content has been removed for copyright reasons

Table 5.5 Bond strength values (eV) of A-B system at room temperature [Lide, 1991].



Aston University

Content has been removed for copyright reasons

Sublimation energy: Using the heat of sublimation as the representation of surface binding energy, and using the values of heat of sublimation for As and Ga from Table 5.4, the ratio of surface binding energy of As to the same for Ga is;

$$\frac{U_{As}}{U_{Ga}} = 0.45 \quad (5.1)$$

Heat of atomization: Taking the heat of atomization for As and Ga atoms as their surface

binding energies and using the values given in Table 5.4, one gets;

$$\frac{U_{As}}{U_{Ga}} = 1.09 \quad (5.2)$$

Kelly's Model: Using equation (1.47) and values of melting point of Ga and As as 29.8°C and 816°C, [Lide, 1991], the ratio of surface binding energy of As to Ga becomes:

$$\frac{U_{As}}{U_{Ga}} = 1.3 \quad (5.3)$$

Malherbe's model: Assuming a stoichiometric GaAs compound with bond strength values taken from Table 5.5, and electronegativity values taken from Table 5.4 for Ga and As atoms respectively and using equations (1.48) and (1.49), one obtains

$$\frac{U_{As}}{U_{Ga}} = 1.07 \quad (5.4)$$

Pair bond Model: According to the pair bond model, the ratio of surface binding energy for a binary target is given as;

$$\frac{U_A}{U_B} = \frac{C_A D(A - A) + C_B D(A - B)}{C_A D(A - B) + C_B D(B - B)} \quad (5.5)$$

Using above equations, and the values of bond strengths given in Table 5.5,

$$\frac{U_{As}}{U_{Ga}} = 1.7 \quad (5.6)$$

Surface tension: Taking surface tension to represent the surface energy and with 0.675 and 0.784 J/m², as the surface tension values for As and Ga atoms, one obtains;

$$\frac{U_{As}}{U_{Ga}} = 0.86 \quad (5.7)$$

From the equations (5.1), (5.2), (5.3), (5.4), (5.6) and (5.7), it is clear that it is hard to make the decision for the value of surface binding energy. In addition to this problem, the surface binding energy can be influenced by contamination, surface stoichiometric changes, surface roughness, surface stress and structural changes. For example, in case of aluminium, the sublimation energy is 3.36 eV, but to check the validity of this value, we considered an ideal case of 60% aluminium and 40% nitrogen. This situation represents the experimentally

calculated saturation state of the target, hence if the target is bombarded with nitrogen ions, the number of sputtered particles should be equal to the number of retained ions. Using TRIM and taking an input surface binding energy of 3.36 eV and assuming an incident nitrogen ion of energy 2 keV the predicted saturation concentration did not correspond to measured values. The number of nitrogen particles residing in the target was greater than the number of sputtered nitrogen particles. By decreasing the surface binding energy in steps of 0.2 eV a best fit surface binding energy value was chosen as 2.0 eV. It was very difficult to make a choice for value of surface binding energy.

5.5 Implant surface concentration:

As mentioned in Chapter 1, ion bombardment results in trapping of ions in the surface and the surface concentration of the implantant depends on many parameters such as ion range distribution, sputter depth and chemical reactivity of ion/target system. Using equation (1.15), the implantant surface concentration could be calculated. For this purpose, the value of sputter yield, Y , is needed. The sputter yield values can be calculated using equation (1.21) and this requires the determination of the reduced energy parameter (ϵ), parameter (α), screening radius (a) and nuclear stopping power cross-section (S_n). The values of these were calculated using equations (1.6), (1.22), (1.2) and (1.5) respectively. The sputter yield concentration values calculated in this manner are plotted in Figure 5.4(a). For comparison, the value of sputter yield calculated using SUSPRE are also shown in Figure 5.4(b). Clearly the values of sputter yield predicted by SUSPRE are much smaller than the calculated sputter yield values, especially for large mass targets. This difference is mainly due to neglect of the surface correction at large mass ratios in the SUSPRE code. The resultant implant concentration values, calculated using the sputter yield values, calculated and those obtained from SUSPRE code, are listed in Tables 5.6 and 5.7 respectively.

Table 5.6 List of surface concentration of implantant in the target materials, using sputter yield values calculated as mentioned above. Here E is the ion beam energy in units of keV.

E	Al	Fe	Cu	Au	Ga	As	GaAs	AlGaAs
2	0.48	0.27	0.19	0.05	0.14	0.06	0.07	0.08
3	0.45	0.24	0.17	0.04	0.13	0.05	0.06	0.07
4	0.43	0.23	0.16	0.04	0.12	0.05	0.05	0.07
5	0.42	0.22	0.16	0.04	0.11	0.05	0.05	0.06

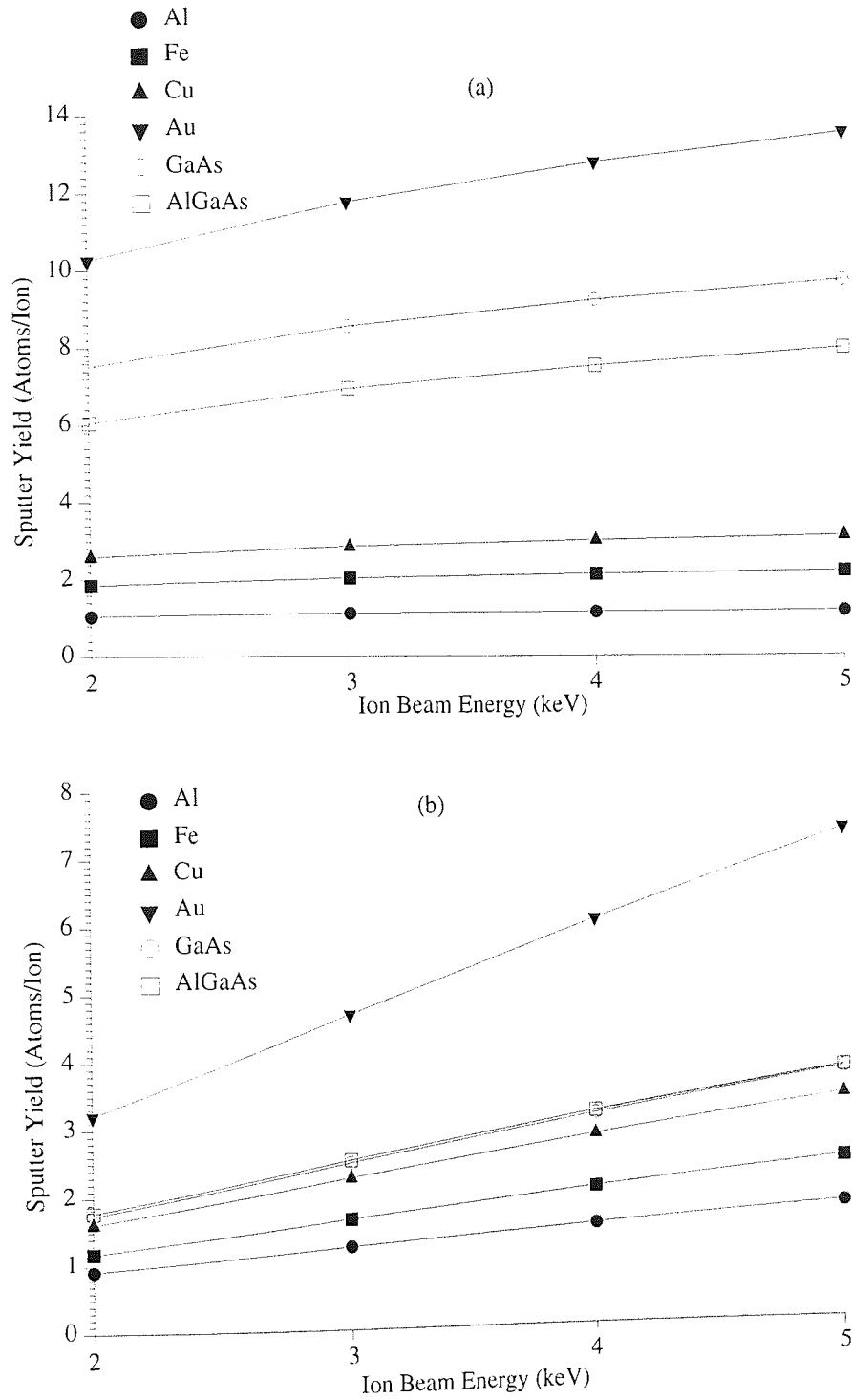


Figure 5.4 Sputter yield values as a function of ion beam energy, for target materials, (a) calculated and (b) obtained from SUSPRE code.

Table 5.7 Tabulation of surface concentration of implantant in the target materials, using sputter yield values obtained by SUSPRE. Here E is the ion beam energy in units of keV.

E	Al	Fe	Cu	Au	Ga	As	GaAs	AlGaAs
2	0.54	0.42	0.31	0.16	0.25	0.12	0.29	0.28
3	0.40	0.30	0.22	0.11	0.18	0.09	0.20	0.20
4	0.33	0.24	0.18	0.08	0.14	0.07	0.16	0.16
5	0.28	0.20	0.15	0.07	0.12	0.06	0.13	0.13

Clearly, the values of implantant concentration are higher for smaller mass targets. Comparing these values with the experimentally obtained values (given in Chapter 4), for the metallic targets, the values given in Table (5.6) agree more closely to the experimental values as compared to those given in Table (5.7). However, the agreement for compound targets, GaAs and AlGaAs is poor.

5.6 Preferential sputtering of implanted Nitrogen:

Because of smaller mass of nitrogen, there will be a tendency for preferential sputtering. The values of (Y_T / Y_N) , determined by equation (1.34), are given in Table 5.8. Here the subscripts T and N stand for target and nitrogen, respectively. In these calculations, the power scattering parameter, m , was taken as 0.165 [Malherbe et al., 1986]. The surface binding energies were determined using equations (1.48) and (1.49). However, due to lack of data, it was not possible to do these calculations for gold.

Table 5.8 A list of the ratio of sputter yields, (Y_T / Y_N) , for target-nitride system.

Al-N	Fe-N	Cu-N	GaAs-N	AlGaAs-N
1.99	3.66	3.64	2.99	2.35

In these calculations, the value of scattering parameter was assumed to be same for all target materials. In Figure 5.5, the variation of ϵ [calculated by using equation (1.6)] with ion beam energy is plotted, showing a linear dependence of ϵ on ion energy, and the value of the reduced energy is smaller for heavy mass targets. The ratio of ion beam energy to reduced energy is shown in Table 5.8, indicating an increase in this ratio for heavy mass targets. As different elements in a target materials have different reduced energy, so a different value of scattering parameter, m , should be used.

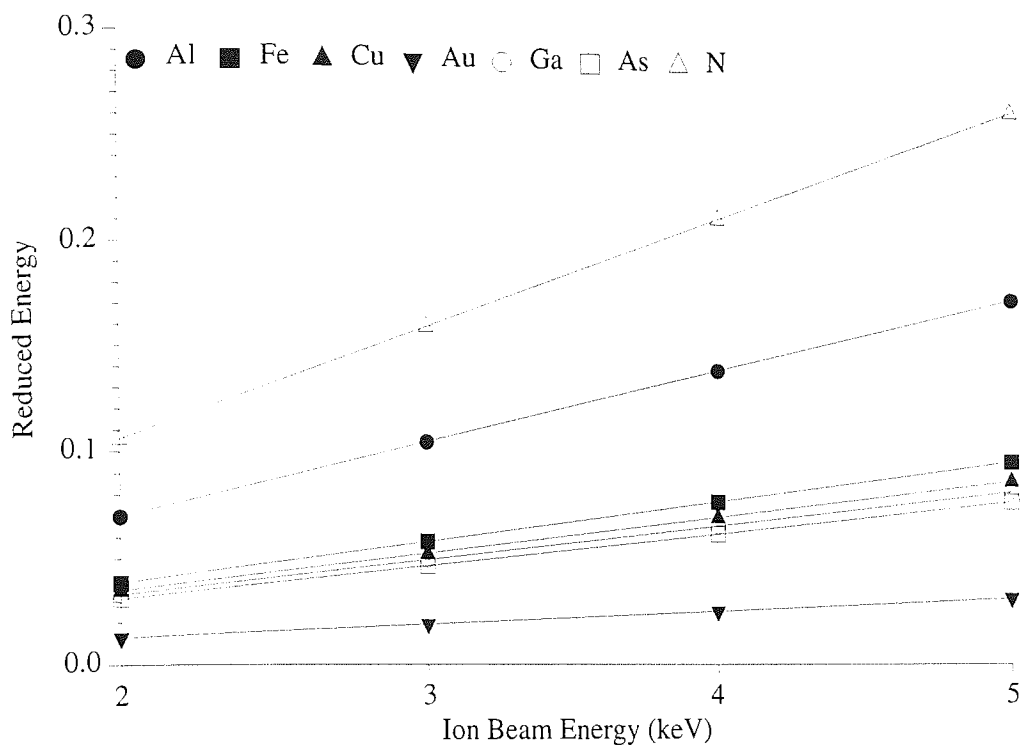


Figure 5.5 Reduced energy parameter, as a function of ion beam energy.

Table 5.9 The ratio of ion beam energy to reduced energy

Target	Al	Fe	Cu	Au	Ga	As	N
E(keV)/ε	14.3	25.8	28.4	78.2	30.2	32.0	9.4

5.6.1 Calculation of scattering parameter, m :

By taking into account the difference in the power scattering parameter for the elements with different mass and using the TF nuclear stopping power, the ratio of partial yield is given as [Sigmund, 1981];

$$\frac{Y_1}{Y_2} = \frac{C_1}{C_2} \cdot f \cdot \left(\frac{M_2}{M_1}\right)^{m_1+m_2} \cdot \frac{U_2^{1-2m_2}}{U_1^{1-2m_1}} \quad (5.8)$$

here f is the correction factor expressed as:

$$f = \frac{1-m_1}{1-m_2} \cdot \frac{\lambda_{m_2}}{\lambda_{m_1}} \cdot \left(\frac{2Z_1Z_2e^2}{a}\right)^{2(m_2-m_1)} \cdot \left[\frac{4M_1M_2}{(M_1+M_2)^2}\right]^{-(m_2-m_1)} \quad (5.9)$$

To calculate the correction factor, one needs to determine the value of scattering parameter, m . For low energy ions, the description of atomic collisions is found to be more realistic by calculating the nuclear stopping powers using universal interatomic potential than that derived from Thomas-Fermi interatomic potential. However, Thomas-Fermi model is still used because of the simplicity of mathematics. In TF model, m represents the magnitude of nuclear stopping power, hence value of m can be predicted by directly comparing TF nuclear stopping power with universal (also called as ZBL) nuclear stopping power [Yu, 1995]. From equations (1.3) and (1.4), TF nuclear stopping power can be written as:

$$S_{TF} = \frac{1}{2(1-m)} \lambda_m \varepsilon^{1-2m} \quad (5.10)$$

The TF screening radius is given as;

$$a_{TF} = \frac{0.8853 a_0}{(Z_1^{\frac{2}{3}} + Z_2^{\frac{2}{3}})} \quad (5.11)$$

The TF and Biersack screening radii were calculated by using equations (5.11) and (1.2), respectively, and the universal nuclear stopping power calculated by using equation (1.5), are plotted in Figure 5.6. Clearly, both types of radii decrease with increase in target atomic mass, however, TF screening radii are smaller compared with Biersack radii. The nuclear

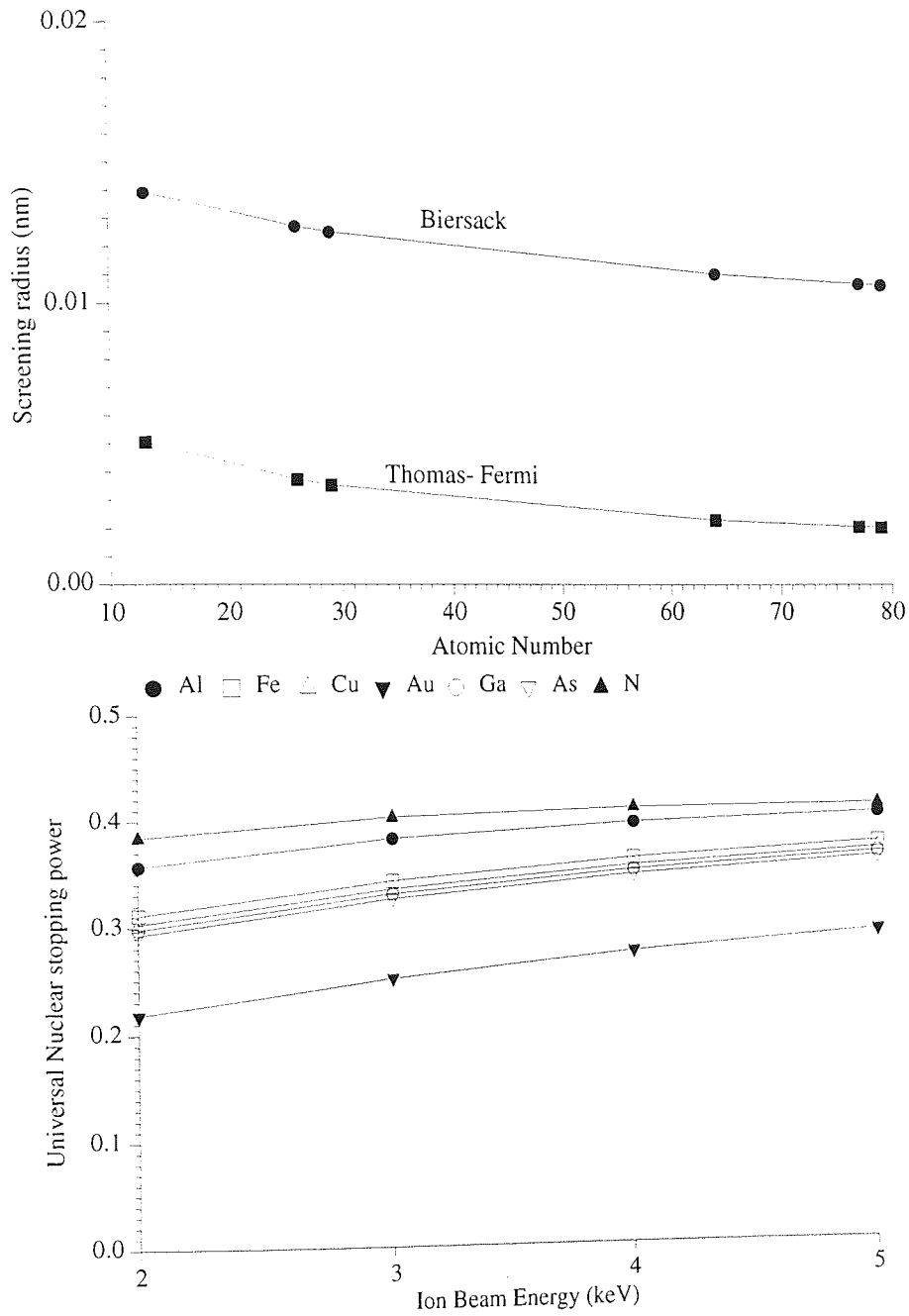


Figure 5.6 TF and Biersack screening radii, as a function of target atomic energy and, universal nuclear stopping power as a function of ion beam energy.

stopping power increases with increase in ion energy and is greater for targets with smaller atomic mass. By comparing the TF nuclear stopping power [defined by equation (5.10)], with universal nuclear stopping power [defined by equation (1.5)], the value of m is determined for all the targets at all the ion energies. The exact mathematical relationship between m and λ_m is unknown, but here λ_m was calculated using the relationship found by Sigmund [1981], by using the semi-empirical methods, given as

$$\lambda_m = 24.108 - 198.782m + 563.956m^2 - 520.72m^3 \quad 0 \leq m \leq 0.4 \quad (5.12)$$

Using above given λ_m - m relationship, the value of TF nuclear stopping power was calculated for various values of m and compared with universal nuclear stopping power, Figure 5.7. Using this plot, the value of m was calculated for all the target materials and is plotted as a function of ion beam energy and target mass in Figure 5.8. The value of m increases with increase in ion energy and at a given ion energy, the scattering parameter is found to be greater for light mass targets.

Using equation (5.9), the correction factor for GaAs is found to be 1, but for AlGaAs, the correction factor is found to be about 0.6. The value of f was also calculated for target nitride systems, and are plotted in Figure 5.9, showing that f is a parabolic function of ion energy. Clearly, the correction factor is appreciable in all the cases, but the value of this factor is closer to unity at higher beam energies in the case of aluminium, showing that the effect of mass difference is comparatively less important at higher ion energies. In the case of gold, because of large difference between gold and nitrogen masses, this factor is very large.

The ratio of sputter yield of target to nitrogen is calculated using equation (5.4) and is plotted in Figure 5.10. It depends on the composition, mass and surface binding energy ratios. Clearly, the sputter yield ratio decreases almost linearly with the ion beam energy.

5.6.2 Depth of sputtered particles:

Sigmund [1969b] derived an expression for the depth, Δx_0 , of sputtered atoms by using Born Mayer interatomic potential, given as;

$$\Delta x_0 = \frac{3}{4 N C_0}; \quad \text{with } C_0 = \frac{1}{2} \pi \lambda_0 a_{BM}^2; \quad a_{BM} = 0.219 \overset{\circ}{\text{A}} \text{ and } \lambda_0 = 24 \quad (5.13)$$

Here a_{BM} is the Born-Mayer screening radius and N is the atomic number density. The

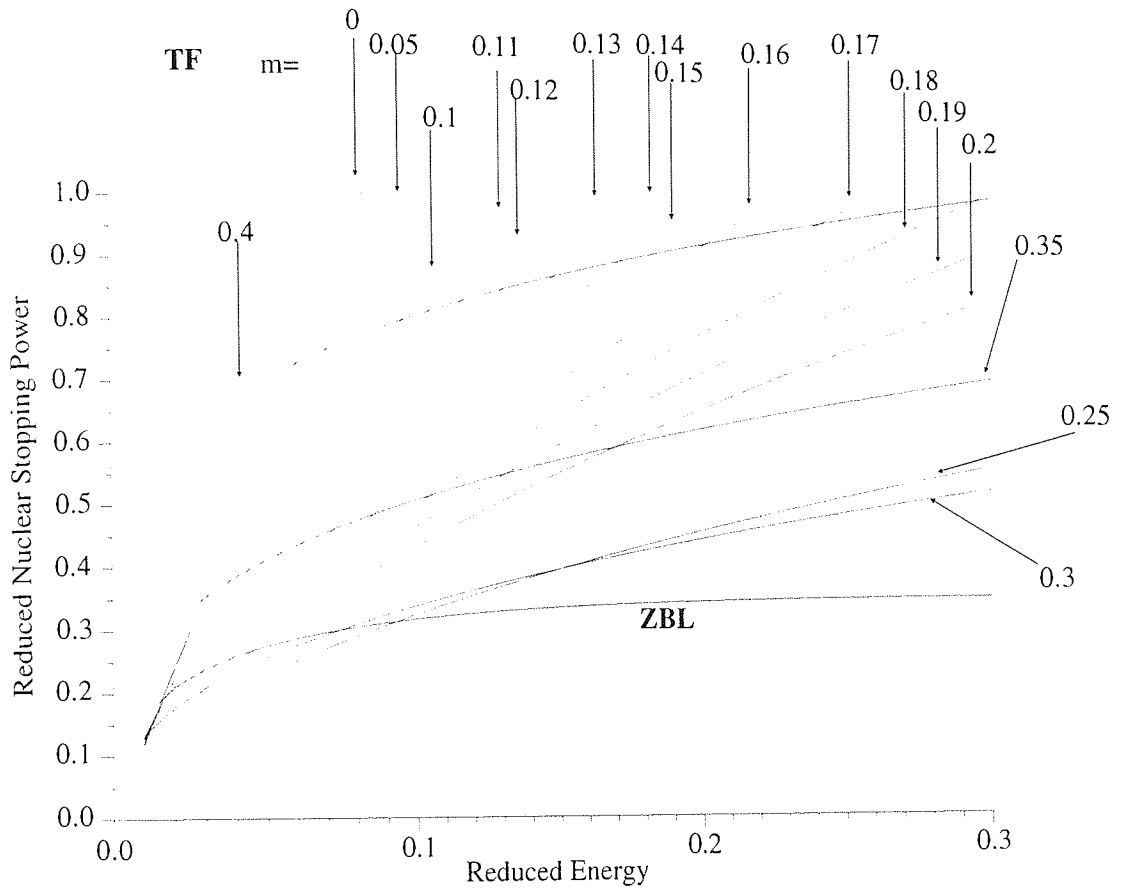


Figure 5.7 Comparison between ZBL and TF nuclear stopping power.

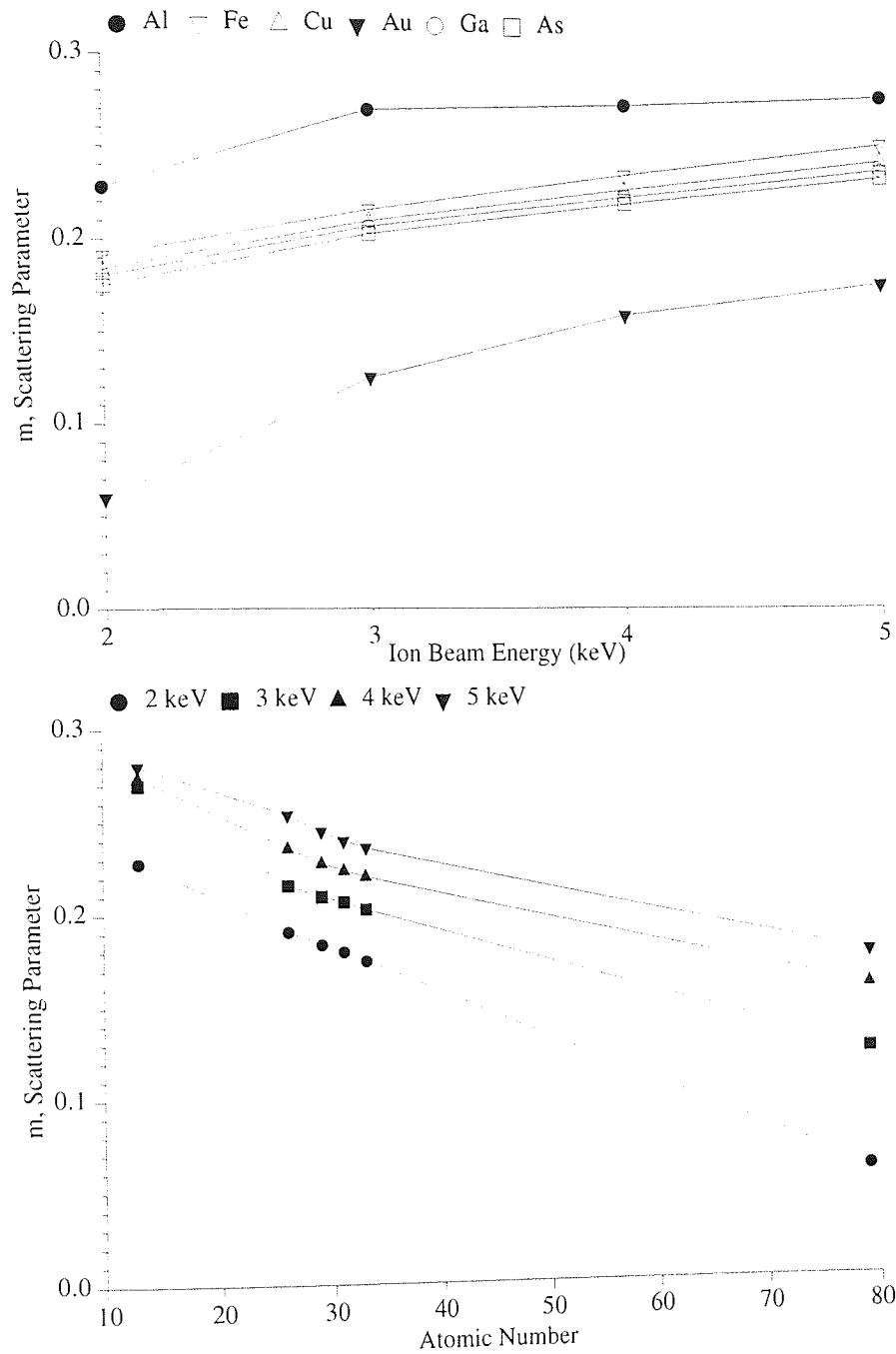


Figure 5.8 The scattering parameter, m , as a function of ion beam energy and Atomic number.

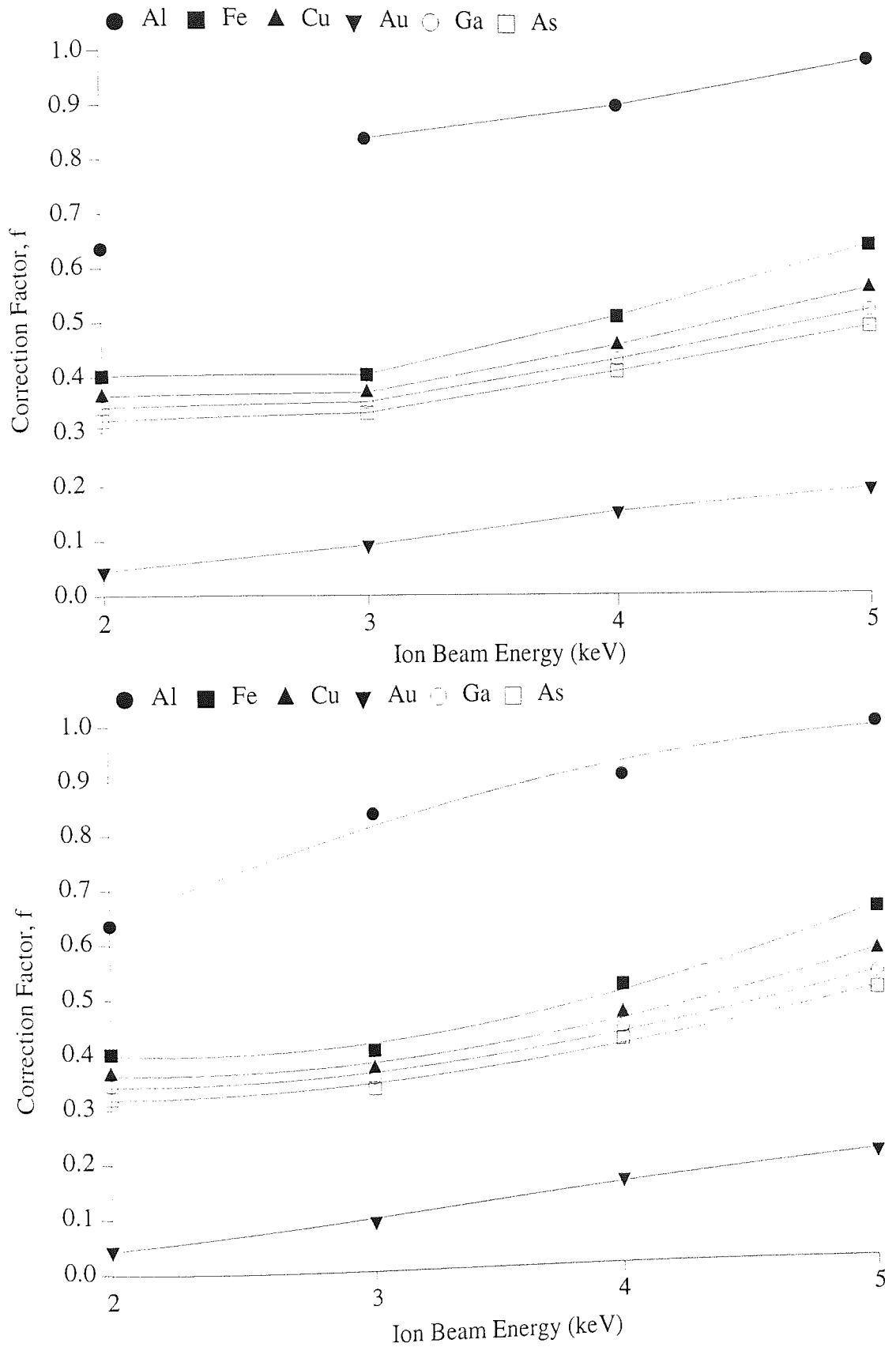


Figure 5.9 The correction factor f for target-nitrogen system, as a function of ion beam energy.

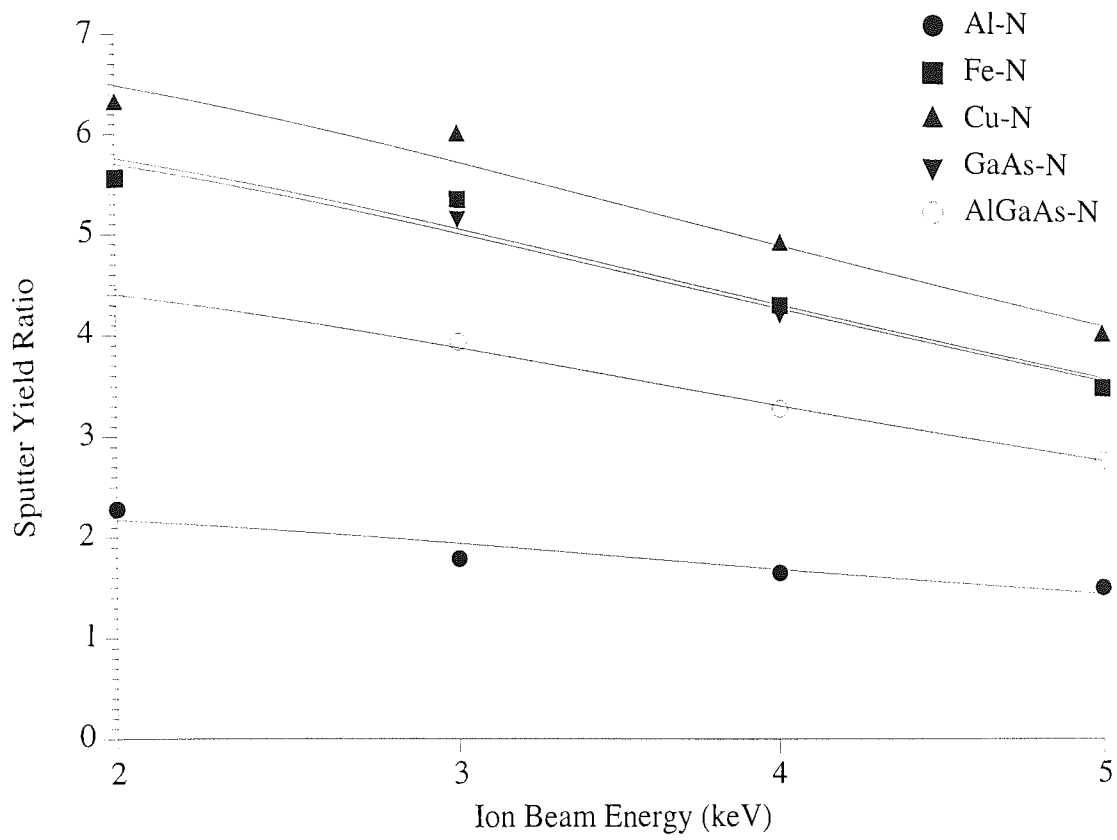


Figure 5.10 Sputter yield ratio, corrected for difference in power scattering parameter for elements with different mass, as a function of ion beam energy. Here it represents the ratio of sputter yield of target material to nitrogen.

calculated depth of the sputtered atoms for various target materials is given in Table 5.10. It is interesting to note that Δx_0 depends on the target density. During ion bombardment, the value of target density changes and hence will the sputter depth.

The Sigmund's method overestimates these depths because of assumption of point particles of the target atoms. In fact, computer simulations and experiments [Oliva et al., 1987] have shown that most sputtered atoms (~80%) come from the first atomic layer, a small number comes from the second layer and a very few come from the deeper region, and the average sputtered depth is accepted to be 1.2 times monolayer [Falcone et al., 1987].

Table 5.10 Average sputter depth Δx_0 for the target materials. Here atomic density is expressed in Atoms/Å³ and depth in Å.

Target	Al	Fe	Cu	Au	GaAs	AlGaAs
Atomic density	0.060	0.085	0.085	0.059	0.022	0.057
Depth	6.872	4.881	4.886	7.011	18.67	7.282

5.6.3 Etch rate:

Using the SUSPRE code, the etch rate values were calculated for the target materials at various ion energies and current densities. The etch rate values for current density 5 $\mu\text{A}/\text{cm}^2$ and at ion beam energies of 2, 3, 4 and 5 keV are given in Table 5.11. For any target, at a given value of ion beam energy, the etch rate value at a current density of 1 $\mu\text{A}/\text{cm}^2$ is 1/5th of the same for current density of 5 $\mu\text{A}/\text{cm}^2$. As expected, the etch rate values increase with increase in ion energy and the etch rates are higher for heavy mass targets. This can be explained by higher sputtering at higher ion energies and for heavy mass targets, Figure 5.4.

Table 5.11 Erosion rate values (nm/s), calculated for various target materials by using SUSPRE code, for ion beams at a given energy and a current density of 5 $\mu\text{A}/\text{cm}^2$.

Ion Beam Energy (keV)	Al	Fe	Cu	Au	GaAs	AlGaAs
2	0.005	0.004	0.006	0.017	0.013	0.011
3	0.006	0.006	0.008	0.025	0.017	0.016
4	0.008	0.008	0.01	0.032	0.022	0.021
5	0.009	0.009	0.012	0.039	0.027	0.024

5.7 Theoretical modelling of implantation:

In order to understand the measured implantation profiles, it is useful to consider model systems. Implantation may be modelled using a number of codes. Here we have chosen two codes, SATVAL and SUSPRE.

5.7.1 SATVAL code:

After irradiation of the sample with N_2^+ beam with energies of $E = 2, 3, 4$ and 5 keV and $5 \mu A/cm^2$, the atomic concentration of the implantant, were calculated from SATVAL as a function of depth. The predicted N implantation profiles, corresponding to the saturation stage are shown in Figure 5.11. The curves shown here will of course not be the same as the measured Ar^+ depth profiles, hence to simulate these profiles the data from SATVAL output file must be modulated according to the electron signal (ES) emitted from the radicals implanted into the target, detected at the surface. The ES for radicals implanted with distribution $n(x)$ into a solid is given by

$$ES = \int n(x) \exp\left(-\frac{x}{\lambda_e}\right) dx \quad \text{for } 0 < x < x_m \quad (5.14)$$

where λ_e is the mean free path of the electrons. For these calculations a simple program in TURBO BASIC was written [Wronski Z.]. The atomic concentration of the implantant at energies of $E = 2, 3, 4$ and 5 keV and $5 \mu A/cm^2$ were calculated from this programme as a function of implantation time and from this the total nitrogen implantation versus time profiles were created. All the implantation profile shown here are for a current density of $5 \mu A/cm^2$, the profiles for $1 \mu A/cm^2$ implantation are exactly the same but the time scale is multiplied by 5. This is because this code takes into account only the athermal processes, which depend upon ion dose and not on current density.

A difficult problem was assigning the value of the surface binding energy. The analysis of different methods available for calculating surface binding energy, (discussed in section 5.3), give different surface binding energy ratios using different models. Some of these models were for calculating only the surface binding energy ratios, but the code requires the absolute value of surface binding energy for implantant and target atoms. In this analysis, the heat of atomization was taken to represent the surface binding energy. The values of this parameter are listed in Table 5.4. For GaAs, the surface binding energy was taken as the average of heat of atomization energies for Ga and As atoms.

Aluminium: The displacement energy for aluminium was chosen as 16 eV [Miyagawa et al., 1998]. The predicted profiles are shown in Figure 5.12. The calculated N/Al saturation ratios are shown in Table 5.12. Figure 5.12 shows that the initial nitrogen concentration values are smaller for higher energy implantation, but nitrogen saturation concentration values are similar for all the ion energies.

Iron: For iron, the displacement energy was taken as 17 eV [Rauschenbach et al., 1984]. The nitrogen ion implantation profiles calculated using this code are shown in Figure 5.13. The calculated N/Fe saturation ratios are shown in Table 5.12. The nitrogen concentration values are nearly same at all the ion energies, but the initial nitrogen atomic concentration is smaller for higher ion energies.

Copper: In the case of copper, the displacement energy was chosen as 16 eV. The predicted profiles are shown in Figure 5.14. The nitrogen concentration values are nearly same at all the ion energies, but the initial nitrogen atomic concentration is smaller for higher ion energies. The calculated N/Cu saturation ratios are given in Table 5.12.

Gold: For gold, the nitrogen ion implantation profiles, calculated using this code are shown in Figure 5.15 and the calculated N/Au saturation ratios are shown in Table 5.12. The displacement energy was taken as 16 eV. The profiles are same as that for copper and other target materials, only the nitrogen saturation is smaller.

Table 5.12 The nitrogen to target atomic concentration ratios (saturated), at various ion energies. These values are predicted by SATVAL.

Energy (keV)	(N/Al)	(N/Fe)	(N/Cu)	(N/Au)	(N/GaAs)
5	0.54	0.22	0.20	0.18	0.23
4	0.54	0.23	0.19	0.18	0.23
3	0.56	0.22	0.19	0.18	0.23
2	0.54	0.22	0.19	0.17	0.22

GaAs: The displacement energy was taken as 15 eV. The nitrogen ion implantation profiles for implantation at $5 \mu\text{A}/\text{cm}^2$, calculated using this code are shown in Figure 5.16. The calculated N/(Ga+As) saturation ratios are given in Table 5.12. Like other target materials, the the initial nitrogen atomic concentration is smaller for higher ion energy implantation, but the nitrogen concentration values are nearly same at all the ion energies.

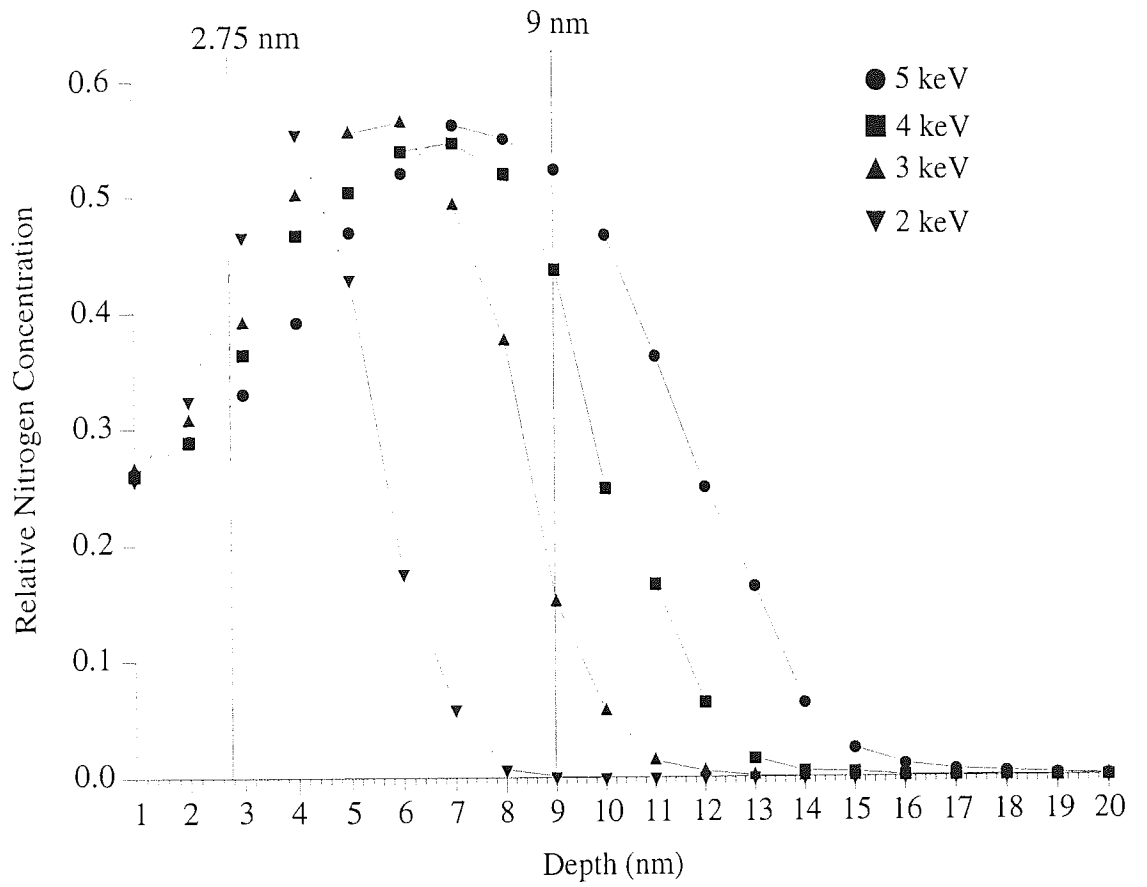


Figure 5.11 Relative areas under the nitrogen ion concentration curves at different energies vs. depth for saturated concentration of nitrogen in aluminium (using SATVAL code).

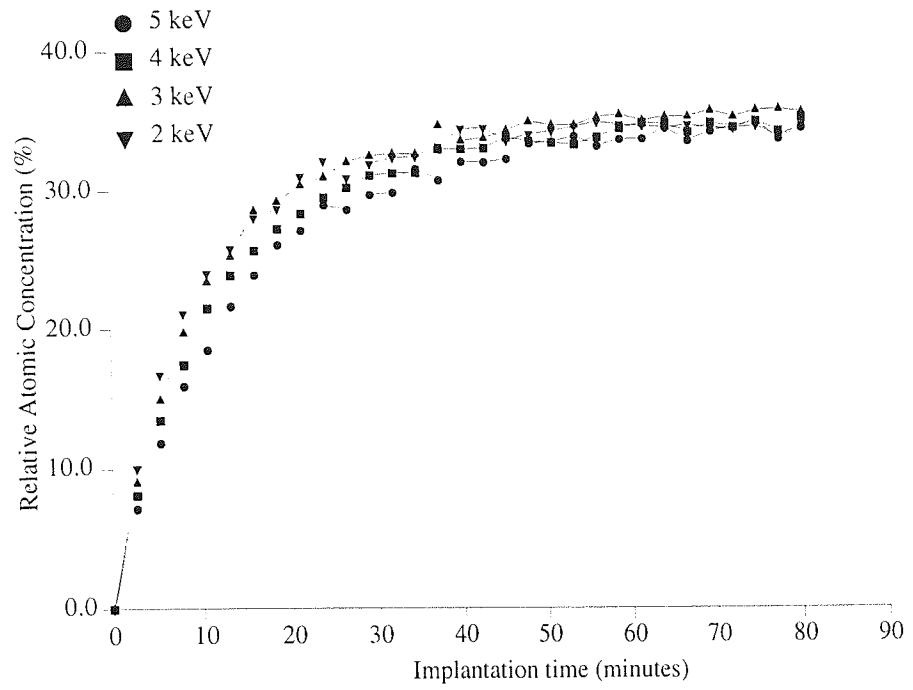


Figure 5.12 Time profile of nitrogen ion implantation on aluminium using SATVAL code at energies $E = 2, 3, 4$ and 5 keV and $\mu = 5 \mu \text{ A/cm}^2$.

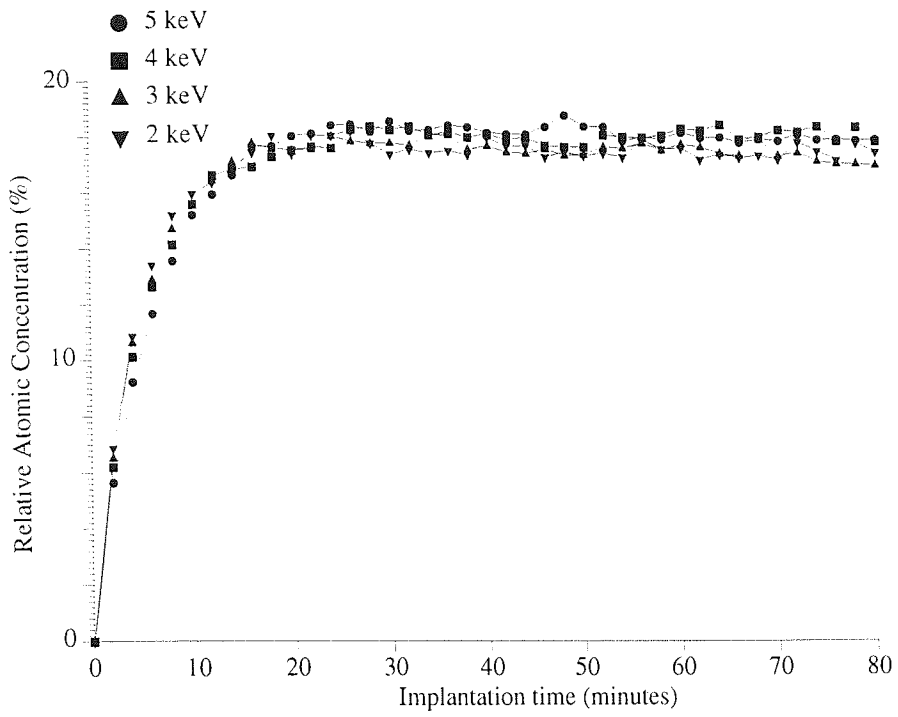


Figure 5.13 XPS time profile of nitrogen ion implantation in iron at 2, 3, 4 and 5 keV at a current density of $5 \mu\text{A}/\text{cm}^2$, calculated from SATVAL code.

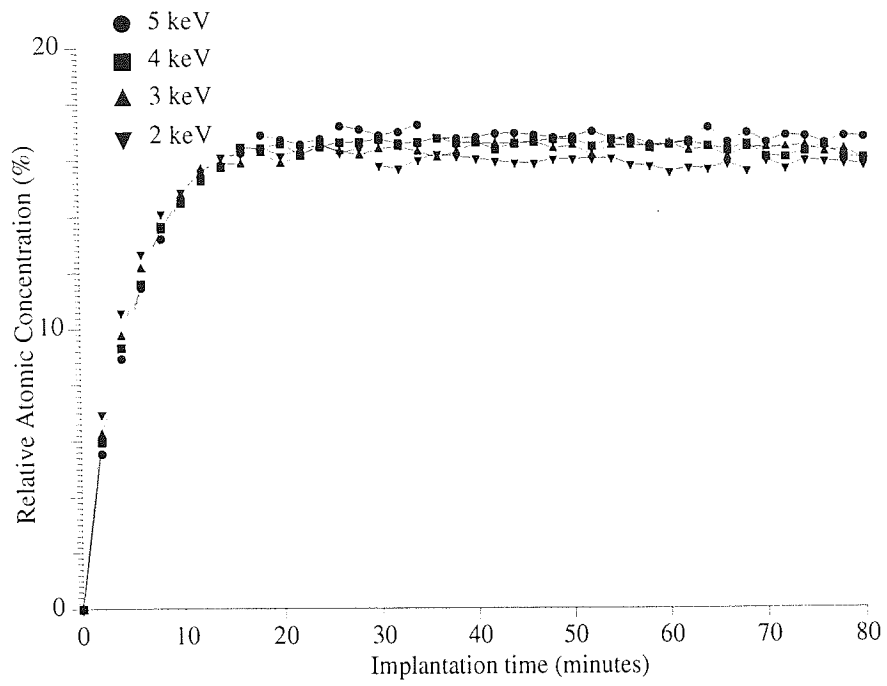


Figure 5.14 XPS time profile of nitrogen ion implantation in copper at 2, 3, 4 and 5 keV at a current density of $5 \mu\text{A}/\text{cm}^2$, calculated using SATVAL code.

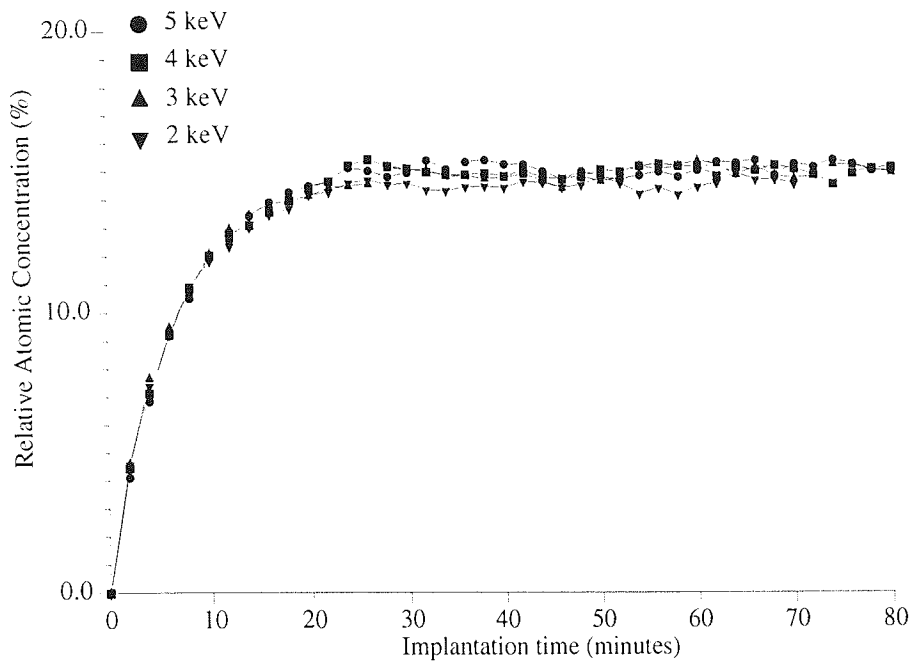


Figure 5.15 XPS time profile of nitrogen ion implantation in Gold at 2, 3, 4 and 5 keV at a current density of $5 \mu\text{A}/\text{cm}^2$, simulated using SATVAL code.

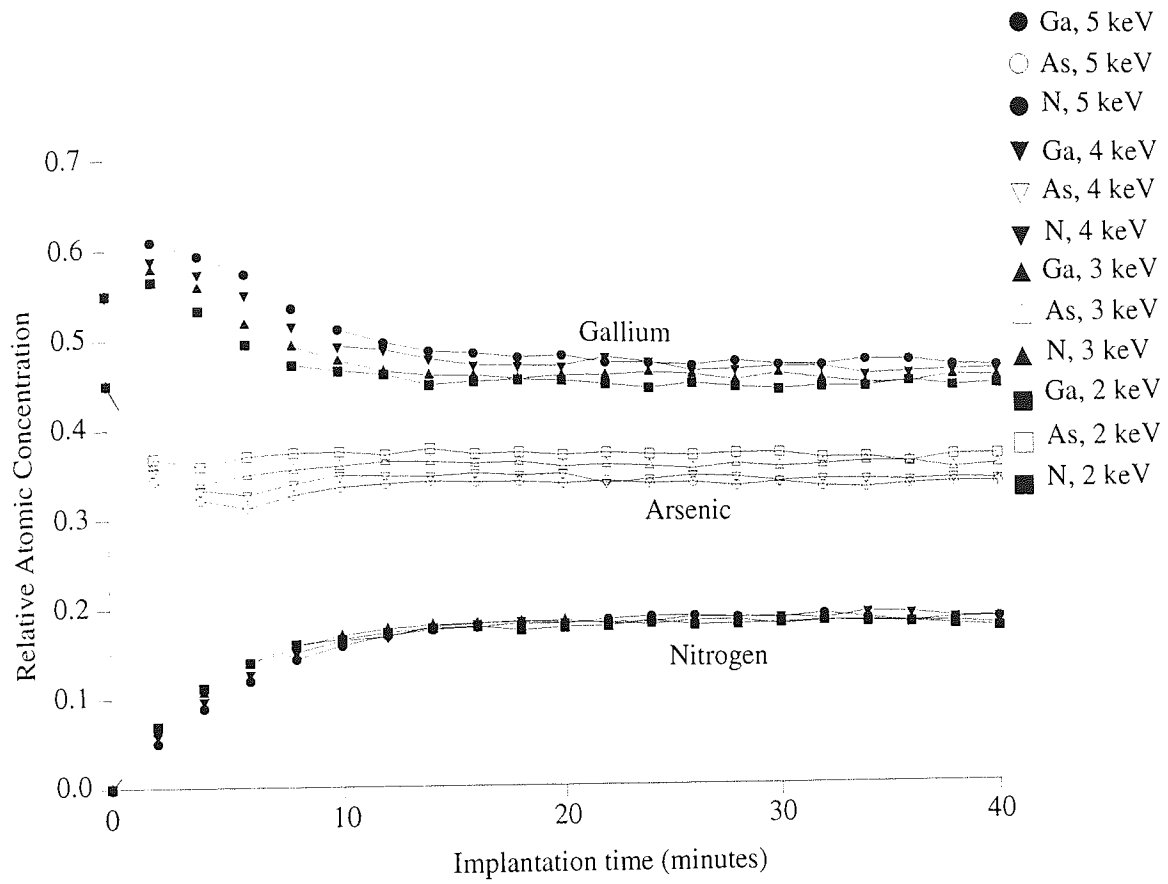


Figure 5.16 XPS time profile of nitrogen ion implantation in GaAs at 2, 3, 4 and 5 keV at a current density of $5 \mu\text{A}/\text{cm}^2$, simulated using SATVAL code.

AlGaAs: In case of AlGaAs, it was not possible to predict profiles using SATVAL, as the code is capable of calculating the implantation only for targets with maximum number of two types of elements, and not for compounds with three or more component elements.

5.7.2 SUSPRE:

SUSPRE calculates high dose implantation profiles by determining the total number of implanted ions and assuming the total number of implanted ions to be uniformly distributed over the nuclear energy deposition profile. It assumes that the implant can be incorporated in the target to a certain solubility limit and then any subsequent implantation results in the loss of implanted particles. For the calculations, the dose for onset of amorphization was set at 3×10^{21} and the solubility limit was selected from the experimental calculations. For example, in the case of iron, experimental data suggests that nitrogen saturates at about 10% and so the solubility limit was set at 0.10. The solubility values and the SUSPRE predicted nitrogen saturation concentration values are tabulated in Table 5.13. The nitrogen saturation concentration values were found to be independent of ion energy.

Table 5.13 The saturated nitrogen to target atomic concentration ratios, predicted by SUSPRE.

	Al	Fe	Cu	Au	GaAs	AlGaAs
(N/Target) _{saturation}	0.50	0.09	0.05	0.002	0.18	0.11
Solubility	1.0	0.1	0.05	0.001	0.2	0.15

5.7.3 Conclusion:

The theoretically predicted values by SATVAL are much higher than the experimentally measured nitrogen saturation concentration and this is almost certainly due to bombardment induced surface segregation of implanted nitrogen, which is eventually preferentially sputtered. This is not taken into account in the code. On the other hand, SUSPRE gives good agreement with experimental nitrogen saturation concentration values, except for AlGaAs. However, the SUSPRE calculations depend very critically on the value chosen for solubility. These values can be obtained only from our experiments and hence the predictions of this code are not independent in the way that the SATVAL results are. The theoretically predicted profiles and nitrogen saturation values are independent of current density but the experimental values are not. This is because the simulation codes are based on athermal processes and do not take into account effects such as surface roughening, diffusion and segregation. The other

factor could be the choice of the surface binding energy. As the sputter yield is very sensitive to the surface binding energy, which we input to the calculation of profiles and the surface binding energy value does change with the surface roughness and the stoichiometric changes. Segregation, which is almost definitely taking place in this case, seems to be contributing to the discrepancy between theoretical and experimental results. The implantation models do not take into account such segregation mechanisms and hence this could explain the smaller amount of nitrogen retention observed from our N saturation measurements and the argon depth profiles. SATVAL is independent of experimental measurement and which should more nearly represent this low energy system, but these codes ignore the chemistry of the process.

5.8 Surface segregation and diffusion:

As discussed in Chapter 1, both surface segregation and diffusion occur frequently at elevated temperature. However, for low energy ion beams with a current of the order of $\sim\mu A$, the power of the beam is not sufficient to heat the target surface to the temperature range, in which thermal segregation and diffusion operate. By assuming the heat generated by the ion beam to be deposited only at the target surface rather than through a finite bulk, the rise in surface temperature can be calculated as [Mack, 1988]

$$\Delta T_s = \frac{2P}{A} \cdot \left(\frac{t}{\pi k d C_p} \right)^{1/2} \quad (5.15)$$

where P is the beam power, A is the bombarding area, t is the bombardment time; k , d and C_p are the thermal conductivity, density and specific heat of the sample, respectively. For aluminium, $C_p = 0.25 \times 10^{-3}$ W hour/g/K, $k = 2.37$ W/cm/K and $d = 2.6$ g/cm³. For a nitrogen ion beam of energy 5 keV and current density of $5 \mu A/cm^2$, hitting the aluminium target area of 0.16 cm², for 1 hour, equation (5.15), gives a surface temperature rise of $2.2^\circ C$. Hence the surface temperature change is not an important factor in surface compositional changes in the target materials.

Ion bombardment of target results in the production of large amount of defects and the process seems to be thermodynamically governed. If one forgets about temperature for a moment, and just consider the increase in entropy caused by ion bombardment, then one could imagine the process to be thermodynamically governed, resulting in segregation and radiation enhanced diffusion.

5.8.1 Surface segregation:

At room temperature, the driving force caused by minimising the surface free energy is so small that the process of surface segregation may not occur or if it occurs, it may be extremely slow. During ion bombardment, the surface atoms may obtain sufficient energy from ions or recoils, to overcome the binding forces and become mobile within the solid surface. This may result in redistribution of atoms and result in surface composition different from the initial composition. According to laws of thermodynamics, the collisions will change the entropy of a system, and this may enhance tendency for thermodynamic segregation which will not be allowed kinetically. Hence surface segregation is possible due to both thermal processes (mainly Gibbsian) and athermal processes.

5.8.1.1 Radiation induced surface segregation:

Surface segregation takes place, normally, within the first two atomic layers and is driven by a force minimising the surface free energy. For a compound A_xB_{1-x} , if the composition at the surface is A_yB_{1-y} , and $y > x$, it means there is a positive adsorption of A on the compound, according to thermodynamics, this adsorption must be accompanied by a decrease in surface energy. The surface energy can be expressed in terms of either heat of sublimation or surface tension. The surface energy changes may be more adequately calculated from the concept of surface tension rather than heat of sublimation or other models, specially under non standard conditions, for example, vacuum.

One of the major problem is lack of surface tension data for solids. A common way for this measurement is by increasing the solid surface by adding more atoms or by stretching the existing solid surface, but then it will be difficult to distinguish between measured surface tension and surface stress. However, in case of liquids, surface stress can be ignored. So for solids, surface tension of pure elements are measured at melting point and on the assumption of linear temperature dependence of surface tension, the surface tension of solids at room temperature is estimated [Zangwill, 1988];

$$\gamma_T = \gamma_0 - \left(\frac{d\gamma}{dT} \right)_P T \quad (5.15)$$

For most of the elements, the term $(d\gamma/dT)$ is changed by no more than 5% in a 100° temperature interval [Ovrbury et al., 1975]. So, a more practical expression derived from equation (5.15) is;

$$\gamma_t = \gamma_m - (t - t_m) \left(\frac{d\gamma}{dT} \right) \quad (5.16)$$

Here γ_m is the surface tension at melting point t_m . The γ_m , t_m , $(d\gamma/dT)$, γ and a are listed in Table 5.14. Here γ is the surface tension at room temperature (298 K) and a is the area of one bulk atom of the elements. The area is estimated by the atomic mass M and ρ density of pure elements, using the equation [Fried et al., 1977];

$$a = \left(\frac{M}{\rho N_A} \right)^{2/3} \quad \text{where } N_A = 6.023 \times 10^{23} \quad (7.17)$$

Table 5.14 Surface tension, melting point and area of one bulk atom of the elements [Lide, 1992]

Element	Al	Fe	Cu	Au	Ga	As	N
γ_m (J/m ²)	0.865	1.806	1.282	1.185	0.718	0.2	0.012
$-d\gamma/dT$ (10 ⁻³ J/m ²)	0.140	0.295	0.150	0.250	0.101	0.600	0.200
M.P.(°C)	660.37	1535	1083.4	1064.4	29.78	817	-209.9
γ_{RT} (J/m ²)	0.954	2.251	1.441	1.445	0.718	0.675	-0.035
a (10 ⁻²⁰ m ²)	6.51	5.18	5.18	6.59	7.27	7.74	0.88

Generally, the surface tension of the solid surfaces depend on the crystallographic orientation. Yu [1995] has taken this into account by defining a ratio $R = (\gamma_{100}/\gamma_0)$. The value of R for (100), (011) and (111) faces of a crystal is 0.224, 0.235 and 0.212, respectively. Yu [1995] expressed the Langmuir-Mclean equation, equation (2.38) as;

$$\left(\frac{x_A}{x_B} \right)_s = \left(\frac{x_A}{x_B} \right)_b \exp(-R(\gamma_A a_A - \gamma_B a_B)) \quad (5.17)$$

Assuming a target with an initial bulk composition predicted by SATVAL, the effect of bombardment induced segregation is determined by calculating the surface composition by using equation (5.17) and the values given in Table 5.14. The initial bulk composition and the resultant surface composition values are listed in Table 5.15. Clearly, in all the cases, there is an enrichment of nitrogen in the top monolayer (BIGS) and this nitrogen will be preferentially sputtered leaving a nitrogen depleted layer in the immediate sub-surface. XPS will show relative depletion that is lower values than predicted for implantation. Results indicate that bombardment induced segregation may be due mainly to thermal processes, but athermal processes cannot be neglected.

5.8.1.2 Segregation due to athermal processes:

Considering athermal processes, in this case collisional cascade effects, and taking the Malherbe modification of Sigmund's relationships for preferential sputtering [equation (1.33)], and the methods outlined by Malherbe to calculate the ratios of surface binding energies and assuming a target with an initial composition predicted by SATVAL, collisional cascade induced segregation composition values are calculated and are given in Table 5.16. It was not possible to perform these calculations for gold and AlGaAs due to lack of required data. In all the cases, except GaAs, there is depletion of nitrogen, as a result of segregation. This shows that segregation is also taking place due to athermal processes, however the extent of segregation is small.

Table 5.15 Tabulation of initial bulk composition and the surface composition values as a result of bombardment induced segregation.

A-B	$(x_A)_b$	$(x_B)_b$	$(x_A)_s$	$(x_B)_s$
Al-N	65	35	32	68
Fe-N	82	18	26	74
Cu-N	84	16	50	50
Au-N	85	15	40	60
GaAs-N	82	18	59	41

Table 5.16 List of initial bulk composition and the collision cascade induced surface segregation composition values.

A-B	$(x_A)_b$	$(x_B)_b$	$(x_A)_s$	$(x_B)_s$
Al-N	65	35	64	36
Fe-N	82	18	85	15
Cu-N	84	16	88	12
GaAs-N	82	18	81	19

5.8.2 Radiation enhanced/induced diffusion:

Ion bombardment may result in the radiation enhanced diffusion (RED) and this effect can be evaluated by comparing diffusion coefficient data of each element in the target. Unfortunately, this data was not available for target-nitride systems. The TRIM simulated distributions of vacancies, Figure 5.17, shows the distribution of target displacements, replacement collisions and vacancies for 2 and 5 keV N_2^+ ions. Here the distribution of collision events are shown only for aluminium, iron and AlGaAs. But the similar

Target Displacements - - - - - Target Vacancies - - - Replacement Collisions

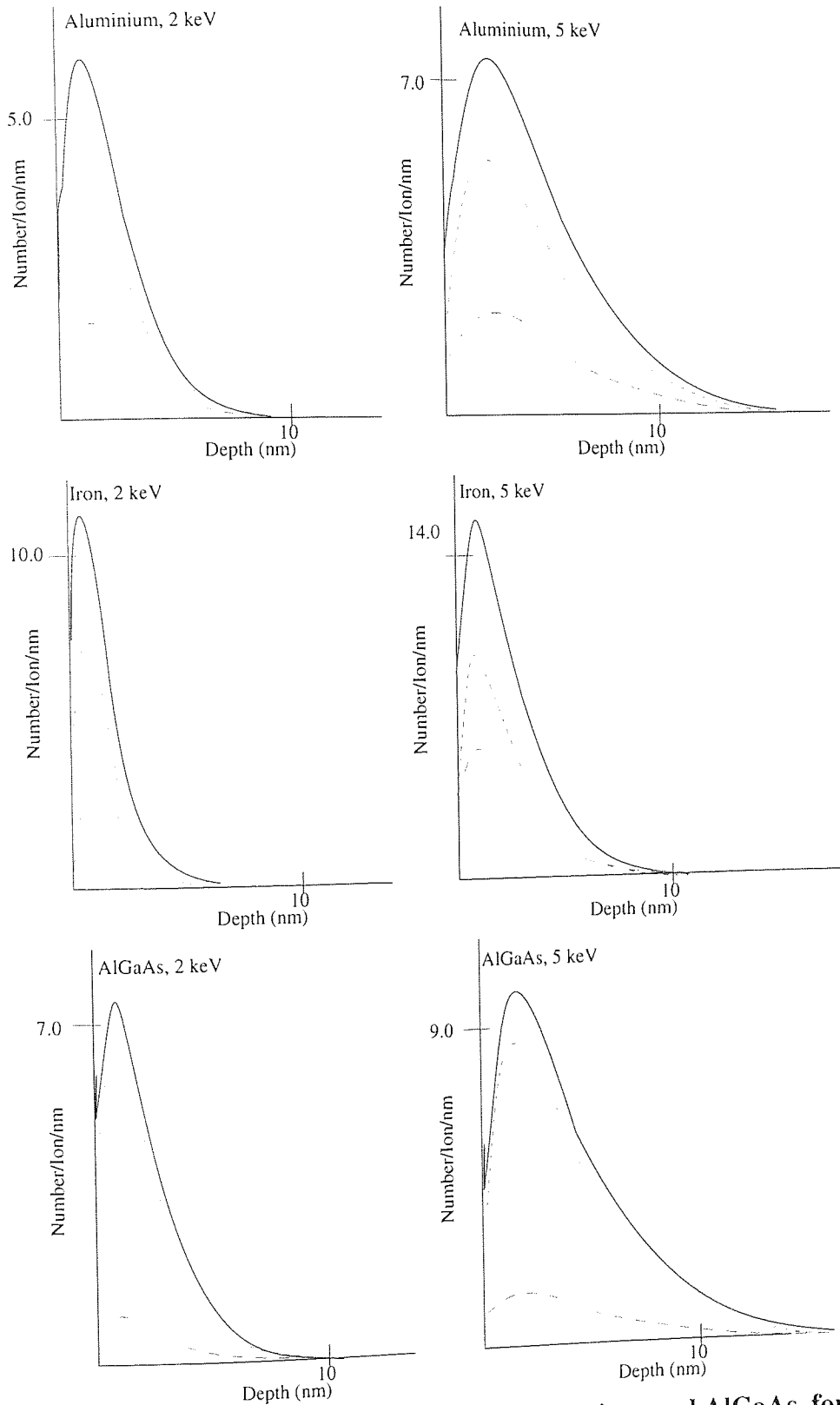


Figure 5.17 Distribution of collision events in aluminium, iron and AlGaAs, for ion beam energy of 2 and 5 keV.

distributions were obtained for the other target materials. Clearly, there is a vacancy-peak at a depth of about 1-2 nm, depending on the ion energy and the target material. According to Weidersich's model [Weidersich et al, 1979] the composition distribution in the radiated region depends on the gradient of total vacancies and preferential coupling between defect fluxes and the fluxes of a certain alloying element. If the migration energy of A atoms via vacancies is lower than that of B atoms, then the concentration of A element may increase in the vacancy rich region. The migration energy of atoms via vacancies is generally unknown, but due to scaling relationship between migration and activation energies [Was, 1990] sometimes latter is used for these predictions. Unfortunately the data for target-nitride systems is unavailable. At room temperatures, the interstitials are more mobile than the vacancies and this leads to a higher fraction of vacancies at the surface compared to the deeper regions. There is a possibility of the formation of stable N-vacancy complexes and hence the nitrogen being segregated to the surface. Ion bombardment will produce traps for migrating vacancies and could reduce the number of free vacancies available during nitrogen implantation.

The diffusion may also may be enhanced by ionisation processes [Bourgoin et al., 1973]. Figure 5.1 shows that the electronic stopping power is also appreciable and as this process depends strongly on the ionisation probability, so the atomic distribution caused by this mechanism is eventually determined by the difference in the first ionisation energy of different elements. The lower the value of first ionisation energy, the greater is the ionisation probability and hence the greater is the mobility. The first ionisation energies of Al, Fe, Cu, Au, Ga, As and N are given in Table 5.17. In the case of compound semiconductors, the ionisation enhanced diffusion will result in Ga and Al enrichment, in GaAs and AlGaAs, respectively. As the ionisation energy of all the target elements is less than that of nitrogen, so in the presence of ionisation enhanced diffusion, they should move faster towards the vacancy spike region, resulting an enrichment of the faster moving target species at depths of about 2-4 nm.

Table 5.17 The first ionisation energy of the target elements [Lide, 1992]

Al	Fe	Cu	Au	Ga	As	N
5.99	7.88	7.73	9.24	6.00	9.83	14.55

In the above discussion, the interstitials related diffusion mechanism is ignored, as the central core region of collisions is generally rich in vacancy related defects while the surrounding layer contains the interstitials [Corbett et al., 1981] and so the interstitial processes may be important in the immediate surface region. But from the analysis of segregation, the compositional changes at the first one or two atomic layers is mainly driven by BIGS.

Chapter 6

Discussion

6.1 Monoenergetic Implantation:

6.1.1 Aluminium:

6.1.1.1 Nitrogen implantation:

Considering the possible experimental uncertainties, the saturation values at various energies and current densities, the relative atomic concentration profiles, Figure 4.1, Figure 4.2, Figure 4.3 and Table 4.1, show no evidence of significant variation in N/Al saturation ratios with energy. Perhaps the mean value of saturation is a little higher at the lower current density. The results for the $5 \mu\text{A}/\text{cm}^2$ might suggest an apparent higher nitrogen relative atomic concentration at lower ion energies, but considering the experimental uncertainties involved one can only conclude that no systematic variation of N/Al saturation values was observed with change in ion energy. Current density can play a role through temperature, but within the range employed in these experiments the possibility of temperature variation large enough to cause the observed changes is negligible. As expected, the saturation is achieved more rapidly for higher current density implantation. According to Tsai and Morabito [1974], the concentration of implanted primary ions reaches a steady-state saturation value when a depth of about $\bar{R}_p + 2\Delta R_p$ has been sputtered away. Taking the values of required parameters from Tables 5.2 and 5.11, the concentration of implanted nitrogen should arrive at a saturation value after about 25 minutes of bombardment time for implantation at $5 \mu\text{A}/\text{cm}^2$ and 125 minutes of bombardment time for implantation at $1 \mu\text{A}/\text{cm}^2$. The saturation time is nearly the same for all ion energies. For example, for implantation at $5 \mu\text{A}/\text{cm}^2$, the time required to reach the saturation stage is 25 minutes at 2 keV ion energy, whilst for 5 keV implantation, the saturation time is 26 minutes. These calculated values of saturation time are slightly higher compared with the same measured experimentally. This is particularly clear for $1 \mu\text{A}/\text{cm}^2$ implantation, however, this is not surprising as in these calculations only ion range distribution and sputtering were considered and all other processes such as segregation and diffusion were ignored.

The theoretically predicted (N/Al) saturation ratios, Table 5.12 and Table 5.13, are also the same for all the ion energies. However the SATVAL predicted values are higher than those

measured. The reasons for this are described in section 5.7.3. Another important factor could be the fact that this simulation code is strictly for atomic beams and does not take account of molecular dissociation. Figure 4.3 and Figure 5.10 show that the initial nitrogen concentration values are smaller for higher energy implantation. During the initial stages of bombardment there is competition between implantation and sputtering. This could be due to higher sputtering of implanted nitrogen at higher ion energies, however, it is unlikely as the etch rates, Table 5.11, are quite small compared to the ion range, Table 5.2. The ion implantation profiles extend deeper into the surface at higher ion energies. The XPS technique, however, detects 85% of emitted photoelectrons from within one inelastic mean free path of the photoelectrons from the surface, which is about 2.7 nm in this case. Hence one would expect that the measurement technique for nitrogen atomic concentration would be more sensitive to the near surface region, giving an apparent higher nitrogen relative atomic concentration at lower ion energies. Looking at the shape of implantation profiles, Figure 5.11, and considering the sampling depth of XPS (discussed in section 2.2.1.3), it seems that the amount of implanted N will be greater at higher ion energies. In fact due to exponential attenuation of the XPS signal combined with deep penetration of ions at higher ion energy, the measured initial nitrogen concentration values are smaller. As the implantation proceeds, there is a pronounced change in the distribution of implanted nitrogen due to sputtering. The sample surface erosion during implantation changes the implantation profile from Gaussian type to a plateau type, Figure 1.5. In the latter type of profile, the effect of exponential attenuation of the XPS signal would be the same in all the cases. Hence towards the saturation state one does not see such an effect. During the generation of XPS depth profiles the information gained from the photoelectron energy spectrum is dependent on the sample state immediately after the period of ion bombardment, but this compositional information will almost certainly be different from the true composition of the compound at that depth.

The width of the implanted profile (sum of range and straggling), Table 5.2 and Figure 5.11, shows the amount of N implanted in the target is greater at higher ion energies. Hence one would expect (N/Al) saturation ratios to increase with ion energy. There may be such a variation but the experimental data does not indicate such a trend. Even if there was such a trend it would be difficult to observe as the scatter is too great to discriminate. This scatter could be due to some errors in quantification (section 2.2.1.3) or due to the initial surface state of the sample being slightly different for different experiments. Although all samples were prepared by following the same procedure (section 3.5), however prior to N_2^+ implantation, all the samples were Ar^+ bombarded to remove the oxide layer. This may have resulted in the surface roughness and the degree of surface roughness may be slightly different in different samples. This may further lead to errors in quantification. Tables 5.12 and 5.13, like the

experimental values, show no discernible variation (N/Al) saturation ratios with ion energy. However, SATVAL predicts the total amount of retained nitrogen will be greater at higher ion energies, Figure 5.11. Here the retained nitrogen at saturation is calculated from the area under the curves shown in this Figure. The area under the curve of nitrogen ion implantation is greater at higher energies. This indicates that the saturation dose increases with increase in ion energy. Hence even though the total retained nitrogen is greater at higher ion energies, due to the deeper penetration of implanted nitrogen at higher ion energies one does not see any change in the (N/Al) saturation ratios within the volume analysed by XPS. This is reflected in our SATVAL predicted (N/Al) saturation ratios because the SATVAL output file is modulated according to the XPS signal (section 5.7.1).

The ion implantation profiles at ion energies $E = 3, 4$ and 5 keV [Figures 4.4 (b), (c) and (d)] show that for a given ion dose the nitrogen relative atomic concentration values are greater at a current density of $1 \mu\text{A}/\text{cm}^2$ compared to those at $5 \mu\text{A}/\text{cm}^2$, but shows no difference in concentration for the 2 keV experiment, Figure 4.4 (a). This suggests the dominance of athermal processes for implantation at an ion energy of 2 keV, but the presence of at least one thermal process for implantation at ion energies of $3, 4$ and 5 keV [Sigmund, 1992]. The most probable thermal process is Gibbsian segregation, resulting in segregation of implanted nitrogen towards the sample surface which is then removed by bombardment. For implantation at $5 \mu\text{A}/\text{cm}^2$ the nitrogen segregates towards the sample surface more rapidly and hence is etched away, giving smaller initial values of relative atomic concentration of nitrogen than in the case of the $1 \mu\text{A}/\text{cm}^2$. The fact that we do not see the effect of this segregation for implantation carried at 2 keV can be explained on the basis of low sputter rate at that ion energy, Table 5.11. The other possibility is that the amount of nitrogen available for segregation is smaller, as the total implanted dose (area under implantation curve, Figure 5.11) is smaller at lower ion energies. This observation is further supported by the ARXPS data, Table 4.3. For ion energies of $E = 3, 4$ and 5 keV, the values of relative atomic concentration of nitrogen at shallow angles are higher for implantation at $5 \mu\text{A}/\text{cm}^2$ as compared to those at $1 \mu\text{A}/\text{cm}^2$.

As discussed in Chapter 5, and section 6.1.1.1, the SATVAL predicted nitrogen saturation concentration values are higher than the experimentally measured nitrogen saturation concentration and this is almost certainly due to bombardment induced surface segregation of implanted nitrogen, which is eventually preferentially sputtered. The calculations show that assuming a target with an initial bulk composition 65% aluminium and 35% nitrogen, bombardment induced segregation results in a surface composition of 32% aluminium and 68% nitrogen. Hence there is an enrichment of nitrogen in the top monolayer and this

nitrogen will be preferentially sputtered leaving a nitrogen depleted layer in the immediate sub-surface (the volume analysed by XPS). Assuming the same initial bulk composition, the collision cascade induced surface segregation results in a surface composition of 64% aluminium and 36% nitrogen. This shows a slight enrichment of nitrogen in the immediate sub-surface (the volume analysed by XPS). These values indicate that in the case of N_2^+ bombarded aluminium, bombardment induced segregation is mainly taking place, resulting in an enrichment of nitrogen in the top layer.

6.1.1.2 Argon ion bombardment:

The Ar^+ bombardment profiles, Figure 4.5, show a fall in N concentration with depth. From the profiles it may be seen that it is not possible to remove all the nitrogen atoms even after a long period of Ar^+ bombardment. This is especially evident for nitrogen ion implantation at higher ion energies. This could be due to deep implantation of nitrogen atoms, recoil implantation of implanted nitrogen or diffusion of weakly bound N via grain boundaries. However the N 1s peak is symmetric, Figure 4.6 and its position indicates the presence of nitrogen atoms in a strongly bound state, hence diffusion seems unlikely unless surface heating is substantial. Thermocouple measurements of surface temperatures during bombardment indicate temperature rises of no more than a few degrees Celsius but the temperatures in the altered layers may be much higher than this. The implantation profiles are expected to show greater persistence of N with depth at higher ion impact energies. This is true for low dose implantation, however for high dose implantation the profiles are inconsistent. As the latter profiles were repeatable and so are true, however there is not a convincing explanation for such behaviour.

6.1.1.3 Al spectra:

The electronegativity values of aluminium and nitrogen, ($\epsilon_{Al} = 1.6$, $\epsilon_N = 3.0$ eV) suggest that the implanted nitrogen atoms will attract valence electrons from the aluminium and as a result of this the Al 2p core level will shift to a higher binding energy. Figure 4.7 shows that by nitrogen ion implantation Al 2p peak broadens and shifts from 72.9 ± 0.1 eV to 73.8 ± 0.1 eV. Wagner [1990] has reported Al 2p peak for AlN at 74.0 eV. This strongly indicates the formation of AlN. Further on nitrogen implantation, the Auger parameter changes from 1466.2 ± 0.2 eV to 1463.2 ± 0.2 and comparison of these values with the values reported by Wagner [1990], Table 4.2, confirm the production of AlN on nitrogen ion implantation and conversion from AlN to Al on Ar^+ bombardment. The comparison of Valence Band XPS spectra, before and after N_2^+ bombardment, Figure 2.5, shows clearly how nitrogen implantation changes metallic aluminium to insulating AlN. As discussed in Chapter 1,

nitrogen ion implantation into aluminium is well known to form AlN [Ohira and Iwaki, 1989], [Lieske and Hezel, 1981], [Raole et al., 1987], [Taylor and Rabalais, 1981], [Rauschenbach and Somer, 1989], [Sullivan et al., 1995], [Rauschenbach et al., 1990], [Carlo et al., 1994], [Terwagne et al., 1991] and [Simson et al., 1998].

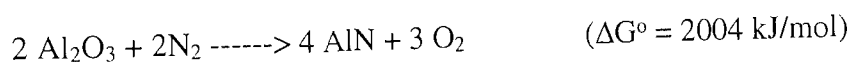
The synthesised Al 2p spectra, Figure 4.8, show the presence of metallic aluminium, AlN and Al₂O₃. The comparison of figures 4.8 (a) and 4.8 (b) shows, how the amount of aluminium in the form aluminium nitride increases with the increase in nitrogen ion bombardment time. The Al 2p peak due to AlN was found to broaden as the concentration of N and the bombardment time increased and this is probably an indication of increasing surface damage, probably lattice distortion or the introduction of lattice defects such as vacancies and interstitials. From Figure 4.9(a) and 4.9(b), it can be seen that the N/Al_{nitride} ratio was greater than 1 during the first few minutes of implantation before settling to an equilibrium value of about 0.7. Ideally covalent bonding of Al and N results in an atomic arrangement in which each species is surrounded by a tetrahedron of four atoms of other species giving 1:1 stoichiometry. The high values recorded during the initial stages of bombardment may be due to N existing in close surface interstitial sites before all N atoms bond with the metal host. It should also be recognised that AlN concentration is low during the initial bombardment period and this can lead to errors in synthesis. For nitrogen ion implantation into an aluminium substrate one might expect stoichiometric AlN to be formed with a N/Al ratio of unity. Our experimental result indicate a measured equilibrium concentration of AlN_{0.7 to 0.8}. Synthesis of the photoelectron Al 2p emission lines shows that not all of the aluminium binds to nitrogen. A small proportion is present at the outer surface as Al₂O₃, but the majority of the remaining aluminium appears to be in the metallic state. The fact that wholly stoichiometric AlN is not formed within the altered layer near to the surface is not too surprising since a degree of reconstruction of surface atoms may occur and during implantation, many vacancies, interstitial and other defects are formed due to radiation damage. All these effects are likely to influence the structure and stoichiometry of the near surface modified region giving rise to a non-ideal phase.

However after considering all the above effects, the major reason for the lower than unity N to Al ratios measured with XPS after N₂⁺ implantation may probably be understood from inspection of the generated experimental time profiles shown in Figure 4.5. Here it can be seen that the N concentration is not constant over the sampling depth of the measurement technique, but is maximum just beneath the oxide layer and then it decreases to some steady state value. This concentration gradient covers much of the analysed depth. Thus the measured total concentrations are effectively the areas under the N concentration curves to a limit of about 9.0 nm modified by an photoelectron exponential decay term.

6.1.1.4 ARXPS results:

The ARXPS results, Table 4.3, are quite interesting, indicating that the nitrogen is present under the oxide contamination layer. This is supported by observations of oxygen and nitrogen Auger peaks. These Auger electrons are of lower kinetic energy and originate from regions closer to the analysed surface. We observed the permanent presence of oxygen O 1s and O KVV peak at low take off angles, but for nitrogen only the N 1s peak was observed. Figure 4.10 also shows that for shallow angles the aluminium is mainly in the form of oxide, but the peak from the bulk shows the presence of aluminium in the form of nitride as well as metallic aluminium. The experimental results show that the concentration of oxygen at the surface remains appreciable even after long periods of ion etching. However, when the amount of oxygen on the sample surface is smaller, relatively larger amounts of nitrogen were found at shallow angles.

Calculations based on these ARXPS results indicate an oxygen rich layer of thickness 0.8 to 1 nm on the surface. During the ion bombardment process the oxygen is removed from the aluminium surface, but due to strong chemical affinity between oxygen and aluminium the oxygen layer is continuously re-formed. Due to this dynamic process the aluminium surface structure becomes very complex, producing a layered system as suggested in Figure 6.1. The thermodynamics at interfaces 1 and 2 would be very different. On the basis of the relationship [Simson et al., 1996],



N_2^+ bombardment of aluminium oxide should only lead to structural defects within the oxide, as the formation of AlN from Al_2O_3 is thermodynamically unfavourable. Similar consideration of the thermodynamics of the system also show that oxy-nitride should not form in this case. As the oxide layer is approximately 1 nm thick and the range of implanted ions is far greater than the thickness, few incident ions will not be stopped in the oxide layer.

6.1.2 Iron:

6.1.2.1 Nitrogen implantation:

The relative atomic concentration profiles, Figures 4.11 and 4.12, Table 4.4 and Figure 4.13, show that within the experimental uncertainties the nitrogen saturation concentration does not vary with ion energy or current density and saturates at approximately 10% for all conditions.

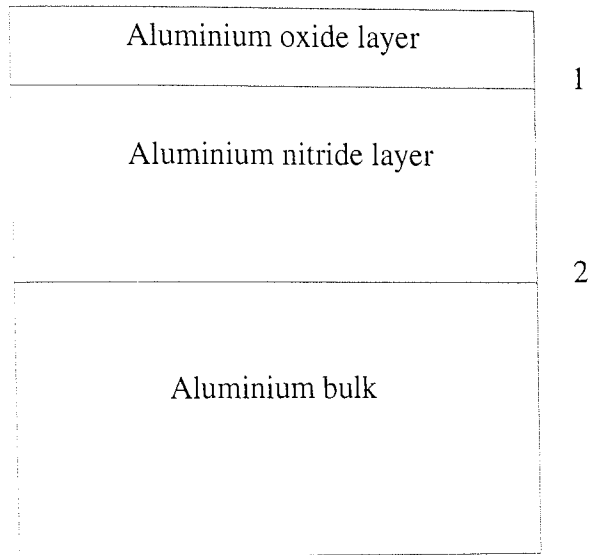


Figure 6.1 Layered structure of aluminium target.

Within the current density range employed in these experiments the current density is not expected to effect the nitrogen saturation concentration, as within this range the possibility of temperature variation caused by current density are not large enough to cause any observed changes. As expected, the saturation is achieved more rapidly for higher current density implantation. According to Tsai and Morabito, [1974], the concentration of implanted primary ions reaches a steady-state saturation value, when a depth of about $\bar{R}_p + 2\Delta R_p$ has been sputtered away [Tsai and Morabito, 1974]. Taking the values of ion range and straggling from Tables 5.2 and etch rates from Table 5.11, the concentration of implanted nitrogen should arrive at a saturation value after about 19 minutes of bombardment time for implantation at $5 \mu\text{A}/\text{cm}^2$ and 95 minutes of bombardment time for implantation at $1 \mu\text{A}/\text{cm}^2$. The saturation time is slightly smaller at higher ion energies. For example, for implantation at $5 \mu\text{A}/\text{cm}^2$, the time required to reach the saturation stage is 19 minutes for 2 keV ion energy, whilst for 5 keV implantation the saturation time is 16 minutes. These calculated values of saturation time are slightly lower compared with the same measured experimentally for $5 \mu\text{A}/\text{cm}^2$ implantation. This could be because these calculations take into account only ion range distribution and sputtering and ignore all the other processes such as segregation and diffusion.

Tables 5.12 and 5.13, show that the theoretically predicted (N/Fe) saturation ratios are similar at all ion energies. The SATVAL predicted values, however, are higher than those measured. This may be due to a number of reasons described in sections 5.7.3 and 6.1.1.1. This will be discussed again under the heading segregation. As the width of the implanted profile (sum of range and straggling), Table 5.2, and hence the amount of N implanted in the target is greater at higher ion energies. Hence one would expect (N/Fe) saturation ratios to increase with ion energy. However, the experimentally measured and theoretically predicted (N/Fe) saturation ratios, Tables 4.4, 5.12 and 5.13, do not show any change with ion energy. The reason for this is deeper penetration of implanted nitrogen at higher ion energies and so although the total amount of retained nitrogen will be greater at higher ion energies, but within the volume analysed by XPS the measured (N/Fe) saturation ratios are independent of ion energy. This is due to exponential attenuation of photoelectron signal and is explained in more detail in the case of aluminium (section 6.1.1.1).

For a given ion dose the ion implantation profiles at ion energies $E = 3, 4$ and 5 keV [Figures 4.14 (b), (c) and (d)] show that the value of nitrogen concentration is higher for implantation performed at $1 \mu\text{A}/\text{cm}^2$ than for $5 \mu\text{A}/\text{cm}^2$, but shows no difference in concentration for the 2 keV implantation, Figure 4.14 (a). This suggests the dominance of athermal processes for implantation at ion energy of 2 keV but the presence of at least one thermal process for

implantation at ion energies of 3, 4 and 5 keV [Sigmund, 1992]. There is a possibility of Gibbsian segregation taking place for implantation carried out at a higher ion dose, resulting in segregation of implanted nitrogen towards the sample surface which is then removed by bombardment. The etch rate of Fe bombarded by nitrogen increases 5 times as the current density increases from $1 \mu\text{A}/\text{cm}^2$ to $5 \mu\text{A}/\text{cm}^2$, (section 5.5.3). Hence, for implantation at $5 \mu\text{A}/\text{cm}^2$, the nitrogen segregated (towards the sample surface) is etched away more rapidly, giving smaller initial values of relative atomic concentration of nitrogen than in the case of the $1 \mu\text{A}/\text{cm}^2$. The fact that we do not see the effect of this segregation for implantation carried at 2 keV can be explained on the basis of low sputter rate at that ion energy, Table 5.11. The other possibility is that the amount of nitrogen available for segregation is smaller as the total implanted dose is smaller at lower ion energies, Table 5.2. [Here, the implanted dose is the area under the implantation curve and the width of the profile (ion range + straggling) is an indication of this area]. Similar results were obtained for nitrogen ion implantation in aluminium (section 6.1.1.1).

6.1.2.3 Argon ion bombardment:

Ar^+ bombardment time and depth profiles, Figure 4.15, show that as expected the nitrogen implantation is shallower at lower ion energies for low dose implantation however high dose implantation profiles are inconsistent. The latter profiles were repeatable and true, however there is not a convincing explanation for such behaviour. From the profiles it may be seen for 5 keV ion implantation, it is not possible to remove all the nitrogen atoms even after a long period of Ar^+ bombardment. This could be due to deep implantation of nitrogen. It should be noted, however, that the absolute depth values will be different from the depth values calculated in this manner, as the sputter yield is matrix dependent.

6.1.2.4 Fe spectra:

Figure 4.16 shows the Fe 2p, Valence band spectra and Auger spectra before and after nitrogen ion bombardment. The electronegativity values of iron and nitrogen, ($\epsilon_{\text{Fe}} = 1.8$, $\epsilon_{\text{N}} = 3.0$ eV) suggest that the implanted nitrogen atoms will attract valence electrons from the iron and as a result of this the Fe 2p core level will shift to a higher binding energy. However, the peak position of Fe 2p remains unchanged, although peak broadening occurs after nitrogen implantation. The separation between Fe $2p_{1/2}$ and Fe $2p_{3/2}$ peaks is unchanged by nitrogen ion implantation. The XPS valence band spectrum of iron similarly did not change on nitrogen ion bombardment and comparison of Auger spectra also shows no chemical shift. All of these results could suggest that N bombardment may not have resulted in chemical change in the metallic iron, although thermodynamic considerations show that this is a very

unlikely event. The enthalpy of formation of iron nitride is negative thus favouring nitride formation. Broadening of the Fe 2p peaks was observed during nitrogen ion bombardment, (FWHM of Fe 2p_{1/2} increases from 2.71 to 2.83 eV and that of Fe 2p_{3/2} increases from 2.55 to 2.61 eV). This indicates some sub-surface modification, possibly lattice distortion or the introduction of lattice defects, but more likely due to a small Fe nitride component peak at higher binding energy. Curve synthesis of Fe 2p_{3/2} is quite unreliable for low concentration to high concentration comparisons due to the asymmetric peak shape and large FWHM. The Auger parameter is sensitive to atomic environment and independent of charge shift and is normally an excellent method of compound identification, but from the results in Table 4.5, it is difficult to say if nitrogen ion bombardment results in any chemical change in the iron, since the values for nitrogen bombarded iron are very close to that of the pure iron. This again, however, is to be expected since the amount of implanted nitrogen is quite small, only 10% and the Fe-N bond photoelectron signal is swamped by the large metallic Fe-Fe peak. Hence even if the chemical interaction is taking place it will be difficult to observe from these spectra and Auger parameter values. However, the formation of nitrides is almost certain because heat of formation of iron nitride is negative, Table 3.4, which means this process is both thermodynamically and kinetically favourable. This point will be discussed in the following sections.

The N 1s peak position, Figure 4.17, was at low binding energy, corresponding to electron-rich nitrogen species such as nitrides. The Auger peak KL₁L₁ was almost absent in most of the cases. When visible its position was found to be at 353.8±0.2 and as N KLL spectra of weakly (molecular like) and strongly (atomic like) bonded nitrogen species on iron surfaces appears in the vicinity of the KL₁L₁ peak, the peak is distinct only in the case of strong bonded nitrogen species [Moncoffre and Jaglieski, 1994].

The XPS analysis was thus not conclusive in deciding whether nitride is formed or not, but the peak position of N 1s for nitrogen bombarded samples (397.4±0.1eV) was found to be similar to that for a mixture of Fe_{2,3,4}N (397.3) [Biwer and Bernasek, 1986 and Zemek, 1987] and this strongly suggests that nitrogen bombardment results in the formation of nitride. Further, the binding energy separation between Fe 2p_{3/2} and N 1s peak was found to be 309.6±0.2 eV, which is similar to that for the standard iron nitride sample at 309.4 eV [Biwer and Bernasek, 1986]. This energy separation coupled with low binding energy of the N 1s confirm the formation of iron nitride. A complication here, however, is that the separation between Fe 2p_{3/2} and N 1s peak is also similar to that reported for nitrogen segregated on iron [Zemek, 1987]. A combination of the two states might thus be possible. Arabczyk and Mussig [1987] suggested that at 5 keV and 100 μA/cm² nitrogen implantation, the nitrogen immediately below the sample surface is in molecule like bonded form and the near surface

region is enriched with nitrogen weakly bonded to iron. For our XPS analysis, the signal comes from the near surface region and not just immediately below the sample surface. The N 1s peak position indicates that nitrogen atoms are present in a strongly bound state, at all the depths analysed by ARXPS.

The amount of implanted nitrogen is quite small (approximately 10%), which can be explained on the basis of reactivity of iron and nitrogen. The heat of formation is an indication of reactivity, as the value of heat of formation of iron nitride is quite high (compared to the same for AlN), Table 3.4, and so the reactivity of nitrogen with iron is small and hence the amount of retained nitrogen is expected to be small. The nitrogen saturation value suggests the formation Fe_9N_1 . However, work on nitrogen ion implantation in iron at high ion energies have indicated the formation of various iron nitride phases [Rauschenbach et al., 1983, 1984 and 1990], [Rauschenbach, 1993], [Moncoffre and Jaglieski, 1994], [Rauschenbach and Hohmuth, 1984] and [Pu et al., 1981]. These seem to support our findings. Zemek and Kral [1987] have shown that nitrogen ion energy of 120 keV, with doses of 8×10^{16} to 5×10^{17} ions/cm², results in the formation of Fe_2N and Fe_{16}N_2 phases, but not all the implanted nitrogen is in a strong nitride bonded state. According to these authors, the nitrogen from the sub-surface region diffuses towards the surface. Rauschenbach et al [1983] have reported the formation of iron nitride phases (Fe_{16}N_2 , Fe_4N , $\text{Fe}_2\text{N}_{1-x}$ etc.) after room temperature nitrogen ion implantation at 30 to 60 keV, with doses from 1×10^{16} to 1×10^{18} ions /cm². They explained the formation of different metastable phases on the basis of thermal spike model and described phase transformation from Fe_{16}N_2 to Fe_4N and $\text{Fe}_2\text{N}_{1-x}$ due to diffusion process resulting in nitrogen enrichment. For implantation carried out at low energies (2 to 5 keV), we do not expect the formation of spikes and hence Fe_{16}N_2 would be retained. Thus from our measurements, in the ion energy range 2 - 5 keV, it seems that iron nitride is formed as Fe_{16}N_2 . Considering the temperature rises in our experiments, diffusion would be insignificant (discussed in detail at later stage) and hence transformation to higher nitrides will not take place. Ideally then, bonding of Fe and N should result in 8:1 stoichiometry, but the fact that the equilibrium value was 9:1, rather than 8:1, may have been due to concentration gradients within the depth integrated by the XPS technique, as explained in the case of previous AlN measurements.

The difference in nitrogen concentration and phases of Fe nitrides in low energy and high energy experiments can also be explained by considering how the energetic ions lose their energy via collisional cascades. The transfer of ion energy to nuclei through collisions, results in deflection of incident ion, movement of target nuclei from their original lattice sites, excitation of electrons to higher energy levels and even ionisation. The processes are

characterised by nuclear stopping power $S_n(E)$ and electronic stopping power $S_e(E)$. For 5 keV N_2^+ implantation, only 19.0 % of the incident energy is lost by electronic (inelastic) collisions while for 200 keV N_2^+ implantation, 52.5 % of the incident energy is lost by electronic energy loss, Table 6.1. The higher value of electronic stopping power for high energy implantation means there will be different structural modification of the target and greater probability of chemical interaction, hence enhancing the possibility of different nitride phases.

Table 6.1 Nuclear and electronic stopping powers of nitrogen ions in iron, calculated using SUSPRE code.

Ion energy (keV)	S_n (E) (keV)	S_e (E) (keV)
5	1.512 (60.4 %)	0.473 (19.0 %)
200	38.033 (38.0 %)	52.486 (52.5 %)

The bombardment of the target by an energetic ion beam changes the composition of the target surface region to a depth comparable to the projectile range. The values of projectile range and range straggling were calculated using TRIM and are listed in Table 5.2. The electronegativity values of iron and nitrogen, suggest chemical interaction between iron and nitrogen and hence significant nitrogen retention in iron. The concentration of the nitrogen atoms in the iron target is dependent of reaction probability of nitrogen atoms with the iron atoms and the probability of sputtering the reaction product of iron and nitrogen by the incident nitrogen ions. In the energy range of 0.2 - 3 keV, the reaction probability of nitrogen with iron is reported to be 0.14 [Pu and Rabalais, 1981]. The reaction cross-section and the probability of sputtering of the reaction product (iron nitride, in this case) both show a small decrease with the increase in ion energy. However, the experimental results show that within experimental uncertainty, the saturation value of the relative atomic concentration of nitrogen is similar at all ion energies. As this process of nitridation is associated with reaction between implanted N atoms and Fe, so the thickness of the iron nitride layer will be of the same order as the penetration depth of incident ions. The values of this quantity for projected ions, shown in Table 5.2, suggest that the nitridation is confined to of few nm depth from the surface.

6.1.2.4 ARXPS results:

The ARXPS results for nitrogen ion implantation, Table 4.7, show the relative concentration

of nitrogen on the surface was higher in almost all the cases compared to the same measured from zero take off angle. This suggests surface segregation of the implanted nitrogen. Also comparison of the data at various ion energies and current densities shows that although the relative atomic concentration of nitrogen is similar for 0° TOA at all implantation energies, its value at high TOA's is higher for implantation carried out at higher ion energies. This suggests that surface segregation is more effective at higher ion energies and supports the findings from the concentration versus dose curves that thermal processes become more important at higher energies.

The thermodynamics and structure of segregation suggests that the enthalpy of segregation of N in Fe (100) surface is about -110 kJ/mole [Grabke et al., 1977]. As the solubility of nitrogen is low in iron and high dose implantation produces a region oversaturated by nitrogen with high defect concentration, surface bombardment enhanced segregation is expected.

Thermal diffusion, on the other hand is most unlikely. The diffusion coefficient of nitrogen in α -iron is given by [Rozenale et al., 1983] $D = D_0 \exp(-Q/RT)$, where $D_0 = 6.6 \times 10^{-7} \text{ m}^2/\text{s}$ and $Q = 779000 \text{ J/mole}$. Thermocouple measurements of surface temperatures during bombardment indicate temperature rises of no more than a few degrees Celsius, however the temperatures in the altered layers may be much higher than this. Assuming that the temperature rise is only a few degree Celcius, one gets $D = 0$, so the thermal diffusion seems unlikely unless surface heating is substantial.

The ARXPS data also suggests that iron carbide is formed below a layer of adventitious carbon, however, the total carbon concentration was very low. The formation of iron carbide and iron carbonitride has been reported to take place for ion implantation carried out at ion energies of 30 keV to 60 keV with doses from 1×10^{16} to 1×10^{18} ions cm^{-2} , at a pressure of 10^{-3} to 10^{-4} Pa [Rauschenbach and Hohmuth, 1984], but there is no suggestion that a carbonitride was formed in these experiments.

Surface segregation

As discussed in Chapter 5 and section 6.1.2.1, the SATVAL predicted nitrogen saturation concentration values are much higher than the experimentally measured nitrogen saturation concentration and this is almost certainly due to bombardment induced surface segregation of implanted nitrogen, which is eventually preferentially sputtered. The calculations in Chapter 5 indicate that both Gibbsian and collision cascade initiated segregation is taking place.

Assuming a target with an initial bulk composition 82% iron and 18% nitrogen (SATVAL predicted) bombardment induced segregation results in a surface composition of 26% iron and 74% nitrogen, that is an enrichment of nitrogen in the top monolayer and this nitrogen will be preferentially sputtered leaving a nitrogen depleted layer in the immediate sub-surface (the volume analysed by XPS). Assuming the same initial bulk composition, the collision cascade induced surface segregation results in a surface composition of 85% iron and 15% nitrogen, that is an enrichment of iron in the immediate sub-surface (the volume analysed by XPS).

Another possible thermal process is Radiation Induced Segregation (RIS), which produces concentration gradients by segregation of impurity complexes towards the defect sink. Moncoffre and Jagielski [1994] have reported RIS of nitrogen in iron for implantation carried out at 50 to 150 keV at 150°C. There is a possibility of the formation of stable N-vacancy complexes and hence the nitrogen being segregated to the surface. Ion bombardment will produce traps for migrating vacancies and could reduce the number of free vacancies available during nitrogen implantation. Figure 5.17 shows the distribution of vacancies created by 2 keV and 5 keV nitrogen ions, with maximum vacancy concentration lying at about 1.0 nm from the surface. The number of vacancies produced is greater at higher ion energies, but the experimentally measured (N/Fe) saturation value is similar for all the ion energies and current densities. However, considering Table 4.7, at shallow electron take-off angles, the N/Fe ratios are slightly higher at higher ion energies and this could be due to vacancies created by nitrogen ions near to the surface. Due to the large sampling depth of XPS, one may not observe the effect of larger number of vacancies at higher ion energies.

Another possibility is that the mixing and preferential sputtering processes result in preferential sputtering of the implanted nitrogen. When the nitrogen beam strikes the nitrided iron, it will break some of the iron-nitrogen bonds and the dissociated nitrogen will be preferentially sputtered due to smaller mass. There is a possibility that the segregated nitrogen atoms combines to form molecular nitrogen, which is desorbed by the X-ray irradiation. Zemek and Kral [1987] have reported this type of desorption.

During ion bombardment of the target, the composition of the surface region of the target to a depth comparable to the projectile range is changed due to the various surface effects such as implantation of primaries, recoil implantation, preferential sputtering, collisional mixing, pressure relaxation, cascade mixing, Gibbsian segregation, BIGS and RIS. In addition to initiating collision cascades, the ion beam itself changes the overall composition of the target and as a result, there may be changes in the processes described above.

6.1.3 Copper:

6.1.3.1 Nitrogen implantation:

The relative atomic concentration profiles, Figures 4.18 and 4.19, and the normalized concentration profiles, Figure 4.20, and list of (N/Cu) saturation ratios, Table 4.8, show no evidence of significant variation in N saturation values with energy and current density. As expected, the saturation is achieved more rapidly for higher current density implantation. As described for nitrogen implantation in the case of aluminium, the calculations show that the concentration of implanted nitrogen should arrive at a saturation value after about 12 minutes of bombardment time for implantation at $5 \mu\text{A}/\text{cm}^2$ and 60 minutes of bombardment time for implantation at $1 \mu\text{A}/\text{cm}^2$. The saturation time is same for all ion energies. These calculated values of saturation time are consistent with those measured experimentally.

As described in the case of nitrogen implantation in the case of aluminium and iron, sections 6.1.1.1 and 6.1.2.1, one would not expect the variation of (N/Cu) saturation ratios with current densities. However one would expect these ratios to increase with increase in ion energy but the experimental data does not indicate such a trend. Even if there was such a trend, it will be difficult to observe as the scatter is too great to discriminate. This scatter could be due to all the reasons described for nitrogen implantation in the case of aluminium plus the fact that the amount of implanted nitrogen is small which will further add to some errors in quantification and hence a scatter in the measured data.

The theoretically predicted (N/Cu) saturation ratios, Table 5.12 and Table 5.13, are also same for all the ion energies. However the SATVAL predicted values are higher than those measured. The reasons for this are described in sections 5.7.3 and 6.1.1.1. The most important factor could be the fact that the simulation code does not take into account the chemistry of the implantation process.

6.1.3.2 Argon ion bombardment:

The Ar^+ bombardment profiles, Figure 4.21, show that nitrogen profile consist of a maximum concentration of nitrogen from surface and then decreasing to a steady state value. Due to statistical variations, it is difficult to see any trend of these profiles with ion energy and current density. The reasons for this scatter in data are as described in section 6.1.3.1.

6.1.3.3 Cu spectra:

Comparison of the Cu 2p, Valence band spectra and Auger spectra before and after nitrogen ion bombardment, Figure 4.22, shows no change. The electronegativity values of copper and nitrogen, ($\epsilon_{\text{Cu}}=1.9$, $\epsilon_{\text{N}}=3.0$ eV) suggest that the implanted nitrogen atoms will attract valence electrons from the copper and as a result of this the Cu 2p core level will shift to a higher binding energy. The peak position of Cu 2p remains unchanged, however, the peak becomes slightly broadened after the nitrogen implantation. As the amount of implanted nitrogen is quite small, a change in Cu 2p peak position would not be expected and the broadening of the peak could be due to implantation of nitrogen or due to the introduction of lattice defects. The energy difference between Cu 2p_{1/2} and Cu 2p_{3/2} peaks remains same, 19.9 ± 0.2 eV, before and after nitrogen ion implantation. The analysis of standard Cu₃N sample shows this difference to be 19.7 ± 0.2 eV. As the energy difference between Cu 2p_{1/2} and Cu 2p_{3/2} peaks is nearly the same for pure Cu and nitrided copper and so the analysis of this separation is not very helpful in deciding the chemical state of N₂⁺ bombarded copper. These results therefore do not show definite evidence of chemical interaction between copper and nitrogen.

From Table 4.9, it is hard to say if nitrogen ion bombardment results in any chemical change in the copper. This is to be expected since the amount of implanted nitrogen is quite small, only 5% relative atomic concentration of nitrogen and 95% of copper, hence even if chemical interaction is taking place it will be difficult to observe from these spectras and Auger parameter values. Curve synthesis is a possible method of finding the various components of copper present in different chemical states, but an accurate peak fitting of Cu 2p_{3/2} is difficult due to small amount of nitrogen.

The spectra of N 1s, Figure 4.23(a), shows the presence of two peaks of nitrogen at peak position 396.8 ± 0.1 eV and 403.3 ± 0.1 eV. The comparison of binding energy separation between Cu 2p_{3/2} and N 1s peak for N₂⁺ bombarded copper and standard copper nitride, suggests that the nitrogen peak at 396.8 ± 0.1 eV is due to copper nitride and the peak at 403.3 ± 0.1 eV is due to weakly bound nitrogen [Rauschenbach and Somer, 1989] or the nitrogen bound to oxygen [Kovacich et al., 1984].

6.1.3.4 ARXPS results:

The ARXPS results, Table 4.10, show that the relative concentration of nitrogen on the surface is slightly higher in almost all the cases compared to the same measured from the near

surface region. This suggests surface segregation of the implanted nitrogen. However considering the experimental uncertainties it is hard to say if the trend is real. The nitrogen peak positions (section 6.1.1.3) remain same at all the angles. This indicates that the segregated nitrogen (if segregated) is bonded to copper and oxygen.

6.1.3.5 Implantation mechanism:

The depth distribution of implantant is governed by nuclear stopping, electronic stopping and the mobility of the implantant. Mobility of the implantant is readily reduced if it reacts with the target atoms to form compounds with physical dimensions too large for high mobility. Reduced mobility will result in the expected near-Gaussian secondary peak and little or no surface peak. However the enhanced mobility will result in a distribution profile different from the expected and is guided by the nature of the mobile species and the nature of the defect fluxes. Using AES, Tougaard et al [1985] have reported a strong surface peak and a significant secondary peak (projected range) for 3 keV nitrogen (mainly N_2^+) implanted in copper. Formation of nitrides is thermodynamically and kinetically favoured if the heat of formation of nitride is negative. The enthalpy of formation of Cu_3N is +0.77 eV/atom but XPS analysis confirms the formation of copper nitride. Hence under the conditions of ion implantation, it is possible to form the nitrides which are thermodynamically and kinetically unfavourable. Formation of Cu_3N will result in some retention of the implanted nitrogen atoms at or near the surface region where they stopped in the target (projected range) but still the effect of segregation is expected to be dominant. Tougaard et al [1985] have indicated that for 3 - 4.5 keV N_2^+ bombardment, nitrogen segregates in the direction of defects.

The effect of current density is an excellent way of distinguishing between athermal and thermal process however the amount of implanted nitrogen being small, the experimental data was not helpful. However the calculations in Chapter 5 indicate that both Gibbsian and collision cascade initiated segregation is taking place in the case of copper. Assuming a target with an initial bulk composition 84% copper and 16% nitrogen, bombardment induced segregation results in a surface composition of 50% copper and 50% nitrogen. This is an enrichment of nitrogen in the top monolayer and this nitrogen will be preferentially sputtered leaving a nitrogen depleted layer in the immediate sub-surface (the volume analysed by XPS). Assuming the same initial bulk composition, the collision cascade induced surface segregation results in a surface composition of 88% copper and 12% nitrogen. This shows an enrichment of copper in the immediate sub-surface (the volume analysed by XPS). These calculations show that bombardment induced segregation is mainly taking place.

6.4 Gold:

The comparison of Au 4d, Au 4f and the valence band spectra of gold, before and after N_2^+ bombardment, Figure 4.24 clearly shows that the peak positions and peak widths of Au remain unchanged by the ion bombardment. In addition to this the nitrogen was very rarely observed and whenever it was observed the amount was very small and the nitrogen Auger lines did not appear. The nitrogen was present at only one or two levels and missing at most of the levels. It seems that occasionally nitrogen is present at interstitial sites. However, SATVAL predicts (N/Au) saturation ratio to be 18%, Table 5.12, but SUSPRE predicted values are in agreement with those measured experimentally. The reasons for these are explained in sections 5.7.3 and 6.1.1.1. The main reason for discrepancy between the experimental and SATVAL results is the fact that the code considers implantation as a physical process and does not take into account the chemistry of the process.

Although there is no chemical interaction between gold and nitrogen but one would still expect some retention of nitrogen, which was absent in most of the experiments performed on gold, in the energy range of 2 to 5 keV. The depth distribution of implanted nitrogen will depend on nuclear stopping, electronic stopping and the mobility of the nitrogen in gold. The chemical reaction between gold and nitrogen is not possible and the physical dimensions of nitrogen are small. Hence the mobility of a single nitrogen atom in a defect-laden gold lattice and Radiation Induced Segregation (RIS) effects will be dominant. This will result in a distribution profile different from the expected and is guided by the nature of the mobile species and the nature of the defect fluxes. At room temperatures the interstitials are more mobile than the vacancies and this leads to a higher fraction of vacancies at the surface compared to the deeper regions [Moncoffre and Jagielski, 1994]. Hence there is a possibility of the formation of stable N-vacancy complexes and hence the nitrogen being segregated to the surface. Using AES, Tougaard et al [1985] have reported a surface localized with a long tail for 3 keV nitrogen (mainly N_2^+) implanted in gold. However using XPS or ARXPS, no such effects were observed in our experiments. The calculations in Chapter 5 indicate that assuming a target with an initial bulk composition 85% Gold and 15% nitrogen, bombardment induced segregation results in a surface composition of 40% Gold and 60% nitrogen, that is an enrichment of nitrogen in the top monolayer and this nitrogen will be preferentially sputtered leaving a nitrogen depleted layer in the immediate sub-surface (the volume analysed by XPS). Although in these calculations, the initial composition values were predicted from the SATVAL code, which do not represent true composition (as the code does not take into account the inertness of gold towards the nitrogen), however the calculations give qualitative information that segregation of nitrogen is taking place.

As the mass of nitrogen is smaller compared to gold and the fact that it is not in a bound state, the segregated nitrogen being sputtered away. So ion-target mismatch combined with surface segregation and preferential sputtering of nitrogen will result in a very little or no nitrogen retention, especially at the depths analysed by XPS. Even at 60° electron take-off-angle (sampling depth ≈ 4.5 nm), there was no nitrogen. Liu et al [1989] have also reported that gold nitrides are not formed even with ions of energy of several tens to hundred keV. Bhattacharya and Prabhawalkar [1991] have reported the N_2^+ bombardment of Au-Cu system at 150 keV and ion dose of 2×10^{16} ions cm^{-2} results in the formation of metastable bonds with copper whilst the nitrogen remains only as an interstitial in the gold matrix. The reason for some retention of nitrogen in the bulk at higher ion energies could be due to greater range at higher energies compared to the same at lower ion energies.

6.1.5 GaAs:

6.1.5.1 Nitrogen implantation:

Figures 4.26, 4.27 and 4.28, show that due to the statistical fluctuations in nitrogen concentration values, especially for implantation at higher energies and higher current density, it is difficult to see the variation of nitrogen saturation concentration values with ion energy and ion current density. The scatter in the data is due to all the reasons described in section 6.1.1.1 for the scatter of (N/Al) relative atomic concentration ratios, and the fact that implantation process is more complicated in the compound targets. In the case of N_2^+ bombarded GaAs, in addition to implantation and sputtering, there is segregation of As initiated by various factors. These processes will be discussed at later stage. Within the experimental uncertainties, the [N/(Ga+As)] relative atomic concentration ratio saturates at approximately 20% for all conditions however for implantation at higher current density the saturation occurs in a shorter period of time. As explained in case of nitrogen implantation in aluminium by taking the values of required parameters from Tables 5.2 and 5.11, the concentration of implanted nitrogen should arrive at a saturation value after about 10 minutes of bombardment time for implantation at $5 \mu A/cm^2$ and 50 minutes of bombardment time for implantation at $1 \mu A/cm^2$. The saturation time is nearly same for all ion energies. For implantation at $5 \mu A/cm^2$, the time required to reach the saturation stage is 10 minutes for 2 keV ion energy whilst for 5 keV implantation, saturation time is 9 minutes. These calculated values of saturation time agree reasonably well with those measured experimentally.

The theoretically predicted N/(Ga+As) saturation ratios, Table 5.12 and Table 5.13, are same

for all the ion energies. However the SATVAL predicted values are slightly higher than those measured. This may be due to the reasons described in sections 5.7.3 and 6.1.1.1. Segregation which is almost definitely taking place in this case, also contributes to a discrepancy between theoretical and experimental results. The other factor could be the choice of the surface binding energy. The sputter yield (an input to the calculation of profiles) is very sensitive to the surface binding energy and the surface binding energy value does change with the surface roughness and the stoichiometric changes. This would also contribute to a discrepancy between the theoretical and experimental results.

N_2^+ bombardment of GaAs results in As depletion. Figure 4.29 shows that most of the As depletion occurred during initial few minutes of N_2^+ bombardment. The depletion appeared to be slightly greater for ion implantation at $5 \mu A/cm^2$ compared to the same at $1 \mu A/cm^2$, but does not depend on ion energy. The factors responsible for As depletion will be discussed in section 6.1.5.5.

6.1.5.2 Argon ion bombardment:

Figure 4.30 shows that the Ar^+ bombardment profiles of implanted nitrogen, consist of a maximum concentration of nitrogen at surface and then decreasing to a steady state value at few nm below the surface. As the process of nitridation is associated with reaction between implanted N atoms and target atoms hence the thickness of the nitride layer will be of the same order as the penetration depth of incident ions. As the ion range is greater at high ion energies, one would expect the thickness of nitride layer to be comparatively greater for high energy implantation, however, such a trend is not apparent from experimental data. This may be due to higher sputter rate at higher ion energies, limiting the growth of nitride layer. However, considering the magnitude of ion range, Table 5.2 and sputter rate values, Table 5.11, it seems unlikely. The other reason could be the amount of segregated nitrogen being greater at higher energy implantation [Williamson et al., 1997], (as the total implanted dose, predicted by sum of ion range and straggling, Table 5.2, is greater at higher ion energies and so will be the amount of nitrogen available for segregation) and this segregated nitrogen will eventually be sputter removed. However, there is no experimental data to support this.

Figure 4.31, shows that the As/Ga ratios increase during the first few minutes of Ar^+ bombardment and then they show a steady increase towards but never quite reaching the pre-bombardment condition.

6.1.5.3 GaAs spectra:

On nitrogen ion bombardment of GaAs, Ga 3d peak broadens and shifts to higher binding energy, while the As 3d peak width remains almost unchanged, Figure 4.32. This broadening of Ga 3d peak could be due to direct binding between gallium and nitrogen atoms or due to the introduction of lattice defects, however the latter would not account for the shift. The comparison of these spectra suggests chemical interaction between nitrogen and Ga atoms and a little or no chemical interaction between nitrogen and As atoms. However, the Auger spectra of Ga and As did not show any appreciable change in peak position or peak shape.

Table 4.11, shows that the change in value of Auger parameter is very small and the value of Auger parameter of N_2^+ bombarded GaAs is closer to GaAs than GaN. Hence in this case the Auger parameter is not useful in identifying chemical interaction between nitrogen and Ga atoms. This is not surprising as the amount of implanted nitrogen is small, only 15 - 20 atomic %, hence even if all the implanted nitrogen binds with gallium, there are still large number of gallium atoms in the form of GaAs and, as a result, Auger peak position change is not observed. To investigate the chemical state of As, a similar analysis was performed, which suggested that nitrogen ion bombardment does not result in any chemical change in the As. To check the chemical interaction between implanted nitrogen and As, pure arsenic samples were bombarded with nitrogen ions. This did not result in any change in the spectra of As. The nitrogen photoelectron signal was very rarely observed and whenever it was, it was very small, confirming no chemical interaction between arsenic and nitrogen atoms. As the melting point of Ga is quite low (29.8 °C), hence it was not possible to carry similar analysis with pure gallium target.

Curve synthesis is a possible method of finding the various components of Ga and As present in different chemical states. The synthesised Ga 3d spectra, Figure 4.33, shows the presence of Ga atoms in the form of GaAs and GaN. The comparison of figure 4.33 (a) and (b) shows, how the amount of gallium in the form gallium nitride increases with the increase in nitrogen ion bombardment time. As the GaN peak is small and hence this may not be seen in Auger transition and as a result one does not see any change in the auger peaks and Auger parameter. The relative atomic concentration ratio of N to Ga in the form of GaN is plotted in Figure 4.34 for implantation at 2, 3, 4 and 5 keV and current densities of $1 \mu A/cm^2$ and $5 \mu A/cm^2$. As expected, this ratio increases with implantation time and after few minutes of implantation, this ratio saturates at about 0.9. Ideally bonding of Ga and N results in atomic arrangement giving 1:1 stoichiometry. The reason for this ratio being less than unity may have been due to concentration gradients within the depth integrated by the XPS technique. This has been

discussed in previous sections.

The comparison of Ga 2p and As 2p spectra, Figure 4.35, points towards little or no chemical interaction of GaAs with nitrogen, but the analysis of 3d peaks shows the formation of Ga-N compounds. In XPS, 85% of the detected photoelectrons originate from a depth corresponding to the electron inelastic mean free path in the target (Chapter 2). For GaAs samples under the irradiation of Al K_{α} X-ray source ($h\nu=1486.6$ eV), the inelastic mean free path value for Ga 3d, As 3d, Ga $2p_{3/2}$ and As $2p_{3/2}$ peaks are 2.9, 2.9, 1.0 and 0.7 nm, respectively [Tanuma, 1991]. Hence for the $2p_{3/2}$ peaks, the maximum signal is coming from the region of As enrichment (to be discussed later) and as a result the number of gallium atoms available to form bonding with N atoms would be small and so the change in the Ga 2p spectra may be too small to be observable .

The implanted nitrogen N 1s spectra shows a peak at 396.9 ± 0.2 , Figure 4.36, and the energy separation between Ga 3d and N 1s peak is found to be 377.6 ± 0.3 eV. This is same as reported for GaN, 377.5 eV [Hedman and Martesson, 1980]. DeLouise [1993] have reported the N 1s position at 396.7 ± 0.1 for nitrogen implanted in GaAs and found that the nitrogen intensity remains unchanged even after annealing at 400°C , suggesting that nitrogen atoms are in a strongly bound state. However the value of the Auger parameter reported for GaN [Hedman and Martesson, 1980] is higher than the same for nitrogen implanted in GaAs,. There was no information about uncertainty in these values, but the result is not surprising as we are looking at a small amount of GaN in a largely GaAs matrix. ARXPS results show that the peak positions for all the above mentioned peaks, at all values of electron take-off-angles, were the same, hence suggesting the nitrogen was in same chemical state at all the depths.

Nitridation of GaAs reduces the electronically active defect sites and information regarding the density of band gap states is manifest in the movement of valence band maximum (VBM) due to band bending [De Louise, 1993]. The surface Fermi level is always pinned near the mid band gap for the non-cleaved III - IV semiconductors. There is a possibility of change in its position during the exposure of the sample to the nitrogen ions. The comparison of valence band spectra before and after nitrogen ion bombardment, Figure 4.37, shows a shift of VBM towards high kinetic energy, by 0.3 eV. De Louise [1992] has related this type of band-bending to lowering of group V depletion. As nitrogen ion bombardment, results in incorporation of nitrogen (group V element) under the surface layer, thereby, increasing group V/III atomic ratio, by forming bonds with gallium atoms.

6.1.5.4 ARXPS results:

The ARXPS results, Table 4.14, show that the relative atomic concentration of nitrogen is small in the immediate sub-surface compared to the region just below. This is probably due to segregation of As towards the surface and the fact that this As region will not interact with the implanted nitrogen. Hence nitrogen will occupy interstitial sites in the region and will be easily removed

6.1.5.5 Implantation mechanism:

Nitrogen ion bombardment in GaAs results in implantation of nitrogen and depletion of arsenic. Due to surface sputtering the maximum achievable concentration in the altered surface layer is about 15 to 20 atomic % of nitrogen. The mean value of the relative atomic concentration of nitrogen seems to be higher at higher current density. Most of the As depletion occurs during the initial few minutes of ion bombardment. This may be because of the accumulation of a significant amount of nitrogen protects the underlying surface from being sputtered. Similar results are reported for low energy carbon ion bombardment of GaAs [Meharg et al., 1992].

After initial Ar⁺ cleaning of GaAs sample, As/Ga ratio is found to be approximately 0.8, which is close to the value obtained by Sullivan et al., [1994]. So at the start of N₂⁺ bombardment, GaAs has a ratio of Ga:As :: 1:0.8. After nitrogen saturation, this ratio becomes Ga:As :: 1:0.6. Assuming that all implanted nitrogen atoms combine with gallium, then the remaining Ga and As are in the ratio of Ga:As :: 1:0.8. This suggests chemical combination of implanted nitrogen with gallium. This analysis shows that after initial Ar⁺ cleaning, the GaAs surface will become amorphous (Ga:As :: 1:0.8). Further bombardment with N₂⁺, will result in the formation of GaN in GaAs matrix. The excess As will be removed due to a combination of factors discussed in following paragraphs.

The fact that after initial Ar⁺ cleaning of GaAs, the compound is with stoichiometric ratio of Ga:As::1:0.8 rather than 1:1, can be explained on the basis of surface segregation of arsenic, resulting in depletion of As in the region sampled by XPS. In the case of GaAs, the size of As atom is similar to that of Ga atom, but the surface energy of As (~0.2 J/m²) is much less than that of Ga (~0.784 J/m²) [Yu, 1995]. Under the influence of ion bombardment, As will preferentially move to the GaAs surface due to surface energy driven segregation. Sullivan et al [1994] have explained that rare gas ion bombardment of GaAs drives As atoms to the

outmost layers (Gibbsian segregation) and hence produces preferential sputtering of As atoms from the surface, which results in As depletion within the sampling depth of XPS. The quantum mechanical solution of GaAs suggests that As occupies surface sites preferentially to Ga in order to minimise surface energy [Spicer et al., 1979]. This leads to increased sputtering of As by increased direct recoils and increase probability of cascade releasing a surface atom.

Ion bombardment produces defects in and/or disordered GaAs. The reaction generally takes place at defects sites and for ion bombarded samples, the defect sites with broken Ga-As bonds are sites for chemical reaction. During bombardment, Ga and N can form covalent bonds similar to Ga-As, but As and N can not form such bonds because both are group V elements or in other words, nitrogen is isoelectronic with arsenic and so the nitrogen is expected to preferentially react with the Ga atoms. Moreover, the electronegativity values of Ga, As and N (1.6, 2.0 and 3.0 eV, respectively) [Pauling, 1967] and bond strength values (Ga-Ga, Ga-As, As-As, Ga-N and As-N, 33 ± 5 , 50.1 ± 0.3 , 91.3 ± 2.5 , 96.8 and 139 ± 3 kcal/mol, at 298 K) [Lide R. D., 1991] suggest a greater probability of the formation of Ga-N compounds and hence more likelihood of preferential sputtering removal of As.

When the bombarding N enters the GaAs surface, some Ga-As bonds will break and the implanted nitrogen atoms will form bonds with gallium atoms. In this process, some of the arsenic atoms will become free and this free As will be removed due to surface segregation. This surface segregation can be initiated due to a number of effects, firstly, the free arsenic residing at interstitial sites will be easily removable, secondly due to lower value of surface binding energy As will move towards the surface to a lower surface binding energy. The fact that it is in an environment full of lattice defects, such as vacancies and interstitials, results in easy paths towards the surface. Hence, the active N_2^+ bombardment leads to further As:Ga segregation and the chemical interaction between Ga and N enhances it and as a result, there is the effect of chemically driven segregation, in addition to Gibbsian equilibrium segregation. The calculations in chapter 5 show the presence of Gibbsian segregation, that is an enrichment of nitrogen in the top monolayer and this nitrogen will be preferentially sputtered leaving a nitrogen depleted layer in the immediate sub-surface.

The calculations in Chapter 5 indicate that both Gibbsian and collision cascade initiated segregation is taking place in the case of GaAs. Assuming a target with an initial bulk composition 82% GaAs and 18% nitrogen, bombardment induced segregation results in a surface composition of 59% GaAs and 41% nitrogen, that is an enrichment of nitrogen in the top monolayer and this nitrogen will be preferentially sputtered. Assuming a target with an

initial bulk composition 50% Ga, 32% As and 18% nitrogen, gives a normalized concentration of Ga and N as 74% and 26%, respectively. Using the method outlined in section 5.8.1.1 and assuming a target with an initial bulk composition 74% Ga, 26% nitrogen bombardment induced segregation results in a surface composition of 47% Ga and 53% nitrogen, that is an enrichment of nitrogen in the top monolayer and this nitrogen will be preferentially sputtered leaving a nitrogen depleted layer in the immediate sub-surface (the volume analysed by XPS).

6.1.6 AlGaAs:

6.1.6.1 Nitrogen implantation:

Due to large fluctuation in nitrogen concentration values, Figures 4.38, 4.39 and 4.40, it is difficult to see the variation with ion energy and ion current density. The reasons for the scatter in the data are the same as described for GaAs implantation. The experimental data shows, however, that nitrogen concentration reaches the saturation stage in less time for implantation at the higher current density. Figure 4.41 shows that (N/Al) ratios saturate rapidly. (N/Ga) ratios are next and the ratios (N/As) are last to saturate. As explained in previous sections [Tsai and Morabito, 1974], the concentration of implanted nitrogen should reach a saturation value after about 12 minutes of bombardment for implantation at $5 \mu\text{A}/\text{cm}^2$, and after 60 minutes of bombardment for implantation at $1 \mu\text{A}/\text{cm}^2$. The saturation time is nearly the same for all ion energies. For example, for implantation at $5 \mu\text{A}/\text{cm}^2$, the time required to reach the saturation stage is 12 minutes for 2 keV ion energy, whilst for 5 keV implantation, the saturation time is 10 minutes. These calculated values of saturation time agree reasonably well with the same measured experimentally, Figure 4.40.

During N_2^+ bombardment, the As/Ga ratios were found to decrease, Figure 4.42. Most of the As depletion occurred during initial few minutes of bombardment and considering the experimental uncertainties, the depletion appeared to be the same at all ion energies and current densities. The factors responsible for As depletion will be discussed in section 6.1.6.5.

As mentioned in chapter 5 in the case of AlGaAs it was not possible to predict profiles using SATVAL as the code is not capable of calculating the implantation for compounds with three or more component elements. The SUSPRE predicted N/(Al+Ga+As) saturation ratios, Table 5.13, are the same for all the ion energies whereas the predicted values are slightly

lower than those measured. The reasons for this discrepancy could be the same as described in previous sections.

6.1.6.2 Argon ion bombardment:

The Ar⁺ bombardment profiles for nitrogen, Figure 4.43, show a fall of nitrogen concentration from maximum to some steady state value. As the ion range is greater at high ion energies, Table 5.2, one would expect the thickness of the nitride layer to be comparatively greater for high energy implantation. Such a trend is not evident from the experimental data. This could be due to the reasons explained in the case of GaAs. Figure 4.43 shows that as the relative atomic concentration of nitrogen falls, the same for As increases with almost a linear relationship. Figure 4.44 shows that the As/Ga relative atomic concentration ratios increase during the first few minutes of Ar⁺ bombardment and reach the pre-bombardment level. However, due to the various sub-surface effects taking place during ion bombardment, the information gained from the photoelectron energy spectrum may be different from the true composition.

6.1.6.3 AlGaAs spectra:

Figure 4.46 shows the comparison of Al 2p, GaAs 3d and As L₃M₄₅M₄₅ spectra, before and after nitrogen ion bombardment. The comparison of these spectra did not show any appreciable change in peak position or peak shape. Figure 4.47, the comparison Ga L₃M₄₅M₄₅ spectra, before and after N₂⁺ ion bombardment of GaAs sample, does not show any appreciable change. Considering the chemical affinity, N atoms are expected to interact chemically with both Al and Ga atoms and this interaction is obviously taking place. However, in this case the spectra analysis, is not helpful in confirming the chemical interaction between nitrogen and target atoms. The comparison of valence band spectra, before and after nitrogen ion bombardment, Figure 4.47, shows a shift of VBM towards high kinetic energy, by 0.3 eV. A similar type of band-bending is found for N₂⁺ bombarded GaAs and De Louise [1992] has related this with the lowering of group V depletion. This is explained in detail in section 6.1.5.3.

The values for the binding energy of Ga 3d, the kinetic energy of the Ga L₃M₄₅M₄₅ line and the Auger parameter, Table 4.15, show that the change in value of the Auger parameter is very small and the value of the Auger parameter of N₂⁺ bombarded AlGaAs is closer to AlGaAs than GaN. Hence, in this case, the Auger parameter is not useful in identifying

chemical interaction between nitrogen and Ga atoms. This is not surprising as the amount of implanted nitrogen is small, only 15 - 20 atomic %, hence even if all the implanted nitrogen binds with gallium, a large amount of gallium atoms will still be in the form of AlGaAs and as a result the Auger peak position change is not observed. Curve synthesis is a possible method of finding the various components of Ga present in different chemical states but looking at Figure 4.46 (b), it will not be possible to derive any significant information from the peak fit. However, in this case the peak seems to be unreliable as in the case of GaAs the implanted nitrogen was shown to form chemical bonds with Ga, sections 6.1.5. This point will be discussed at later stage. Similar results were obtained for As, Table 4.16. However N_2^+ bombardment of pure As samples did not result in any nitrogen implantation. This confirms that no chemical interaction between arsenic and nitrogen atoms takes place. This is explained in a previous section. Due to the low melting point of Ga (29.8 °C), it was not possible to carry similar analysis with pure gallium target.

The values of binding energy of Al 2p, the kinetic energy of the Al KLL line and Auger parameter, Table 4.17, show a small change in the value of Auger parameter. As the amount of aluminium was only 15-20% the uncertainties in the values may be more than those reported here. However, this analysis indicates that nitrogen ion bombardment does result in some chemical change in Aluminium. Curve synthesis is a possible method of finding the various components of Al present in different chemical states but looking at Al 2p peak position for AlGaAs and AlN, Table 4.17, and the peak shape, Figure 4.46 (a), it will not be possible to get any significant information from the peak fit.

The N 1s and Auger spectra of nitrogen is shown in Figure 4.48 and the values of binding energy of N 1s, the kinetic energy of the N $KL_{23}L_{23}$ line and the Auger parameter are listed in Table 4.18. The implanted nitrogen N 1s spectra shows a peak at 396.6 ± 0.2 . The low binding energy position of the N 1s line is the position of electron-rich nitrogen species such as nitrides [Pu and Rabalais, 1981] indicating the formation of nitrides. The value of the Auger parameter for N_2^+ bombarded AlGaAs, Table 4.18, lies between the value of the same reported for N_2^+ bombarded GaAs and N_2^+ bombarded aluminium. The energy difference between Ga 3d and N 1s peak is found to be 377.6 ± 0.3 eV which is same as that reported for GaN, 377.5 eV [Hedman and Martesson, 1980]. The energy gap between the Al 2p and the N 1s peak is found to be 323.0 ± 0.4 eV which is the same as that for AlN (323.1 eV). This points towards the binding of nitrogen atoms with both aluminium and gallium atoms.

6.1.6.4 ARXPS results:

The ARXPS results for the nitrogen ion implantation, Table 4.19, show that the relative concentration of nitrogen on the surface is lower in almost all the cases compared to the same measured from below the near surface region. However, considering the experimental uncertainties, it is difficult to say that this trend is real.

6.1.6.5 Implantation mechanism:

The nitrogen ion bombardment of AlGaAs results in implantation of nitrogen and depletion of arsenic. Due to surface sputtering the maximum achievable concentration in the altered surface layer is about 15 to 20 atomic % of nitrogen. The mean value of the relative atomic concentration does not show any apparent dependence on ion energy or current density. Before nitrogen implantation the given compound is with stoichiometric configuration $\text{Al}_x\text{Ga}_{1-x}\text{As}_y$, with $x = 0.3$ and $y = 0.7$. Most of the As depletion appears to occur during the initial few minutes of ion bombardment and the nitrogen concentration reaches saturation during the same time. Similar results are reported for ion bombardment of GaAs and are explained in section 4.1.4. Nitrogen ion bombardment results in replacement of As atoms with N atoms and due to strong chemical affinity between aluminium and nitrogen atoms, aluminium seems to act as a catalyst for this process.

The electronegativity values of Al, Ga, As and N (1.5, 1.6, 2.0 and 3.0 eV, respectively) [Pauling, 1967] and bond strength values (Al-Al, Ga-Ga, Ga-As, As-As, Al-N, Ga-N and As-N, 44.5 ± 2.2 , 33 ± 5 , 50.1 ± 0.3 , 91.3 ± 2.5 , 71 ± 23 , 96.8 and 139 ± 3 kcal/mol, at 298 K), [Lide, 1991], suggest probability of formation of nitride compounds in the order $\text{Al-N} > \text{Ga-N} > \text{As-N}$. As the heat of formation of AlN and GaN is negative, Table 3.4, the formation of these nitrides is thermodynamically and kinetically favoured [Liu et al., 1989]. Also, the heat of formation of AlN is more negative than the same for GaN. Hence there will be a greater driving force for the formation of AlN. However, the formation of AsN is not expected due to the reasons outlined in section 6.1.5. This suggests a chemical interaction of implanted nitrogen with both aluminium and gallium atoms will take place.

Al and Ga are both group III elements and As is a group V element. For a crystalline solid, one would expect a group III to group V ratio of 1:1. However, at the start of N_2^+ bombardment, AlGaAs has a ratio of (Al+Ga):As :: 1:0.7. For GaAs Sullivan et al., [1994] explained that this type of As depletion is due to Gibbsian segregation of As. This is explained in detail in section 6.1.5.5. The same mechanism is responsible for As depletion in the case of AlGaAs. After nitrogen saturation, this ratio becomes (Al+Ga):As :: 1:0.5. A

similar type of As depletion was observed in N_2^+ bombarded GaAs, section 6.1.5.5. This strongly suggests chemical combination of implanted nitrogen with aluminium and gallium. As discussed in the case of GaAs, N_2^+ bombardment will result in the formation of defects which will act as sites for chemical reaction. Al and Ga atoms can form covalent bonds with implanted N atoms whereas As and N can not form such bonds because both are group V elements. Moreover, as discussed in a previous section, there is greater probability of the formation of AlN and GaN compounds and hence more likelihood of preferential removal of As. During N_2^+ bombardment some of the arsenic atoms will become free and this free As will be removed due to surface segregation. There is the effect of chemically driven segregation, in addition to Gibbsian equilibrium segregation, and the reasons for this are explained in section 6.1.5.5.

6.1.7 As:

Nitrogen ion bombardment of As did not result in any implantation of nitrogen. This could be because nitrogen is isoelectronic with As but even then some nitrogen can occupy interstitial sites and so some amount of nitrogen retention is expected. The bond strength values (As-As and As-N, 2.1 and 6.04 eV, at 298 K), [Lide R. D., 1991], suggest more likelihood of the presence of As in the form of As-As bonds than in the form of As-N. Moreover, As and N are group V elements and being isoelectronic, they are not expected to form any bonds between them.

As discussed in section 6.4, chemical inertness of nitrogen towards As means the mobility of a single nitrogen atom in a defect-laden As lattice. Hence Radiation Induced Segregation (RIS) effects will be dominant. Like gold, in this case, there is a possibility of formation of stable N-vacancy complexes and hence nitrogen being segregated to the surface [Moncoffre and Jagielski, 1994]. There is also a possibility of the segregated nitrogen being sputtered away as the mass of nitrogen is smaller compared to As and also the fact that it is not in a bound state. Thus ion-target mismatch combined with surface segregation and preferential sputtering of nitrogen will result in a very little or no nitrogen retention, especially at the depths analysed by XPS. Even at a 60° electron take-off-angle, there was no nitrogen.

6.2 Plasma implantation:

In the case of the nitrogen glow discharge, although all the samples were prepared in the same manner as for monoenergetic implantation, on transfer to the discharge chamber the samples

were contaminated due to vapours coming from the diffusion pump. This was confirmed by the XPS analysis of the samples. The Al 2p, Fe 2p and Cu 2p peaks were same as those obtained for samples exposed to monoenergetic ion bombardment except that the former showed a large proportion of the target atoms in the form of oxide. Tables 4.20, 4.21 and 4.22 clearly show that aluminium, iron and copper were highly contaminated with oxygen and carbon. The glow discharge samples were analysed by XPS in the same way as those for monoenergetic implantation. Figure 4.49 shows that in each of the samples the nitrogen is present in two forms. The low binding energy component of N 1s corresponds to electron-rich nitrogen species such as nitrides and the high binding energy component corresponds to nitrogen weakly bound to oxygen [Kovacich et al., 1984]. Hence in each of the samples the nitrides are formed. As expected from the reactivity, the relative atomic concentration ratios of nitrogen and target, Tables 4.20, 4.21 and 4.22, are in the order of Al > Fe > Cu. However, considering the experimental uncertainties, the effect of voltage and pressure is not clear in the range considered. The relative atomic concentration of nitrogen was smaller at shallow angles which is probably due to high levels of contamination. Comparing the relative atomic concentration ratios of nitrogen to target, the values are higher for monoenergetic nitrogen implantation in the case of aluminium, whilst for iron and copper the values are higher for glow discharge exposure. The same is true even if one considers the relative atomic concentration ratios of nitrogen bound with target and target itself.

The higher values of nitrogen retention in iron and copper can be explained on the basis of sputtering and contamination. The average energy of nitrogen ions in the glow discharge is quite small (~ 0.2 and 0.9 keV) and hence sputtering of retained nitrogen will be smaller. Moreover the process of nitrogen implantation in the glow discharge chamber is very different compared to the classical monoenergetic implantation in the ESCALAB. In the latter case the target was bombarded with ions, but in the case of plasma, the sample were exposed to nitrogen molecules and ions at high temperatures (~ 200°C). Also the environment of the sample was not very clean in the case of the glow discharge chamber. The reasons for higher nitrogen values in the case of the glow discharge chamber could be either the higher temperature enhancing the nitrogen retention or the presence of impurities such as oxygen and carbon, resulting in the formation of oxynitrides and carbonitrides. Tables 4.20, 4.21 and 4.22, show that at 0° TOA, the ratio of relative atomic concentration of nitrogen in the form of nitride and the target atoms is 0.22, 0.15 and 0.12 for aluminium, iron and copper, respectively. Compared with monoenergetic implantation, these values are higher in the case of iron and copper, but lower in the case of aluminium. Nitrides are more likely to be formed at higher temperatures and this explains the higher amount of nitrides in the case of iron and copper. The reason for low retention in plasma exposed aluminium compared to the same

implanted by monoenergetic ion bombardment could be thermal desorption of nitrogen. After exposure to nitrogen plasma all the samples were cooled with Ar gas for about 15 - 20 minutes before transferring to the ESCALAB to analyse by XPS. During the cooling process there is a possibility of some thermal processes, maybe adsorption or desorption of nitrogen, although desorption of nitrogen is more likely compared to adsorption. However the aluminium nitrides (decomposition temperature 2400°C) are more stable compared to iron nitride (decomposition temperature 200°C) and copper nitrides (decomposition temperature 300°C). So the desorption of nitrogen does not explain the low retention in plasma exposed aluminium compared to the same implanted by monoenergetic ion bombardment. The low retention in plasma exposed aluminium is definitely due to the presence of a thicker oxide layer on the plasma exposed sample surface. As mentioned in section 6.1.1.4, formation of aluminium nitride is thermodynamically unfavourable in the oxide layer. This fact combined with the high contamination of the aluminium sample explains the smaller amount of nitride formation in the glow discharge chamber.

6.3 Summary:

The results of monoenergetic ion implantation are summarized in Table 6.2. During ion bombardment the ions are trapped in the surface and subsequently change the surface composition. Ion bombardment is a very complex process, involving some processes which induce compositional changes leading to mass correlation and some processes based on other effects like chemical bonding, electronic processes and diffusion. From the experimental results, in the range of 2-5 keV, the effect of ion energy and current density on the nitrogen saturation value is not important. However for a given dose, the value of nitrogen concentration is higher for implantation performed at $1 \mu\text{A}/\text{cm}^2$ than the same for $5 \mu\text{A}/\text{cm}^2$, which is probably due to thermal processes.

Figure 5.4 shows the sputter yield values for various targets for all ion energies. Clearly, sputter yield values, Y , follow the trend; $(Y)_{\text{Au}} > (Y)_{\text{GaAs}} > (Y)_{\text{AlGaAs}} > (Y)_{\text{Cu}} > (Y)_{\text{Fe}} > (Y)_{\text{Al}}$ and the amount of nitrogen retained, Table 6.2, $(N)_{\text{Al}} > (N)_{\text{GaAs}} \approx (N)_{\text{AlGaAs}} > (N)_{\text{Fe}} > (N)_{\text{Cu}} > (N)_{\text{Au}}$. Thus for metal targets it is clear that the higher the sputter yield the smaller the amount of nitrogen retained. However this is not necessarily the most important factor since there are more important chemical factors present. Figure 5.4 also shows that in the energy range 2-5 keV the sputter yield value increases with ion energy and hence this may suggest that the amount of nitrogen retained should be smaller at higher implantation energies. However the experimental data did not show such a trend. This is probably due to higher ion range at higher ion energies (Figure 5.2) or due to the fact that the total implanted dose is higher at

higher implantation energies.

Table 6.2 Summary of monoenergetic ion implantation results.

Target	N saturation conc. (Atomic %)	Nitride formation	Variation of N sat. conc. with		Variation of N with current density at a given ion dose
			ion energy	ion current density	
Aluminium	40	yes	not significant	slight	decreases
Iron	10	yes	not significant	not significant	decreases
Copper	5	yes	not significant	not significant	not clear
Gold	None	no	--	--	--
Arsenic	None	no	--	--	--
GaAs	20	yes	not significant	slight increase	not clear
AlGaAs	20	yes	not significant	not significant	not clear

The other aspect to consider is the mass and size difference between the nitrogen and target atoms, as this may cause the energy transfer processes to be significantly different in an implanted substrate, and hence surface composition. If we look at the effect of mass, Table 5.1, for targets $(M)_{Al} < (M)_{Fe} < (M)_{Cu} < (M)_{AlGaAs} < (M)_{GaAs} < (M)_{Au}$. The mass of Al is similar to the mass of nitrogen and the masses of Fe, Cu, GaAs, AlGaAs and Au are higher compared to the mass of nitrogen. It is thus possible that for higher mass targets, the nitrogen is being preferentially removed. However the binding energy effects will be more dominant than the mass effects. As the atomic mass of a target metal increases the ion range decreases and as a result the nitrogen distribution peak appears at shallow depth. The density of the target, ρ , could also be one of the factors, $\rho_{Al} < \rho_{GaAs} \approx \rho_{AlGaAs} < \rho_{Fe} < \rho_{Cu} < \rho_{Au}$ (Table 7.1). The ion range will be smaller in the case of dense targets, and hence the chance of sputtering will also be greater. The ion range values at various ion energies are plotted in Figure 5.2. As the radius of nitrogen atoms is very small compared to the radii of the target atoms, there is a good possibility of the trapping of the nitrogen at the interstitial sites. The radii of the atoms were estimated from the area of atoms, as determined in section 5.8.1.1 and are tabulated in Table 6.3. Looking at the radii, the radius of aluminium and gold atoms are larger compared to iron and copper indicating a higher possibility of nitrogen retention in the case of Al and Au compared to Fe and Cu. However it is not only the radii that matter but also the crystal structure. Depending on the size of an interstitial site, some crystal structures have more probability of interstitial retention. The calculated size of an interstitial site for all the targets are reported in Table 6.3. In all the target materials, the size of interstitial site is either equal

to or greater than the size of nitrogen atoms. Hence, the nitrogen retention at interstitial sites is feasible for all the targets. The mass, density, radius, ion range and the size of interstitial site are not the only parameters. For example, in the case of Fe and Cu, they have almost the same density, radius and ion range but the nitrogen saturation value is higher in the case of iron. This could be partly due to lesser sputtering in the case of Fe but is mainly due to higher chemical affinity of Fe towards N, compared to that in the case of the Cu target.

Table 6.3 Radius of one bulk atom of the elements, r and radius of an interstitial site, r_i , in the crystal lattice.

Element	Al	Fe	Cu	Au	Ga	As	N
r (10^{-10}m)	1.44	1.28	1.28	1.45	1.52	1.57	0.53
r_i (10^{-10}m)	0.59	0.53	0.53	0.60	0.63	0.65	--

Considering the average saturation time for all the targets to be 40 minutes, the total incident dose for $5 \mu\text{A}/\text{cm}^2$ implantation will be 1.5×10^{17} ions/ cm^2 . Assuming a sticking factor of 0.3 [Rabalais and Marton, 1992], the nitrogen saturation concentration is about 70 atomic %, which is much higher than the experimental values discussed in previous sections. For these calculations the following simple expression was used;

$$\frac{n_N}{n_N + n_T} \times 100 = x \% \text{ of nitrogen}$$

here n_T is the target atomic density, n_N is the atomic density of retained nitrogen and x is the relative atomic concentration of nitrogen in the altered layer. However this is a very simple calculation and points that it is not possible to take a generalized value for the sticking probability and the latter will depend on the ion-target combination.

The values for stored nitrogen ion fluence at saturation $F_{r,s}$ are calculated using equation (1.17) (described in chapter 1) and tabulated in Table 6.4. For this calculation the values of ion range were taken from Table 5.2. Using the simple expression described above the nitrogen saturation concentration values were also calculated and are listed in Table 6.4. Table 6.4 shows that the stored nitrogen fluence is slightly higher at higher ion energies. However due to deeper penetration of nitrogen, the nitrogen saturation value is slightly higher at lower energies of implantation. The nitrogen saturation concentration values show the trend $\text{Al} > \text{Fe} > \text{Cu} > \text{AlGaAs} > \text{GaAs} > \text{Au}$, while the same measured experimentally are in the order $\text{Al} > \text{Fe} > \text{Cu} > \text{AlGaAs} \approx \text{GaAs} > \text{Au}$. In case of Al, Fe, Cu and Au, the predicted

values are higher than the experimental values whilst for GaAs and AlGaAs targets, the latter are higher. This discrepancy is because of the fact that these calculations are simply based on ion range, target atomic density and sputter yield and do not take into account the chemical interaction between the ion-target system.

Table 6.4 Calculation of stored nitrogen ion fluence at saturation, $F_{r,s}$, and nitrogen saturation concentration value, for various target materials. The values outside the bracket are for implantation at ion energy 2 keV and those inside the bracket are for implantation at ion energy 5 keV.

Target	Al	Fe	Cu	Au	GaAs	AlGaAs
Y	1.04(1.19)	1.85(2.26)	2.59(3.19)	10.3(13.9)	7.51(9.96)	6.05(6.98)
$F_{r,s}$ (10^{16} ions/cm ²)	1.9(3.2)	1.0(1.4)	0.6(1.1)	0.2(0.2)	0.2(0.3)	0.3(0.5)
$N_{\text{saturation}}$ value	50(45)	36(30)	26(25)	10(6)	11(9)	15(13)

From the above discussion it is clear that the target mass, density, sputter yield and ion range distribution may all affect nitrogen retention at interstitial sites, but by far the predominant factor is the ion-target chemical combination. The retention characteristics of implantants at high dose seem to strongly depend on the chemical reactivity between ion species and target material. The electronegativity values, Table 5.4, show that the chemical interaction of metals towards nitrogen is in the order of ; Al > Ga > Fe > Cu > As > Au. Here the interaction is measured by the electronegativity difference between the metal and nitrogen; the chemical interaction being higher for a greater value of electronegativity difference. Based on the chemical reactivity of target with nitrogen one expects nitrogen saturation value to follow the trend, $(N_{\text{saturation}})_{\text{Al}} > (N_{\text{saturation}})_{\text{Ga}} > (N_{\text{saturation}})_{\text{Fe}} > (N_{\text{saturation}})_{\text{Cu}} > (N_{\text{saturation}})_{\text{As}} > (N_{\text{saturation}})_{\text{Au}}$. This trend is proved to be true by our experimental results. The saturated relative atomic concentration ratios of nitrogen and target atoms, $(N/T)_{\text{saturation}}$, are plotted as a function of electronegativity difference (the difference between the electronegativity values of nitrogen and target atoms), Figure 6.2. As expected the nitrogen saturation concentration is greater for the target with larger electronegativity difference from nitrogen atoms, and the graph shows a parabolic relationship between the ion to target saturation atomic concentration ratio and electronegativity values difference. However this relationship is derived using only five ion-target combinations and there are some uncertainties in the experimental data and hence this relationship may not be very accurate. It would be interesting to carry out similar work in the future and check the validity of this relationship with the data from various ion-target systems.

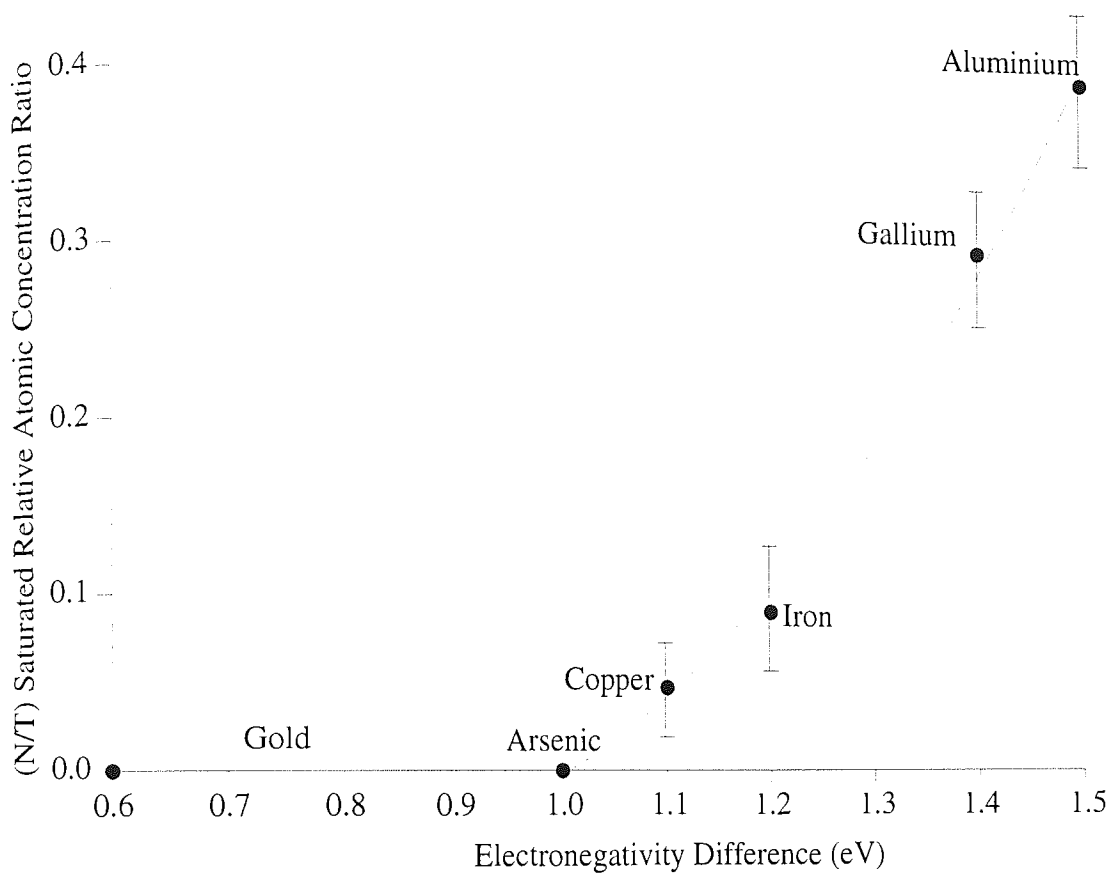


Figure 6.2 The saturated relative atomic concentration ratios of nitrogen and target atoms, (N/T), as a function of electronegativity difference between the electronegativity values of nitrogen and target atoms.

Using the model proposed by Pu et al., [1981] for molecular beams striking the metallic targets, the reaction cross-section, calculated from our experimental data for nitridation of aluminium, iron, copper and gold, are found to be 2×10^{-17} , 0.5×10^{-17} , 0.2×10^{-17} and 0 cm^2/atom , respectively. This means $\sigma_r(N_2^+/\text{Al}) \approx 4 \times \sigma_r(N_2^+/\text{Fe}) \approx 10 \times \sigma_r(N_2^+/\text{Cu})$. These cross-sections are found to be slightly smaller for implantation carried out at a current density of $5 \mu\text{A}/\text{cm}^2$ as compared to the same for $1 \mu\text{A}/\text{cm}^2$. For 5 keV and $1 \mu\text{A}/\text{cm}^2$ implantation the probability of nitride formation upon collision is found to be 0.5 , 0.1 and 0.03 , for (N_2^+/Al) , (N_2^+/Fe) and (N_2^+/Cu) system, respectively, and this probability is found to slightly decrease with decrease in ion energy. These results are consistent with the enthalpies of nitride formation, Table 3.4. Figure 6.3 shows the variation of probability of nitride formation (calculated using our experimental data and method outlined by Pu et al., [1981]) with heat of formation for nitrogen ion bombardment of aluminium, iron and copper. However it was not possible to perform these calculations for compound targets.

The injected ions stop in the surface layer and are deposited into the matrix lattice in the form of precipitates in approximately 10^{-10} s [Johnson et al., 1985]. Hence the kinetic conditions available for structural transformation are very limited [Ma et al., 1987] and the mechanism of nitride formation in the environment of direct implantation is not completely the same as in conventional treatment. In addition to thermodynamic factors the structural transformation may play a dominant role. Formation of nitrides is thermodynamically and kinetically favoured if the heat of formation of nitride is negative. The more negative the heat of formation of a nitride, the greater is the driving force for its nucleation and growth and, as a result, the easier is its formation. From Table 3.4 the formation of aluminium nitride, iron nitride and gallium nitride is favoured whilst formation of copper nitride is not. As the value of heat of formation is most negative for aluminium compared to other metals chosen for this work it will be the easiest to form. However in the case of iron, data was not available for Fe_{16}N_2 and hence the value is reported for Fe_4N . The formation of copper nitride shows that under the conditions of ion implantation, formation of nitrides, which is thermodynamically and kinetically unfavourable, is also possible. The failure to detect any gold nitride under implantation conditions suggests that the behaviour of gold upon irradiation is not the same as that of copper despite the fact that they are of the same group in the periodic table. This is probably due to the chemical inertness of gold, but still one would expect some retention of nitrogen which was absent in most of the experiments performed on gold. Generally the mobility of N atoms will be high in most b.c.c. metals (open lattices) such as iron compared with the same in f.c.c. metals such as aluminium, copper and gold [Liu et al., 1989]. However the effect of this mobility on the compound formation would be observed only for low-dose implantation and when implanted nitrogen reaches saturation the influence of

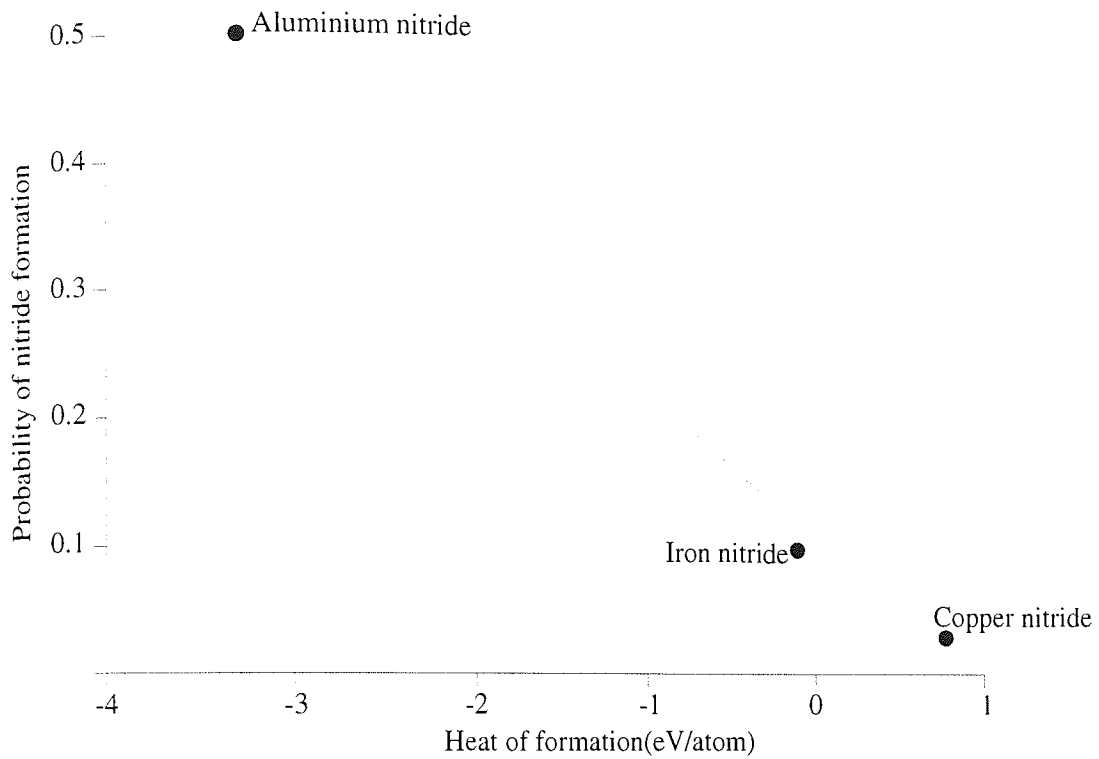


Figure 6.3 Relation between probability of nitride formation and heat of formation, for nitrogen ion bombardment of aluminium, iron and copper. The probability of nitride formation is calculated using our experimental data and method outlined by Pu et al., [1981].

mobility will not be important. In the case of GaAs there is an indication of formation of mainly Ga-N compounds whilst in AlGaAs there is competition between aluminium and gallium atoms for the formation of nitrides and the analysis suggests that both types of compounds are formed.

The above analysis indicates that bombardment of a target with low energy high dose nitrogen ions results in retention of a part of implanted nitrogen and the retention of N is only possible if there is a chemical interaction between N and the target atoms. The amount of retained nitrogen has a relationship with the reactivity of the target atoms to nitrogen. As the heat of formation is a good indication of this chemical reactivity [Yabe et al., 1994], so retention of nitrogen and formation of nitride seem to be affected strongly by the reactivity of the metal towards nitrogen. Even for low doses of implanted nitrogen the nitride is formed, so the average concentration of implanted nitrogen does not seem to be a critical factor determining the formation of nitrides.

The nitride formation through implantation is not controlled only by thermodynamic factors but also by geometrical and structural relationships [Liu et al., 1989]. The structure of nitrides has a close relationship to the matrix, with a little change of arrangement of metal atoms to accommodate nitrogen. However in this project we did not look at the changes in the matrix structure on nitride formation.

Chapter 7

Conclusions and Future Work

7.1 Conclusions:

The bombardment of the target by an energetic ion beam changes the composition of the surface region to a depth comparable with the projectile range. This is due to the ion implantation, cascade mixing, recoil implantation, preferential sputtering, radiation induced diffusion, Gibbsian segregation, radiation enhanced segregation and surface topographical changes. Ion bombardment is a very complex process, involving some processes which induce compositional changes leading to mass correlation and some processes based on other effects like chemical bonding, electronic processes and diffusion. The surface concentration of the implantant may depend on several parameters such as, ion energy, ion fluence and target properties (the mass, binding energy and chemical structure etc.), sputter yield, ion range distribution, and chemical reactivity of the ion/target combination. However the experimental data presented here indicates that retention of nitrogen is possible only if chemical interaction takes place. Considering possible experimental uncertainties, there is no evidence of significant variation in nitrogen saturation concentration with ion energy or ion current density in the range of 2-5 keV, but at a given dose, the nitrogen concentration is higher for implantation carried out at current density of $1 \mu\text{A}/\text{cm}^2$ compared to the same for $5 \mu\text{A}/\text{cm}^2$. This suggests the presence of at least one thermal process in the implantation.

The argon profiles show nitrogen concentration to be maximum at the surface and falling to some steady state value depending on the bombardment conditions. As implanted profiles are the result of electronic stopping, nuclear stopping, target related effects (such as surface roughening and surface erosion due to sputtering and effects due to the fact that the surface is a discontinuity which is overlaid by contaminants) and after-effects on the implantation atom once it has come to rest (such as recoil ejection, diffusion, segregation and sputtering). The as measured profiles consist of convolution of the as implanted profile with various broadening functions introduced by the analytical technique. Moreover, during ion bombardment of the target, the composition of the surface region of the target to a depth comparable to the projectile range is changed due to the various surface effects and hence, the information gained from the photoelectron energy spectrum is dependent on the sample state immediately after the ion bombardment, but this may be different from the true composition.

The mass and size difference between the nitrogen and target atoms result in a significant difference in the energy transfer processes and hence, may play a role in determining the amount of nitrogen retained at interstitial sites. However, these are not the most important parameters. The retention characteristics of implantants for low energy high dose seem to depend strongly on the chemical reactivity between ion species and target material. The electronegativity values, shows the chemical interaction of target atoms with nitrogen is in the order of ; $Al > Fe > Ga > Cu > As > Au$ and the same trend is found for nitrogen retention.

Formation of nitrides is thermodynamically and kinetically favoured if the heat of formation of nitride is negative. The more negative the heat of formation for a nitride, the greater is the driving force for its nucleation and growth, and as a result the easier is the formation of nitride. As the injected ions stop in the surface layer and are deposited into the matrix lattice in the form of precipitates in approximately 10^{-10} s hence, the kinetic conditions available for structural transformation are very limited and the mechanism of nitride formation in the environment of direct implantation is not completely the same as in conventional treatment. The values of heats of formation indicate that the formation of aluminium nitride, iron nitride and gallium nitride is favoured, while formation of copper nitride is not. The data for gold and arsenic was not available, but nitrides are not expected to form in these metals. As the value of heat of formation is most negative for aluminium as compared to other metals chosen for this work and hence it will be easiest to form. The formation of copper nitride shows that under the conditions of ion implantation, formation of nitrides, which are thermodynamically and kinetically unfavourable, is also possible. The failure to detect any gold nitride under implantation conditions suggests that behaviour of gold upon irradiation is not same as that of copper, despite the fact that they are of same group in periodic table. This is due to the chemical inertness of gold. As nitrogen does not form any compounds with gold, this may result in segregation of any implanted nitrogen and subsequent sputtering due to its smaller mass. In the case of GaAs, GaN compounds are formed, whilst in AlGaAs, there is competition between aluminium and gallium atoms for the formation of nitrides. As the probability of nitride formation increases linearly with the decrease of heat of formation and because the enthalpy of formation of aluminium nitride is more negative, so the probability of formation of AlN is greater compared to GaN, however, the analysis suggests that both types of compounds are formed. In the case of both GaAs and AlGaAs, Gibbsian and chemical-enhanced segregation of As takes place, which results in the depletion of As in the volume analysed by XPS. Even for low doses of implanted nitrogen, the nitride is formed, so the average concentration of implanted nitrogen does not seem to be a critical factor determining the formation of nitrides.

The reaction cross-sections, calculated from our experimental data, show $\sigma_r(N_2^+/Al) \approx 4 \times \sigma_r(N_2^+/Fe) \approx 10 \times \sigma_r(N_2^+/Cu)$. The probability of nitride formation upon collision, is found to be 0.5, 0.1 and 0.03, for (N_2^+/Al) , (N_2^+/Fe) and (N_2^+/Cu) system. Considering the enthalpy of nitride formation to be an indication of reactivity, the probabilities of nitride formation for metals calculated from the experimental results are consistent. However, as this model was only for metals, it was not possible to do a similar analysis for compound semiconductor targets. Measured nitride concentrations are not wholly stoichiometric which could be due to influence of reconstruction of surface atoms or defect formation during implantation, resulting in a non-ideal phase, or due to concentration gradients within the depth integrated by the XPS.

The metal nitride formation through implantation is not controlled only by thermodynamic factors, but also by geometrical and structural relationships [26]. The structure of nitrides has a close relationship to the matrix, with a little change of arrangement of metal atoms to accommodate nitrogen. However, in this programme we did not look at the changes in the matrix structure on nitride formation.

Ion bombardment is a very complex process. Conceptually, the phenomena of bombardment induced compositional changes is simplest when only athermal processes take place. However very often at least one thermally activating process is present. In particular Gibbsian segregation, accelerated by ion irradiation, is capable of causing substantial changes in the surface composition of an alloy even in the absence of the competing processes. Any component which segregates to the surface will be preferentially sputtered. So true preferential sputtering is hard to distinguish experimentally from Gibbsian segregation. RED may cause the altered layer to extend considerably beyond the penetration depth of the beam. RIS, which is driven by the gradients in the defect concentration, tends to drive the alloy system away from thermodynamic equilibrium and may cause significant distribution. This process is quite effective in spreading changes in the alloy composition to large depths. The theoretical calculations show that in ion bombardment, the segregation is taking place both due to athermal and thermal processes. The experimental data indicates the presence of thermal processes.

In the case of nitrogen glow discharge, as expected from the reactivity, the relative atomic concentration ratios of nitrogen and target are in the order of $Al > Fe > Cu$. However, considering the experimental uncertainties, little effect of voltage and pressure was detected in the range considered. As the samples were contaminated, the nitrogen was found in two forms: strongly bound to target atoms and bound with oxygen atoms. For iron and copper, the

relative atomic concentration ratios of nitrogen to target are higher for glow discharge exposure, compared to the same for monoenergetic implantation. This can be explained on the basis of sputtering and contamination and the fact that nitrides are more likely to be formed at higher temperature. The average energy of nitrogen ions in the glow discharge is quite small (~ 0.2 and 0.9 keV), and hence sputtering of retained nitrogen will be smaller. The other reasons could be the higher temperature enhancing the nitrogen retention or the presence of impurities like oxygen and carbon, resulting in the formation of oxynitrides and carbon nitrides, and so higher nitrogen concentration. However, in the case of aluminium, the relative atomic concentration ratios of nitrogen to target are higher for monoenergetic nitrogen implantation compared to the same for glow discharge exposure. This could be due to the presence of a thicker oxide layer on the plasma exposed sample surface and the fact that the formation of AlN is thermodynamically unfavourable in the oxide layer. The process of nitrogen implantation in the glow discharge chamber is very different compared to the classical monoenergetic ion implantation in the ESCALAB.

One of the problems faced in this project was to find the correct value of the surface binding energy. This is a very difficult problem, especially in the case of compound semiconductors. For the sputtering of compounds, the problem is correctly recognising the sputtered species. The choice of surface binding energy representation by ΔH_s or ΔH_a is only a generalized energy for the substrate. In this project, the heat of atomization was taken to represent the surface binding energy. The surface binding energy for individual surface atoms may vary considerably, depending on the position of the atom, its neighbours and the bonds between the atoms. The surface binding energy of a substrate may change when a crystalline substrate changes to amorphous state under ion bombardment. So the surface binding energy should be a population weighted average over the individual binding energy and the experimental evidence suggest that surface binding energies indeed depend on alloy composition.

It has been shown that the codes such as SUSPRE may be used to determine N saturation values, and give good agreement with experimental results but the SUSPRE calculations depend very critically on the value chosen for solubility. These values can be obtained only from our experiments and hence the predictions of this code are not independent in the way that the SATVAL results are. The nitrogen saturation values predicted by SATVAL are higher than the experimentally calculated values, especially in the case of iron, copper and gold. This is because of the fact that the codes do not take into account the chemical interaction between and target atoms. The other important reason could be that codes are based on athermal process, but thermal processes have to be a part of a theoretical treatment for a realistic prediction of implanted profiles. Most of the simulation codes do not fulfil this

criteria. Any attempt to resolve this faces the problem that the most of the input information required is either unavailable or not very accurate. The choice of binding energy for target atoms and especially for implantant was a difficult problem. It was also not possible to translate the change of binding energy with change in surface composition. The other reason for discrepancy between the theoretical and experimental results could be the inability of the codes to account for molecular ion impact. When a nitrogen molecular ion strikes the target surface, it dissociates and hence there is a superposition of two cascades. In simulation codes, however, they are treated as separate cascades with a finite time interval between them. The simulation codes also do not take into account the surface topographical changes.

7.2 Future Work:

In spite of the large amount of experiments performed, ion implantation and sputtering is not fully understood. The work on ion implantation of metals and compound semiconductors is far from complete. The effort needs to be made on both experimental and theoretical sides;

- As the results suggest the presence of thermal processes, such as Gibbsian segregation, but due to large sampling depth of XPS, a complementary technique, such as ISS will be helpful. However, the surface contamination may still be a problem.
- Effect of different bombarding ion species and if possible, with mass analysed ion beams should be carried.
- The surface topography developed and the change in crystalline structure should be investigated using techniques such as AFM and electron diffraction.
- To establish the influence of diffusion and segregation processes, the effect of ion bombardment at different temperatures should be investigated.
- The measurement of sputtered flux to establish fluence-dependent partial sputtering yields.
- To carry similar analysis at higher ion energies and to compare the results with low energy implantation.
- Proper algorithms are required for the deconvolution of the ARXPS data.
- The thermal processes should be included in the simulation codes.
- The chemical interaction, calculated from heats of formation of compounds should be incorporated in the codes.

References

- Andersen H. H., "Depth resolution in sputter profiling", **Appl. Phys.** **18**(1979)131-140.
- Andersen H. H., "Sputtering of multicomponent metals and semiconductor targets", **J. Vac. Sci. Technol.** **16**(1979) 770-771.
- Andersen H. H. and Bay H. L., "Non linear effects in heavy ion sputtering", **J. Appl. Phys.** **45**(1974)953-954.
- Andersen H. H. and Bay H. L., "Sputtering by Particle Bombardment I", Ed. Behrisch R., Springer-Verlag, 1981, Heidelberg, Germany.
- Appleton B. R., "Ion implantation and beam processing", Eds., William J. S. and Poate J. M., Academic Press, 1984, London, UK.
- Arabczyck W. and Müssig H. J., "Nitrogen bonding states on iron studied by PES and AES", **Vacuum** **37**₍₁₋₂₎(1987)137-140.
- Averbeck R. S., Rehn L. E., Wagner W., Wiedersich H. and Okamoto P. R., "Kinetics of radiation-induced segregation in Ni- 12.7 At % Si", **Phys. Rev.** **B28**₍₆₎(1983)3100-3109.
- Baldwin D. A., Murray P. T. and Rabalais J. W., "Kinetic-energy dependence of the reactions of N⁺ and N₂⁺ with Molybdenum" **Chem. Phys. Lett.** **77**(1981)403-404.
- Barnett R. N., Landman U. and Cleveland C. L., "Surface segregation in simple metal alloys: an electronic theory", **Phys. Rev.** **B28**(1983)6647-6658.
- Baschenko O. A., "Taking account of the electron inelastic mean free path dependence on the elemental composition in depth-concentration profile restoration from Angle-Resolved XPS data", **Phys. Chem. Mech. Surfaces** **8**₍₂₎(1992) 340-348.
- Behrisch R., "Sputtering by Particle Bombardment I", Ed. Behrisch R., Springer-Verlag, 1981, Heidelberg, Germany.
- Belyi A. V., Kukareko V. A., Lobodaeva O. V. and Shikh S. K., "Phase and structural transformation in iron-base alloys irradiated with low-energy nitrogen ions at high current densities", **The Physics of Metals and Metall.** **80**₍₆₎(1995)657-667.
- Benninghoven A., Rüdener F. G. and Werner H. W., "Secondary Ion Mass Spectrometry", Eds. Elving P. J. and Kolthoff I. M., John Wiley & Sons, 1987, New York.
- Betz G. and Wehner G. K., "Sputtering by Particle Bombardment II", Ed. Behrisch R., Springer-Verlag, 1983, Heidelberg, Germany.
- Bhattacharya V. P. and Prabhawalkar P. D., "Effect of nitrogen ion bombardment on copper-gold interface", **Vacuum** **42**_(8/9)(1991)543-546.
- Biersack J. P., "Computer simulations of sputtering", **Nucl. Instrum. and Meth. in Phys. Res.** **B27**(1987)21-36.

- Biersack J. P. and Eckstein W., "Sputtering studies with the Monte-Carlo program TRIM.SP" **Appl. Phys.** **A34**(1984)73-94.
- Biersack J. P. and Ziegler J. F., "Refined Universal Potentials in atomic Collisions", **Nucl. Instrum and Meth.** **194**(1982)93-100.
- Biwer B. M. and Bernasek S.L., "Electron spectroscopic study of the iron surface an its interaction with oxygen and nitrogen", **J. Elec. Spec. Rel. Phen.** **40**(1986)339-351.
- Bourgoin J. C., Corbett J. W. and Frisch H. L., "Ionized enhanced Diffusion", **J. Chem. Phys.** **59**(8)(1973)4042-4046.
- Briggs D. and Rivie're J. C., "Practical surface analysis", second edition, volume 1, Eds. Briggs D and Seah M. P., John Wiley & Sons Ltd., 1990, Chichester, UK.
- Bussing T. D. and Holloway P. H., "Deconvolution of Concentration Depth Profiles from Angle Resolved X-ray Photoelectron Spectroscopy data", **J. Vac. Sci. Technol.** **A3**(1985) 1973-1981.
- Calvo L., Perez-Rodriguez A., Romano-Rodriguez A., Morante J. R. and Montserrat J., "Structural-analysis of buried AlN thin films formed by nitrogen implantation into microelectronics and grade Aluminium", **Nucl. Instrum. Meth. and Phys. Res.** **B84**(1994)214-217.
- Carter G. and Collins R., "The spatial distribution of ions implanted into solids subject to diffusion, local trapping and surface sputtering", **Rad. Eff.** **28**(1976)123-125.
- Carter G., Webb R., Collins R. and Thompson D. A., "The influence of incident flux dependent radiation enhanced diffusion on composition changes of sputtered binary alloy systems", **Rad. Eff.** **40**(1979)119-121.
- Collins R. and Carter G., "The spatial distribution of ion implanted into solids subject to diffusion and surface sputtering", **Rad. Eff.** **26**(1975)181-186.
- Collins R. and Sigmund P., "Pressure relaxation in atomic mixing and preferential sputtering", **J. Appl. Phys.** **72**(5)(1992) 1993-1995.
- Comas J. and Cooper C. B., "Mass spectrometric study of sputtering of single crystals of GaAs by low energy Ar ions", **J. Appl. Phys.** **38**(1967)2956-2960.
- Comas J. and Cooper C. B., "Sputtering yields of several semiconducting compounds under Argon ion bombardment", **J. Appl. Phys.** **37**(1966)2820-2822.
- Conard U. and Urbassek H. M., "Monte Carlo study of fluence dependent mixing and sputtering of isotopic targets under ion bombardment", **Surf. Sci.** **278**(1992)414-426.
- Corbett J. W., Karins J. P., Tan T. Y., "Ion-induced defects in semiconductors", **Nucl. Instrum. and Meth. in Phy. Res.** **182/183**(1981)457-476.
- Cumpson P. J., "Angle-resolved XPS and AES: depth-resolution limits and a general comparison of properties of depth-profile reconstruction methods", **J. of Elect. Spec. and**

Rel. Phen. **73**(1995)25-52.

Cumpson P. J. and Seah M. P., "Elastic scattering corrections in AES and XPS. II. Estimating attenuation lengths and conditions required for their valid use in overlayer/substrate experiments", **SIA** **25**(1997)430-446.

Davis W. D. and Vanderslice T. A., "Ion energies at the cathode of a glow discharge", **Phys. Rev.** **131**(1963) 219-228.

Dearnaley G., "Ion beam modifications of metals", **Nucl. Instrum. and Meth. in Phys. Res.** **B50**(1990)358-367.

DeLouise L. A., "Reactive N_2^+ ion bombardment of GaAs{110}: A method for GaN thin film growth", **J. Vac. Sci. Technol. A** **10**(4)(1992)1637-1641.

DeLouise L. A., "Nitridation of GaAs(110) using energetic N^+ and N_2^+ ion beams", **J. Vac. Sci. Technol. A** **11**(3)(1993)609-614.

Epp J. M. and Dillard J. G., "Effects of ion bombardment on chemical reactivity of Gallium Arsenide", **Chem. of Mtls.** **1**(1989)325-330.

Falcone G., Kelly R. and Oliva A., "Corrections to the collisional sputtering yield", **Nucl. Instrum. & Meth.** **B18**(1987)399-401.

Friedland E. and Fletcher M., "Structure dependence of radiation damage depths after ion implantation", **Nucl. Instrum. & Meth.** **B64**(1992)242-245.

Fujihana T., Sekiguchi A., Okabe Y., Takahashi K. and Iwaki M., "Effects of room temperature carbon, nitrogen and oxygen implantation on the surface hardening and corrosion protection of iron", **Surf. and Coat. Tech.** **51**(1992)19-23.

Fukui Y., Nishimura O., Yabe K. and Iwaki M., "XPS study of iron surface layers implanted with both titanium and nitrogen", **Nucl. Instrum. and Meth. in Phys. Res.** **B59/60**(1981)812-816.

Fulghum J. E., "Determination of overlayer thickness by Angle-Resolved XPS: a comparison of algorithms", **SIA** **20**(1993) 161-173.

Gibbons J. F., Johnson W. S. and Mylorie S. W., "Projected Range Statistics", 2nd Edition, Halstead press, 1975, New York.

Giles M. D. and Gibbons J. F., "Calculation of channelling effects during ion-implantation using the Boltzmann transport equation", **IEEE Tran. Computer-Aided Des. CADA** **362**(1985)362-368.

Goel A. K., Sharma N. D., Mohindra R. K., Gosh P. K. and Bhatnagar M. C., "AES and XPS studies of nitrogen molecule ion implanted aluminium", **Indian J. Phys.** **67**(A1)(1993)75-78.

Grabke H. J., Paulitschke W., Tauber G. and Viefhaus H., "Equilibrium surface segregation of dissolved nonmetal atoms in iron", **Surf. Sci.** **63**(1977)377-389.

- Gries W. H. and Wybenga F. J., "Determination of the centroid depths of shallow impurity profiles by X-ray Fluorescence Spectrometry", **SIA** 3(1981) 251-257.
- Harrison D. E., "Application of molecular-dynamics simulations of ion-bombarded metal surfaces", **Crit. Rev. in Sol. Stat. and Mtl. Sc.** 14(1)(1988)S1-S78.
- Hautala M., "Nuclear stopping in polycrystalline materials-Range distributions and Doppler-shift attenuation analysis", **Phys. Rev.** B30(9)(1984) 5010-5018.
- He Z. Q., Ding X. Y., Hou X. Y. and Wang X., "Molecular-beam epitaxy growth of GaN on GaAs(100) by using reactive nitrogen-source", **Appl. Phys. Lett.** 64(1994)315-317.
- Hedman J. and Martesson J., "Gallium Nitride studied by electron spectroscopy", *Phys. Scr.*, 22(1980)176-178.
- Hofmann S., "Segregation of surfaces and interfaces", **Scanning Electr. Micr.** 3(1985)1071-1086.
- Hoffman S., "Quantitative depth profiling in surface analysis: A review", **SIA** 2(1980)148-160.
- Hofmann S., "Practical surface analysis", second edition, volume 1, eds., Briggs D and Seah M. P., John Wiley & Sons Ltd., 1990, Chichester, UK.
- Hofmann S. and Zalar A., "Auger electron spectroscopy depth profiling of Ni/Cr multilayers by sputtering with N_2^+ ions", **Thin Sol. Films** 60(1979)201-211.
- Holloway P. H. and Bussing T. D., "Quantitative surface analysis of layered materials", **SIA** 18(1992)251-256.
- Hösler W. and Palmer W., "Effects of crystallinity on depth resolution in sputter depth profiles", **SIA** 20(1993)609-620.
- Jablonski A. and Powell C. J., "Formalism and parameters for quantitative surface analysis by Auger electron spectroscopy and X-ray photoelectron spectroscopy", **SIA** 20(1993)771-786.
- Jagielski J., Moncoffre N., Marest G., Thome' L., Barcz A. J., Gawlik G. and Rosinski W., "Radiation-induced segregation of nitrogen-implanted into iron", **J. Appl. Phys.** 75(1)(1994)153-160.
- Jisl R., "Restoration of the depth-concentration profile from Angle-resolved relative intensities of X-ray photoelectron spectra", **SIA** 15(1990)719-726.
- Johar S. S. and Thomson D. A., "Spike effects in heavy-ion sputtering of As, Au and Pt thin films", **Surf. Sci.** 90(1979)319-330.
- Johnson W. L., Cheng Y. T., Rossum M. Van and Nicolet M. A., "When is thermodynamics relevant to ion-induced atomic arrangement in metals", **Nucl. instrum. & Meth.** B7/8(1985)657-665.
- Kelly R., "On the problem of whether mass or chemical binding is more important to

- bombardment induced compositional changes in alloys and oxides", **Surf. Sci.** **100**(1980) 85-107.
- Kelly R., "An attempt to understand preferential sputtering", **Nucl. Instrum. & Meth.** **149**(1978)553-558.
- Kelly R., "Factors determining the compound phases formed by oxygen or nitrogen implantation in metals", **J. Vac. Sci. Technol.** **21**(1982)778-789.
- Kelly R., "The surface binding energy in slow collisional sputtering", **Nucl. Instrum. & Meth.** **B18**(1987)388-398.
- Kelly R., "Bombardment-induced compositional change with alloys, oxides, oxysalts and halides II. the role of segregation", **Nucl. Instrum. & Meth. in Phys.** **B39**(1989)43-56.
- Kelly R., "Bombardment-induced Gibbsian segregation and its role in secondary ion formation", **Nucl. Instrum. & Meth. in Phys.** **B14**(1986)421-428.
- Kelly R., "Ion bombardment modification of surfaces", eds., Auciello O. and Kelly R., Elsevier Science Publishers, 1984, USA.
- Kelly R. and Oliva A., "New estimates of the characteristic depth of sputtering and the bombardment-induced segregation ratio", **Nucl. Instrum. & Meth.** **B13**(1986)283-294.
- Kelly R. and Oliva A., "The theory of preferential sputtering of alloys, including the role of Gibbsian segregation", **NATO ASI Series E** **112**(1986)41-69.
- Kelly R. and Harrison D. E., "A summary of the theory of the preferential sputtering of alloys", **Mater. Sci. Engg.** **69**(1985)449-455.
- Kelly R. and Miotello A., "Ion-beam mixing with chemical guidance II: Analysis of positive heat of mixing", **Surf. and Coat. Tech.** **51**(1992)343-351.
- Kerker G., Mor'an-Lo'pez, Bennemann, K. H., "Electronic theory for segregation at surfaces of transition-metal alloys", **Phys. Rev.** **B15**(1977)638-642.
- Kirschner J., "Surface segregation and its implications on sputtering", **Nucl. Instrum. & Meth. in Phys.** **B7/8**(1985)742-749.
- Kovacich J. A., Kasperkiewicz J., Lichtman D. and Aita C. R., "Auger electron and X-ray photoelectron spectroscopy of sputter deposited aluminium nitride", **J. Appl. Phys.** **55**⁽⁸⁾(1984)2935-2939.
- Kumar K., Mookerjee A. and Kumar V., "Surface segregation in random alloys", **J. Phys.** **F6**(1976)725-738.
- Lam N.Q. and Wiedersich H., "Bombardment-induced segregation and redistribution", **Nucl. Instrum. Meth.** **B18**(1987)471-485.
- Li R. S., "Influence of bombardment-induced Gibbsian segregation on alloy sputtering", **Nucl. Instrum. and Meth. in Phy. Res.** **B82**(1993) 283-290.
- Li R. S., Koshikawa T. and Goto K., "Changes in gold concentration at the surfaces of a Au-

- Cu alloy sputtered at low-temperature", **Surf. Sci.** **121**(1982) L561-L568.
- Liau Z. L. and Mayer J. W., "Limits of composition achieved by ion-implantation", **J. Vac. Sci. Technol.** **15**(5)(1978)1629-1635.
- Lide R. D., (ed), "CRC handbook of chemistry and physics", 72nd edition, CRC press, Boca Raton, 1991, USA.
- Lieske N. and Hezel R., "Formation of Al-nitride films at room temperature by nitrogen-ion implantation into aluminium", **J. Appl. Phys.** **52**(9)(1981)5806-5810.
- Lindhard J. E., Scharff M. and Schiott H. E., "Range concepts and heavy ion ranges", **Mat.-Fys. Medd. K. Dan. Vidensk. Selsk.** **33**(14)(1963)1-42.
- Liu B. M., Zhou X. and Li H. D., "Thermodynamics and growth kinetical consideration of metal-nitride formation by nitrogen implantation", **Phys. Stat. Sol. (a)** **113**(1989)11-21.
- Liversey A. K. and Smith G. C., "The determination of depth profiles from Angle-dependent XPS using maximum entropy data analysis", **J. of Electron Spec. and Rel. Phen.** **67**(3)(1994)439-461.
- Ma E., Liu B. X., Chen X. and Li H. D., "Structural transformation induced by nitrogen implantation in thin metal films", **Thin Solid Films** **147**(1987)49-55.
- Mack M. E., "Ion implantation science and technology", second edition, eds., Ziegler Z. F., Academic Press Inc., Boston, 1988, USA.
- Makimoto T., Kasu M., Bendchimol J. L. and Kobayashi N., "In-situ STM observation of GaAs surfaces after nitridation", **Jpn. J. Appl. Phys.** **36**(1997)1733-1735.
- Malherbe J. B., "Sputtering of compound semiconductor surfaces. I. Ion-Solid Interactions and Sputtering Yields", **Crit. Rev. in Sol. Stat. and Mtl. Sci.** **19**(2)(1994)55-127.
- Malherbe J. B., "Sputtering of compound semiconductor surfaces. II. Compositional changes and Radiation-Induced Topography and Damage", **Crit. Rev. in Sol. Stat. & Mtl. Sci.**, **19**(3)(1994)129-195.
- Malherbe J. B. and Barnard, W. O., "Preferential sputtering of InP: an AES investigation", **Surf. Sci.**, **255**(1991)309-320.
- Malherbe J. B., Hofmann S. and Sanz J. M., "Preferential sputtering of oxides: a comparison of model predictions with experimental data", **Appl. Surf. Sci.** **27**(1986) 355-365.
- Massignon D., Pellerin F., Fontaine J. M., le Gressus C. and Ichinkaw T., "Comparison of the secondary-electron spectrum with the electron loss spectrum on pure Al by low energy electron reflection spectroscopy", **J. Appl. Phys.** **51** (1980)808-811.
- Meharg P. F. A., Ogryzlo E. A., Bello I. and Lau W. M., "Surface damage and deposition on gallium arsenide resulting from low energy carbon ion bombardment", **Surf. Sci.** **271**(1992)468-476.
- Miedema A. R., "Surface segregation in alloys of transition metals", **Metallkunde**

69(1978)455-461.

Miotello A. and Kelly R., "Ion-beam mixing with chemical guidance IV. Thermodynamic effects without invoking thermal spikes", **Surf. Sci.** **314**(1994)275-288.

Miyagawa Y., Ikeyama M., Saitoh K., Nakao S. and Miyagawa S., "High-fluence nitrogen implantation into metals", **Surf. and Coat. Tech.** **83**(1998)275-279.

Moller W. and Eckstein W., "TRIDYN - A TRIM simulation code including dynamic composition changes", **Nucl. Instrum. and Meth. in Phy. Res.** **B2**(1984)814-818.

Moncoffre N. and Jaglieski J., "Redistribution of nitrogen implanted into iron: role of carbon and radiation effects", **Surf and Coat. Tech.** **65**(1994)30-36.

Morrison G. H., Cheng K. C. and Grasserbauer, "General aspects of trace analytical methods IV: Recommendations for nomenclature, standard procedures and reporting data for surface analytical techniques", **Pure and Appl. Chem.** **51**(1979)2243-2250.

Muscat J. P., "Surface segregation in binary alloys: a simple theoretical model", **J. Phys.**, **C15**(1982)867-879.

Nakamura H., Morita K. and Itoh N. "RBS measurement of compositional changes of alloy induced by ion bombardment", **Nucl. Instrum. and Meth. in Phy. Res.** **191**(1981)119-123.

Nefedov V. I. and Baschenko O. A., "Relative intensities in ESCA and quantitative depth profiling", **J. of Electron Spectr. and related Pheno.** **47**(1988)1-25.

Oechsner H., "Sputtering - a review of some recent experimental and theoretical aspects" **Appl. Phys.** **8**(1975)185-189.

Ohira S. and Iwaki M., "Properties of oxide and nitride layers in aluminium produced by high dose ion implantation", **Mat. Sci. and Engg.** **A116**(1989)153-160.

Ohtani S., Watanabe M. and Iwamoto N., "Low energy nitrogen implantation into iron and iron-titanium alloy thin films", **J. Japan Inst. Metals** **59**(8)(1995)851-856.

Okamura H., Misawa S., and Yoshida S., "Epitaxial growth of cubic and hexagonal GaN and GaAs by gas-source molecular beam epitaxy", **Appl. Phys. Lett.** **59**(1991)1058-1060.

Oliva A., Kelly R. and Falcon G., "Comments on collisional sputtering theory", **Nucl. Instrum. & Meth.** **B19/20**(1987)101-108.

Ovrbury S. H., Bertrand P. A. and Somorjai G. A., "The surface composition of binary systems: Predictions of surface phase diagrams of solid solutions", **Chem. Rev.** **75**(5)(1975)547-560.

Paote J. M., "Metastable alloy formation", **J. Vac. Sci. Technol.** **15**(1978)1636-1643.

Pauling L. "The chemical bond" Cornell University Press, 1967, New York.

Pickering H. W., "Ion sputtering of alloys", **J. Vac. Sci. Technol.** **13**(1976)618-621.

Plessis Du J. and Wyk G. N., "A model for surface segregation in multicomponent alloys-Part

III: The Kinetics of surface segregation in a binary alloy", *J. Phys. Chem. Sol.* **50**₃(1989)237-245.

Prabhawalkar D., Kothari D. S., Nair M. R. and Raole P.M., "XPS studies at various temperatures of nitrogen implanted copper", *Nucl. Instrum. Meth.* **B7/8**(1985)147-150.

Pu H. K., Fukuda Y., Baldwin D. A., Murray P. T., and Rabalais J. W., "Interaction of ion beams with surfaces: Dynamics of the reaction of N_2^+ with rhenium", *J. Chem. Phys.* **72**₍₁₁₎(1980)6158-6165.

Pu H. K., Murray P. T., Fukuda Y. and Rabalais J. W., "Absolute cross sections for beam-surface reactions: N_2^+ on Ti from 0.25 to 3.0 keV kinetic energy", *J. Chem. Phys.* **74**(1981)2247-2255.

Pu H. K. and Rabalais J. W., "Ion beam nitridation of the first row transition metals", *J. Chem. Phys.* **85**(1981)2459-2463.

Rabalais J. W. and Marton D., "Atomic collisions in surface chemistry and film deposition", *Nucl. Instrum. & Meth. in Phys. Res.* **B67**(1992)287-295.

Raole P. M., Prabhawalkar P. D., Kothari D. C., Pawar P. S. and Gogawale S. V., "XPS studies of N^{++} implanted aluminium", *Nucl. Instrum. Meth. and Phys. Res.* **B23**(1987)329-336.

Rauschenbach B., "Phase formation in iron after high-fluence ion implantation", *Nucl. Instrum. and Meth. in Phys. Res.* **B80/81**(1993)303-308.

Rauschenbach B. and Hohmuth K., "Formation of Iron Carbonitride and Iron Carbide phases during nitrogen ion implantation", *Crystal Res. and Technol.* **19**(1984)1425-1431.

Rauschenbach B., Kolitsch A. and Hohmuth K., "Iron nitride phase formed by nitrogen ion implantation and thermal treatment", *Phys. Stat. Sol.* **80**(1983)471-482.

Rauschenbach B. and Somer H., "Temperature influence on carbon ion-implantation of iron", *Thin Solid Films* **170**(1989)81-90.

Rauschenbach B., Blasek G. and Dietsch R., "Modification of concentration profile in iron and aluminium by high-fluence implantation of nitrogen and boron ions", *Phys. stat. Sol.* **85**(1984)473-480.

Rauschenbach B., Breuer K. and Leonhardt G., "Characterization of nitrogen-ion implanted aluminium", *Nucl. Instrum. Meth. and Phys. Res.* **B47**(1990)396-403.

Rehn L. E., Okamoto P. R., Potter D. I. and Wiedersich H., "Effect of solute misfit and temperature on irradiation induced segregation in binary Ni alloys", *J. Nucl. Mater.* **74**(1978)242-251.

Richards A. D., Thomson B. E. and Sawin H. H., "Continuum modelling of argon radio frequency glow discharge", *Appl. Phys. Lett.* **50**(1987)492-494.

Robbins M. O. and Falicov L. M., "Electronic theory of ordering and segregation in binary

- alloys -Applications to simple metals", **Phys. Rev. B**25(1982)2343-2357.
- Robinson M. T., " Computer-simulations of the self-sputtering of Uranium", **J. Appl. Phys.** 54(1983) 2650-2659.
- Robinson M. T. and Torrens I. M., "Computer simulation of atomic-displacement cascades in solids in the binary collision approximation", **Phys. Rev. B**9(1974)5008-5024.
- Roush M. L., Andreadis T. D. and Goktepe O. F., "EVOLVE, A Time-dependent Monte-Carlo code to simulate the effects of ion-beam induced atomic mixing", **Rad. Eff.** 55 (1981)119-123.
- Schultz F. and Wittmack K., "Model calculation of ion collection in the presence of sputtering I. Zero order approximation", **Rad. Eff.** 29(1976)31-40.
- Seah M. P., "Practical surface analysis", second edition, volume 1, eds., Briggs D and Seah M. P., John Wiley & Sons Ltd., 1990, Chichester, UK.
- Seah M. P. and Dench W., "Quantitative electron spectroscopy of surfaces: a standard data base for electron inelastic mean free path in solids", **SIA** 1(1979)2-11.
- Seighbahn K., Nordling C., Fahlman A., Nordberg R., Hamrin K., Hedman J., Johansson G., Bergmark T., Karlsson S. E., Lindgren I. Lindberg B., "Atomic, molecular and solid state structure studies by means of electron spectroscopy" Almqvist and Wiksells, 1967, Uppsala.
- Sherwood P. M., in Appendix 3 of "Practical surface analysis", second edition, volume 2, eds., Briggs D and Seah M. P., John Wiley & Sons Ltd., 1992, Chichester, UK.
- Shin J., Geib K. M., Wilmsen C. W., Chu P. and Wieder H. H., "The thermal oxidation of AlGaAs", **J. Vac. Sci. Technol. A** 9(3)(1991)1029-1034.
- Shinno H., Uehara M. and Saito K., "Synthesis of alpha-Fe₁₆N₂ iron nitride by means of nitrogen ion implantation into iron thin films" **J. Mat. Sci.** 32(9)(1997)2255-2261.
- Shirley D. A., "High resolution X-ray photoemission spectrum of valence band of gold", **Phys. Rev. B**5(1972)4709-4714.
- Shulga V. I., "Computer-simulations of single-crystal and polycrystalline sputtering", **Rad. Eff. and def. in sol.** 70 (1983)65-83.
- Sielanko J. and Szyszko W., "Simple Monte-Carlo computer procedure for sputtering and depth parameter determination of implanted ions in amorphous targets", **Surf. Sci.** 161(1985) 101-114.
- Sielanko J. and Szyszko W., "Monte-Carlo simulation of sputtering and saturation phenomena for low-energy noble gas ions", **Nucl. Instrum. and Meth. in Phy. Res.** B16(1986) 340-344.
- Sigmund P., "Theory of sputtering I: sputter yield of amorphous and polycrystalline targets", **Phys. Rev.** 184(1969b)384-416.
- Sigmund P., "Sputtering by Particle Bombardment I", Ed. Behrisch R., Springer-Verlag,

1981, Heidelberg, Germany.

Sigmund P., "Exact solutions of balance equation governing ion-beam-induced composition changes and sputtering", **Appl. Phys. Lett.** **66**(4)(1995)433-435.

Sigmund P., "Alloy and isotope sputtering", **Mat. Fys. Medd. Dan. Vidensk. Selsk.** **43**(1992)255-349.

Sigmund P., "Recoil implantation and ion-beam induced compositional changes in alloys and compounds", **J. App. Phys.** **50**(1979)7261-7263.

Sigmund P., "Mechanisms and theory of physical sputtering by particle impact", **Nucl. Instrum. and Meth. in Phys. Res.** **B27**(1987)1-20.

Sigmund P., Bitsensky I. S., and Jensen J., "Molecule and cluster bombardment: Energy loss, trajectories and collision cascades" **Nucl. instrum & Meth.** **B112**(1-4)(1996)1-11.

Sigmund P. and Oliva A., "Momentum asymmetry and the isotope puzzle in sputtering by ion-bombardment", **Nucl. instrum & Meth.** **B82**(1993)242-254.

Sigmund P. and Oliva A., "Alloy sputtering at high fluence: preferential sputtering and competing effects", **Nucl. Instrum. & Meth.** **B82**(1992)269-282.

Sigmund P. and Gras-Marti A., "Theoretical aspects of atomic mixing by ion beams", **Nucl. Instrum. & Meth.** **182/183**(1981)25-41.

Simson S., Reier T., Schultz J. W. and Buchal C., "Electrochemical and surface analytical characterization of radiation effects after N_2^+ implantation into Al and Al_2O_3 " **Surf. and Coat. Tech.** **83**(1996)49-54.

Sizmann R., "Effect of radiation upon diffusion in metals", **J. Nucl. Mater.** **69&70** (1978)386-412.

Skinner D. K., Swanson J. G. and Haynes C. V., "Ion beam induced compositional changes during Auger sputter profiling of thin Al films on InP", **SIA** **5**(1983)38-42.

Smith G. C. and Liversey A. K., "Maximum entropy - A new approach to nondestructive deconvolution of depth profiles from angle dependent XPS", **SIA** **19**(1992)175-180.

Smith G. C., "Quantitative surface analysis by Auger and X-ray photoelectron spectroscopy **Mater. Characterization** **25**(1990)37-71.

Spicer W. E., Chye P.W., Garner C. M., Lindau I. and Pianetta P., "The surface electronic structure of III-V compounds and the mechanism of Fermi level pinning by oxygen (passivation) and metals (Schottoky barriers)", **Surf. Sci.** **86**(1979)763-788.

Steinbrüchel C., "A simple formula for low-energy sputtering yields", **Appl. phys.** **A36**(1985)37-42.

Strite S., Ruan, J., Li Z., Salvador A., Chen H., Smith D. J., Choyke W. J. and Morkoc H., "An investigation of the properties of cubic GaN growth of GaAs by plasma-assisted molecular beam epitaxy", **J. Vac. Sci. Technol.** **B9**(1991)1924-1929.

- Strydom H. J. and Gries W. H., "A comparison of three versions of Sigmund's model of sputtering using experimental results", **Rad. Eff. Lett.** **86**(1984)145-151.
- Sullivan J. L., Yu W. and Saied, S. O., "ARXPS and LEISS characterization for chemically etched and Ion-bombarded GaAs(100) surfaces", **SIA** **22**(1994)515-519.
- Sullivan J. L., Wronski Z., Saied, S. O. and Sielanko J., "Experimental and simulated XPS depth profiles of Low-energy High-dose nitrogen implanted into aluminium", **Vacuum** **46**(11)(1995)1333-1335.
- Swartzfager D. G., Ziemecki S. B. and Kelly M. J., "Differential sputtering and surface segregation: the role of enhanced diffusion", **J. Vac. Sci. Technol.** **19**(1981)185-191.
- Tarnag M. L. and Fisher D., "Auger depth profiling of thick insulating films by angle mapping", **J. Vac. Sci. Technol.** **15**(1978)50-53.
- Taglauer E. and Heiland W., "Ion impact desorption cross-section of hydrogen and oxygen from metals by light ion bombardment", **J. Nucl. Mater.** **76, 77**(1978)328-331.
- Tanuma S., Ichimura S. and Yoshihara K., "Calculation of 'effective' inelastic mean free paths in solids", **App. Surf. Sci.** **100/101**(1996)47-50.
- Tanuma S., Powell C. J. and Penn D. R., "Calculation of electron inelastic mean free paths II. Data for 27 elements over the 50-2000 eV range", **SIA** **17**(1991)911-926.
- Tanuma S., Powell C. J. and Penn D. R., "Calculation of electron inelastic mean free paths III. Data for 15 inorganic compounds over the 50-2000 eV range", **SIA** **17**(1991)927-939.
- Taylor J. A. and Rabalais J. W., "Reaction of N_2^+ beams with aluminium surfaces", **J. Chem. Phys.** **75**(4)(1981)1735-1745.
- Tersoff J., "New empirical model for the structural properties of silicon", **Phys. Rev. Lett.** **56**(1986) 632-635.
- Terwagne G., Lucas S. and bodart F., "Measurement of sputter yields induced by molecular nitrogen bombardment of aluminium", **Nucl. Instrum. Meth. and Phys. Res.** **B59/60**(1991)93-97.
- Thomas J. H. and Hoffman S., "Ion bombardment induced changes in silicon oxide surface composition studied by X-ray photoelectron spectroscopy", **J. Vac. Sci. Technol.** **A3**(1985)1921-1928.
- Thomson D. A. and Johar S. S., "Non linear sputtering effects in thin metal films", **Appl. Phys. Lett.** **34**(1979)342-345.
- Tougaard S., Zomorrodian A. R., Kornblit L. and Ignatiev, "Summary abstract: Defect induced segregation of nitrogen implanted in copper", **J. Vac. Sci. Technol.** **A3**(3)(1985a)819-820.
- Tougaard S., Zomorrodian A. R., Kornblit L. and Ignatiev, "Defect induced segregation of nitrogen implanted in Cu", **Surf. Sci.** **152/153**(1985b)932-939.

- Troost D., Baier H. U., Berger A. and Monch W., "Nitride layers on GaAs(100) surfaces", **Surf. Sci.** **242**(1991)324-330.
- Tsai J. C. C. and Morabito J. M., "The mechanisms of simultaneous implantation and sputtering by high energy oxygen ions during secondary ion mass spectrometry (SIMS) analysis", **Surf. Sci.** **44**(1974)247-252.
- Tyler B. J., Castner D. G. and Ratner B. D., "Regularization: a stable and accurate method for generating depth profiles from angle dependent XPS data", **SIA** **14**(1989)443-450.
- Wagner W., Rehn L. E., Weidersich H. and Naundorf V., "Radiation-induced segregation in Ni-Cu alloys", **Phys. Rev.** **B28**(12)(1983)6780-6794.
- Wang K. L. and Storms H. A., "A study of Germanium/SiO₂ MIS structure by the use of secondary ion mass spectrometry", **J. Appl. Phys.** **47**(1976)2539-2549.
- Was G. S., "Ion beam modifications of metals: compositional and microstructural changes", **Prog. in Surf. Sci.** **32**(1990)211-332.
- Webb R. P., "Practical surface analysis", second edition, volume 2, eds., Briggs D and Seah M. P., John Wiley & Sons Ltd., 1992, Chichester, UK.
- Webb R. P., Harrison Jr. D. E. and Jakas M. M., "The computer simulations of ion-induced atomic collision cascades", **Nucl. Instrum. and Meth. in Phys. Res.** **B15**(1986)1-7.
- Wehner G. K. and Hajicek D. J., "Cone formation on metal targets during sputtering", **J. Appl. Phys.** **42**(1971)1145-1149.
- Wiedersich H., Andersen H. H., Lam N. Q., Rehn L. E. and Pickering H. W., "Surface Modification and Alloying", eds., J. M. Poate, G. Foti and D. C. Jacobso, Plenum Press, 1983, New York.
- Wiedersich H. and Lam N. Q., "Phase Transformation during Irradiation", Ed. Nolfi F. V. Jr., Applied Science Publishers, LTD, 1983, New York.
- Wiedersich H., Okamoto P. R. and Lam N. Q., "Theory of radiation-induced segregation in concentrated alloys", **J. Nucl. Mater.** **83**(1979)98-108.
- Williamson D. L., Davis J. A., Wilbur P. J., Vajo J. J., Wei R. and Matossian, "Relative roles of ion energy, ion flux, and sample temperature in low-energy ion implantation of Fe-Cr-Ni stainless steel", **Nucl. Instrum. and Meth. in Phys. Res.** **B127/128**(1997)930-934.
- Wilson W. D., Haggmark L. G. and Biersack J. P., "Calculation of nuclear stopping, ion ranges and straggling in the low energy region", **Phys. Rev.** **B15**(1977)2458-2468.
- Wittmack K., "Assessment of the extent of atomic mixing from sputtering experiments", **J. Appl. Phys.** **53**(1982)4817-4820.
- Wittmack K., "Sputtering by Particle Bombardment III", Ed. Behrisch R. and Wittmack K., Springer-Verlag, 1991, Heidelberg, Germany.
- Wittmack K., "Practical surface analysis", second edition, volume 2, eds., Briggs D and Seah

M. P., John Wiley & Sons Ltd., 1992, Chichester, UK.

Wronski Z., "Energy distribution of cathode fall ions in the light of Boltzmann equation", **Vacuum** **40**(4)(1990)387-394.

Wronski Z., private communication.

Xu Q. J., Ding X. M., Hou X. Y. and Wang X., "Nitridation of GaAs surface stimulated by nitrogen glow discharge", **App. Surf. Sci.** **104/105**(1996)468-471.

Yabe K., Nishimura O., Fujihana T. and Iwaki M., "Characterization of the surface layers of various metals implanted with nitrogen", **Surf. And Coat. Tech.** **66**(1994)250-254.

Yamamoto A., Tsubakino H., Ando M., Tarasawa M. and Mitamura T., "Effects of ion-implantation with nitrogen ion on microstructures in deformed iron" **Nucl. Instrum. Meth.** **B121**(1-4)(1997)275-278.

Yamamura Y., "A simple analysis of the angular-dependence of light-ion sputtering", **Nucl. Instrum. Meth.** **B2**(1984)578-582.

Yang H., Brandt O., Trampert A. and Ploog K. H., "Initial stage of growth of GaN/GaAs(001) in plasma-assisted molecular beam epitaxy", **Appl. Surf. Sci.** **104/105**(1996)461-467.

Yu W., thesis "Ion bombardment induced compositional changes in compound semiconductor surfaces studied by XPS combined with LEISS", Surface Science Research Group, Aston University, UK, 1995.

Yu W., Sullivan J. L. and Saied, S. O., "Ion bombardment effects in GeSi(100) surfaces studied by XPS and ISS", **Surf. Sci.** **307-309**(1994)691-697.

Zalm P. C., "Some useful yield estimates for ion beam sputtering and ion plating at low bombardment energies", **J. Vac. Sci. Technol.** **B2**(1984)151-154.

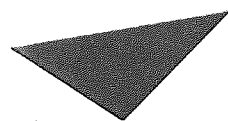
Zangwill A., Physics at surfaces, Cambridge University Press, 1988, Cambridge, U. K.

Zemek J. and Kral J., "Nitrogen implanted in iron: AES and PES study", **Czech. J. Phys.** **B37**(1987)954-973.

Ziegler J. F., "Ion implantation science and technology", second edition, ed. Ziegler J. F., Academic Press Inc., (1988), USA.

H.K.Sanghera and J.L.Sullivan

E.E.A.P., Aston University, Aston Triangle, Birmingham, UK



Aston University

Content has been removed for copyright reasons



ELSEVIER

Nuclear Instruments and Methods in Physics Research B 152 (1999) 65-79

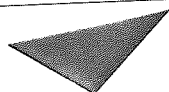
NIM B
Beam Interactions
with Materials & Atoms

A study of low energy high dose nitrogen ion implantation in iron – Effect of ion energy and current density

H.K. Sanghera *, J.L. Sullivan

Surface Science Research Group, Aston University, Birmingham B4 7ET, UK

Received 18 August 1998; received in revised form 17 November 1998



Aston University

Content has been removed for copyright reasons

all

—
fax

016
PII:



ELSEVIER

Applied Surface Science 141 (1999) 57–76

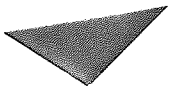
applied
surface science

A study of nitrogen implantation in aluminium—a comparison of experimental results and computer simulation

H.K. Sanghera, J.L. Sullivan *, S.O. Saied

Surface Science Research Group, Aston University, Birmingham B4 7ET, UK

Received 10 June 1998; accepted 18 October 1998



Aston University

Content has been removed for copyright reasons